

UNLV Theses, Dissertations, Professional Papers, and Capstones

8-1-2017

Understanding Progenitors of Gamma Ray Bursts with Multi-Wavelength Properties

Ye Li

University of Nevada, Las Vegas, liye@nao.cas.cn

Follow this and additional works at: <https://digitalscholarship.unlv.edu/thesesdissertations>



Part of the [Astrophysics and Astronomy Commons](#)

Repository Citation

Li, Ye, "Understanding Progenitors of Gamma Ray Bursts with Multi-Wavelength Properties" (2017). *UNLV Theses, Dissertations, Professional Papers, and Capstones*. 3087.
<https://digitalscholarship.unlv.edu/thesesdissertations/3087>

This Dissertation is protected by copyright and/or related rights. It has been brought to you by Digital Scholarship@UNLV with permission from the rights-holder(s). You are free to use this Dissertation in any way that is permitted by the copyright and related rights legislation that applies to your use. For other uses you need to obtain permission from the rights-holder(s) directly, unless additional rights are indicated by a Creative Commons license in the record and/or on the work itself.

This Dissertation has been accepted for inclusion in UNLV Theses, Dissertations, Professional Papers, and Capstones by an authorized administrator of Digital Scholarship@UNLV. For more information, please contact digitalscholarship@unlv.edu.

UNDERSTANDING PROGENITORS OF GAMMA RAY BURSTS WITH
MULTI-WAVELENGTH PROPERTIES

by

Ye Li

Bachelor of Science - Physics
East China Normal University, China
2007

Master of Science - Astronomy
Yunnan Observatories, Chinese Academy of Science
2012

A dissertation submitted in partial fulfillment
of the requirements for the

Doctor of Philosophy - Astronomy

Department of Physics and Astronomy
College of Sciences
The Graduate College

University of Nevada, Las Vegas
August 2017

Copyright by Ye Li, 2017
All Rights Reserved



Dissertation Approval

The Graduate College
The University of Nevada, Las Vegas

August 11, 2017

This dissertation prepared by

Ye Li

entitled

Understanding Progenitors of Gamma Ray Bursts with Multi-Wavelength Properties

is approved in partial fulfillment of the requirements for the degree of

Doctor of Philosophy - Astronomy
Department of Physics and Astronomy

Bing Zhang, Ph.D.
Examination Committee Chair

Kathryn Hausbeck Korgan, Ph.D.
Graduate College Interim Dean

Daniel Proga, Ph.D.
Examination Committee Member

George Rhee, Ph.D.
Examination Committee Member

Amei Amei, Ph.D.
Graduate College Faculty Representative

ABSTRACT

Understanding Progenitors of Gamma Ray Bursts with multi-wavelength properties

by

Ye Li

Dr. Bing Zhang, Examination Committee Chair
Professor of Physics
University of Nevada, Las Vegas

Gamma-ray bursts (GRBs) are among the most brilliant explosions in the universe, named for their intense, seconds-duration γ -ray emission. They are generally classified into two categories according to the durations of their γ -ray emission: the long-duration GRBs (LGRBs) with durations more than 2 seconds, and the short-duration GRBs (SGRBs) with durations less than 2 seconds. Most SGRBs are believed to originate from mergers of compact stars (e.g., neutron star-neutron star and neutron star-black hole; also known as Type I GRBs by their physical mechanism), while the LGRBs are thought to originate from core-collapse of massive stars (Type II). In addition to providing clues about the extreme conditions of their sources, both SGRBs and LGRBs are useful probes of the universe. Because massive stars are in the star forming regions, Type II GRBs are effective to study the star formation history and perhaps to probe Pop III stars. Type I GRBs are very likely to be associated with gravitational wave signals. However, the classification by duration is not a direct reflection of the physical nature of GRBs. In this dissertation, I use multi-wavelength data to study the difference between these two populations (Type I and II), with the purpose of finding a more efficient way to classify GRBs and searching for special cases.

My dissertation consists of four parts. (1) A comprehensive comparison between LGRBs and SGRBs. In order to compare LGRBs and SGRB comprehensively, we gather the properties of prompt emission and host galaxies of 407 GRBs, which is by far the most complete sample of GRBs with such data, from literature. It is found that all of the parameters of

Type II GRBs overlap with those of Type I GRBs, even in two-dimensional (2D) distributions. It indicates that a physical classification of GRBs requires a multi-parameter and multi-wavelength approach. (2) Classifying GRBs with their multi-wavelength properties. With the catalog we compiled, we develop a likelihood method to distinguish Type I GRBs from Type II ones. Only $\sim 1.3\%$ of Type II GRBs and $\sim 3\%$ of Type I GRBs overlap with each other, which is much better than any conventional one parameter method (e.g., the duration T_{90}). (3) A search for Neutron Star-Neutron Star mergers as SGRB-less extended emissions. With the likelihood ratio method, we search, from the LGRB sample, for GRBs with prompt emission properties similar to extended emissions of SGRBs, as well as host galaxy properties similar to that of SGRBs. These sources might be merger-origin GRBs without short spikes, due to off-axis jets. There are ten candidates found and it indicates a free zone/jet zone ratio $k_\Omega \sim 1$. (4) The redshift dependence of lethal GRBs. GRBs are powerful sources. The amount of energy and its form (gamma-ray) emitted by GRBs are so extreme that GRBs must affect the environment of planets nearby. GRBs are proposed to be one of the reasons of mass extinctions on the Earth. It is worthwhile to study the role of GRBs on life evolution in the framework of the universe. Lethal GRBs tend to locate in dwarf galaxies with intense star formation and low metallicity. We investigate the redshift and galaxy type dependence of the event rate of lethal GRBs, and find that there is a relatively low lethal GRB rate in low redshift and early type massive galaxies.

ACKNOWLEDGMENTS

First of all, I want to thank my supervisor, Professor Bing Zhang. He leads me not only in academic studies but also in the secular life. I am always trying to achieve the three characters he suggests as an eligible researcher:

1. Hard working. It is easy to work hard, but it is not easy to always work hard. Bing himself always works very hard. When you receive his emails in the night, weekends, and even holidays, you should remind yourself to work harder.

2. Enjoyng. I was always led by interests when I was an independent without dependent. Thus, ‘enjoy‘ was quite easy for me to achieve. But a dependent arouses the demands to Rights and Desires. Luckily, I still enjoy the time when I work hard and achieve any interesting results. Hope it will go on with me.

3. Being Self-confident. It is the hardest thing for me. I did not realize until I figured out that most of my pain, sometimes self-conceited and sometimes self-abasement, are results of lack of self-confidence. ‘Self-confidence‘ is what I am pursuing, and may need to be pursuing for the whole life of mine – see, lack of self-confidence again.

I also want to thank Bing’s family, Zhao-Hui Huang, Rachel Zhang and Raymond Zhang. They make a model of a “family”, full with love, respect and hard-working. I would never have the confidence to establish a happy family without such an example.

I sincerely appreciate Dr. Xue-Feng Wu and Dr. He Gao, who helped me much as collaborators and good friends. I got lots of benefits from them, in both the research and the daily life. I would like to thank professors in Department of Physics & Astronomy of UNLV, especially Dr. Daniel Proga, Dr. George Rhee, Dr. Stephen Lepp, and Dr. Rebecca

Martin for their classes of a wealth of knowledge. In particular, I thank Dr. Daniel Proga, Dr. George Rhee, and Dr. Amei Amei for serving as my committee members, and for their comments and suggestions which inspired my thoughts and improved my work. Specially Thanks to Dr. Daniel Proga for his suggestions about the three most important elements about a dissertation: hypothesis, original and ‘yours’. He helps me rethink the essence of research.

I would like to thank other members of our group, including Dr. Hou-Jun Lü, Dr. Tong Liu, Dr. Ang Li, Dr. Xiang-Gao Wang, Dr. Yuan-Pei Yang, Dr. Wei-Hua Lei, Dr. Hui Sun, Dr. Wei Deng, Dr. Fuwen Zhang, Dr. Jin-Jun Geng, Dr. Zhi-Bin Zhang, Dr. Shuang-Xi Yi, Dr. Lucas Uhm, Jared Rice, Divya Palaniswamy, for beneficial and joyful discussions. I also thank my colleagues instructing astronomy labs, Dr. David Jeffery, Jonn Boisvert, for all the nights together, sharing the cloudless or cloudy sky, and my classmates Sandamalli Weerasooriya, Timothy Waters, and Keita Todoroki for their help during my study. I want to express my special thanks to our secretary staff Gail Michel-Parsons and the Graduate Affairs Coordinator Keala Kiko for their help with various affairs and paperwork.

I want to express my special thanks to my parents, who are always there along with me, whenever I am happy or sad, successful or frustrated.

Last but not the least, I want to thank my husband, Qiang Yuan. He serves me as a collaborator, a friend, a brother, and a lover. We pursue the fulfillment of both life and science, hand in hand. Also thank my little angel, Zhu-Xuan Yuan, for her appearance in my life.

TABLE OF CONTENTS

ABSTRACT	iii
ACKNOWLEDGMENTS	iv
LIST OF TABLES	ix
LIST OF FIGURES	xi
CHAPTER 1 INTRODUCTION TO GAMMA RAY BURSTS	1
Multiwavelength properties of GRBs	4
Prompt emission	4
Afterglow	7
Host Galaxy	10
Classifications	12
CHAPTER 2 A COMPARATIVE STUDY OF LONG AND SHORT GRBS. I. OVERLAPPING PROPERTIES	19
Introduction	19
Samples	23
Prompt Emission properties	23
Host Galaxy Properties	28
Distribution of properties	37
Prompt emission properties	38
Host galaxy properties	41
Simulated 1-D distribution	45
2-D distributions of the properties	46
Conclusions and Discussion	49
CHAPTER 3 A COMPARATIVE STUDY OF LONG AND SHORT GRBS. II. A MULTIWAVELENGTH METHOD TO DISTINGUISH TYPE I AND TYPE II GRBS	68
Introduction	68

Distributions of GRB parameters	70
Classification	72
Bayesian method to classify Type I and Type II GRBs	72
Prompt versus host properties	74
Combined prompt emission and host galaxy probabilities	77
Conclusion and Discussion	78
CHAPTER 4 SEARCHING FOR NEUTRON STAR-NEUTRON STAR MERGERS AS SGRB-LESS EXTENDED EMISSIONS	83
Introduction	83
Sample selection	86
Extended emission properties	86
A Bayesian method to select SLEE candidates	88
Candidates properties	90
Conclusions	92
CHAPTER 5 CAN LIFE SURVIVE GAMMA RAY BURSTS IN THE HIGH-REDSHIFT UNIVERSE?	100
Introduction	100
Methodology	101
Lethal GRB RATE IN MILKY WAY	104
Lethal GRB rate in other galaxies	106
SDSS DR8 and SDSS/BOSS DR12 Samples	106
Monte Carlo Simulations	110
GRB host galaxies	111
Conclusions and Discussion	112
APPENDIX: PROPERTIES OF GRBS	115
REFERENCES	157

CURRICULUM VITA	184
-----------------------	-----

LIST OF TABLES

Table 1	Statistical results of properties for consensus LGRB/SGRB definition.	64
Table 2	Statistical results of properties for T90 defined LGRB/SGRB.	65
Table 3	Statistical results of Simulated 1D distributions.	66
Table 4	Statistical results of 2D.	67
Table 5	Gaussian fitting results of each parameter for the preliminary type II and I samples of Li et al. (2016).....	72
Table 6	The Gaussian fitting results of each parameter of the EE with data from Kaneko et al. (2015).	88
Table 7	Candidate of SGRB-less Extended Emissions	97-99
Table 8	GRB host galaxy properties	112
Table 9	Basic	116-123
Table 10	Prompt	124-134
Table 11	Host Information from the Spectrum	135-145
Table 12	Host Information from the Image	146-156

LIST OF FIGURES

Figure 1 Left: γ -ray lightcurve of GRB 120412A (bn120412920) with a 1.024 s time resolution (von Kienlin et al., 2014). Right: γ -ray spectrum of GRB 911127 observed by BATSE (Preece et al., 2000). The best-fit Band function, with parameters $\alpha = -0.968 \pm 0.022$, $\beta = -2.427 \pm 0.070$, and $E_0 = 149.5 \pm 2.1$ keV, is shown by the solid line.	5
Figure 2 A canonical lightcurve of X-ray afterglow of GRBs (Zhang et al., 2006).	8
Figure 3 Left: a canonical GRB optical afterglow (Li et al., 2012). Right: spectrum of the optical afterglow of GRB 970508 (Metzger et al., 1997b).	9
Figure 4 Examples of LGRB host galaxies (Blanchard et al., 2016).	10
Figure 5 Examples of SGRB host galaxies. Images are from Fong et al. (2010). Spectra are from Prochaska et al. (2006)(GRB 050509B), Fox et al. (2005) (GRB 050709), and Berger et al. (2005b) (GRB 050724).	13
Figure 6 Left: rest frame peak energy $E_{p,\text{rest}}$ as a function of isotropic energy E_{iso} (Zhang et al., 2012). Right: peak luminosity L_{peak} as a function of spectral lag t_{lag} (Gehrels et al., 2006).	15
Figure 7 Classification flowchart of Type I and Type II GRBs. Multiwavelength information is applied. From: Zhang et al. (2009)	17
Figure 8 Distribution of prompt and host galaxy parameters of LGRBs (red lines) and SGRBs (blue lines). Left panels show distributions with consensus defined LGRBs and SGRBs, and right panels show distributions with T_{90} only defined LGRBs and SGRBs. Dotted lines show distribution of $z < 1.4$ subsamples.	52
Figure 9 Prompt emission VS host galaxy property 2D plots of LGRBs (red dots) and SGRBs (blue dots). Black lines show the rotated new x-axis for the lowest P_{KS}	56
Figure 10 Left: The posterior probability ratios of the prompt emission properties $\log O(\text{II} : \text{I})_{\text{prompt}}$ and host galaxy properties $\log O(\text{II} : \text{I})_{\text{host}}$. Red dots indicate the preliminary Type II GRBs, and blue squares indicate the preliminary Type I GRBs. Green symbols are the highly debated GRBs. Right: The same with the left panel, with supernovae information added. Triangles represent GRBs with SN associations, with spectral (magenta) or photometric (orange) detections. Cyan lines and points show the correction with SN limits included. The GRBs without SN information (red dots and blue squares in the left panel) are plotted as gray for clearness.	75
Figure 11 The distribution of $\log O(\text{II} : \text{I} x)$, without (left) and with (right) the SN limits. GRB 060121, GRB 060505, GRB 060614 and GRB 090426 are labelled with green lines.	77
Figure 12 Left panels: Distribution of prompt and host galaxy parameters of LGRBs (red lines) and SGRBs (blue lines), with fitted Gaussian distributions (red and blue solid lines) overplotted. The dashed red line in [X/H] panel shows the two-Gaussian fitting result of LGRB distribution. Right panels: The Gaussian distributions are normalized to have the integrated probability in observational ranges to be unit. The green lines show the ratio between red lines and blue lines.	79
Figure 13 The probability ratios of prompt emission properties $\log O(\text{LGRB} : \text{SLEE})_p$ and host galaxy properties $\log O(\text{LGRB} : \text{SLEE})_h$ of LGRBs (red dots), SGRBs (magenta dots), and EEs (green dots).	91

Figure 14 Gamma-ray lightcurves of SLEE candidates, compared with SGRBs with EEs (dark blue). Panels from top to down are those with peak luminosities on the order of 10^{49} erg/s, 10^{50} erg/s, and 10^{51} erg/s.	93
Figure 15 X-ray lightcurves of SLEE candidates (red to green), compared with those of LGRBs (grey) and SGRBs with EEs (blue).	94
Figure 16 Left panels: Distribution of prompt properties of the extended emissions of SGRBs (green histogram), with the best fit gaussian overplotted (green solid line). The distribution of SGRBs (blue) and LGRBs (red) are also plotted for comparison. Right panels: The Gaussian distributions are normalized to have the integrated probability in observational ranges to be unit.	95
Figure 17 The number of lethal LGRBs (red solid line) and SGRBs (blue solid line) within 500 Myr as a function of distance r_0 from the Galactic Center. Two vertical black dashed lines indicate the half-mass radius ($r_{M/2}$) and the Earth position, respectively.	105
Figure 18 3-D maps of SDSS DR8 (filled circles) and DR12 (open circles) galaxies with Dec in the range $[0^\circ, 0.5^\circ]$. Colors are encoded with the number of lethal GRBs within 500 Myr at the half mass radius $N_{M/2}$ for each galaxy. The larger the $N_{M/2}$, the more dangerous the galaxy. Left Panel: $10^{10} M_\odot < M_* < 10^{11} M_\odot$; Right Panel: $10^{11} M_\odot < M_* < 10^{12} M_\odot$	107
Figure 19 The number of lethal GRBs within 500 Myr at the half mass radius $N_{M/2}$ in the galaxies at different redshifts. Blue points indicate the SDSS DR8 galaxies, and green dots indicate the SDSS/BOSS DR12 galaxies. Red stars are LGRB host galaxies and magenta squares are SGRB host galaxies. Left panel: $10^{10} M_\odot < M_* < 10^{11} M_\odot$; Right panel: $10^{11} M_\odot < M_* < 10^{12} M_\odot$. GRB hosts are plotted in both panels regardless of their masses.	107
Figure 20 Left panel: The fraction of benign galaxies with $N_{M/2} < 1$ as a function of redshift for the galaxies. SDSS DR8 galaxies (blue line) and SDSS/BOSS DR12 galaxies with $10^{10} < M < 10^{11} M_\odot$ (green line) are shown. Monte Carlo simulated galaxies in the same mass bin (grey) are also shown for comparison. Right panel: The fraction of benign galaxies as a function of redshift according to Monte Carlo simulations. Different black lines denote different mass bins: from bottom up: $10^8 < M_* < 10^9 M_\odot$, $10^9 < M_* < 10^{10} M_\odot$, $10^{10} < M_* < 10^{11} M_\odot$ and $10^{11} < M_* < 10^{12} M_\odot$, respectively. Red line shows the mass weighted fraction, which is similar to the result of mass bin $10^{10} < M_* < 10^{11} M_\odot$. The shaded regions denote the uncertainty range of the sSFR factor between red and blue galaxies for each redshift bin (grey) or for mass-weighted case (orange). The green line shows a Gaussian fit with $G(\text{peak} = 0.96, \mu = -0.24, \sigma = 1.44)$	108

CHAPTER 1

INTRODUCTION TO GAMMA RAY BURSTS

Gamma Ray Bursts (GRBs) are intense, seconds-duration γ -ray flashes of cosmic origin. They were first discovered by the Vela series γ -ray satellites, with peak energies around Mega-electron-Volts (MeV). Temporally, GRBs are non-repeating transients with durations from ~ 0.01 to $\sim 1,000$ seconds. These γ -ray flashes are now regarded as “prompt” emission, which is believed to be originated from the internal dissipation inside the relativistic jets launched by their central engines.

GRBs can also be detected as long-lasting transients in a wide band of radio, infrared (IR), optical, ultraviolet (UV), X-ray, and γ -rays. These so-called “afterglow” emissions are widely accepted to be due to interactions between relativistic jets and the interstellar medium (ISM). The afterglow emission lasts from hours to years. The excellent position accuracy of optical and X-ray observations is very helpful to identify host galaxies, and hence to measure the redshifts, of GRBs. Host galaxies characterize the environment of GRBs, and are very important in understanding the origin of GRBs.

In the following, I introduce briefly the milestones in the history of GRBs.

Discovery (1967-1973): GRB 670702 was the first GRB detected by the human being. It was detected by γ -ray satellites Vela IVa and b on July 2nd, 1967, in $0.2 - 1$ MeV band. The detection was reported in 1973, five years later than the detection (Strong et al., 1974; Klebesadel et al., 1973). Fig. 1 shows the lightcurve of GRB 670702. It consists of two asymmetric peaks with duration ~ 10 seconds each. Another 16 GRBs were also reported in these papers. The presence of GRBs was then confirmed by the IMP-6 satellite (Cline et al., 1973) and the Russian satellite Cosmos 461 (Mazets et al., 1974).

Models (1973-1993): For a long time, the understanding of nature of GRBs developed slowly, mainly due to the lack of sufficient data with good localization. The isotropic distribution of GRBs was noticed in the very beginning, suggesting an extragalactic origin (Cline et al., 1973). However, the deviation from $-3/2$ power law for the $\log N - \log S$ distribu-

tion and the deficit of V/V_{\max} from 0.5 indicate a galactic origin (see Higdon & Lingenfelter (1990) for a review). There were also contradictory results of observations in the early time, e.g., whether there were cyclotron lines or not, made the theoretical modeling ambiguous Nemiroff (1994).

Evidence of extragalactic origin (1992): Things changed after the launch of the Compton Gamma Ray Observatory (CGRO) on April 5th, 1991. One of its four detectors, Burst and Transient Source Explorer (BATSE), is dedicated to detecting GRBs. It was proved that the $\log N - \log S$ distribution of GRBs deviated from the Galactic plane origin, and the nearly isotropic distribution of GRBs clearly supported an extragalactic origin Meegan et al. (1992).

Long and short GRBs (1993): Another important discovery made by BASTE is the establishment of two classes of GRBs. It was first proposed by Mazets et al. (1981) that there might be two types of GRBs, but the evidence was not clear. (Fishman et al., 1993) showed strong evidence that there was a bimodal distribution of durations of GRBs, T_{90} , the timescale during which the cumulative energy ranges from 5% to 95%, with a separation around 2 seconds. It indicated that there were two classes of GRBs. Shorter ones ($T_{90} < 2$ s) have a mean duration of 0.33 seconds, and longer ones have a mean of 26.2 seconds. This bimodal property was confirmed by later observations by other detectors. They are now called as short and long GRBs (SGRBs/LGRBs), respectively, which may have different physical origins.

First detection of afterglow (1997): GRB 970228 was the first GRB with X-ray and optical afterglow detected, thanks to the X-ray Satellite BeppoSAX which was launched on April 30, 1996. There were five instruments on board BeppoSAX. The GRB 970228 first triggered the GRB Monitor (GRBM, 40-700 keV), and was then precisely located by the Wide Field Cameras (WFC, 2-30 keV) (Costa et al., 1997b). The follow-up observation by the Medium Energy Concentrator Spectrometer (MECS, 1.3-10 keV) and Low Energy Concentrator Spectrometer (LECS, 0.1-10 keV) successfully caught its X-ray afterglow, and

located the source with a position accuracy of 50 arcseconds (Costa et al., 1997c,a). The precise location further enabled the detection of the optical afterglow (Groot et al., 1997a), as well as the potential host galaxy (Groot et al., 1997b; van Paradijs et al., 1997; Sahu et al., 1997).

Smoking Gun of cosmological origin (1997): GRB 970508, also discovered by BeppoSAX, was the second GRB with optical afterglow detected (Heise et al., 1997). It was also the first GRB with redshift and radio afterglow. The spectrum of the afterglow emission taken with the 10-m Keck II telescope showed absorption lines with redshift $z = 0.835$ (Metzger et al. 1997). The redshift was further confirmed by the emission lines of its host galaxy (Metzger et al., 1997a,b). The redshift of the spectrum confirms the cosmological origin of GRBs. It indicates that the energy of a GRB is around 10^{53} erg, which turns out challenges most of the models.

Core-collapse origin of LGRBs: The core-collapse of massive stars was proposed to be progenitors of LGRBs (Woosley, 1993). Due to the short life of massive stars, those GRBs are expected to be located in star-forming regions (Paczyński, 1998; MacFadyen & Woosley, 1999). The star forming hosts of GRB 970228, GRB 970508 and GRB 970828 did support the postulation of core-collapse origin of LGRBs Paczyński (1998). The discovery of the association of LGRB 980425 with Type Ic supernova (SN) 1998bw gave a direct evidence of its core-collapse origin.

Up to date, accumulating LGRB sample shows that they are generally located in the brightest region of the hosts with small offsets from the center of the galaxies (Bloom et al., 2002; Fruchter et al., 2006; Blanchard et al., 2016), which further supports the core-collapse origin of them.

Compact star merger origin of SGRBs: During the early stage of GRB studies, it was proposed that SGRBs might originate from mergers of compact stars, e.g., Neutron Star - Neutron Star/Black Hole (Paczynski, 1986; Eichler et al., 1989). However, there was lacking observational evidence for a long time, until the launch of Swift in 2004. SGRBs are

generally fainter and rarer than LGRBs, and thus there was no detection of the afterglow of SGRBs before 2005. Thanks to the quick slew capability of Swift, its X-ray Telescope (XRT) successfully discovered the X-ray afterglow of SGRB 050509B, 53 seconds after the trigger by Burst Alert Telescope (BAT) (Kennea et al., 2005). No SN association was found for the follow-up deep exposure of GRB 050509B (Hjorth et al., 2005a,b). The location of GRB 050509B also had a large offset from the center of its host, a massive elliptical galaxy (Gehrels et al., 2005).

The cumulative SGRB sample shows that their hosts are of various types, early or late (Gehrels et al., 2005; Berger et al., 2005b), and the distribution of their position offsets is consistent with the expectation of compact star mergers (Fong et al., 2010; Kann et al., 2011; Fong & Berger, 2013). The merger origin of SGRBs was further supported by the discovery of the so-called “kilonova/macronova” in GRB 130603B (Li & Paczyński, 1998; Tanvir et al., 2013b; Berger et al., 2013).

Open questions: With BeppoSAX, HETE, Swift and Fermi, many significant progresses in understanding the nature of GRBs have been made in past decades. However, there are still a few fundamental open questions, including 1) the central engine (black hole or magnetar), 2) the mechanism of prompt emission (fireball or magnetization), and 3) the classification.

Multiwavelength properties of GRBs

We focus on the classification of GRBs in this thesis, which requires multiwavelength data. We describe briefly the multiwavelength properties of GRBs in the following.

Prompt emission

Observationally, the prompt emission indicates the sub-MeV γ -ray emission which triggers the detector. Physically, it is expected to be from the “internal” emission from the relativistic jets of GRB progenitors. The “internal” indicates that the dissipation occurs

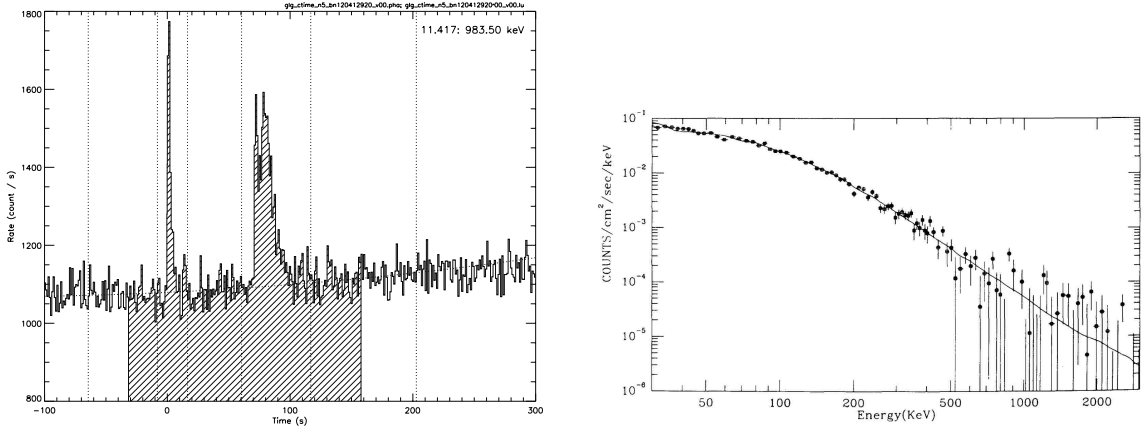


Figure 1 Left: γ -ray lightcurve of GRB 120412A (bn120412920) with a 1.024 s time resolution (von Kienlin et al., 2014). Right: γ -ray spectrum of GRB 911127 observed by BATSE (Preece et al., 2000). The best-fit Band function, with parameters $\alpha = -0.968 \pm 0.022$, $\beta = -2.427 \pm 0.070$, and $E_0 = 149.5 \pm 2.1$ keV, is shown by the solid line.

within the ejecta, via either the fireball or the magnetic process. From this point of view, there is also prompt emission in optical, X-ray or GeV γ -ray bands (Vestrand et al., 2005).

The lightcurve of GRB prompt emission show irregular and non-repeating spikes. The left panel of Fig. 1 shows an example of such lightcurve, for GRB 120412A detected by Fermi/GBM. The time interval which covers the γ -ray emission energy from 0.5% to 95%, namely T_{90} , is usually used to represent the duration of a GRB. T_{90} ranges from around 0.01 seconds to 10,000 seconds. The distribution of T_{90} of BATSE GRBs shows clearly double peaks, with a division at 2 seconds (Kouveliotou et al., 1993). GRBs with $T_{90} < 2$ s are usually called as SGRBs, and those with $T_{90} > 2$ s are LGRBs.

Generally, SGRBs have harder spectra than LGRBs. The hardness ratio (HR), which is the photon flux ratio between two energy bands, is usually employed to describe the hardness of the spectrum. Therefore, LGRBs and SGRBs are also called “long/soft” and “short/hard” GRBs.

The spectra of both L- and SGRBs can be well fitted by a smooth joint broken power-law

function, the Band function (Band et al., 1993),

$$N(E) = \begin{cases} A \left(\frac{E}{100 \text{ keV}} \right)^\alpha \exp \left(-\frac{E}{E_0} \right), & E < (\alpha - \beta)E_0 \\ A \left(\frac{E}{100 \text{ keV}} \right)^\beta \left[\frac{(\alpha - \beta)E_0}{100 \text{ keV}} \right]^{\alpha - \beta} \exp(\beta - \alpha), & E \geq (\alpha - \beta)E_0 \end{cases} \quad (1.1)$$

where $N(E)$ is the photon flux (photon fluence) as a function of energy E , in unit of photon s⁻¹ cm⁻² keV⁻¹ (photon cm⁻² keV⁻¹), α is the low energy power-law index, β is the high energy power-law index, and E_0 is the break energy. The more often quoted E_p is the peak energy in the $E^2 N(E)$ spectrum, and $E_p = (2 + \alpha)E_0$. For LGRBs, the median value of α (β) is -1 (-2.3) (Band et al., 1993; Preece et al., 2000). E_p is around 200 keV, with a large diverse from several keV to MeV. For SGRBs, the median value of α is about -0.5 , and the results of β and E_p are similar to those of LGRBs. Roughly, there is a correlation between α and E_p , as well as the Lorentz factor Γ , $\log E_p = (4.34 \pm 0.48) - (1.32 \pm 0.13)\Gamma$ (Zhang et al., 2007; Sakamoto et al., 2009; Virgili et al., 2012). The right panel of Fig. 1 gives an example of the GRB spectrum, together with a Band function fit.

More frequently, the energy band of the detector is not broad enough, or there are not enough photons to constrain the parameters of the Band function. A cutoff power-law (CPL) function $N(E) = AE^\alpha \exp(-E/E_0)$, or even a simple power-law $N(E) = AE^{-\Gamma}$, are applied to fit the spectra.

The time-resolved spectral analysis reveals quite complex behaviors. The time-resolved hardness ratio (HR) displays hard-to-soft evolution, or hardness-intensity tracking. The energy-resolved lightcurve shows that the pulses are narrower in higher energy bands. For energies below 10 MeV, high energy peaks are earlier than lower energy ones, while for $E > 100$ MeV, opposite behaviors are observed. The low energy delayed phenomena below 10 MeV are usually called “positive lag”, with the spectral lag being defined as the low energy arrival time minus the high energy arrival time $t_{\text{low}} - t_{\text{high}}$. LGRBs generally show positive lags, while SGRBs show negligible spectral lags or even “negative lags”. Thus, the spectral lag is proposed to classify GRBs. However, the lag sometimes depends on the

binning and the detailed analysis method. Furthermore, different pulses of the same burst would sometimes show diverse behaviors, which makes the application of spectral lags to classify GRBs difficult.

Afterglow

Observationally, the afterglow of GRBs represents the emission after the prompt phase. It is usually found by follow-up observations after the trigger of GRBs. When γ -ray detectors are triggered by GRBs, an announcement calling for follow-up observations would be posted in the Gamma-ray Coordinates Network (GCN)¹, or the International Astronomical Union Circulars (IAUC)². If the follow-up X-ray/optical/radio observations find a transient within the error box of the GRB direction, they would be considered as a GRB afterglow. Some satellites, such as Swift and BeppoSAX, have both γ -ray and X-ray instruments, which enable a quick follow-up observation after the trigger.

Theoretically, the afterglow indicates the emission through “external” processes, i.e., the interaction between relativistic jets and the interstellar medium (ISM). High energy electrons accelerated by such external shocks produce broadband emission through synchrotron as well as synchrotron self-Compton (SSC) processes (Paczynski & Rhoads, 1993; Mészáros & Rees, 1997; Sari et al., 1998; Zhang & Mészáros, 2001b), both are characterized by power-law spectra. Due to the blastwave deceleration of the shock, the flux of afterglow emission is expected to decrease following a power-law of time. Therefore, we have

$$F_\nu \propto t^{-\alpha} \nu^{-\beta}. \quad (1.2)$$

A canonical lightcurve of X-ray afterglow is portrayed in Fig. 2. There are five components presented. Component I shows a steep decay phase, with a power-law index from -3 to -8 . Early Swift/XRT follow-ups revealed that it could be extrapolated to the prompt

¹<https://gcn.gsfc.nasa.gov>

²<http://www.cbat.eps.harvard.edu/cbat.html>

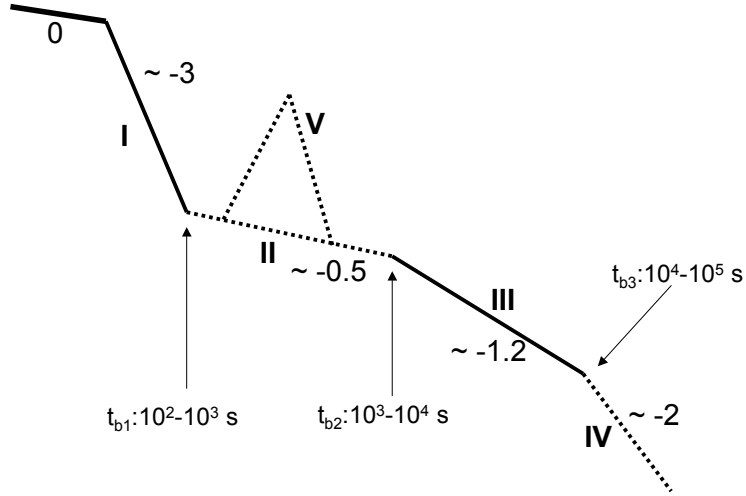


Figure 2 A canonical lightcurve of X-ray afterglow of GRBs (Zhang et al., 2006).

phase. It is therefore believed to be the “tail” of the prompt emission. The steep decay phase breaks into a shallow decay or plateau phase (II), with an index about 0 to -0.7 . The X-ray plateau phase may be followed by a normal decay phase (III) with an index of ~ -1 , or a very steep decay phase with an index steeper than -2 . The former is expected from an external shock model (Zhang et al., 2006; Nousek et al., 2006). The normal decay phase (III) is a result of the standard forward shock sweeping through the ISM, and the plateau is caused by continuous energy injection, which may be a result of different ejecta speed (Rees & Mészáros, 1998; Sari & Mészáros, 2000), or continuous central engine activities (Dai & Lu, 1998; Zhang & Mészáros, 2001a). Sometimes the normal decay phase (III) experiences a “jet-break” to the post-jet-break phase (IV). The X-ray plateau followed by a steep decay is expected to be an internal plateau which may be powered by a magnetar (Troja et al., 2007; Liang et al., 2007b; Rowlinson et al., 2010b, 2013; Lü & Zhang, 2014; Lü et al., 2015). The X-ray flare (V) is believed to be due to re-activities of the central engine. It usually has

similar properties to the prompt phase.

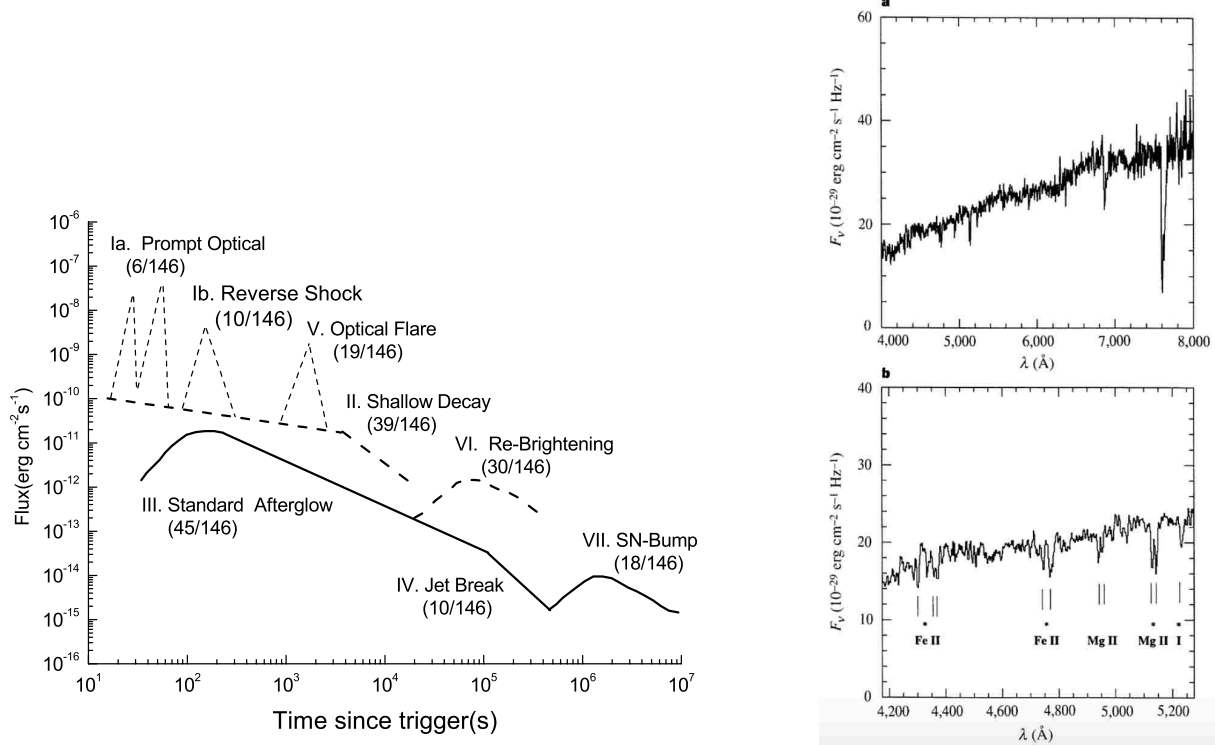


Figure 3 Left: a canonical GRB optical afterglow (Li et al., 2012). Right: spectrum of the optical afterglow of GRB 970508 (Metzger et al., 1997b).

The optical afterglows are usually detected by ground optical telescopes, as well as space instruments such as Swift/UVOT and HST. A canonical GRB optical afterglow is presented in the left panel of Fig. 3. Similar to the X-ray afterglow, there is a shallow decay phase (II), a standard normal decay phase (III), and a jet break phase (IV). Occasionally, there are optical flares (V) detected during the shallow decay phase. Before the shallow decay phase, there could be a smooth increase phase which is consistent with the onset of the forward shock, or steep increase followed by steep decay, which is consistent with the reverse shock.

The optical spectrum is generally power-law, superposed with absorption features. For those with significant absorption, the shape of the spectrum would be modified. The dust extinction A_V could be estimated through fitting to the spectrum. In the spectrum with modest or little absorption, there are often absorption lines superposed in the continuum spectrum (Fynbo et al., 2009), as shown in the right panel of Fig. 3. They are produced by the ISM

in the host galaxy, as well as galaxies in the light of sight. The equivalent widths of these lines reveal the column density of atoms, which could be estimated with the curve of growth (Draine, 2011). If the Ly α line is detectable, the metallicity of the host, $[X/H] = \log(N_X/N_H) - \log(N_{X_\odot}/N_{H_\odot})$, could be estimated for various elements (Cucchiara et al., 2015).

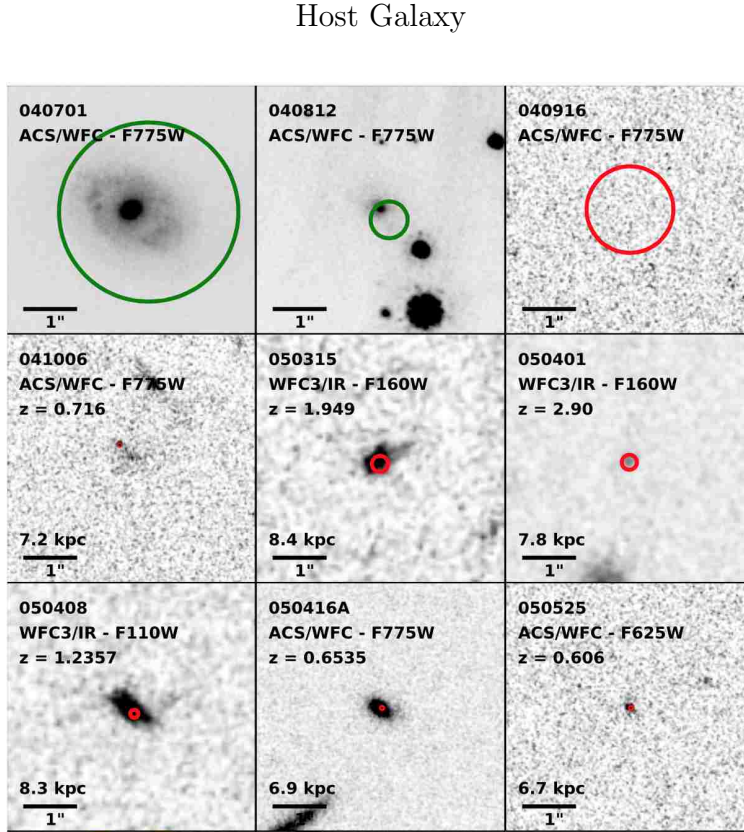


Figure 4 Examples of LGRB host galaxies (Blanchard et al., 2016).

After the GRB afterglows fade out, galaxies could be detected around the GRB locations (Sahu et al., 1997; Bloom et al., 1998, 2002; Chary et al., 2002; Christensen et al., 2004; Savaglio et al., 2009; Krühler et al., 2015). A common question is whether such galaxies are the hosts of GRBs or not. Assuming background unrelated galaxies are spatially uniformly distributed, the chance coincidence probability could be calculated as

$$P_{cc} = 1 - \exp [-\pi r_i^2 \sigma(\leq m)] , \quad (1.3)$$

where $\sigma(\leq m) = \frac{1}{3600^2 \times 0.334 \ln 10} \times 10^{0.334(m-22.963)+4.320}$ galaxy arcsec $^{-2}$ is the surface density of galaxies with magnitude less than m (Hogg et al., 1997). The effective radius r_i depends on the relation between the GRB afterglow and the candidate host galaxy. If the afterglow is well located within the light region of a galaxy, then the effective radius is defined as $r_i = 2R_{50}$, where R_{50} is the half light radius of the galaxy. P_{cc} then represents the probability of finding the afterglow within the detectable light region of the galaxy. It happens often in LGRBs with optical or X-ray afterglows. If the position uncertainty of GRB is large, it is quite easy to find a galaxy within the error box. In this case, the position uncertainty dominates the chance coincidence, and one defines $r_i = 3\sigma_{R_0}$, where R_0 is the distance between the afterglow and the galaxy. It usually happens for GRBs without well-located afterglow. Sometimes, afterglows are well localized. However, no apparent host galaxy is found, i.e., the afterglow is not located within the light region of any galaxy. Then, both the distance of the afterglow from the galaxy and the radius of the galaxy contribute to the chance coincidence, $r_i = (R_0^2 + 4R_{50}^2)^{1/2}$. It usually happens for SGRBs with optical afterglows. In summary, $r_i = \max [2R_{50}, 3\sigma_{R_0}, (R_0^2 + 4R_{50}^2)^{1/2}]$.

Fig. 4 shows some examples of LGRB hosts. They are generally irregular, dwarf, and blue star forming galaxies, sometimes interacting with other galaxies (Sahu et al., 1997; Bloom et al., 1998, 2002; Chary et al., 2002; Christensen et al., 2004; Savaglio et al., 2009; Krühler et al., 2015). The stellar mass M_* determines the total flux of a galaxy, which depends also on the age distribution of the stars and the dust extinction. M_* is usually obtained by fitting the broadband spectral energy density (SED) with stellar population synthesis models, such as Bruzual & Charlot (2003). The stellar mass M_* of LGRBs is around $10^{9.5} M_\odot$, 1/20 of that of the Milky Way. The star formation rate (SFR) can be estimated by emission lines such as H α , H β , and [OIII]. Continuum such as UV, IR may also be used as a probe of the SFR, but with a longer time range. The SFR generally characterize the total star formation in a galaxy, and is regulated by the total stellar mass. The specific SFR, sSFR=SFR/ M_* , is more directly relevant to reveal the physical star-forming status of a galaxy. The LGRB

host galaxies generally have intense star formation. However, their host galaxies usually have low M_* . Thus the SFR of LGRBs is not as large as those of SGRB. The sSFR of LGRBs, however, is generally much higher than that of SGRBs.

The half light radius, R_{50} , within which the circle embraces one-half of the total flux of the galaxy, is usually used to represent the size of a galaxy. It correlates with the stellar mass of the galaxy. The R_{50} values of LGRBs are generally less than 2 kpc.

The position of a GRB within the host galaxy gives the local environment of it. It is usually examined as the offset, R_{off} , of the GRB from the galaxy center (Bloom et al., 2002). A normalized offset, $r_{\text{off}} = R_{\text{off}}/R_{50}$, is also usually used. However, the GRB host galaxies are usually irregular, and the definition of the centers of the galaxies and their R_{50} are sometimes confusing. Moreover, for interacting galaxies, the regions with the highest star formation rate may not be in the centers of the hosts. As a result, the light fraction F_{light} , which is the fraction of region fainter than that at the GRB location, is introduced (Fruchter et al., 2006). For most of the LGRBs, F_{light} is around 100%, indicating that LGRBs lie in the brightest region of the hosts.

Fig. 5 presents some examples of SGRB hosts. SGRB hosts include elliptical galaxies (for example, GRB 050509B and GRB 050724) (Gehrels et al., 2005; Berger et al., 2005b) and irregular ones (for example, GRB 050709). They can be either massive or dwarf. In general, there is no star formation in elliptical galaxies, as evidenced by the lack of emission lines in their spectra. But SGRB hosts could also be star forming (irregular), such as GRB 050709. SGRBs usually locate in faint regions of the hosts, with large offsets from the galaxy centers. Some SGRBs also lie in bright regions with small offsets, e.g., GRB 061006 and GRB 051221 (Fong et al., 2010; Kann et al., 2011; Fong & Berger, 2013).

Classifications

1. Duration classification: LGRBs and SGRB

GRBs are generally classified as LGRB ($T_{90} > 2$ s) and SGRB ($T_{90} < 2$ s) based on their

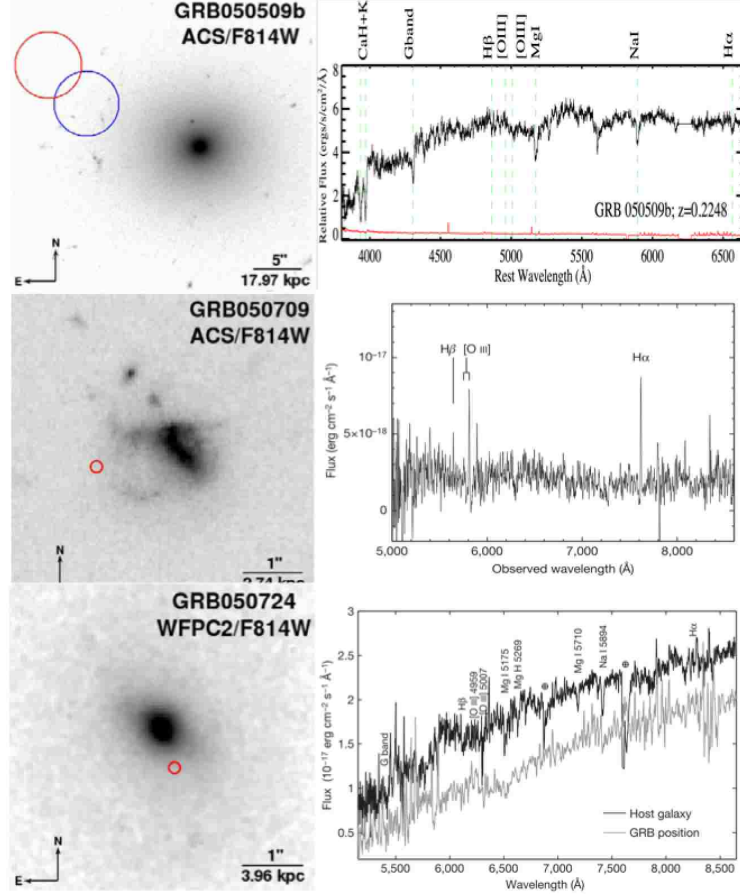


Figure 5 Examples of SGRB host galaxies. Images are from Fong et al. (2010). Spectra are from Prochaska et al. (2006)(GRB 050509B), Fox et al. (2005) (GRB 050709), and Berger et al. (2005b) (GRB 050724).

prompt γ -ray durations. Most LGRBs are consistent with core-collapse of massive stars, and most SGRBs likely originate from mergers of compact stars. Although the names “LGRB” and “SGRB” are defined by the prompt emission durations of GRBs, they are often used as the synonyms of physical classes, i.e., core-collapses and compact star mergers. However, the duration criterion is not always reliable.

The duration itself depends on many factors, including the definition of the duration, energy band, and the sensitivity of the detector (Richardson et al., 1996; Bissaldi et al., 2011; Zhang et al., 2012; Qin et al., 2013). For the BATSE 50 – 300 keV band, T_{90} shows a clear bimodal distribution with a separation of 2 s. For the same energy band, the separation of T_{50} , the duration within which 25% to 75% of its γ -ray fluence is detected, between the

two populations of GRBs range from 0.3 s to 1 s (Kouveliotou et al., 1993; Meegan et al., 1996; Paciesas et al., 1999). T_{90} also depends on detectors. For the BeppoSAX GRBM (40 – 700 keV), the bimodal feature seems to be less pronounced (Frontera et al., 2009), and SGRBs tend to have longer T_{90} . Despite a relatively small sample, INTEGRAL also shows the requirement of two components of T_{90} , although the short component is quite tenuous (Foley et al., 2008; Savchenko et al., 2012; Bošnjak et al., 2014). Swift/BAT (15 – 150 keV) shows that the SGRB sample lies in the tail region of the LGRB component (Sakamoto et al., 2011b), due to harder spectra and lower trigger efficiency of SGRBs. T_{90} of LGRBs in Swift has a peak of 70 s, which is 10 – 30 s for the BATSE sample. The Fermi/GBM (50 – 300 keV) sample shows a similar distribution with that of BATSE GRBs, with a similar division of 2 s (Paciesas et al., 2012; von Kienlin et al., 2014). Therefore, the canonical 2 s division may misclassify GRBs for different detectors.

Moreover, by taking the cosmological redshift effect into account, the intrinsic duration of GRBs should be $T_{90}/(1+z)$. Many lab frame LGRBs would be actually intrinsic SGRBs. Zhang et al. (2009) simulated two high-z GRBs, GRB 080913 ($z = 6.7$) and GRB 090423 ($z = 8.2$), by placing them at $z = 1$, and found that they would appear to be short/hard GRBs.

What's more, the T_{90} criterion is not theoretically well justified. The core-collapse of massive stars can produce GRBs with duration less than 2 seconds, in theory (Janiuk et al., 2008).

There are indeed many GRBs showing disguising properties. Here are some examples.

GRB 060614: This is a LGRB with a 4.5 s hard spike followed by \sim 190 s extended emission (EE) (Gehrels et al., 2006; Norris et al., 2010b). The host galaxy is a dwarf galaxy (stellar mass $M_* = 10^{7.95} M_\odot$) with a low SFR ($0.0035 M_\odot \text{ yr}^{-1}$) (Gal-Yam et al., 2006). The stellar mass of its host is less than any SGRB host galaxy, while the SFR is the lowest one in the LGRB sample. No SN was found, and a very stringent limit of $< 1/100$ of SN 1998bw luminosity was set (Gal-Yam et al., 2006; Della Valle et al., 2006; Fynbo et al., 2006). There

was a putative kilonova reported (Yang et al., 2015). Zhang et al. (2007) suggested it to be of a compact star merger origin.

GRB 060505: It is also a LGRB, with $T_{90} = 4$ s. There is stringent SN limit (Fynbo et al., 2006). Compared with other LGRBs, its host's sSFR is relatively low, and the offset is relatively large. However, it is located in the brightest region of the host (Fynbo et al., 2006; Blanchard et al., 2016).

GRB 090426: It is a SGRB with $T_{90} = 1.24$ s. The redshift ($z = 2.609$) is much larger than any other SGRBs. It is within the LGRB region on the $E_{p,\text{rest}} - E_{\gamma,\text{iso}}$ plot (Antonelli et al., 2009; Levesque et al., 2010b). Compared to other SGRBs, its isotropic energy E_{iso} and peak luminosity $L_{p,\text{isp}}$ are relatively large, and the offset is relatively small. The host is a blue, star-forming galaxy, and the GRB is within the bright region of the host galaxy. However, compared to typical LGRBs, its host is more massive.

2. Other phenomenological classifications

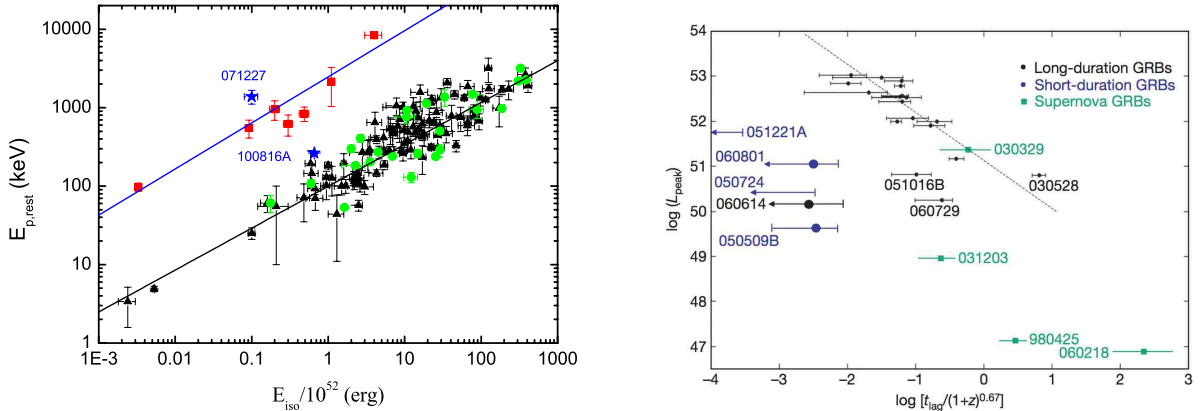


Figure 6 Left: rest frame peak energy $E_{p,\text{rest}}$ as a function of isotropic energy E_{iso} (Zhang et al., 2012). Right: peak luminosity L_{peak} as a function of spectral lag t_{lag} (Gehrels et al., 2006).

There were many methods proposed to assist to classify GRBs, most of which are based on the prompt emission.

The famous “Amati relation” describes the correlation between the rest frame peak energy $E_{\text{p,rest}} = (1 + z)E_{\text{p}}$ and the isotropic γ -ray energy E_{iso} of LGRBs (Amati et al., 2002). The SGRBs turn out to fall onto a parallel track above the Amati relation. As presented in the left panel of Fig. 6, the best fit relation is $E_{\text{p,rest}} = 100 \times (E_{\text{iso}}/10^{52}\text{erg})^{0.51}$ for LGRBs, and $E_{\text{p,rest}} = 2455 \times (E_{\text{iso}}/10^{52}\text{erg})^{0.59}$ for SGRBs. Zhang et al. (2012) suggested that it could be helpful to classify GRBs. However, there are some objects not following these relations, such as the LGRB 071227 locating in the SGRB region, and SGRB 100816A in the LGRB region.

The spectral lags in LGRBs are usually more significant than those of SGRBs. There is also a correlation between the peak luminosity L_{peak} and the spectral lag t_{lag} , as presented in the right panel of Fig. 6 (Norris et al., 2000; Gehrels et al., 2006). The black dots indicate LGRBs from Swift/BAT. The blue dots are SGRBs with L_{peak} estimated with 64 ms binning peak flux. LGRBs generally follow the correlation shown by the dashed line, while SGRBs generally do not. Gehrels et al. (2006) proposed to assist classification with this $L_{\text{peak}} - t_{\text{lag}}$ correlation. However, the value of the spectral lag depends on the binning (Burgess, 2014). In addition, there are many GRBs locating in the intermediate region, such as GRB 051016B, 060729, 031203, 980425.

Lü et al. (2014) defineid an “amplitude” f parameter and an effective f parameter, f_{eff} , to examine the “tip-of-iceberg” effect of GRBs. The f parameter is the ratio between the 1 s peak flux and the background. The f_{eff} parameter is the f when a pseudo-background makes the T_{90} of the GRB to be 2 s. It turns out that LGRBs generally have $f_{\text{eff}} < 1.5$, and SGRBs have $f_{\text{eff}} > 1.5$. It thus could be used to help classify GRBs. However, there are still some GRBs being misclassified by this method.

3. Physical classification: Type I vs. Type II

Since the canonical LGRBs and SGRBs do not always reveal the physical origins of GRBs, Zhang (2006) proposed to distinguish the phenomenological classification (LGRB vs. SGRB) and the physical classification (core-collapse vs. merger). In the same line of SN

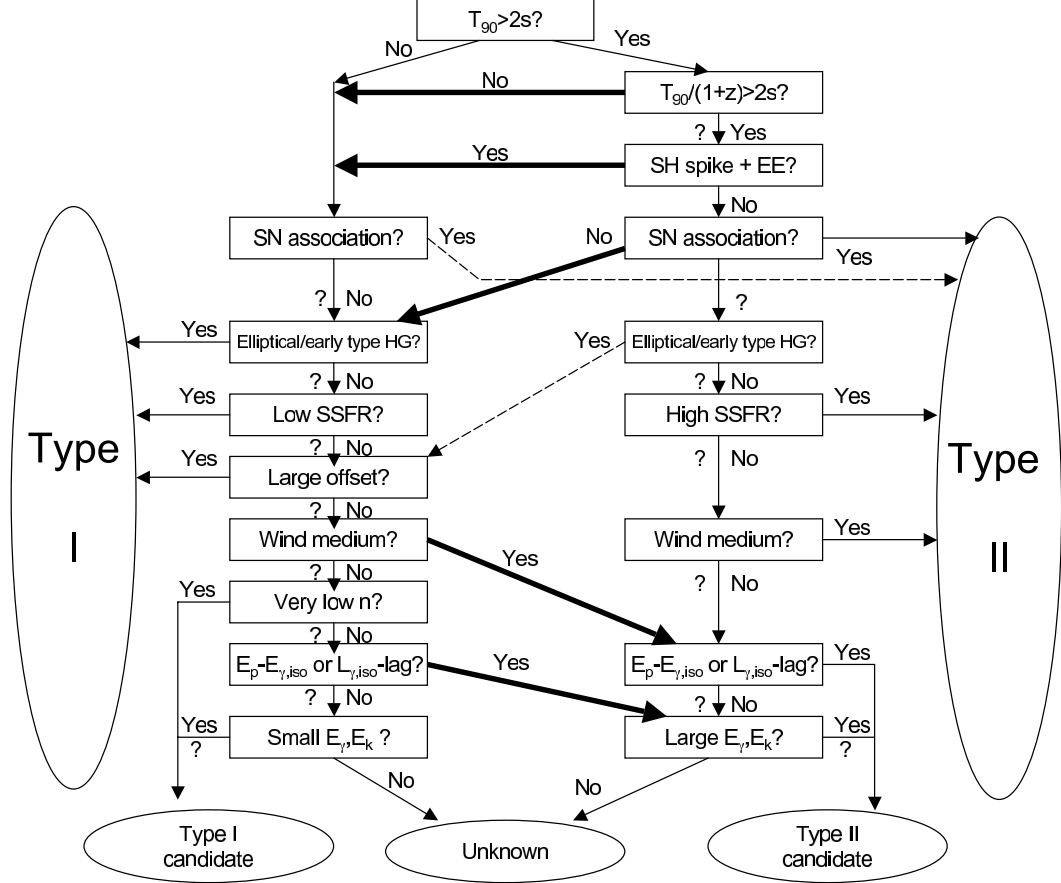


Figure 7 Classification flowchart of Type I and Type II GRBs. Multiwavelength information is applied. From: Zhang et al. (2009)

classification, the compact star merger origin GRBs are named as Type I GRBs, and the core-collapse ones are called Type II GRBs.

Zhang et al. (2009) connected the multiwavelength observational properties with the physical classes of GRBs (Type I or Type II), and suggested a flowchart to classify GRBs. As presented in Fig. 7, the flowchart classifies GRBs into Type I, Type I candidates, unknown, Type II candidate, and Type II GRBs. The T_{90} criterion and short/hard spike with EE pattern give a basic judgement of the type. Type I GRBs require elliptical/early type host galaxies, or low sSFR, or large offset from the centers of their hosts. Type II GRBs require SN association, or High sSFR, or wind medium estimated from the afterglows. An indistinct host galaxy property without SN association leads to an unclear Type I/II candidate or

unknown type. It depends on some putative classification criteria, including whether the $E_p - E_{\gamma,iso}$ and/or $L_{\gamma,iso}$ -lag relation lies in LGRB or SGRB region, wind medium or low ISM density index n , small or large E_γ and E_k .

CHAPTER 2

A COMPARATIVE STUDY OF LONG AND SHORT GRBS. I. OVERLAPPING PROPERTIES

This chapter is part of the following published paper :

Ye Li, Bing Zhang, Hou-Jun Lü, The Astrophysical Journal Supplement Series, Volume 227, Issue 1, article id. 7, 32 pp. (2016)

Introduction

The Gamma-Ray Burst (GRB) duration has a bimodal distribution. It had been seen in the early GRB data (Mazets et al., 1981), and was more clearly seen in the GRB sample collected by Burst And Transient Source Experiment (BATSE) on board the Compton Gamma Ray Observatory (CGRO) (Kouveliotou et al., 1993). The division line between the long-duration GRBs (LGRBs) and short-duration GRBs (SGRBs) is around 2 seconds in the BATSE 50 – 300 keV band. Although the significance of this bimodality and the division line depend on the sensitivity and energy band of the detectors (Richardson et al., 1996; Bissaldi et al., 2011; Zhang et al., 2012; Qin et al., 2013), the authenticity of the bimodal T_{90} distribution is confirmed not only with a larger BATSE sample (Meegan et al., 1996; Paciesas et al., 1999), but also by GRB data collected from other instruments such as BeppoSAX (Frontera et al., 2009), INTEGRAL (Foley et al., 2008; Savchenko et al., 2012; Bošnjak et al., 2014), Swift (Sakamoto et al., 2011b) and Fermi (Paciesas et al., 2012; von Kienlin et al., 2014). The existence of two phenomenological classes of GRBs is firmly established. The connection between these two phenomenological classes of GRBs with two physically distinct progenitor systems are theoretical motivated and observationally confirmed through observations of afterglow and host galaxies of both LGRBs and SGRBs.

LGRBs, typically with duration $T_{90} > 2$ s, are supposed to originate from core-collapse of massive stars (Woosley, 1993; Paczyński, 1998; MacFadyen & Woosley, 1999). A direct

observational support comes from the associations of some LGRBs with Type Ic supernovae (SNe) (Galama et al., 1998; Hjorth et al., 2003a; Stanek et al., 2003; Woosley & Bloom, 2006; Hjorth & Bloom, 2012; Xu et al., 2013b). It strongly suggests that LGRBs are related to the death of massive stars, $> 30 M_{\odot}$ in general. Also, host galaxies of LGRBs are generally dwarf star-forming galaxies with low metallicity, sometimes interacting with other galaxies (Sahu et al., 1997; Bloom et al., 1998, 2002; Chary et al., 2002; Christensen et al., 2004; Savaglio et al., 2009; Krühler et al., 2015). Within their host galaxies, LGRBs are also located in bright star-forming regions with a small offset from the center of the host galaxy (Bloom et al., 2002; Fruchter et al., 2006; Blanchard et al., 2016). Both galactic and sub-galactic environments of LGRBs are consistent with an association of LGRBs with recent star formation, supporting the massive star origin of LGRBs.

SGRBs, typically with duration $T_{90} < 2$ s, are believed to be products of compact star mergers, i.e., neutron star - neutron star (NS-NS) or neutron star - black hole (NS-BH) mergers (Paczynski (1986); Eichler et al. (1989); Narayan et al. (1992), see Berger (2014) for a review). Contrary to LGRBs, so far no SN was found associated with any SGRB and the limits for the existence of a SN are 2-7 magnitudes deeper than typical SNe associated with LGRBs (Fox et al., 2005; Hjorth et al., 2005a,b; Kann et al., 2011; Berger et al., 2013). The absence of SN associations strongly disfavors a massive star origin, but is consistent with the compact star origin of SGRBs. Also, SGRBs reside in diverse types of galaxies, including both late-type galaxies and early-type galaxies, e.g. GRB 050509B (Gehrels et al., 2005) and GRB 050724 (Berger et al., 2005b). The offset of SGRBs from the center of their host galaxy is generally large, which is generally consistent with the theoretical prediction of compact star mergers (Fong et al., 2010; Kann et al., 2011; Fong & Berger, 2013). The compact star merger origin is also supported by the putative discovery of r-process-powered “kilonovae/macronovae” associated with SGRBs 130603B, 060614, and probably 080503, 050709 as well (Li & Paczyński, 1998; Metzger et al., 2010; Tanvir et al., 2013b; Berger et al., 2013; Yang et al., 2015; Gao et al., 2015; Jin et al., 2016a).

However, the duration criterion alone is not always reliable to reveal the physical origin of individual GRBs, i.e., a massive star collapsar or a compact star merger. GRB 060614 is classified as a LGRB by duration since its prompt emission shows 4.5-s hard spikes followed by \sim 190 s extended emission (Gehrels et al., 2006; Norris et al., 2010b). However, no SN was found down to hundreds of times less luminous than SN 1998bw, the Type Ic SN associated with GRB 980425 (Gal-Yam et al., 2006; Della Valle et al., 2006; Fynbo et al., 2006). Moreover, its host galaxy is much more passive than normal LGRB host galaxies, and its afterglow is located at a relatively faint position within the host galaxy (Gal-Yam et al., 2006; Fynbo et al., 2006; Blanchard et al., 2016). There is even a putative kilonova associated with it (Yang et al., 2015). The analogy of GRB 060614 with some SGRBs with extended emission allows Zhang et al. (2007) to suggest a compact star merger origin of this apparently long duration GRB. Another nearby long-duration GRB 060505 also showed a similar puzzle: stringent SN limit, low sSFR host galaxy and large offset (Fynbo et al., 2006; Blanchard et al., 2016). On the other hand, GRB 090426 is classified as a SGRB by duration $T_{90} = 1.24$ s. However, it has a blue, star-forming and interacting host galaxy, its afterglow had a small offset with respect to the galaxy, and it is located in the LGRB region in $E_{\text{p,rest}} - E_{\gamma,\text{iso}}$ plot (Antonelli et al., 2009; Levesque et al., 2010b). All these indicate that it might be of a collapsar origin. Indeed, it can be understood as a long GRB with a short-duration “tip-of-iceberg” detected above the background level (Lü et al., 2014).

Motivated by these observations, Zhang (2006) suggested to separate the phenomenological classification scheme (short vs. long) from the physical classification scheme (compact star origin or Type I vs. massive star origin or Type II). Zhang et al. (2009) presented a detailed study of observational and theoretical motivations of connecting various observational properties with progenitor systems, and suggested that one should apply multi-wavelength criteria (including properties of prompt emission, afterglow emission and host galaxy) to judge the physical category of individual GRBs.

In order to apply these multi-wavelength criteria, the first task is to investigate how

different/similar the two phenomenological types of GRBs are from each other for each individual observational property. In previous papers, some individual properties of LGRBs and SGRBs have been compared, such as prompt emission properties (Zhang et al., 2012), afterglow properties (Gehrels et al., 2008, 2009; Kann et al., 2010, 2011), and host galaxy properties (Fong & Berger, 2013). However, these studies mostly focus on one particular type of properties. In order to get a global understanding of the differences and similarities between LGRBs and SGRBs, we need a comprehensive comparative study of multiple criteria, especially between prompt emission properties and host galaxy properties, both carry important information to diagnose the physical origin of GRBs.

In this paper, we gather prompt emission and host galaxy properties for a large sample of LGRBs and SGRBs detected/observed before June 30th, 2014, and examine how much LGRBs and SGRBs properties overlap with each other. We compare the properties of T_{90} -defined LGRBs and SGRBs, and also the “consensus” LGRBs and SGRBs. The latter are based on the definition in Jochen Greiner’s online catalog,¹ with SGRBs labeled as ‘S’.² Some of the bursts in consensus SGRB sample have T_{90} longer than 2 s, so the classification is not based on duration only. It reflects the consensus of the community, which already takes into account multi-wavelength criteria (e.g. spectral lag, host galaxy type, offset) in the definition. In a sense, the consensus classification of short vs. long GRBs are more analogous to physical classification scheme of Type I vs. Type II by Zhang et al. (2009).

The cosmological parameters $H_0 = 71 \text{ km s}^{-1} \text{ Mpc}^{-1}$, $\Omega_m = 0.27$, and $\Omega_\Lambda = 0.73$ are adopted in this paper. The sample and the observational properties we are interested in are presented in Section 2. Section 3 shows the 1D distributions of each parameter for both LGRBs and SGRBs, which show overlapping behaviors. In Section 4, we show a series of 2-D distribution plots, each with a pair of prompt emission vs. host galaxy parameters, and quantify their overlapping properties. We conclude and discuss the implications of these

¹<http://www.mpe.mpg.de/~jcg/grbgen.html>

²One exception is GRB 061210, which has a 0.13s spike with a 77s extended emission. It does not have a label ‘S’ in Greiner’s catalog, while other catalogs such as Sakamoto et al. (2011b) classify it as SGRB with extended emission. We use it as a SGRB hereafter.

distributions for GRB classification schemes in Section 5.

Samples

Our main sample includes 375 GRBs with spectroscopic redshift measurements in the literature before June 30th, 2014. Also included are 32 GRBs with host galaxy information, even though no spectroscopic redshifts have been reported for these bursts. Altogether we have 407 GRBs in total.

Column 2–4 of Table 9 show the redshift, the method of redshift measurement/estimate, and the reference for each GRB in our sample. They are obtained from refereed papers when possible, otherwise GCN circulars. The redshifts of GRBs are usually measured/estimated via host galaxy emission lines (E), afterglow absorption lines (A), or broad band SED fitting based on photometric properties (P). For a few objects such as GRB 050509B, host galaxies spectra are obtained and only absorption lines are detected. They are indicated by ‘HA’. Redshifts measured with emission lines are favored when possible, since absorption lines strictly speaking only give the lower limit of the redshift. When no emission line is detected, we adopt the highest redshift in absorption line systems if no conflict with photometric redshift is claimed. There are 187 GRBs with emission line redshifts, and 188 GRBs with absorption line redshifts. For those GRBs whose spectroscopic redshift is not available but are included in our sample due to their host galaxy information, we list their photometric redshifts (16 GRBs) if available. One object, GRB 080123, has a redshift reported in Leibler & Berger (2010), but no measurement/estimate method is given. There are 15 GRBs included in our sample that do not have any redshift information.

Prompt Emission properties

Duration

The most basic prompt emission property of GRBs is duration T_{90} , the timescale during which 5% to 95% of its γ -ray fluence is detected. It shows a clear bimodal distribution in

the BATSE 50 - 300 keV Band (Kouveliotou et al., 1993), which is used as the criterion to classify SGRBs and LGRBs. Column 6 and 7 of Table 9 present the observed duration the T_{90} and related reference for each GRB. Also shown in Column 5 is the GRB detector from which the T_{90} is derived. For Swift GRBs, T_{90} values are derived in the 15 – 150 keV band, which are obtained from Sakamoto et al. (2011b) when possible, otherwise from the Swift GRB table³. For Fermi GRBs without Swift detections, the T_{90} (10 – 1000 keV) values from the Fermi GRB table (von Kienlin et al., 2014) are presented. For GRBs before the Swift era, the T_{90} values from BeppoSAX (Frontera et al., 2009) and HETE-2 (Pélangeon et al., 2008) are adopted when possible. Some GRBs were detected from other detectors, e.g. Konus-Wind, INTEGRAL, and Suzaku. Their T_{90} values are obtained from GRB GCN circulars or related publications when available.

Spectral parameters, fluence and flux

The broad band spectra of GRB prompt emission are usually fitted with the so-called “Band function” (Band et al., 1993), which is a smoothly joint broken power law defined by

$$N(E) = \begin{cases} A \left(\frac{E}{100 \text{ keV}} \right)^\alpha \exp \left(-\frac{E}{E_0} \right), & E < (\alpha - \beta)E_0 \\ A \left(\frac{E}{100 \text{ keV}} \right)^\beta \left[\frac{(\alpha - \beta)E_0}{100 \text{ keV}} \right]^{\alpha - \beta} \exp(\beta - \alpha), & E \geq (\alpha - \beta)E_0 \end{cases} \quad (2.1)$$

where α is low energy photon index, β is high energy photon index and E_0 is the break energy. Instead of E_0 , more frequently quoted is E_p , the peak energy in the energy spectrum E^2N , where $E_p = (2 + \alpha)E_0$. The spectral parameters α , β , and E_p in time-integrated spectra are provided in columns 4 – 6 of Table 10 when Band function fitting is available (Amati et al., 2002; Goldstein et al., 2013). Sometimes not all of these parameters are well constrained, due to the narrowness of the detector’s energy band (Swift/BAT, Sakamoto et al. (2011b)), and the low fluence of the bursts. In these cases, a cutoff power law (CPL)

³http://swift.gsfc.nasa.gov/archive/grb_table/

model, which is essentially the first half of Eq.(2.1), or a simple power law (PL) model

$$N(E) = AE^{-\Gamma} \quad (2.2)$$

are used for spectral fitting instead. If a CPL fitting is available, the parameters α and E_p are recorded. If the spectrum can be fitted with a PL model without an E_p estimation, the PL index Γ is recorded in the third column of Table 10. The PL Γ shows a systematic difference from Band α (Virgili et al., 2012). For sake of fair comparison, Γ is presented whenever available, regardless of whether α is provided or not.

Table 10 also shows fluence S_γ and peak flux F_p of each GRB, as well as the respective energy band and the detector used to derive them. The fluence S_γ is given as energy fluence, in units of erg cm $^{-2}$. If not specified, the peak flux is energy flux at the peak time t_p , in units of erg s $^{-1}$ cm $^{-2}$, with a time bin of 1 second. The photon peak flux P_p , in units of photons s $^{-1}$ cm $^{-2}$, is shown with superscript ‘P’. Peak flux from Konus-Wind is usually not binned in 1 second. The binning timescale is labelled in Table 10 using the following convention: 1) 0.004 s; 2) 0.016 s; 3) 0.064 s; 4) 0.128 s; 5) 0.256 s; 6) 2.944 s; 7) 3 s, respectively.

Parameters of BeppoSAX are obtained from Amati et al. (2002) and Frontera et al. (2009) in general. Parameters from BASTE are obtained from Yonetoku et al. (2004) and 5B BASTE catalogue (Goldstein et al., 2013). The 5B BASTE catalogue does not come with traditional GRB names, so we match 5B BASTE catalogue burst IDs with traditional GRB names by requiring the positional difference smaller than 10 degrees and a close temporal match (typically the difference less than a few seconds). Spectral parameters from HETE-II are obtained from Sakamoto et al. (2005a) and Pélangeon et al. (2008), covering 2-400 keV in general. Spectral parameters from INTEGRAL are obtained from Bošnjak et al. (2014) and Foley et al. (2008), covering a time span from 2002 to 2012. While Bošnjak et al. (2014) makes a joint IBIS/SPI spectral fit covering 20-1000 keV, spectral fitting in Foley et al. (2008) uses data from IBIS only, covering 20-200 keV. So data from Bošnjak et al.

(2014) are favored if parameters of the same burst are provided in both catalogs. Spectral parameters from Fermi/GBM are obtained from the Fermi GRB catalog (Gruber et al., 2014), typically covering 10 - 1000 keV. Sometimes, parameters from Konus-Wind, RHESSI or Suzaku/WAM are used, obtained from GCN circulars in general. Otherwise, Swift-BAT parameters are presented, including Γ , fluence and flux for those with PL as the best fit model, and α , E_p , fluence and flux for those with CPL as the best fit model.

$E_{\gamma,\text{iso}}$ and $L_{\text{p},\text{iso}}$

The isotropic gamma-ray energy $E_{\gamma,\text{iso}}$ and peak luminosity $L_{\text{p},\text{iso}}$ in the cosmological rest frame $1 - 10^4$ keV are estimated with parameters presented in the previous sections. The estimated values are shown in Column 8 and 9 of Table 9.

The isotropic energy $E_{\gamma,\text{iso}}$ is estimated as

$$E_{\gamma,\text{iso}} = 4\pi D_L^2 S_\gamma k / (1 + z), \quad (2.3)$$

where S_γ is the γ -ray fluence, in units of erg cm^{-2} , D_L is the luminosity distance estimated with redshift, and k is a k -correction factor from the lab frame to the bolometric rest frame, defined as

$$k = \frac{\int_{1/(1+z)}^{10^4/(1+z)} EN(E)dE}{\int_{e_{\min}}^{e_{\max}} EN(E)dE}. \quad (2.4)$$

Here e_{\max} and e_{\min} are the observational energy range of fluence, presented in Column 8 of Table 10, $N(E)$ denotes the photon spectrum of GRBs. All the GRB spectra are assumed to be a Band function as shown in Eq. 2.1, with the spectral parameters listed in Table 10. For those GRBs fitted with a CPL, $\beta = -2.3$ is assumed. For the GRBs with PL fitting only, the rough correlation between power law index Γ and the peak energy E_p , i.e.

$$\log E_p = (4.34 \pm 0.48) - (1.32 \pm 0.13)\Gamma \quad (2.5)$$

is used to estimate E_p (Zhang et al., 2007; Sakamoto et al., 2009; Virgili et al., 2012). For bursts without α and β , $\alpha = -1.0$ and $\beta = -2.3$ are assumed for LGRBs, and $\alpha = -0.5$, $\beta = -2.3$ for SGRBs (Band et al., 1993; Preece et al., 2000). For the bursts without redshift estimation, $z = 2$ is assumed for LGRBs, and $z = 0.5$ for SGRBs. One exception is GRB 020410, for which $z = 0.5$ is assumed according to the redshift estimation based on the possible SN detection in Levan et al. (2005).

The peak luminosity $L_{p,\text{iso}}$ is estimated as

$$L_{p,\text{iso}} = 4\pi D_L^2 F_p k, \quad (2.6)$$

with the same k correction as $E_{\gamma,\text{iso}}$ estimation, and the peak flux F_p in units of $\text{erg s}^{-1} \text{cm}^{-2}$. For GRBs with photon peak flux P_p (in units of $\text{photon s}^{-1} \text{cm}^{-2}$) reported only, F_p is estimated from P_p

$$F_p = P_p \frac{\int_{e_{\min}}^{e_{\max}} E N(E) dE}{\int_{e_{\min}}^{e_{\max}} N(E) dE}, \quad (2.7)$$

where e_{\max} and e_{\min} define the observational energy range of flux, presented in Column 10 of Table 10.

Amplitude f and f_{eff}

Lü et al. (2014) introduced the amplitude parameters f and f_{eff} to assist classification of GRBs. The f parameter is defined as the ratio between 1-s peak flux and background flux $f = \frac{F_p}{F_B}$, which measures how bright the brightest peak of a burst is above the background level. The effective amplitude parameter is defined as $f_{\text{eff}} = \frac{F'_p}{F_B}$, which is the amplitude of a pseudo GRB which was scaled down from the original burst until the new duration T_{90} is shorter than 2 s. It reflects the measured f value for an intrinsically long GRB to be confused as a short GRB when the bulk of the emission is buried below the background. Since short GRBs already have $T_{90} < 2$ s, their f_{eff} parameter is the same as the f parameter. Lü et al. (2014) showed that the f_{eff} values of long GRBs are typically smaller than 2, which means

that the “tip-of-iceberg” effect cannot give very high-amplitude short GRBs. In contrast, short GRBs typically have $f_{\text{eff}} = f$ greater than 2. As a result, the f and f_{eff} parameters are useful parameters to diagnose the physical origin of a burst. We include all the f and f_{eff} parameters published in Lü et al. (2014)⁴ in our analysis. The f and f_{eff} values of later Swift GRBs are also calculated using the same method of Lü et al. (2014). They are presented in the last two columns of Table 9.

Host Galaxy Properties

In general, GRB host galaxies can be detected with deep observations after the GRB afterglows fade away. With images of the host galaxies, morphological properties such as galaxy size R_{50} , angular and physical offsets of GRBs from the center of host galaxies, in units of arcsec θ_{off} and kpc R_{off} , as well as normalized offset $r_{\text{off}} = R_{\text{off}}/R_{50}$, can be obtained. If multi color photometric properties are available, especially if the rest frame 4000 Å is covered, the host galaxy stellar mass M_* may be estimated through stellar population syntheses. With emission lines, which are quite common in GRB host galaxies, physical properties such as SFR and metallicity [X/H] can be studied. Together with the stellar mass information, one can estimate specific SFR (sSFR), average SFR per unit stellar mass. We go through the refereed papers and GCN reports related to each GRB to gather host galaxy property information and present them in this section. For each GRB with redshift, we use ADS⁵ to search for papers and reports with the GRB name in the title and abstract, and use SIMBAD⁶ to search for papers and reports that refer to the burst, regardless of in which parts of the paper and reports it is mentioned.

⁴Available at <http://grb.physics.unlv.edu/f/data.txt>

⁵http://adsabs.harvard.edu/abstract_service.html

⁶<http://simbad.u-strasbg.fr/simbad/>

Stellar mass, Star formation rate, and Metallicity

Stellar mass, M_* , which is the main control of luminosity, SFR, and metallicity of a galaxy, is the most important host galaxy parameter. It is also used to estimate the specific SFR (sSFR), defined as SFR per unit stellar mass (SFR/M_*), which shows the intrinsic star formation status of a galaxy. Broad band spectral energy distribution (SED) fitting to stellar population synthesis models is the most common method to estimate M_* . For most of the bursts in our sample, the SED-fitted M_* is collected from the catalogs of Savaglio et al. (2009) and Leibler & Berger (2010). Others are obtained from individual papers. When SED estimated M_* is not available, a single band luminosity such as the K band magnitude (Svensson et al., 2010) or infrared magnitude (Laskar et al., 2011) is used as the indicator of stellar mass. In these cases, the uncertainty is larger than one order of magnitude. For GRBs from Laskar et al. (2011), upper limits of M_* are used when only upper limits are available. For those with detections, $M_{70\text{Myr}}$ are used since 70 Myr is a typical age of LGRB hosts at $z \sim 1$ (Leibler & Berger, 2010). The values of M_* and the method to estimate them are presented in column 4 and 5 of Table 11.

SFR indicates average rate of star formation in a “recent” time range. It can be estimated with emission lines, ultra-violet (UV) light, infrared (IR), radio, and X-rays (see Kennicutt (1998) and Kennicutt & Evans (2012) for reviews). Among different diagnostics, emission lines such as H α , H β , and [OII] represent the most recent 0-10 Myr SFR, best matching the life of LGRB progenitor, stars with $> 30 M_\odot$ (Kennicutt & Evans, 2012). Among different emission lines, H α is the best indicator of SFR, due to its relative strength, small dust extinction and independence of metallicity. However, for objects with redshift larger than 0.4, H α shifts out of the optical band and requires an infrared detection. For these cases, H β and [OII] emission lines become good indicators instead in the optical band, which are applicable up to the redshift 0.9 and 1.4, respectively. The benefit of H β over [OII] is its independence of metallicity. Moustakas et al. (2006) shows that the dependence of [OII] estimated SFR on metallicity is weak in the range of $8.2 < 12+\log(\text{O/H}) < 8.7$, but is

significant in the range of $12+\log(\text{O/H}) < 8.2$ and $12+\log(\text{O/H}) > 8.7$. Since a lot of GRB hosts show $12+\log(\text{O/H}) < 8.2$ (Savaglio et al., 2009; Krühler et al., 2015), $\text{H}\beta$ is, in general, a better indicator than [OII]. However, [OII] is usually stronger than $\text{H}\beta$. So [OII] is more frequently used as the SFR indicator for galaxies with redshifts as high as 1.4. For objects with redshifts higher than 2, the $\text{Ly}\alpha$ emission line shifts into optical and may be used as an SFR indicator (Milvang-Jensen et al., 2012). The SFR and the method used to estimate it are shown in column 6 and 7 of Table 11, with column 3 presenting the instrument offering the spectrum. For those without SFR information, column 3 gives the instruments of spectral observations that provide redshift information. The criteria mentioned above are used.

The two largest LGRB SFR catalogs are from Savaglio et al. (2009) and Krühler et al. (2015). Savaglio et al. (2009) summarized emission line information of GRBs before Dec 2006 and presented a systematic estimation of SFR using $\text{H}\alpha$, $\text{H}\beta$, [OII] and UV, respectively. We record the SFR of each GRB host according to the criteria mentioned above. Krühler et al. (2015) estimated the host galaxy SFR for GRBs later than April 2005, with emission line luminosities obtained from the VLT/X-Shooter spectra. Due to the infrared coverage of VLT/X-Shooter, Krühler et al. (2015) extended $\text{H}\alpha$ detection to $z \sim 2.5$. It enables SFR estimation with $\text{H}\alpha$ and better dust extinction A_V estimation. There are only two objects presented in both of these two catalogues, GRB 050416A and GRB 051022A, with redshift 0.653 and 0.807 respectively. Krühler et al. (2015) showed that their Balmer decrement estimated A_V are $1.62_{-0.36}^{+0.36}$ mag and $1.86_{-0.13}^{+0.17}$ mag, respectively, and made dust extinction correction with these values. It turns out that the estimated SFR of these two bursts by Krühler et al. (2015) are around two times larger than those estimated by Savaglio et al. (2009), who applied a mean $A_V = 0.53$ to their LGRB sample due to the lack of A_V estimate for both of bursts. As both of GRB 050416A and GRB 051022A have dust extinction A_V much larger than $A_V = 0.53$, the diversity between these two papers can be easily accounted for by the discrepancy of the A_V applied. On the other hand, the average A_V and SFR for the same redshift range are consistent with each other between Krühler et al. (2015) and

Savaglio et al. (2009), so that these two GRBs do not indicate a statistically inconsistency between these two catalogs.

Two largest SGRB SFR catalogs are from Savaglio et al. (2009) and Berger (2009), each presenting 5 bursts. Three of their host galaxies, GRB 051221, GRB 050709 and GRB 061006, show active star formation with emission lines and their emission-line-estimated SFRs show consistency between these two papers. The other two, GRB 050509B and GRB 050724, have passive hosts without emission lines. While the emission-line-estimated SFR upper limits are < 0.1 and $< 0.05 M_{\odot} \text{ yr}^{-1}$, respectively (Berger, 2009), their UV-estimated SFRs are as high as 16.87 and $18.76 M_{\odot} \text{ yr}^{-1}$, respectively (Savaglio et al., 2009). The discrepancy could be understood by the difference of the age of stars that emission lines and UV light trace, i.e., $0 - 10$ Myr for emission lines and $10 - 200$ Myr for UV light. Since LGRBs originate from stars with mass $> 30 M_{\odot}$ and age ~ 10 Myr, emission lines are better diagnostics than UV light. As a result, we do not include UV SFRs in our analysis even though we still list them in Table 11 for completeness.

Metallicity, abundance of elements other than hydrogen and helium, is generally described by the number density ratio between a specific element and hydrogen. It may be estimated with absorption lines or emission lines. Although these two methods provide metallicity estimation for somewhat different regimes in GRB host galaxies, they show consistency in GRB 121024A, which has both emission- and absorption-line estimated metallicities (Friis et al., 2015). The two methods also cover complementary redshift ranges, so we include both of them here. We caution that one needs more objects with both absorption lines and emission lines to provide metallicity estimates to confirm the consistency between the two methods. Metallicities estimated by absorption lines are generally described by $[X/H] = \log(N_X/N_H) - \log(N_{X_{\odot}}/N_{H_{\odot}})$, where N_X indicates column density of element X. Metallicities estimated by emission lines, on the other hand, are generally described by $12 + \log(O/H)$, with solar value $12 + \log(O/H)_{\odot} = 8.69$. In order to be consistent with each other, we convert $12 + \log(O/H)$ to $[X/H]$ with $X = O$ by $12 + \log(O/H) - 8.69$ (Asplund et al., 2009). The estimated values

as well as the corresponding methods are presented in column 8 and 9 of Table 11.

Emission line ratios are the most common diagnostics for late type galaxy metallicity (Kewley & Dopita, 2002; Kobulnicky & Kewley, 2004; Pettini & Pagel, 2004). This method estimates the metallicities in HII regions of the host galaxy. It is based on photoionization models (Kewley & Dopita, 2002) and local HII region and galaxies observations (Pettini & Pagel, 2004). If the host galaxy redshift is larger than 0.2, it is hard to obtain a spatially resolved spectrum of a specific point. Since most GRBs have redshifts greater than 0.2, emission-line-estimated metallicity is generally the luminosity-weighted metallicity of the hosts.

The largest two LGRB samples with metallicity measurements are Savaglio et al. (2009) and Krühler et al. (2015). Savaglio et al. (2009) used different emission line diagnostics for different GRBs, due to different available emission lines. A direct estimation comes from electron temperature T_e , which requires a comparison of different ionization lines with the same elements (Izotov et al., 2006). This is only valid for a few cases where both $[\text{OIII}]\lambda 4363$ and $[\text{OIII}]\lambda 4959, 5007$ are available. For most cases, other indicators with higher uncertainties are generally used. If $\text{H}\alpha$ is detected, for GRBs with $z < 0.4$ in general, $\text{O3N2} = \log\{([\text{OIII}]\lambda 5007/\text{H}\beta)/([\text{NII}]\lambda 6583/\text{H}\alpha)\}$ is used, with (Pettini & Pagel, 2004)

$$12 + \log(\text{O/H}) = 8.73 - 0.32 \times \text{O3N2}. \quad (2.8)$$

If $\text{H}\alpha$ is not available, for most high redshift GRBs,

$$\log R_{23} = \log\{([\text{OII}]\lambda 3727 + [\text{OIII}]\lambda 4959, 5007)/\text{H}\beta\} \quad (2.9)$$

are used for metallicity estimation, with

$$\log O_{32} = \log\{([\text{OIII}]\lambda 4959, 5007)/([\text{OII}]\lambda 3727)\} \quad (2.10)$$

as an indicator of the ionization parameter. However, the relation between R_{23} and $12+\log(\text{O/H})$ is double-valued. Following Kewley & Ellison (2008), equation (18) of Kobulnicky & Kewley (2004) is applied for the upper branch and Kewley & Dopita (2002) for the lower branch. These R_{23} metallicities are corrected to O3N2 values as suggested by Kewley & Ellison (2008). Due to the lack of [NII], which is usually needed to decouple the double value effect, the two values are sometimes both listed (Savaglio et al., 2009). Krühler et al. (2015) used a combination of the methods by estimating the probability density profile (PDF) of metallicities for each GRB. Benefiting from IR spectra with $\text{H}\alpha$ lines and [NII] lines, their values do not encounter the double value problem.

The largest SGRB sample is from Berger (2009). The R_{23} method is used and only the upper branch is presented, as suggested by Kobulnicky & Kewley (2004). However, the event available for O3N2, i.e. GRB 061210, shows $12+\log(\text{O/H})=8.47$ by the method applied in Savaglio et al. (2009), which is 0.35 smaller than the value $12+\log(\text{O/H})=8.82$ estimated with the upper R_{23} branch. It indicates that the upper R_{23} branch method may overestimate the metallicities of SGRB host galaxies, and the diversity of SGRB and LGRB metallicities may not be as significant as shown. However, due to the complexity of metallicity estimation and the lack of $\text{H}\alpha$ and [NII] line information of other three events, GRB 061006, GRB 070724 and GRB 051221A, we still present the values of Berger (2009) in Table 11. We notice here that the true metallicities may be a factor of 0.4 smaller than the listed values. More observations, especially of the IR spectra, are required to verify the metallicities of these SGRBs.

With the absorption line equivalent width (EW) and line profile, column densities of various elements N_X along the line of sight can be estimated (Draine, 2011). By comparing with hydrogen column density N_H obtained from $\text{Ly}\alpha$, metallicities $[\text{X}/\text{H}]=\log(N_X/N_H)-\log(N_{X_\odot}/N_{H_\odot})$ can be estimated for various elements X, such as Oxygen. The condition to produce absorption lines is that the probed regions are cooler than those probed with emission lines. These absorption line regions are estimated to be around 100 pc away from

GRBs (Vreeswijk et al., 2012; Krühler et al., 2013; D’Elia et al., 2014), so that they can reveal the properties of the local environment of GRBs. Since generally the detection of Ly α absorption line is needed, the absorption line metallicity estimation is generally valid for high redshift GRBs, i.e. $z > 1.8$ in general. If metallicity is estimated for more than one element, the value for the most abundant element is recorded, e.g., in the order of O, C, N, Mg, Si, Fe, S (Asplund et al., 2009). The largest absorption line estimated metallicity catalog is from Cucchiara et al. (2015), and other cases are obtained from individual papers. These values are labelled as ’A’ in the metallicity method column and the specific elements used to estimate it is also recorded. Lower limits for metallicity is usually due to saturation of the absorption lines, e.g., in GRB 140515A. Although these values are lower limits in definition, they are generally used as the metallicity in the literature, so we treat them as the measured metallicity in the rest of the paper. The upper limits are usually due to non-detection of metal lines, e.g. in GRB 140518A.

Morphological properties: galaxy size and offset

Morphological properties of GRB host galaxies are obtained from optical images. Due to the faintness of GRB hosts, it usually requires deep and high angular resolution photometric observations, e.g. with Hubble Space Telescope (HST). The identification of a GRB host galaxy is not straightforward (Bloom et al., 2002; Berger, 2010; Church et al., 2011; Tunnicliffe et al., 2014). If the position uncertainty is large, there might be many galaxies within the error box. Sometimes, especially for SGRBs, the offset of the GRB location from the center of host galaxy may be larger than the size of host galaxy itself, so that it is not straightforward to identify the host galaxy without a probability argument. It is also possible that the host galaxy of a particular GRB is too faint to be detected, but there is a galaxy near the afterglow location by chance, so that it may be misidentified as the GRB host. Following Bloom et al. (2002), a chance coincidence probability P_{cc} is usually defined

as the possibility of a non-host galaxy identified as the host galaxy by chance

$$P_{\text{cc}} = 1 - \exp(-\pi r^2 \sigma(\leq m_i)), \quad (2.11)$$

where $\sigma(\leq m_i)$ is the surface densities of the galaxies with magnitude $\leq m_i$, and r is the effective radius, which is a function of position uncertainty, offset and the size of a candidate host galaxy. In order to indicate how much the candidate host galaxy is trustable, we list the instrument used to take the image, and P_{cc} in column 3 and 4 in Table 12 when possible.

The basic morphological property of host galaxies is size, represented by the half brightness radius R_{50} , which indicates the semi-major axis of the ellipse within which one-half flux of the entire galaxy is enclosed. Sometimes the host surface brightness is fitted with the Sérsic profile

$$\Sigma(r) = \Sigma_e \exp\{-k_n[(r/r_e)^{1/n} - 1]\}, \quad (2.12)$$

with the effective radius r_e as the size indicator (Wainwright et al., 2007; Fong et al., 2010; Fong & Berger, 2013). Sometimes, the size of a host galaxy is defined as the eighty-percent radius R_{80} (Fruchter et al., 2006; Svensson et al., 2010), which is the major axis radius of a similar ellipse that encloses 80 percent of flux. For these cases, we convert R_{80} to R_{50} by assuming that the surface brightness profile of the galaxy is an Sérsic profile. Since nearly all LGRB host galaxies and most SGRB host galaxies are disk (spiral) galaxies, $n = 1$ is assumed. This is equivalent to an exponential profile, which is consistent with the disk galaxy surface density profile. For $n = 1$, one has $R_{50} = R_{80}/1.79$, and $R_{50} = r_e$. The host galaxies of three SGRBs, GRB 050509B, GRB 050724 and GRB 100117A, are obviously elliptical galaxies with $n \sim 4$, so that the conversion factor $R_{50} = 0.968r_e$ is applied. If R_{50} of more than one band is given, the value for the band mostly close to optical is used since the blue band may be affected by dust extinction. Sometimes, no precisely defined radius is available, and only vaguely defined “size” or “radius” are quoted in the literature. In these cases, we treat them as R_{80} which covers most flux of galaxy. R_{50} in units of arcsec and kpc

are presented in column 5 and 6 of Table 12. The parameter n is also presented in column 7 when possible. Some GRBs with angular R_{50} values do not have redshift detections. For these cases, $z = 0.5$ for SGRBs and $z = 2.0$ for LGRBs are assumed to estimate physical size of the galaxy.

Angular and physical offsets, the angular/physical separation of a GRB from the center of its host galaxy, are given in column 8 and 9 of Table 12, in units of arcseconds and kpc, respectively. If an offset is smaller than the positional uncertainty of the GRB or host galaxy, an upper limit is given. The largest samples of LGRB offsets are from Bloom et al. (2002) and Blanchard et al. (2016), and the largest SGRB offset samples are from Fong et al. (2010) and Fong & Berger (2013). For GRBs from Table 2 of Perley et al. (2013), the angular distance between the afterglow and the host galaxy is used to define the offset. Similar to R_{50} , $z = 0.5$ for SGRB and $z = 2.0$ for LGRB are also assumed for those without redshift detections. In some problems, one cares more about the relative offset with respect to the size of the host galaxy. The normalized offset (the true offset normalized to R_{50} of the host galaxy) is shown in column 10 of Table 12.

Many GRB hosts are irregular and interacting galaxies. For these, the size R_{50} , the center, and hence, the offset of the galaxy are not well defined. In these cases, the fraction of brightness F_{light} , which is the ratio between the area of the host fainter than the GRB position and the area of the entire host galaxy, is defined. It delineates how bright the GRB location is relative to the other regions of the host galaxy, and reveals the local SFR, especially if the UV band image is used. The largest LGRB F_{light} samples are from Fruchter et al. (2006), Svensson et al. (2010) and Blanchard et al. (2016), and the largest SGRB F_{light} samples are from Fong et al. (2010) and Fong & Berger (2013). Others are collected from individual papers. The parameter F_{light} is given in column 11 of Table 12. $F_{\text{light}} = 1$ indicates that the GRB is located in the brightest region of the host, and $F_{\text{light}} = 0$ indicates that the GRB is in the faintest region of the host.

Distribution of properties

With the comprehensive prompt and host galaxy properties in Table 9, 10, 11 and 12, we are able to study the differences and similarities of LGRBs and SGRBs. We present the distributions of both LGRBs and SGRBs for each property in this section. The histograms are shown in Fig. 8, and the statistical results are presented in Table 1 and Table 2. In all the figures, LGRBs are shown in red and SGRBs in blue. In Fig. 8, the histograms of all the GRBs are presented in black. Dotted lines show objects with redshift $z < 1.4$, within which most SGRBs are located. Inspecting this sample allows one to compare SGRBs to LGRBs in the similar redshift range, and examine the influence of redshift on each parameter. In the left column of all the figures, LGRBs and SGRBs are defined by the “consensus” criteria, i.e., GRBs with label “S” in Greiner’s catalog are defined as SGRBs, otherwise LGRBs. Their statistical results are shown in Table 1. In the right column of all figures, LGRBs and SGRBs are defined by T_{90} only, i.e., GRBs with $T_{90} < 2$ s are defined as SGRBs, otherwise LGRBs. Their statistical results are shown in Table 2. In Table 1 and 2, the numbers of LGRBs and SGRBs with each parameter are given in column 2 and 4. The median values and dispersion of them are given in column 3 and 5.

In order to investigate how different the LGRB sample is from the SGRB sample, we employ the Kolmogorov-Smirnov test (KS test), and examine the fraction of LGRBs and SGRBs overlapping with each other. Column 6 of Table 1 and 2 show the null probability P_{KS} of KS test between LGRBs and SGRBs for these two definitions of SGRBs and LGRBs, respectively. The smaller P_{KS} is, the more different LGRBs and SGRBs are from each other for that particular property. The overlapping range of each parameter is shown in column 7 of both tables. The fractions of LGRBs and SGRBs located in the overlapping region (defined as “overlapping fraction” hereafter) are presented in column 8 and 9. In the following, we discuss each property in detail.

The redshift distributions of the consensus and T_{90} -defined LGRBs and SGRBs are presented in the left and right column of Fig. 8, Row 1. Photometric redshifts are not included.

It is apparent that SGRBs show a much lower redshift distribution than LGRBs, with $z_{\text{SGRB}} = 0.45 \pm 0.51$ as compared with $z_{\text{LGRB}} = 1.64 \pm 1.30$. The highest-redshift GRB in our sample is GRB 090423, with $z = 8.23$ obtained from absorption lines (Tanvir et al., 2009a; Salvaterra et al., 2009). GRB 090429B has a photometric redshift $z = 9.2$ (Cucchiara et al., 2011c) without absorption/emission lines, and there is no host galaxy information available. It is not included in our sample according to our primary selection criteria given in Section 2. The highest redshift SGRB is GRB 090426, which is an ambiguous event with $T_{90} = 1.24$ s (Antonelli et al., 2009; Levesque et al., 2010b). If it is considered as a short GRB based on the duration criterion, the overlapping fraction of LGRB redshift is as large as 72 %. If it is classified as a Type II GRB based on other information (and hence join the LGRB sample), the LGRB overlapping fraction in redshift is 29 %. Consensus SGRBs have less high redshift objects than T_{90} -defined SGRBs, which results in a smaller P_{KS} and indicates a more significant difference between the two groups. Note that even with a redshift cut $z < 1.4$, LGRBs still show a higher median redshift than SGRBs, due to the dominance of high redshift events over low redshift events in this LGRBs sub-sample.

Prompt emission properties

Duration T_{90} denotes the (observed) time scale of GRB explosions. Physically, Type I GRBs, which have a neutron-star dense accretion torus from the debris of NS-NS or NS-BH mergers, have a small free-fall time scale to allow short-duration GRBs. Type II GRBs, on the other hand, having an extended stellar envelope with stellar density, have a free-fall time scale longer than several seconds, which is natural to explain long-duration GRBs. The distributions of T_{90} for the consensus and T_{90} -defined LGRBs and SGRBs are presented in the left and right panels of Figure 8, Row 2, respectively. The T_{90} distribution of the entire GRB population (both LGRBs and SGRBs) (black lines) show a peak around 50 s and a flat tail in the range smaller than 2 s. The bimodality is not as significant as in the BATSE sample (Kouveliotou et al., 1993), due to the dominance of LGRBs. The dominance of

LGRBs is a result of the dominance of the Swift sample, since 325/407 events in our sample are discovered by Swift, and Swift is dominated by LGRBs due to its insensitivity to SGRBs (Sakamoto et al., 2011b; Qin et al., 2013). For T_{90} -defined LGRBs (red solid line) and SGRBs (blue solid line), the T_{90} criterion gives the lowest P_{KS} among all the parameters as shown in Table 1 and 2, i.e. $\sim 10^{-27}$. This is simply because the definitions of LGRBs and SGRBs are based on the duration criterion. For the consensus LGRB and SGRB samples, the SGRB T_{90} distribution extends to as long as 5.66 s, GRB 090510, and the LGRB T_{90} distribution extends to as short as 1.30 s, GRB 000926. Such an overlap increases P_{KS} by one order of magnitude but still allows a very low P_{KS} value, suggesting that the T_{90} criterion is truly a good indicator to separate the two physically distinct populations. The significant overlap in the T_{90} properties (7% in LGRBs and 20% in SGRBs), on the other hand, suggests that other properties are needed to correctly place a certain GRB into the right physical category (Type I vs. Type II).

Isotropic gamma-ray energy $E_{\gamma,\text{iso}}$ gives a rough indicator of the energy budget of a GRB. In the BH central engine scenario, the total energy budget is related to the total material available for accretion. Type II GRBs, having plenty of fuel from the massive star progenitor ($M > 30M_{\odot}$ for the total mass budget), are expected to be more energetic than Type I GRBs, which are related to compact star mergers ($M \sim (2 - 3)M_{\odot}$ for the total mass budget). In the magnetar scenario, some energy from a NS-NS merger may be released in the form of gravitational waves (GWs) or falls into the collapsed BH, resulting in less energetic Type I GRBs than Type II GRBs (e.g. Gao et al., 2016). Observationally, our sample shows that the $E_{\gamma,\text{iso}}$ distribution of LGRBs is nearly a Gaussian, with an extremely low energy tail extending to 10^{47} erg. The LGRBs with $E_{\gamma,\text{iso}} < 10^{49}$ erg are usually defined as low luminosity GRBs (llGRBs), probably with a somewhat different physical origin from normal LGRBs (Campana et al., 2006; Soderberg et al., 2006b; Liang et al., 2007a; Virgili et al., 2009; Bromberg et al., 2011; Sun et al., 2015). Due to their rareness, the inclusion of llGRBs does not significantly influence the median $E_{\gamma,\text{iso}}$ and the overlapping fraction of LGRBs.

Nearly all SGRBs have $E_{\gamma,\text{iso}} > 10^{49}$ erg, so the inclusion of llGRBs does not influence the overlapping fraction with SGRBs much, either. The median $E_{\gamma,\text{iso}}$ of SGRBs is about 1.6 dex lower than the entire sample of LGRBs, and P_{KS} of the $E_{\gamma,\text{iso}}$ criterion is as significant as 10^{-14} . However, the low redshift LGRBs shows a 0.5 dex smaller $E_{\gamma,\text{iso}}$, making P_{KS} eight orders of magnitude larger (but still small) if one focuses on the $z < 1.4$ sample. Due to their wide distributions ($\sigma=1.0$ dex), the SGRBs and LGRBs show significant overlap in the $E_{\gamma,\text{iso}}$ domain. If there were no duration information, SGRBs look like the low energy tail of LGRBs, suggesting that the $E_{\gamma,\text{iso}}$ property alone is not a good criterion to differentiate between the two populations.

The typical peak luminosity $L_{\text{p},\text{iso}}$ of LGRBs is about 0.8 dex larger than that of SGRBs. However, due to the large dispersion, 1.1 dex, the difference between these two samples is not significant, either, with $P_{\text{KS}} = 0.007$. LGRBs at $z < 1.4$ have 0.6 dex smaller $L_{\text{p},\text{iso}}$ than the entire LGRB sample, making it more difficult to apply the $L_{\text{p},\text{iso}}$ criterion for classification. This is consistent with Zhang et al. (2009) and Ghirlanda et al. (2009), who showed that LGRBs and SGRBs have similar $L_{\text{p},\text{iso}}$, and their differences in $E_{\gamma,\text{iso}}$ is mostly due to different durations.

It has been long known that LGRBs have softer spectra than SGRBs. Theoretically, such a connection is not straightforward and is model dependent (e.g. Zhang et al. 2009 for a detailed discussion), but it may be somewhat related to a possible higher Lorentz factor in SGRBs, originating from a relatively cleaner environment of Type I GRBs. The hardness of a spectrum is a combination effect of the peak energy E_{p} , and the low energy photon index α . Consistent with previous work, LGRB α is -1.01 ± 0.34 , softer than that of SGRBs, $\alpha = -0.60 \pm 0.25$. The difference between them is moderately strong, with $P_{\text{KS}} = 10^{-7}$. The E_{p} center value of LGRBs is 0.49 dex smaller than SGRBs, and the two samples have about 80% overlaps, which shows a moderately strong difference between LGRBs and SGRBs.

The amplitude parameter f shows 43% LGRBs and 100% SGRBs within the overlap region, The K-S test gives $P_{\text{KS}} \sim 10^{-7}$, indicating a moderately strong difference between

LGRBs and SGRBs. As suggested by Lü et al. (2014), the f_{eff} is expected to be a better indicator. Our analysis shows $P_{\text{KS}} \sim 10^{-20}$ between LGRBs and SGRBs, which is indeed a good indicator. It is still not as significant as the T_{90} criterion, due to the smaller sample of f_{eff} than T_{90} . The LGRB and SGRB overlapping fractions of f_{eff} are 7% and 79% in the consensus samples. GRB 130427A, which has the largest $f_{\text{eff}} = 4.75$ is an obvious outlier. It shows an intense initial pulse with a weak tail in Swift/BAT while the peak is not significant in Fermi/GBM. If excluding it from the LGRB sample, The LGRB and SGRB overlapping fractions of f_{eff} are 7% and 48%, respectively.

Host galaxy properties

Stellar mass, Star formation rate, and metallicity

The properties of galaxies are mainly controlled by their stellar mass M_* (van der Wel et al., 2014; Ilbert et al., 2015). Host galaxy masses of the consensus and T_{90} -defined LGRBs and SGRBs are presented in the left and right columns of Fig. 8, Row 9. In order to be consistent, only stellar masses obtained with SED fitting are used here. Most SGRB and LGRB host galaxies are smaller than the turnover mass of galaxies extending to redshift 3 (Mortlock et al., 2015). Although the median of SGRB hosts is 0.6 dex larger than that of all LGRB hosts, their difference is not statistically significant. LGRB hosts with $z < 1.4$ show a 0.2 dex lower stellar mass than the whole sample. It may be a selection effect, since the galaxies with larger stellar masses are brighter and easier to be observed at high redshifts. It makes the low- z LGRBs more significantly different from SGRBs. Since the median redshift of low- z LGRBs is still larger than that of SGRBs, a true same-redshift comparison between LGRB and SGRB host stellar masses should show even more significant differences. Also, it indicates that there should be more small stellar mass host galaxies that are not been discovered yet, especially in the high redshift range. The overlapping fractions are around 90% for both LGRBs and SGRBs. The results of the consensus and T_{90} -defined LGRB and SGRB samples are consistent with each other.

The SFR represents the global star formation status of the entire galaxy. It is expected to be large in LGRB hosts, since LGRBs are presumed to be massive star collapsars and are expected to be associated with star formation. SGRBs are believed to be related to compact star mergers, so at least some of them are expected to be associated with the old stellar populations and no recent star formation is required for the presence of SGRBs. SFR of consensus and T_{90} -defined LGRBs and SGRBs are presented in Fig. 8, Row 10. In order to be consistent, only SFRs obtained with emission lines are used. The median SFR of LGRBs is around 0.4 dex larger than that of SGRBs, although their difference is not statistically significant, due to the large dispersion, both around 0.8 dex. It may be also due to the generally more massive host galaxies of SGRBs, since SFR is proportional to the stellar mass of the galaxies. The low- z LGRB hosts are similar to those of low- z SGRBs. It may be a result of the decrease of the LGRB host mass at low redshifts. Both LGRBs and SGRBs show around 90% overlapping fraction for SFR. The T_{90} -defined samples show even less difference and larger overlaps, suggesting the limitation of T_{90} to define the physical category of GRBs.

In the sample of the consensus SGRBs, the one with an extremely large SFR is GRB 100816A. Its T_{90} is reported to be 2.9 s in the Swift GRB table and 1.99 s in Pérez-Ramírez et al. (2013). With a small spectral lag 10 ± 25 ms(Norris et al., 2010a), it is suggested to be a SGRB in Greiner’s catalog. Considering its high SFR (Krühler et al., 2015) and possible interacting nature of the host galaxy (Tanvir et al., 2010b), we would suggest it to be still a Type II GRB. We still keep it in the consensus SGRB sample based on our sample selection criterion. Changing it to the consensus LGRB sample makes the median log(SFR) of SGRB to be 0.08, i.e., $1.2 M_{\odot} \text{ yr}^{-1}$, with a dispersion 0.71, and results in a lower P_{KS} 0.04 for this criterion.

For the bursts with both SFR and stellar mass M_* , specific SFR ($\text{sSFR} = \text{SFR}/M_*$) of the host galaxy is available. Since sSFR describes SFR per unit stellar mass, it is a more relevant parameter to describe the star formation status in the GRB location. The distributions of

sSFRs are presented in Fig. 8, Row 11. sSFR shows a more significant difference between LGRBs and SGRBs than SFR. In general, the sSFR of LGRBs is 0.5 dex higher than SGRBs. The redshift evolution of the sSFR for the LGRB host is not significant, even though the redshift evolution of sSFR of the entire universe is apparent, with a peak at $z = 2 - 3$. This may indicate that sSFR is directly related to the LGRB rate. Another factor might be the selection effects. Since the massive hosts with less sSFR are easier detected, high redshift samples should on average show smaller sSFRs relative to the true distribution. The T_{90} -defined sample shows a 0.3 dex less difference than the consensus sample, again indicating the limitation of the T_{90} -only criterion.

In the consensus LGRB sample, the GRB with the lowest sSFR, 0.006 Gyr^{-1} , is GRB 050219A (Rossi et al., 2014). Its host was discovered by GROND and confirmed by VLT. No HST image is available. It is an elliptical galaxy $4.6''$ away from the GRB XRT location, with a $1.9''$ positional uncertainty. The estimated chance coincide probability is $P_{cc} = 0.8\%$. If we exclude GRB 050219, the LGRB sSFR becomes $0.05 \pm 0.62 \text{ Gyr}^{-1}$ and $P_{KS} = 0.01$. The overlap range becomes $(-1.17, 1.05)$ and the overlapping fraction becomes 90% and 78% for the consensus LGRBs and SGRBs, respectively.

LGRB progenitor models prefer a low metallicity environment, since it would keep enough angular momentum in the core the star to launch a jet. On the other hand, no metallicity limitation is required for SGRBs. The distributions of metallicity [X/H] of the consensus and T_{90} -defined LGRBs and SGRBs are presented in the left and right columns of Fig. 8, Row 12. If one event has double values, the average value is plotted. For the consensus samples, SGRBs show a 0.5 dex richer metallicity than LGRBs, and are consistent with the highest end of the consensus LGRBs. The P_{KS} value is 0.0007, indicating a relatively significant difference. The overlapping fractions are 47% and 100% for LGRBs and SGRBs, respectively, which is as low as that of the amplitude parameter f . However, the $z < 1.4$ LGRB sample is much metal richer than the whole LGRB sample. In this redshift range, the difference between median LGRBs and SGRBs becomes 0.3 dex, and the overlapping

fraction of LGRBs increases to 73%. Since the average redshift of low- z LGRBs is still higher than SGRBs, and metallicity from Berger (2009) may overestimate the SGRB metallicity, the difference between SGRBs and LGRBs in the same redshift bin may be even milder. This makes metallicity not a good indicator of the physical origin of individual GRBs.

Morphological properties: galaxy size and Offset

Galaxy size is correlated with stellar mass, according to the galaxy types (van der Wel et al., 2014). The R_{50} distributions of the consensus and T_{90} -defined LGRB and SGRB samples are presented in Fig. 8, Row 13. The LGRB host size is typically 0.31 dex smaller than that of SGRBs in the consensus samples, with a small $P_{KS} = 4 \times 10^{-4}$. The overlapping fraction of LGRBs is $\sim 69\%$. For $z < 1.4$, the R_{50} distribution of LGRB hosts is consistent with that of the whole sample, only 0.06 index larger. However, due to shrinkage of the sample size, The P_{KS} value is one order of magnitude larger. The T_{90} defined SGRB sample includes more small size hosts, again indicating the limitation of the T_{90} criterion.

SGRB offsets are expected to be larger than LGRBs, since the explosion of SNe that formed the NSs and BHs in the merger systems would have given the system two kicks, so that the system may have a large offset from the original birth location in the host galaxy. The cumulative offset distribution of SGRBs indeed differs from that of LGRBs (Fong et al., 2010; Fong & Berger, 2013; Berger, 2014). Our analysis shows that the typical physical offset of SGRBs, in units of kpc, is 0.77 dex larger than that of LGRBs. The KS test gives $P_{KS} = 10^{-4}$. However, the overlapping fractions of both LGRBs and SGRBs are as large as 80%. Only 5 of the 28 SGRBs show offsets larger than all LGRBs. The redshift evolution of the offsets is not significant. At $z < 1.4$, LGRBs have the same median physical offset as the whole sample.

The offset normalized to the host size R_{50} is a more physical parameter to delineate the location of a SGRB within the host galaxy. Also, normalized offset does not require the measurements of the absolute values of the offset and host size, so one can include events

without redshift measurements as well. The normalized offset distributions are presented in Fig. 8, Row 15. In general, SGRBs are 0.27 dex larger than LGRBs, and mildly different with $P_{\text{KS}}=0.02$. No redshift evolution is seen. Only 3 SGRBs have normalized offset larger than all LGRBs, and only 8 LGRBs have normalized offset smaller than all SGRBs. The overlapping fractions are as high as 90%.

The surface brightness fraction F_{light} is expected to be large for LGRBs since they are believed to be associated with the highest local SFR in the galaxy. The F_{light} of SGRBs is expected to be small since compact star mergers usually are expected to be kicked from the star forming regions by the time the merger happens. It is also a parameter that does not require a redshift measurement. They are presented in the last row of Fig. 8. It can be seen that SGRBs tend to be located in the faint regions of their hosts and LGRBs tend to be located in the bright regions of their hosts. A SGRB within the brightest region of its host is the ambiguous GRB 090426, which has $F_{\text{light}} = 0.82$. Although the numbers of both consensus SGRBs and LGRBs with F_{light} measurement are relatively small, F_{light} shows the most significant difference between the two types of GRBs in the host galaxy properties, with $P_{\text{KS}} = 7 \times 10^{-5}$. The regions where LGRBs are located are 60% fraction brighter than the regions where SGRBs reside. Excluding GRB 090426, the overlapping fractions become 48% and 100% for LGRB and SGRBs. At $z < 1.4$, LGRBs are located in even brighter regions of their hosts, and SGRBs are located in even fainter regions due to the exclusion of ambiguous GRB 090426. It makes the difference between LGRBs and SGRBs even more significant, and the overlapping fractions are as low as 40%. It is one of the best physical origin indicator candidates. Similar to other parameters, T_{90} -defined samples show less difference between LGRBs and SGRBs.

Simulated 1-D distribution

The KS test provides a statistical judgement about how different two groups of data are. By definition, it is sensitive to the sample size, the number of objects within each group.

T_{90} has the largest sample size among all the tested properties, with 403 in total, so it is easier to show more significant differences, with very small P_{KS} values. Physically, however, we want to examine how efficient each property of GRB is for distinguishing SGRBs from LGRBs. It is a fair comparison only if we use equal sample size for each property. We then simulate 400 GRBs (which is roughly the T_{90} sample size) for each property, based on the observational sample we already have.

The simulated numbers of LGRBs and SGRBs, median, and dispersion of each property, and null probability of the KS test are presented in Table 3.⁷ For each property, the sum of the LGRB and SGRB numbers are 400. The median and dispersion of each property are generally the same as the observed sample. According to P_{KS} , f_{eff} shows the most significant difference between LGRB and SGRBs, $P_{\text{KS}} \sim 10^{-38}$. This suggests that f_{eff} is the most efficient criterion for LGRB and SGRB classification, even better than T_{90} . Besides T_{90} and f_{eff} , two prompt emission properties, the host galaxy property F_{light} shows $P_{\text{KS}} = 4 \times 10^{-19}$, In the $z < 1.4$ sample, F_{light} shows an even more significant difference between LGRBs and SGRBs, with $P_{\text{KS}} = 4 \times 10^{-32}$. It suggests that F_{light} , as a representative of the host galaxy properties, is also a good indicator of LGRB and SGRB classification. Besides these, f , α , $E_{\gamma,\text{iso}}$, physical offsets, and size of the host galaxy R_{50} also show significant differences between LGRBs and SGRBs. However, opposite to common sense, SFR does not show a significant difference between the two classes. This may be due to the generally larger mass of SGRB host galaxies, which compensate their relatively low sSFR. On the other hand, the 8% to 100% overlapping fractions of each parameter do not change with the sample size. As a result, multiple parameters are always needed to tell the physical categories of GRBs.

2-D distributions of the properties

Two-dimensional distributions of properties play an important role in classifications of astronomical objects. A famous example is the Hertzsprung - Russell diagram for stars. In

⁷Although the absolute P_{KS} value depends on the seed of random generator, the relative significance of difference physical parameters do not change.

GRBs, the duration - hardness ratio plot played an important role in defining LGRBs and SGRBs (e.g. Kouveliotou et al. 1993).

Since in this paper we perform a joint analysis of prompt emission properties and host galaxy properties of GRBs, it is interesting to investigate these two types of properties in pairs in 2-D distribution plots. This would allow us to investigate whether there are distinct 2-D distribution plots that can clearly separate two physical classes of GRBs. In the following, we examine the difference between LGRBs and SGRBs in different combinations of prompt emission properties vs. host galaxy properties. Redshift vs. host galaxy property plots are also presented, in order to study the selection effects and possible redshift evolution. Since the eventual goal is to investigate the differences between Type I and Type II GRBs using these plots, we use the consensus SGRB and LGRB samples (which already considered multiple criteria other than T_{90}) in the analysis. All the 2-D distribution plots are presented in Figure 9, and the statistical results are presented in Table 4. The numbers of LGRBs and SGRBs for each pair of parameters are shown in column 2,7,12,17 of Table 4.

Since the standard 2-D KS test only works well for samples without correlations, and since some of our 2-D plots show mild to significant correlations, we perform a rotated KS test to investigate how different LGRB and SGRB samples are from each other. For each 2-D plot, we rotate the axis with 180 trial angles from 0 – 180 degrees and calculate the P_{KS} along the new x -axis for each angle. We then choose the lowest P_{KS} as the P_{KS} of that particular 2-D plot. The angle with the lowest P_{KS} and the corresponding P_{KS} value are presented in Table 4 for each plot. The black line segment in the circle at the lower left corner of each plot shows the direction of the x -axis with the lowest P_{KS} . We also test the possible correlation among LGRB sample between each parameter pair with the Spearman correlation. The Spearman correlation ρ_s and the null probability of the Spearman correlation P_S are also presented in Table 4.

Since T_{90} defines LGRBs and SGRBs, plots related to T_{90} have LGRBs and SGRBs are well separated and show low P_{KS} values, with the lowest P_{KS} angle at about 90° , especially if

the host galaxy parameters do not show a significant difference between LGRBs and SGRBs. There is generally no correlation between T_{90} and the host galaxy parameters.

In the plots with gamma-ray spectral parameters α and E_p , in general SGRBs have harder α , larger E_p and show a mild difference from LGRBs. However, the overlap is still significant, and one cannot clearly distinguish the two classes by any of these plots.

In the plots with $E_{\gamma,\text{iso}}$, LGRBs and SGRBs show obvious differences but still overlap with each other. The P_{KS} value is not as significant as the 1D plots due to about two thirds reduction of the total number. The best separated plot is $E_{\gamma,\text{iso}}$ vs. offset. Plots with $L_{p,\text{iso}}$ do not show as a significant difference between LGRBs and SGRBs as $E_{\gamma,\text{iso}}$ plots. There are some correlations for LGRBs in $E_{\gamma,\text{iso}}/L_{p,\text{iso}}$ vs M_*/SFR plots, as is also shown in Rhoads (2010). Some anticorrelations are also shown in $E_{\gamma,\text{iso}}/L_{p,\text{iso}}$ vs [X/H] plots.

The 2D plots involving f and f_{eff} are similar to those involving T_{90} . In particular, those involving f_{eff} show significant differences between LGRBs and SGRBs, even though significant overlapping is observed.

In several plots involving redshift, LGRBs show apparent correlations between z and other parameters. Most of these correlations may be partially attributed to observational selection effects. In the plots of $\log M_*$ vs. z and SFR vs. z , LGRB hosts with higher redshifts generally have larger stellar masses and larger SFRs. This is likely due to a selection effect, since galaxies with larger stellar masses are usually brighter and therefore detectable at higher redshifts, and since SFR is mainly determined by stellar mass. However, this selection effect is not obvious for SGRBs. SGRB hosts are generally more massive than LGRB hosts at a same redshift, while having nearly the same SFR. This results in a smaller sSFR for SGRB hosts, as shown in the plot of sSFR vs. z , as expected. In the plot of sSFR vs. z , the influence of stellar mass on SFR is generally removed and no significant redshift evolution is shown. A strong evolution of metallicity can be seen in the [X/H] vs. z plot, which also shows higher metallicity of SGRB hosts relative to the LGRB hosts at the same redshift.

The host sizes R_{50} of SGRBs are generally larger than those of LGRBs at all redshifts, even though much overlap is seen. A mild, negative correlation between galaxy size R_{50} and redshift can be noticed. Since selection effects may create a positive correlation, this negative correlation should be intrinsic, even though it is not significant. There is also a mild, negative correlation between F_{light} and redshift. F_{light} of SGRBs shows a tentative positive correlation with redshift despite a wide spread. SGRBs and LGRBs are generally more separated at $z < 1$ than at $z > 1$.

Conclusions and Discussion

In this paper, we present a sample of 407 GRBs detected before June 30th, 2014, with both prompt emission and host galaxy properties. Most GRBs (375) have spectroscopic redshift measurements. The other 32 bursts are included because of their host galaxy information. The prompt emission properties include duration T_{90} , spectral peak energy E_p , low energy photon index α , isotropic γ -ray energy $E_{\gamma,\text{iso}}$, peak luminosity $L_{p,\text{iso}}$, amplitude parameters f and f_{eff} . The host galaxy properties include star formation rate SFR, stellar mass M_* , specific star formation rate sSFR, metallicity [X/H], galaxy size R_{50} , physical offsets of GRBs from the center of the host R_{off} , normalized offset $r_{\text{off}} = R_{\text{off}}/R_{50}$, and brightness fraction F_{light} . We pay special attention to the comparison between T_{90} -defined SGRBs and LGRBs, and more importantly, the physically defined Type I vs. Type II GRBs. For the latter, we compare the “consensus” samples of SGRBs and LGRBs as listed in Jochen Greiner’s catalog, in which the definition of each SGRB was based on multiple criteria, with some of them having T_{90} longer than 2 s. For both definitions of SGRB/LGRB samples, we present the one-dimensional (1D) histograms of the two types, compare their distributions, and quantify their overlapping fractions. For the consensus samples, we further presented series two-dimensional (2D) scatter plots between prompt emission properties and host galaxy properties, aiming at identifying good parameters to separate the two types of bursts. Our results can be summarized as follows.

1. In 1D diagrams, all the prompt emission properties and host galaxy properties show more or less overlaps between SGRBs and LGRBs. No property shows a clear separation between consensus SGRBs and LGRBs. The duration T_{90} and the effective amplitude parameter f_{eff} are two parameters that have the lowest overlaps. The overlapping fractions for the f_{eff} histograms are 7% for LGRBs and 20% for SGRBs. The overlapping fractions for the f_{eff} histograms are 7% for LGRBs and 79%⁸ for SGRBs, respectively. Other parameters have much larger overlapping fractions, typically 50%-80% for LGRBs and 80%-100% for SGRBs. This suggests that no single parameter alone is good enough to place a particular burst into the right physical category.
 2. The T_{90} -defined LGRB and SGRB samples show more overlaps than the consensus LGRBs and SGRBs in most properties other than T_{90} , especially in host galaxy properties. This indicates that the T_{90} -only criterion mis-classifies some GRBs. Other properties are needed as supplementary criteria to classify GRBs physically.
 3. None of the 2D prompt emission vs host galaxy property plots show a clear separation between the consensus LGRBs and SGRBs. It suggests that simple 2D plots are not good enough for Type I and Type II GRB classifications.
 4. The three best parameters to classify GRBs are the effective amplitude f_{eff} , T_{90} , and the brightness fraction F_{light} . They show the smallest overlapping fractions and the smallest null probability P_{KS} in the simulated 1-D distributions.
 5. Some correlations between prompt emission properties and host galaxy properties are found in some 2D plots, such as $L_{\text{p,iso}}/E_{\gamma,\text{iso}}$ vs. M_* , $L_{\text{p,iso}}/E_{\gamma,\text{iso}}$ vs. SFR, $L_{\text{p,iso}}/E_{\gamma,\text{iso}}$ vs. [X/H], etc. (see Fig. 9 and Table 4). However, all these parameters show even more significant correlation with redshift, indicating that the correlations may be significantly subject to observational selection effects.
- The significant overlapping nature of the observed properties suggests that it is not always easy to identify the correct physical category of GRBs. Multiple observational criteria are

⁸48% if the outlier GRB 130427A is excluded.

needed to give more robust judgement, as suggested by Zhang et al. (2009). This first paper in a series presents all the observational data and 1-D and 2-D overlapping properties. In a follow-up paper, we will develop a quantitative method to apply the multiple observational criteria to classify GRBs into the Type I vs. Type II physical categories.

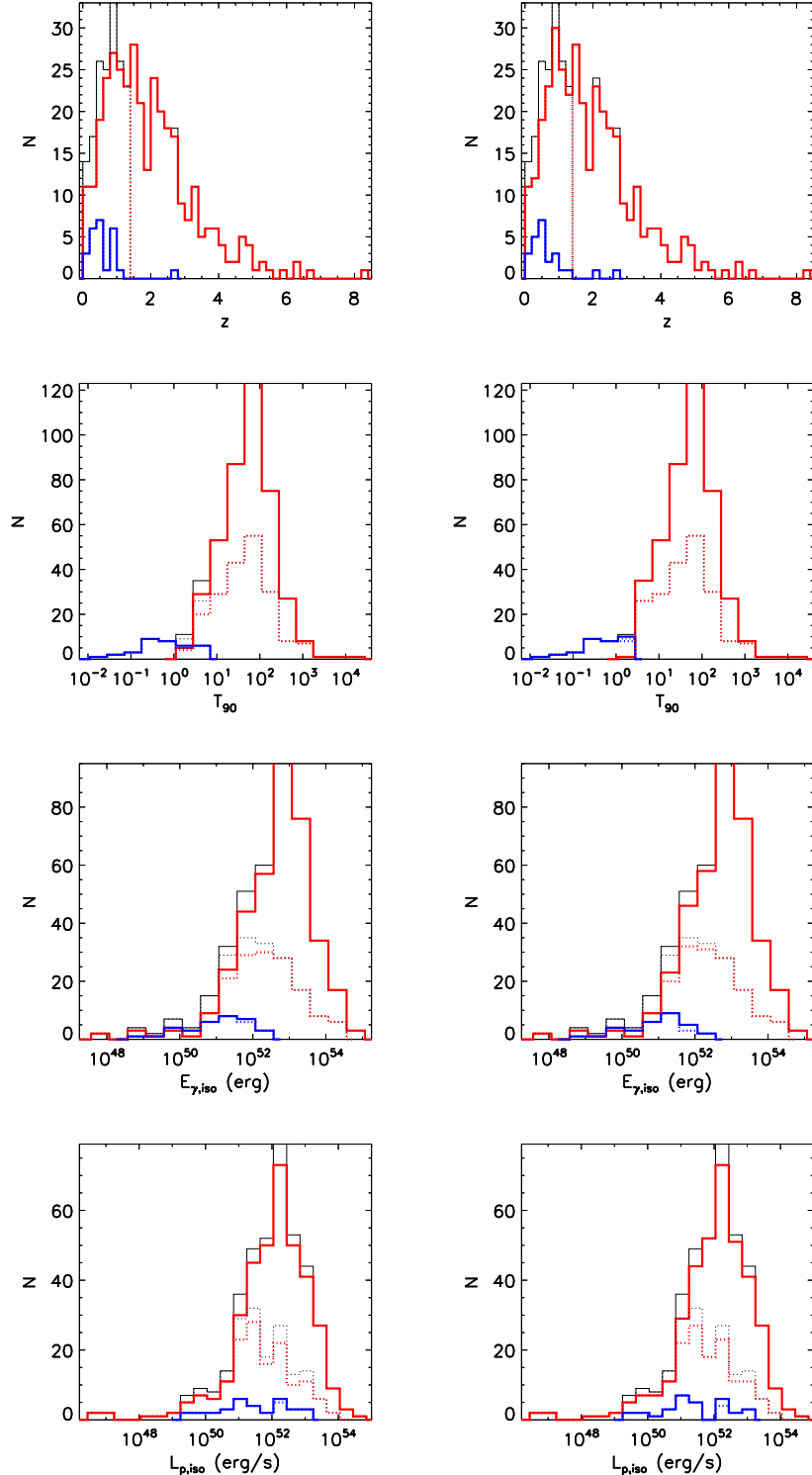


Figure 8 Distribution of prompt and host galaxy parameters of LGRBs (red lines) and SGRBs (blue lines). Left panels show distributions with consensus defined LGRBs and SGRBs, and right panels show distributions with T_{90} only defined LGRBs and SGRBs. Dotted lines show distribution of $z < 1.4$ subsamples.

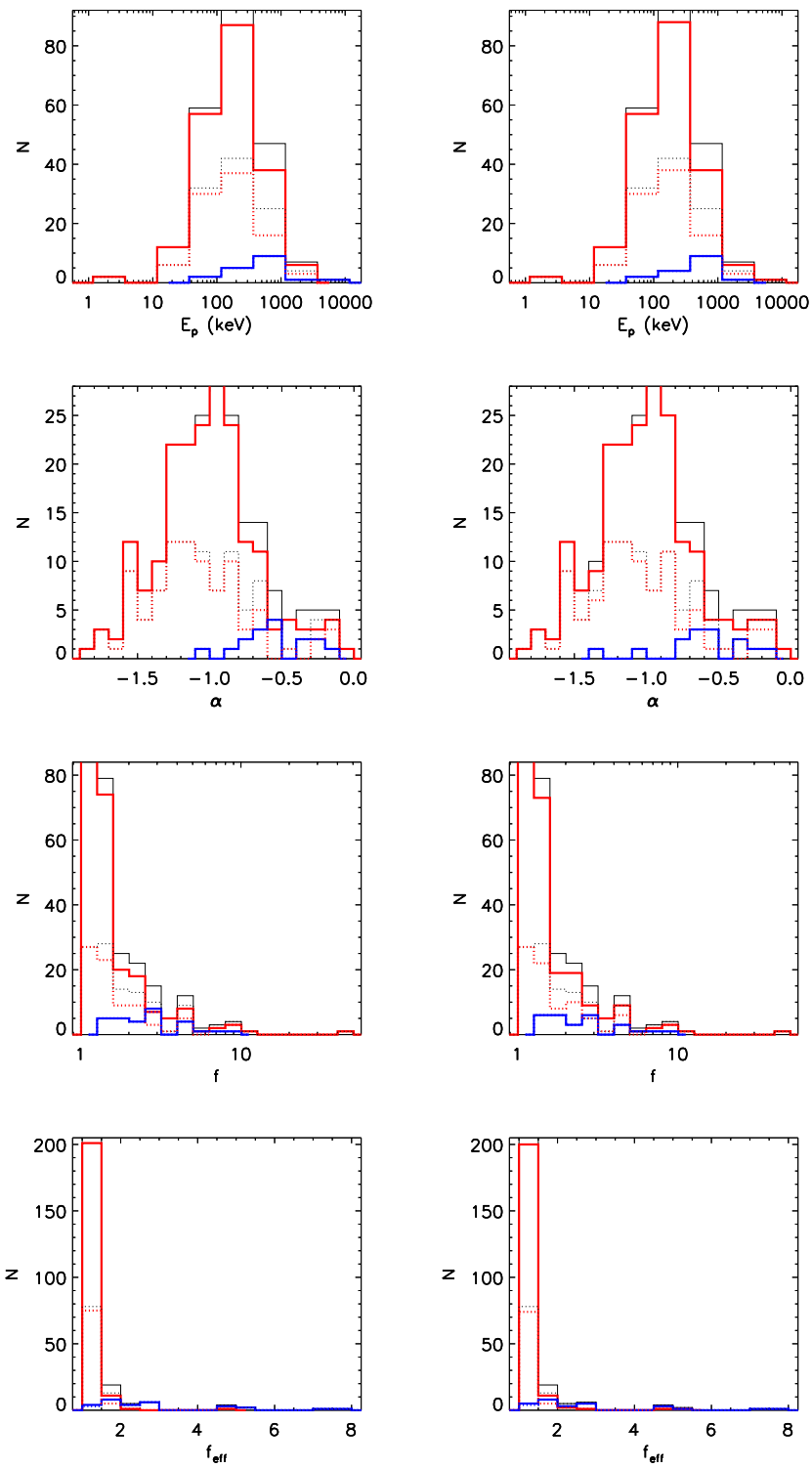


Fig. 8—Continued

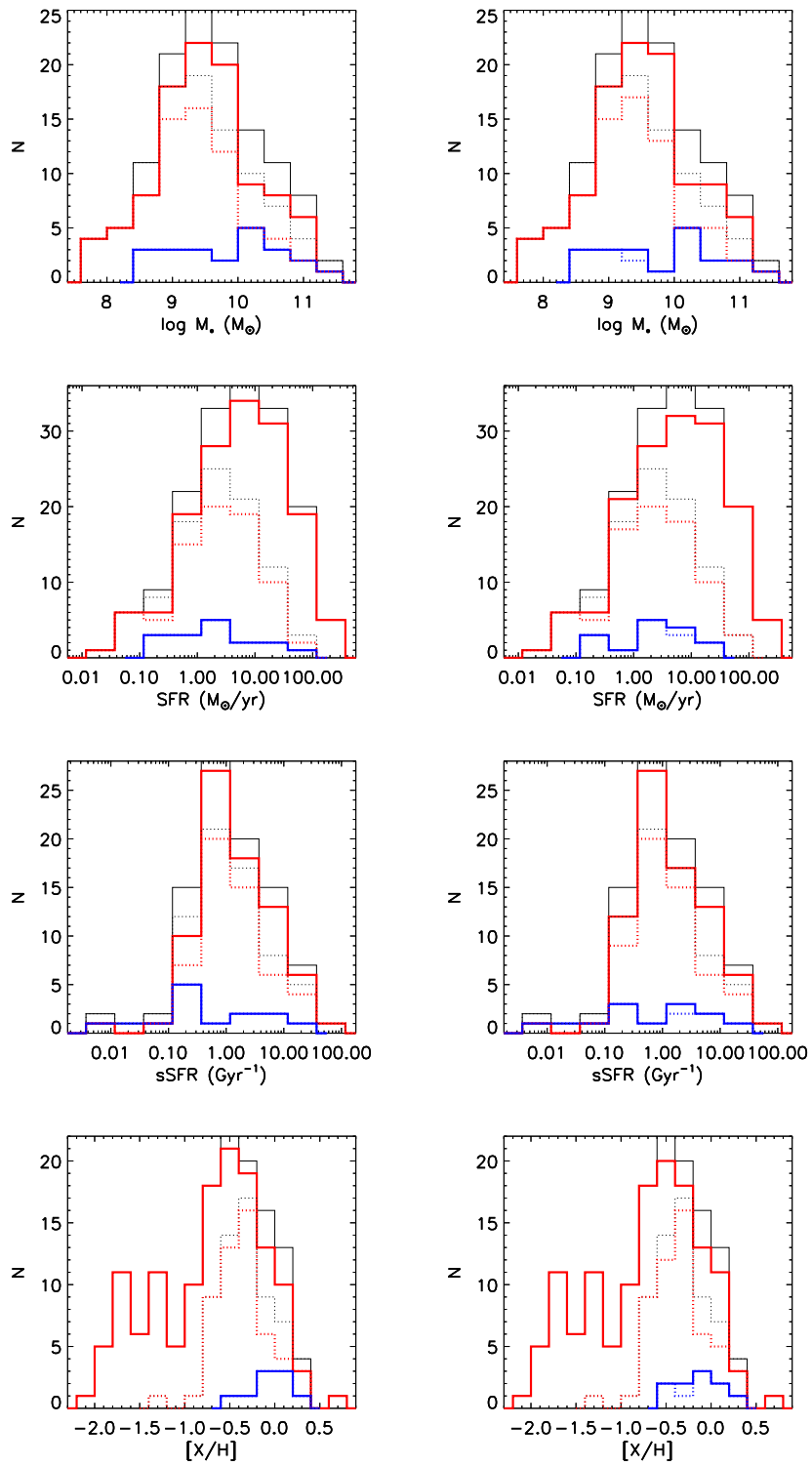


Fig. 8—Continued

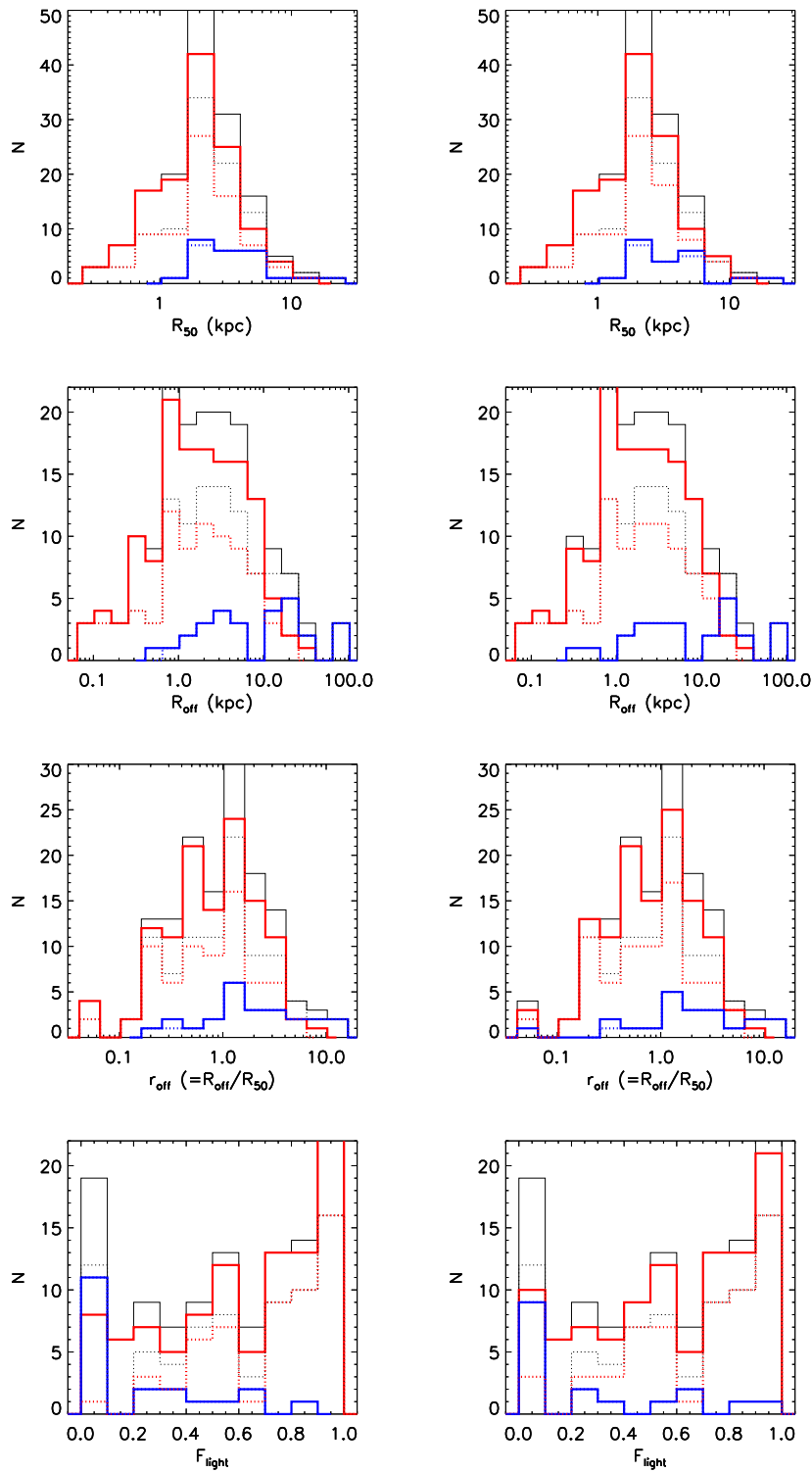


Fig. 8—Continued

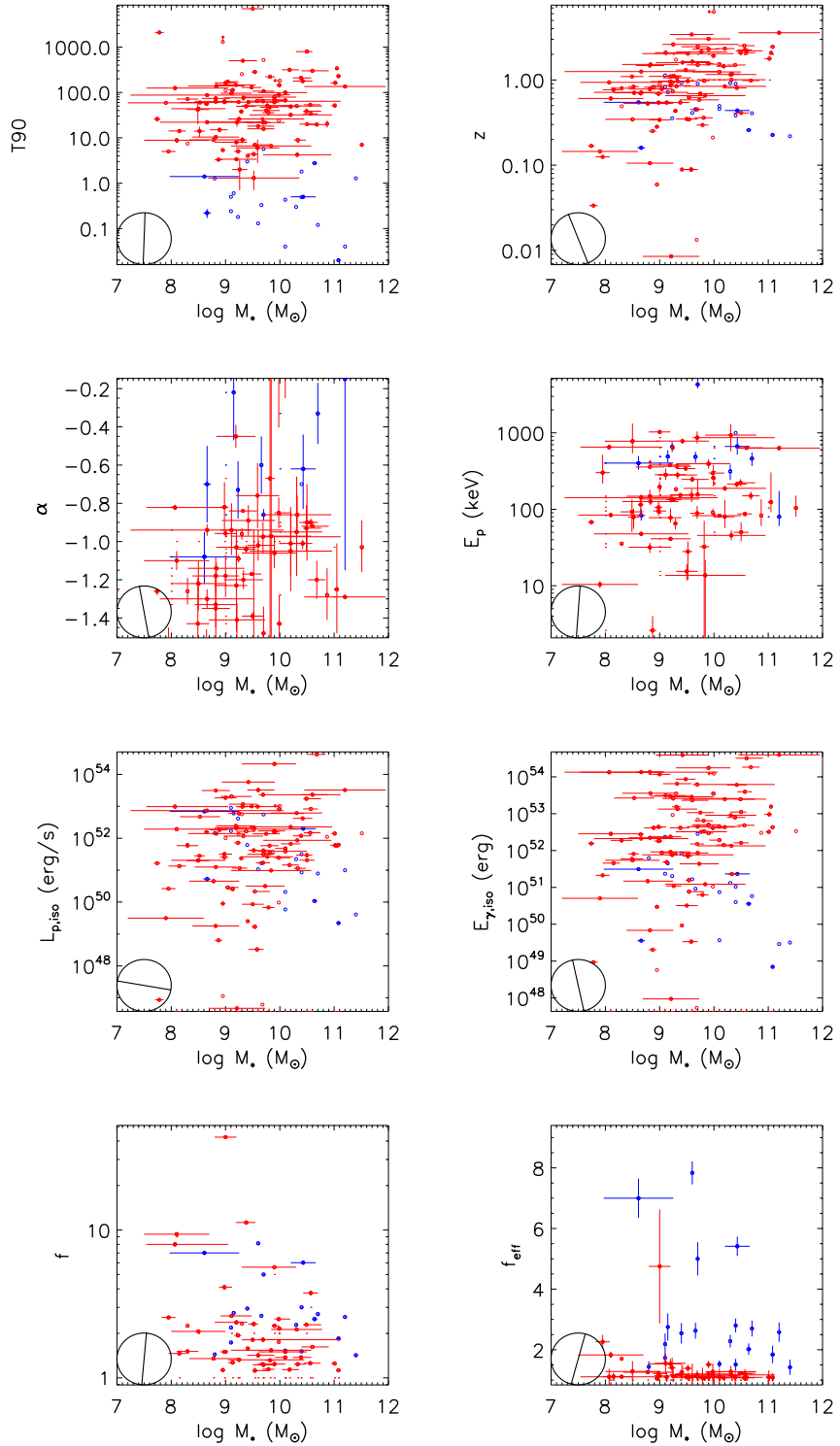


Figure 9 Prompt emission VS host galaxy property 2D plots of LGRBs (red dots) and SGRBs (blue dots). Black lines show the rotated new x-axis for the lowest P_{KS} .

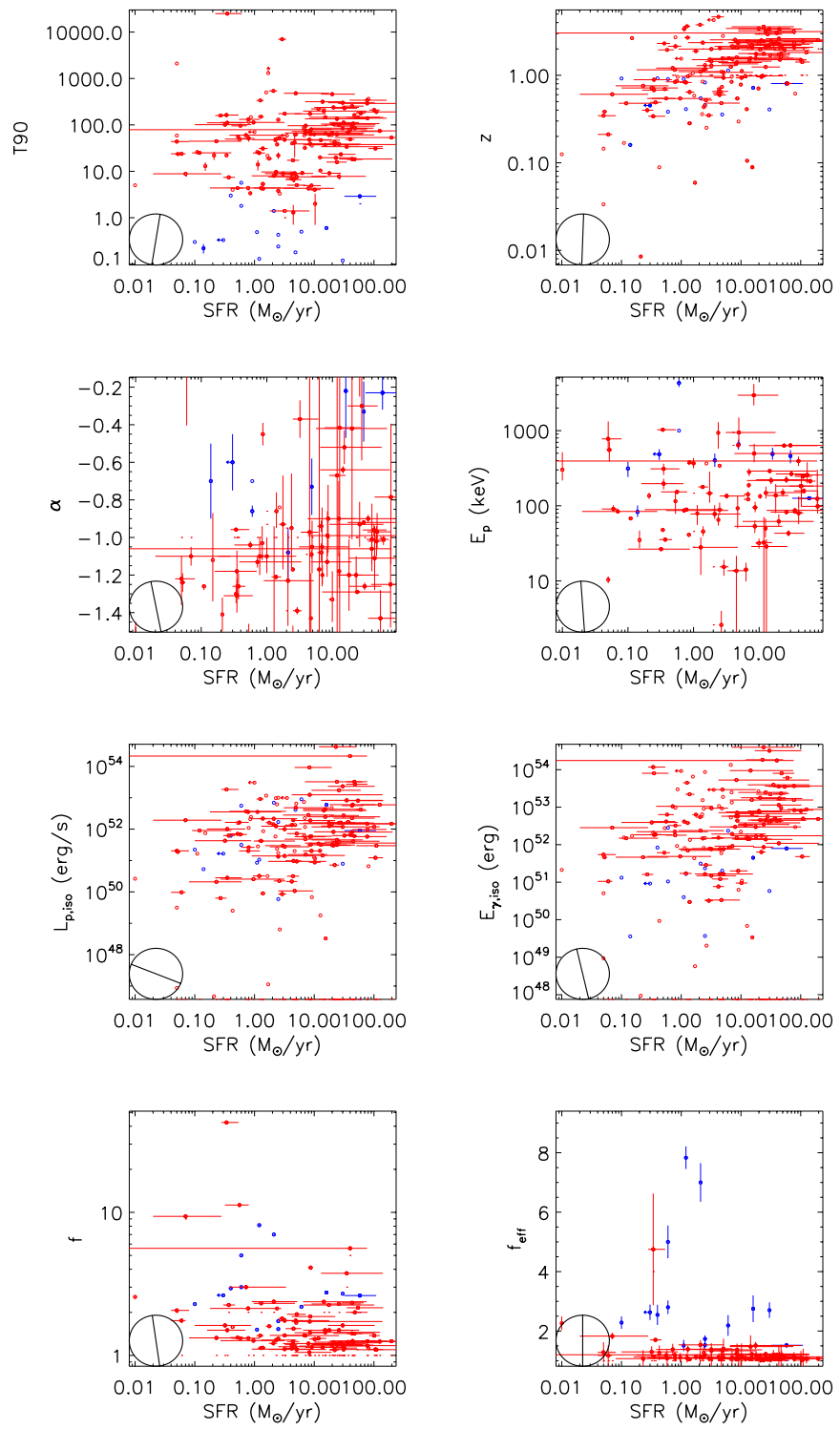


Fig. 9—Continued

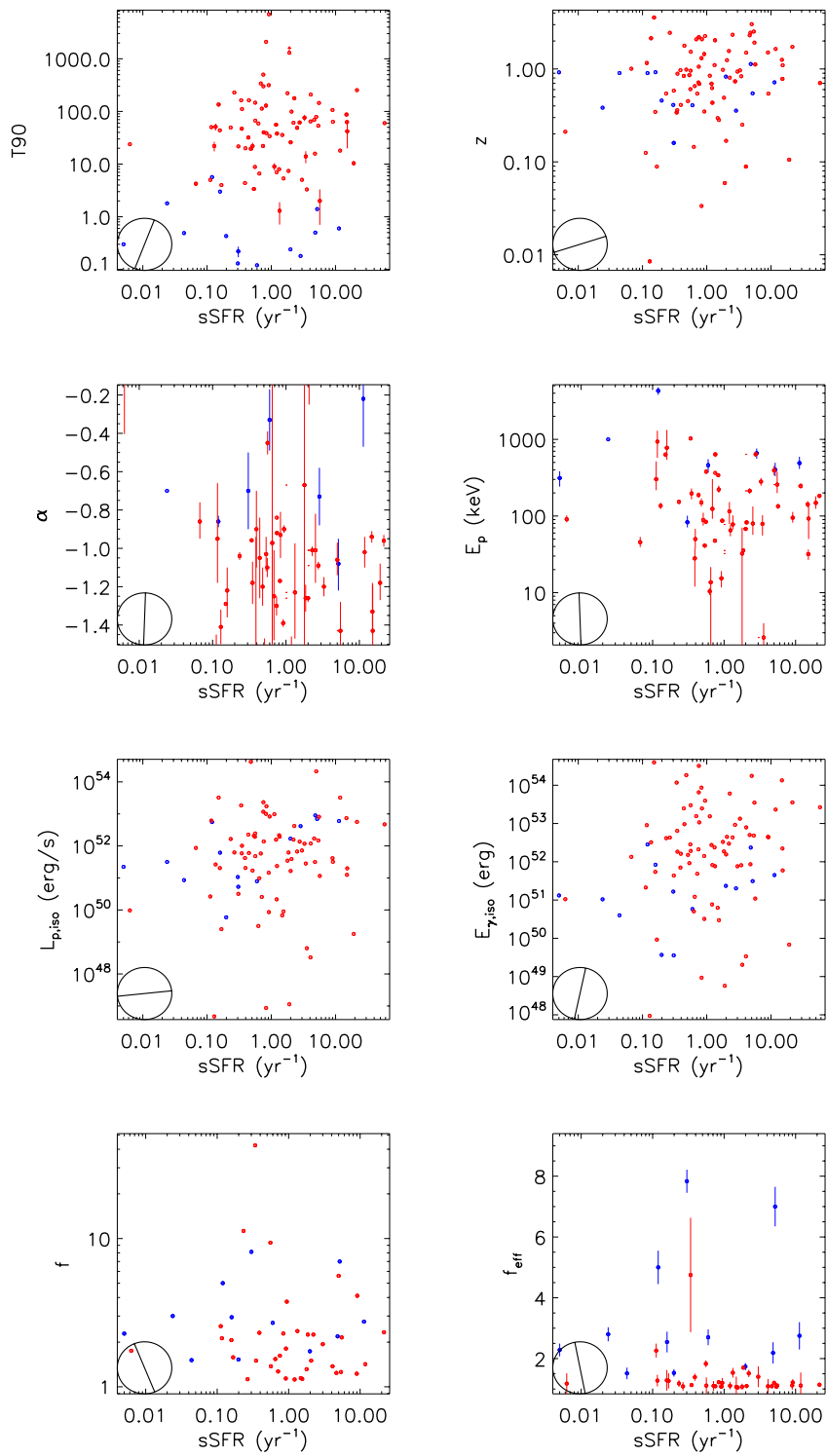


Fig. 9—Continued

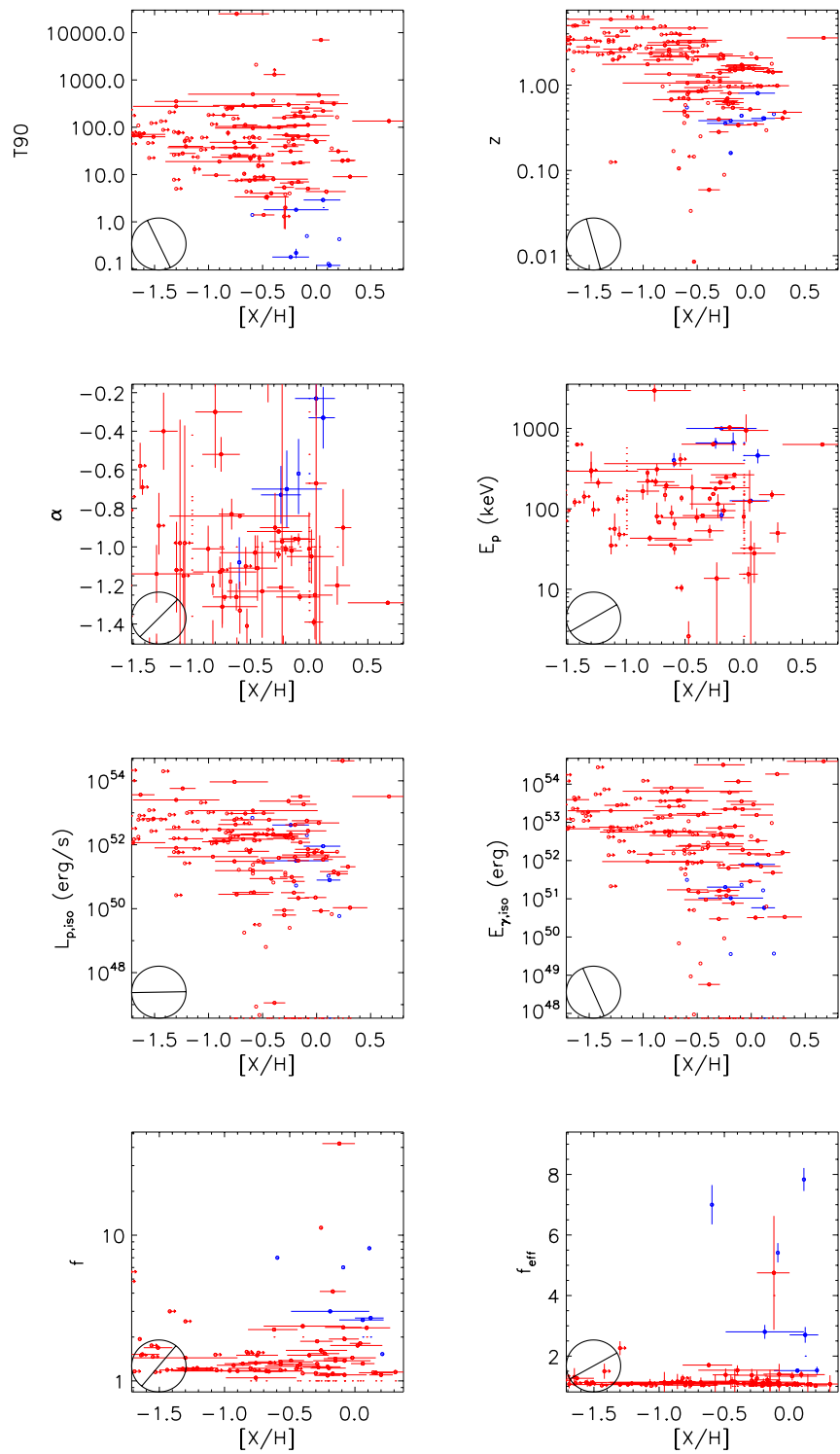


Fig. 9—Continued

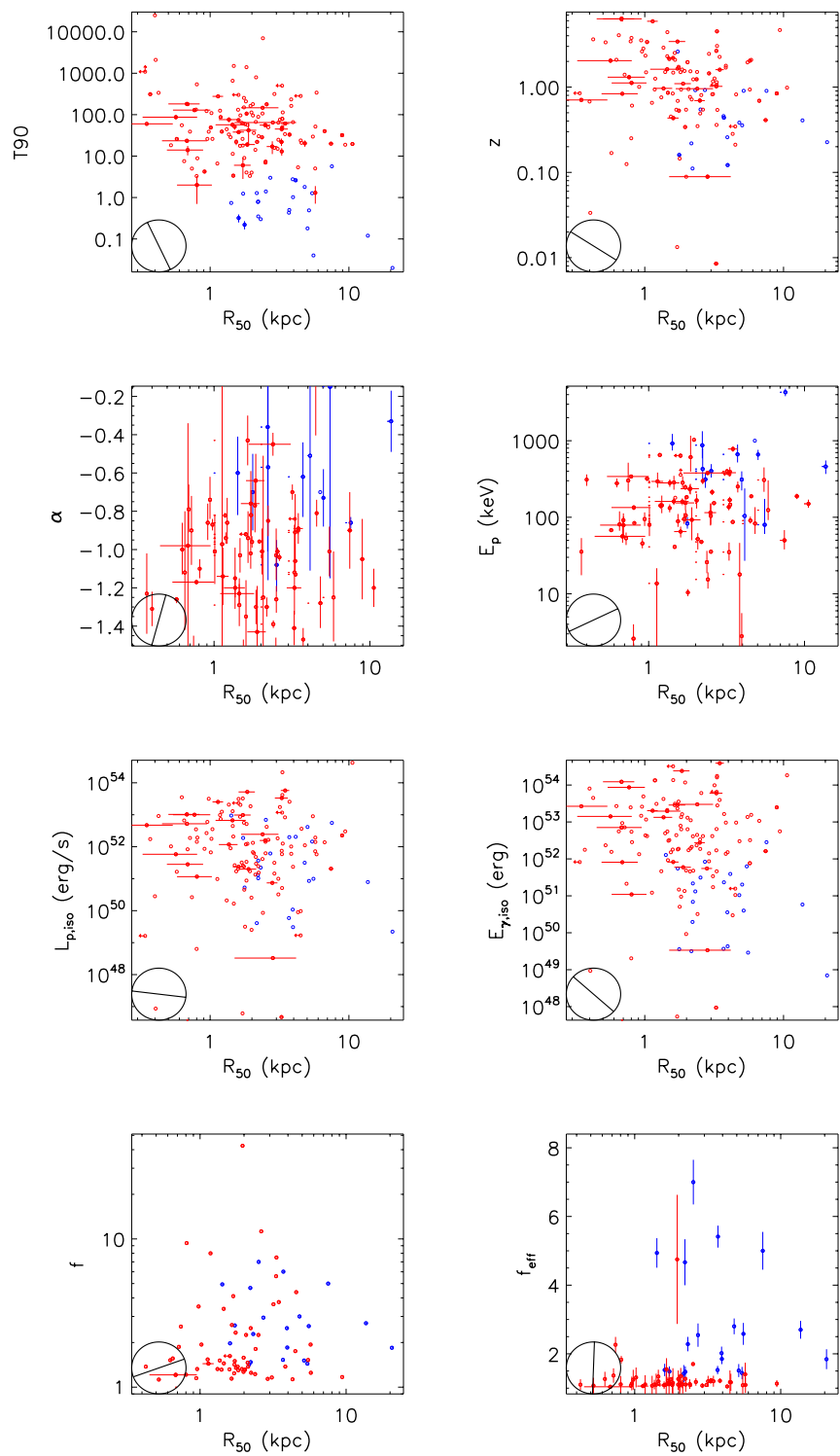


Fig. 9—Continued

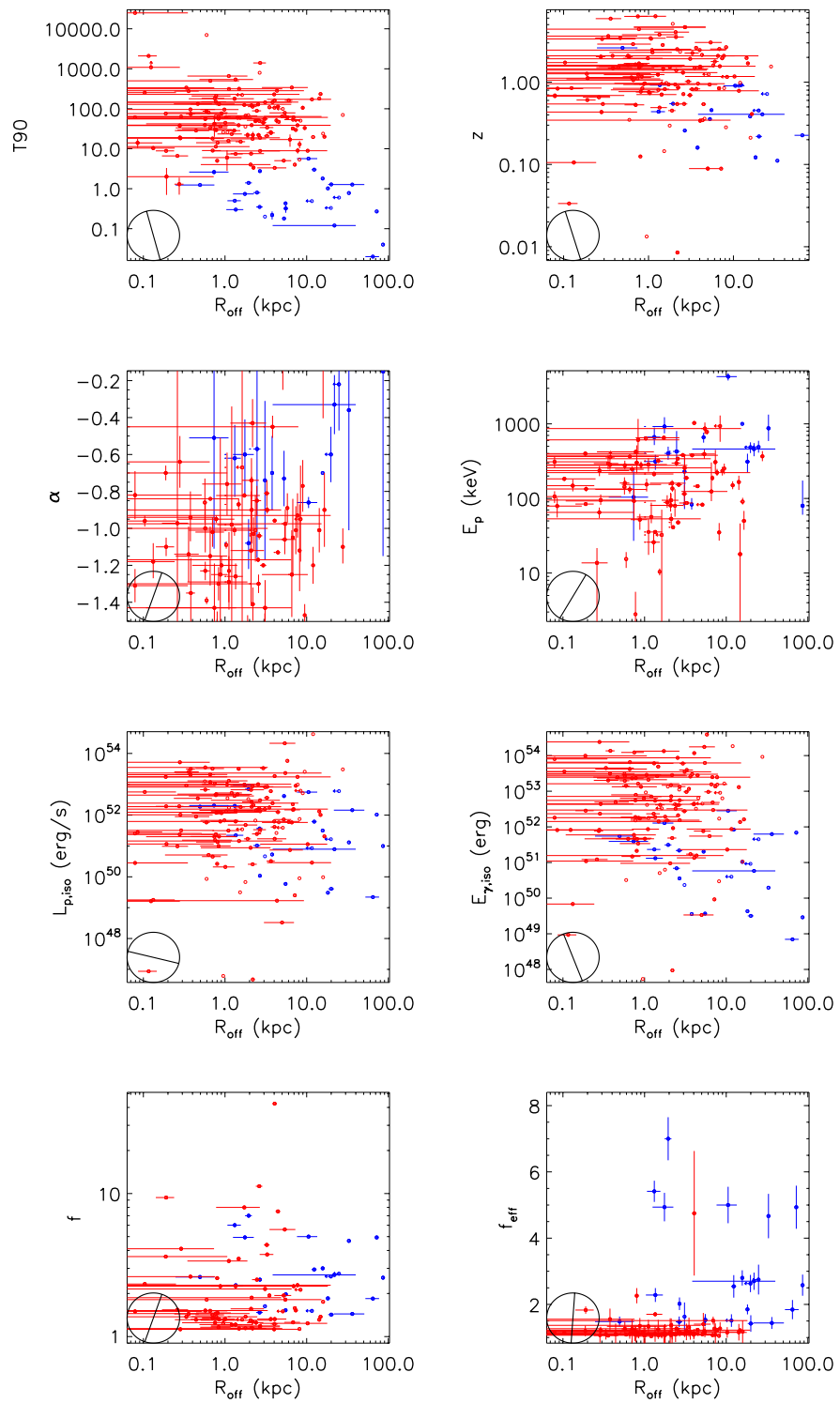


Fig. 9—Continued

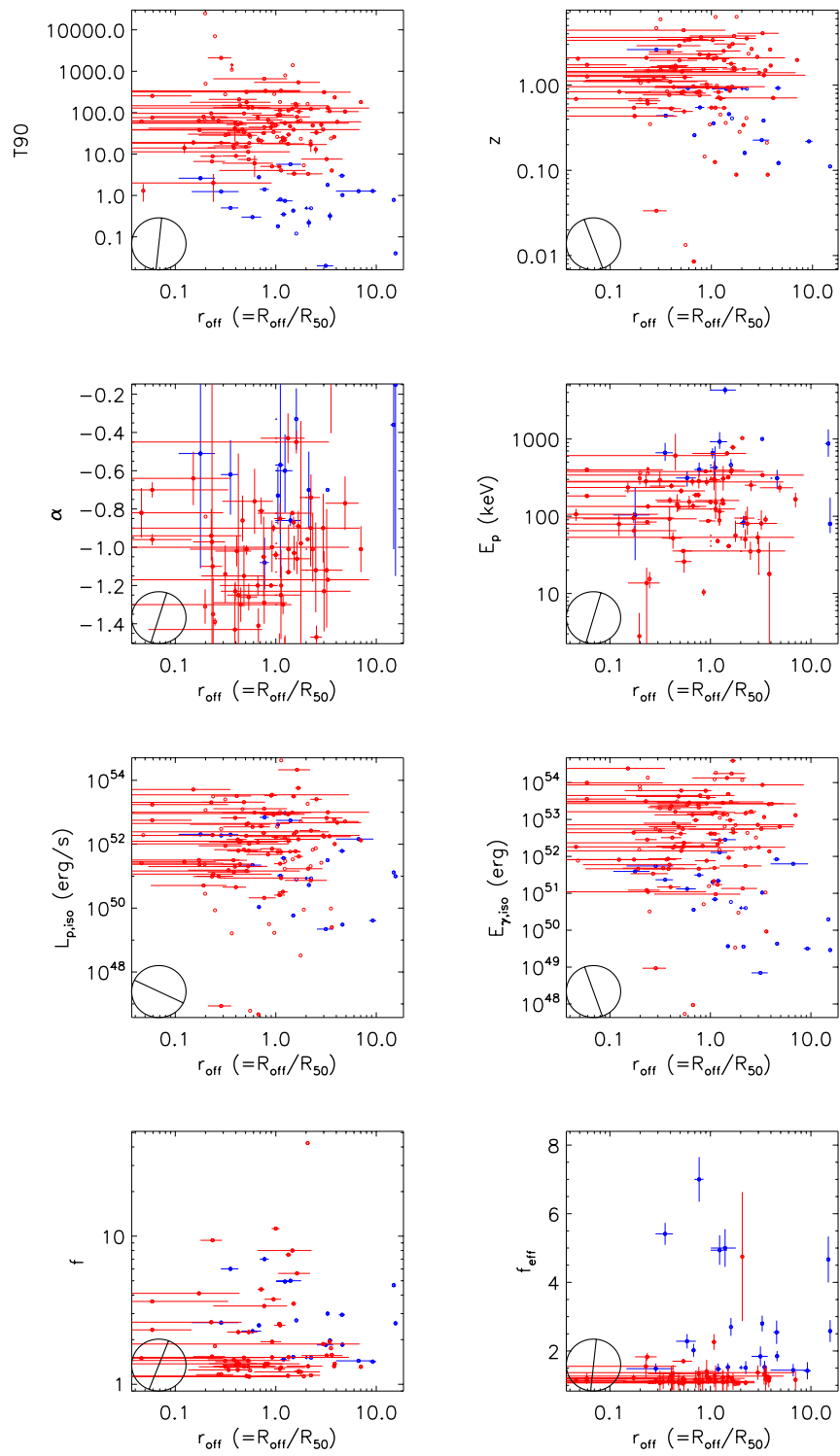


Fig. 9—Continued

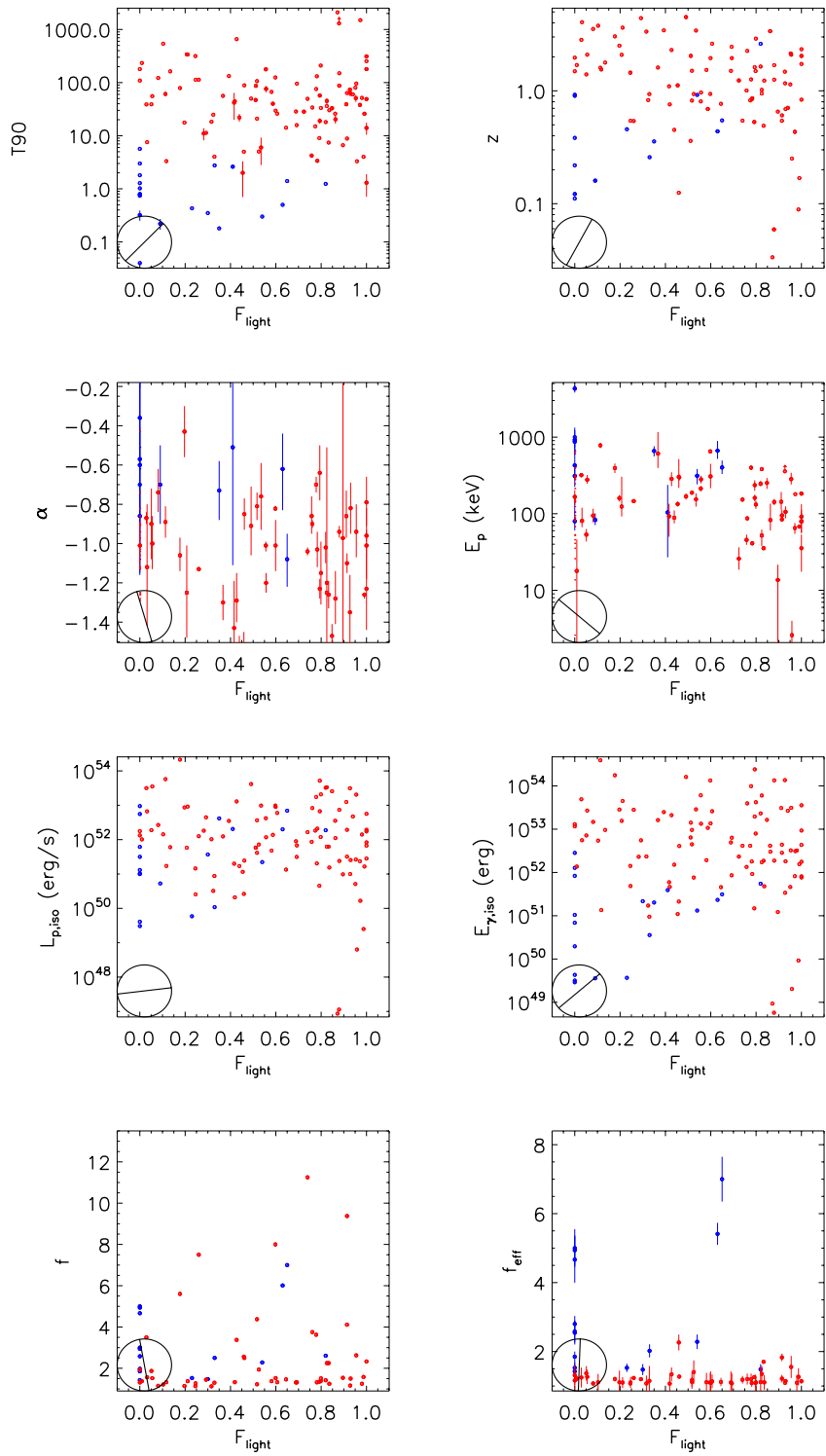


Fig. 9—Continued

Name	Consensus L/S							
	No. LGRB	No. value	No. SGRB	value	P_{KS}	Overlap range	LGRB in overlap (%)	SGRB in overlap (%)
$\log T_{90}$ (s)	369	1.70 ± 0.60	34	-0.30 ± 0.57	3.e-26	(0.11,0.75)	7	20
z	351	1.64 ± 1.30	25	0.45 ± 0.51	8.e-11	(0.11,2.61)	72	100
$\log E_{\text{iso}}$ (erg)	369	52.7 ± 1.0	33	51.1 ± 0.9	5.e-14	(48.8,52.5)	36	100
$\log L_{\text{iso}}$ (erg s ⁻¹)	366	52.1 ± 1.1	33	51.3 ± 1.1	7.e-03	(49.3,53.0)	78	100
α	196	-1.01 ± 0.34	16	-0.60 ± 0.25	2.e-07	(-1.08,-0.15)	55	100
$\log E_{\text{p}}$ (keV)	202	2.17 ± 0.47	18	2.66 ± 0.43	2.e-04	(1.90,3.5)	73	94
$\log f$	224	0.13 ± 0.22	29	0.41 ± 0.22	1.e-07	(0.15,0.91)	43	100
f_{eff}	214	1.11 ± 0.30	29	2.28 ± 1.76	2.e-20	(1.42,4.8)	7	79
$\log \text{SFR}$ ($M_{\odot} \text{ yr}^{-1}$)	149	0.70 ± 0.85	16	0.32 ± 0.80	8.e-02	(-1.00,1.76)	88	100
$\log \text{sSFR}$ (Gyr ⁻¹)	77	-0.03 ± 0.67	14	-0.51 ± 0.97	2.e-02	(-2.20,1.05)	90	92
$\log M_{*}$ (M_{\odot})	101	9.5 ± 0.8	22	10.1 ± 0.8	1.e-01	(8.6,11.4)	86	100
[X/H]	134	-0.59 ± 0.60	9	-0.09 ± 0.25	7.e-04	(-0.59,0.21)	47	100
$\log R_{50}$ (kpc)	128	0.26 ± 0.32	24	0.57 ± 0.29	4.e-04	(0.15,1.03)	69	91
$\log R_{\text{off}}$ (kpc)	136	0.25 ± 0.55	28	1.02 ± 0.62	1.e-04	(-0.31,1.44)	83	82
$\log r_{\text{off}}$ (= R_{off}/R_{50})	117	-0.07 ± 0.44	24	0.20 ± 0.51	2.e-02	(-0.75,0.85)	93	87
F_{light}	99	0.69 ± 0.31	20	0.09 ± 0.27	7.e-05	(0.00,0.82)	65	100
<i>z < 1.4</i>								
$\log T_{90}$ (s)	158	1.61 ± 0.70	33	-0.31 ± 0.57	1.e-22	(0.15,0.75)	11	21
z	140	0.83 ± 0.36	24	0.45 ± 0.30	1.e-03	(0.11,1.13)	72	100
$\log E_{\text{iso}}$ (erg)	158	52.2 ± 1.2	32	51.1 ± 0.9	2.e-06	(48.8,52.5)	57	100
$\log L_{\text{iso}}$ (erg s ⁻¹)	156	51.5 ± 1.3	32	51.3 ± 1.1	8.e-01	(49.3,53.0)	81	100
α	90	-1.13 ± 0.37	16	-0.60 ± 0.25	2.e-07	(-1.08,-0.15)	40	100
$\log E_{\text{p}}$ (keV)	94	2.11 ± 0.53	18	2.66 ± 0.43	3.e-04	(1.90,3.5)	70	94
$\log f$	84	0.18 ± 0.29	28	0.41 ± 0.22	8.e-05	(0.15,0.91)	47	100
f_{eff}	82	1.15 ± 0.44	28	2.33 ± 1.77	4.e-16	(1.42,4.8)	9	78
$\log \text{SFR}$ ($M_{\odot} \text{ yr}^{-1}$)	78	0.38 ± 0.79	16	0.32 ± 0.80	1.e+00	(-1.00,1.76)	88	100
$\log \text{sSFR}$ (Gyr ⁻¹)	55	-0.08 ± 0.68	14	-0.51 ± 0.97	2.e-02	(-2.20,1.05)	90	92
$\log M_{*}$ (M_{\odot})	72	9.3 ± 0.8	22	10.1 ± 0.8	4.e-02	(8.6,11.4)	80	100
[X/H]	53	-0.39 ± 0.31	9	-0.09 ± 0.25	1.e-02	(-0.59,0.21)	73	100
$\log R_{50}$ (kpc)	78	0.32 ± 0.33	23	0.57 ± 0.28	4.e-03	(0.15,1.03)	73	91
$\log R_{\text{off}}$ (kpc)	79	0.25 ± 0.58	27	1.02 ± 0.58	2.e-04	(-0.13,1.22)	77	62
$\log r_{\text{off}}$ (= R_{off}/R_{50})	69	-0.12 ± 0.44	23	0.20 ± 0.49	1.e-02	(-0.75,0.69)	91	82
F_{light}	55	0.79 ± 0.24	19	0.00 ± 0.24	2.e-07	(0.05,0.65)	36	47

Table 1 Statistical results of properties for consensus LGRB/SGRB definition.

Name	No. LGRB	value	No. SGRB	T90 L/S			SGRB in overlap (%)
				value	P_{KS}	Overlap range	
$\log T_{90}$ (s)	371	1.70 ± 0.60	32	-0.31 ± 0.50	2.e-27	(0.30,0.26)	0
z	352	1.63 ± 1.31	24	0.46 ± 0.60	6.e-08	(0.11,2.61)	73
$\log E_{\text{iso}}$ (erg)	371	52.7 ± 1.0	31	51.0 ± 0.9	5.e-15	(48.8,52.4)	35
$\log L_{\text{iso}}$ (erg s $^{-1}$)	368	52.1 ± 1.1	31	51.2 ± 1.0	1.e-03	(49.3,53.0)	80
α	198	-1.01 ± 0.34	14	-0.60 ± 0.32	3.e-03	(-1.36,-0.15)	84
$\log E_{\text{p}}$ (keV)	204	2.17 ± 0.48	16	2.66 ± 0.35	3.e-04	(1.90,3.00)	71
$\log f$	226	0.14 ± 0.22	27	0.36 ± 0.23	2.e-06	(0.14,0.91)	45
f_{eff}	216	1.12 ± 0.40	27	2.19 ± 1.78	5.e-18	(1.38,5.0)	10
$\log \text{sSFR}$ ($M_{\odot} \text{ yr}^{-1}$)	150	0.71 ± 0.86	15	0.40 ± 0.70	5.e-02	(-1.00,1.48)	78
$\log M_{*}$ (M_{\odot})	78	-0.04 ± 0.68	13	-0.22 ± 1.00	2.e-01	(-2.20,1.05)	89
$[\text{X}/\text{H}]$	103	9.5 ± 0.8	20	10.1 ± 0.9	2.e-01	(8.6,11.4)	86
$\log R_{50}$ (kpc)	133	-0.61 ± 0.61	10	-0.19 ± 0.26	1.e-02	(-0.59,0.21)	43
$\log R_{\text{off}}$ (kpc)	131	0.27 ± 0.32	21	0.57 ± 0.30	3.e-03	(0.15,1.03)	70
$\log r_{\text{off}}$ ($=R_{off}/R_{50}$)	139	0.25 ± 0.55	25	0.74 ± 0.68	6.e-04	(-0.56,1.44)	91
F_{light}	120	-0.05 ± 0.43	21	0.20 ± 0.60	3.e-02	(-1.32,0.85)	99
F_{light}	102	0.65 ± 0.32	17	0.09 ± 0.34	4.e-03	(0.00,1.00)	100
<i>z < 1.4</i>							
$\log T_{90}$ (s)	161	1.59 ± 0.70	30	-0.37 ± 0.49	1.e-23	(0.30,0.26)	0
z	142	0.83 ± 0.36	22	0.45 ± 0.32	1.e-03	(0.11,1.29)	85
$\log E_{\text{iso}}$ (erg)	161	52.2 ± 1.2	29	51.0 ± 0.9	4.e-08	(48.8,52.4)	57
$\log L_{\text{iso}}$ (erg s $^{-1}$)	159	51.5 ± 1.3	29	51.2 ± 1.0	5.e-01	(49.3,53.0)	83
α	92	-1.13 ± 0.38	14	-0.60 ± 0.32	4.e-06	(-1.36,-0.15)	75
$\log E_{\text{p}}$ (keV)	96	2.11 ± 0.54	16	2.66 ± 0.35	3.e-04	(1.90,3.00)	66
$\log f$	86	0.18 ± 0.29	26	0.36 ± 0.23	8.e-04	(0.14,0.91)	50
f_{eff}	84	1.15 ± 0.61	26	2.28 ± 1.80	4.e-13	(1.38,5.0)	92
$\log \text{sSFR}$ ($M_{\odot} \text{ yr}^{-1}$)	80	0.36 ± 0.81	14	0.40 ± 0.72	1.e+00	(-1.00,1.48)	87
$\log M_{*}$ (M_{\odot})	57	-0.08 ± 0.69	12	-0.22 ± 1.04	2.e-01	(-2.20,1.05)	89
$[\text{X}/\text{H}]$	75	9.3 ± 0.8	19	10.1 ± 0.9	3.e-02	(8.6,11.4)	81
$\log R_{50}$ (kpc)	53	-0.35 ± 0.31	9	-0.19 ± 0.27	9.e-02	(-0.59,0.21)	67
$\log R_{\text{off}}$ (kpc)	82	0.33 ± 0.33	19	0.57 ± 0.30	3.e-02	(0.15,1.03)	74
$\log r_{\text{off}}$ ($=R_{off}/R_{50}$)	83	0.28 ± 0.58	23	1.06 ± 0.58	5.e-04	(0.12,1.22)	59
F_{light}	73	-0.12 ± 0.45	19	0.33 ± 0.46	7.e-03	(-0.45,0.69)	75
F_{light}	59	0.78 ± 0.28	15	0.00 ± 0.25	4.e-05	(0.00,0.65)	40
							93

Table 2 Statistical results of properties for T90 defined LGRB/SGRB.

Name		N(LGRB)	value	Consensus L/S N(SGRB)	value	P_{KS}	N(LGRB)	value	T90 L/S N(SGRB)	value	P_{KS}
$\log T_{90}$ (s)		359	1.67 ± 0.57	41	-0.13 ± 0.61	5.e-30	365	1.67 ± 0.57	35	-0.30 ± 0.50	1.e-29
z		380	1.75 ± 1.38	20	0.44 ± 0.31	5.e-09	378	1.75 ± 1.38	22	0.46 ± 0.46	6.e-08
$\log E_{\text{iso}}$ (erg)		363	52.6 ± 1.0	37	51.0 ± 1.0	7.e-14	370	52.6 ± 1.0	30	50.9 ± 0.9	4.e-16
$\log L_{\text{iso}}$ (erg s $^{-1}$)		368	52.2 ± 1.1	32	51.2 ± 1.2	3.e-04	370	52.2 ± 1.1	30	51.2 ± 1.2	3.e-04
α		367	-1.03 ± 0.33	33	-0.60 ± 0.17	7.e-15	369	-1.01 ± 0.33	31	-0.62 ± 0.30	2.e-12
$\log E_p$ (keV)		362	2.19 ± 0.49	38	2.69 ± 0.41	4.e-10	365	2.19 ± 0.50	35	2.66 ± 0.33	1.e-09
$\log f$		358	0.12 ± 0.22	42	0.36 ± 0.21	1.e-12	356	0.12 ± 0.22	44	0.30 ± 0.21	1.e-12
f_{eff}		346	1.11 ± 0.32	54	2.54 ± 1.84	4.e-38	352	1.11 ± 0.46	48	2.19 ± 1.92	2.e-32
$\log \text{SFR}$ (M $_{\odot}$ yr $^{-1}$)		364	0.83 ± 0.86	36	0.08 ± 0.72	3.e-03	367	0.80 ± 0.87	33	0.40 ± 0.67	1.e-02
$\log \text{sSFR}$ (Gyr $^{-1}$)		345	-0.03 ± 0.71	55	-0.51 ± 0.92	3.e-02	339	-0.04 ± 0.71	61	0.13 ± 0.93	2.e-04
$\log M_*$ (M $_{\odot}$)		327	9.5 ± 0.8	73	9.7 ± 0.8	2.e-05	336	9.5 ± 0.8	64	9.7 ± 0.8	2.e-04
[X/H]		375	-0.59 ± 0.62	25	-0.19 ± 0.23	4.e-09	367	-0.59 ± 0.62	33	-0.19 ± 0.24	3.e-08
$\log R_{50}$ (kpc)		342	0.28 ± 0.30	58	0.57 ± 0.29	6.e-10	344	0.28 ± 0.30	56	0.36 ± 0.32	9.e-08
$\log R_{\text{off}}$ (kpc)		347	0.21 ± 0.53	53	0.72 ± 0.66	4.e-06	349	0.24 ± 0.52	51	0.72 ± 0.74	9.e-06
$\log r_{\text{off}}$ (=R $_{\text{off}}$ /R $_{50}$)		326	-0.04 ± 0.44	74	0.20 ± 0.44	4.e-07	329	-0.04 ± 0.42	71	0.17 ± 0.57	1.e-05
F_{light}		326	0.69 ± 0.30	74	0.09 ± 0.25	4.e-19	330	0.69 ± 0.31	70	0.30 ± 0.28	2.e-11
$z < 1.4$											
$\log T_{90}$ (s)		323	1.48 ± 0.66	77	-0.30 ± 0.55	0.e+00	336	1.41 ± 0.66	64	-0.30 ± 0.43	0.e+00
z		341	0.81 ± 0.37	59	0.45 ± 0.33	3.e-05	342	0.82 ± 0.37	58	0.46 ± 0.36	7.e-05
$\log E_{\text{iso}}$ (erg)		313	52.2 ± 1.1	87	51.3 ± 1.0	2.e-10	325	52.2 ± 1.1	75	51.0 ± 0.9	2.e-15
$\log L_{\text{iso}}$ (erg s $^{-1}$)		310	51.4 ± 1.3	90	51.3 ± 1.1	3.e-01	317	51.4 ± 1.3	83	51.2 ± 1.0	4.e-02
α		339	-1.18 ± 0.36	61	-0.70 ± 0.19	1.e-28	346	-1.13 ± 0.37	54	-0.70 ± 0.25	9.e-27
$\log E_p$ (keV)		339	2.16 ± 0.49	61	2.63 ± 0.45	9.e-11	348	2.15 ± 0.51	52	2.69 ± 0.36	3.e-11
$\log f$		304	0.17 ± 0.32	96	0.34 ± 0.21	1.e-16	301	0.18 ± 0.32	99	0.29 ± 0.21	2.e-14
f_{eff}		306	1.15 ± 0.50	94	2.28 ± 1.88	0.e+00	304	1.15 ± 0.62	96	2.19 ± 1.84	0.e+00
$\log \text{SFR}$ (M $_{\odot}$ yr $^{-1}$)		318	0.38 ± 0.81	82	0.08 ± 0.61	6.e-06	323	0.32 ± 0.81	77	0.40 ± 0.58	6.e-02
$\log \text{sSFR}$ (Gyr $^{-1}$)		317	-0.08 ± 0.69	83	-0.52 ± 0.89	7.e-13	325	-0.12 ± 0.70	75	-0.22 ± 0.95	8.e-05
$\log M_*$ (M $_{\odot}$)		309	9.3 ± 0.7	91	9.6 ± 0.8	2.e-03	315	9.3 ± 0.7	85	9.3 ± 0.8	3.e-03
[X/H]		331	-0.39 ± 0.28	69	-0.09 ± 0.19	4.e-21	326	-0.35 ± 0.29	74	-0.19 ± 0.20	4.e-12
$\log R_{50}$ (kpc)		313	0.35 ± 0.33	87	0.60 ± 0.34	5.e-11	321	0.37 ± 0.32	79	0.57 ± 0.40	6.e-06
$\log R_{\text{off}}$ (kpc)		300	0.31 ± 0.57	100	1.02 ± 0.56	2.e-14	312	0.34 ± 0.56	88	0.74 ± 0.70	3.e-11
$\log r_{\text{off}}$ (=R $_{\text{off}}$ /R $_{50}$)		293	-0.18 ± 0.43	107	0.20 ± 0.51	4.e-13	305	-0.17 ± 0.43	95	0.33 ± 0.52	2.e-11
F_{light}		296	0.78 ± 0.23	104	0.09 ± 0.25	2.e-32	300	0.78 ± 0.26	100	0.23 ± 0.25	5.e-24

Table 3 Statistical results of Simulated 1D distributions.

	No.	angle	T_{90}	P_{KS}	ρ_s	P_s	No.	angle	P_{KS}^z	ρ_s	P_s	No.	angle	P_{KS}^α	ρ_s	P_s	E_p (keV)	P_{KS}	ρ_s	P_s	
$M_*(M_\odot)$	101/22	87	4.e-15	2.e-01	1.e-01	94/20	111	1.e-04	5.e-01	3.e-01	60/10	2.e-02	63/11	86	6.e-04	1.e-01	4.e-01				
$\text{SFR} (M_\odot \text{ yr}^{-1})$	149/16	80	7.e-12	3.e-01	2.e-03	149/16	87	4.e-05	5.e-01	4.e-11	74/9	101	4.e-03	5.e-03	3.e-01	5.e-03	8.e-04	1.e-01	3.e-01		
$\text{sSFR} (\text{yr}^{-1})$	77/14	68	2.e-10	1.e-01	3.e-01	77/14	18	1.e-02	2.e-01	7.e-02	48/7	87	8.e-04	-1.e-01	4.e-01	4.e-04	92	4.e-04	-1.e-01	4.e-01	
$[\text{X}/\text{H}]$	134/9	115	3.e-08	-8.e-02	4.e-01	134/9	104	1.e-05	-6.e-01	7.e-14	65/7	46	2.e-04	-3.e-01	4.e-02	68/7	31	2.e-03	-1.e-01	3.e-01	
$R_{50} (\text{kpc})$	128/24	115	8.e-19	-1.e-01	2.e-01	113/17	147	3.e-06	-2.e-01	7.e-02	74/12	75	2.e-07	5.e-02	7.e-01	79/14	26	6.e-06	8.e-02	5.e-01	
$R_{\text{off}} (\text{kpc})$	136/28	104	1.e-20	-5.e-02	6.e-01	124/19	107	2.e-08	-1.e-02	9.e-01	75/15	71	5.e-09	2.e-01	1.e-01	79/17	60	5.e-05	8.e-02	5.e-01	
$r_{\text{off}} (= R_{\text{off}}/R_{50})$	117/24	84	9.e-17	9.e-03	9.e-01	106/17	110	4.e-06	9.e-02	4.e-01	65/12	73	3.e-06	2.e-01	1.e-01	69/14	74	1.e-04	-2.e-02	9.e-01	
F_{light}	99/20	46	3.e-15	-8.e-02	4.e-01	89/14	62	9.e-07	-4.e-01	4.e-04	55/11	106	4.e-07	-2.e-01	1.e-01	58/13	139	7.e-05	-3.e-01	3.e-02	
$M_*(M_\odot)$	100/22	169	1.e-02	2.e-01	2.e-02	101/22	102	1.e-07	2.e-03	2.e-01	49/19	84	1.e-03	-3.e-01	3.e-02	48/19	75	6.e-11	-4.e-01	6.e-03	
$\text{SFR} (M_\odot \text{ yr}^{-1})$	147/16	158	9.e-03	3.e-01	1.e-03	149/16	103	6.e-06	4.e-01	8.e-06	87/14	98	3.e-05	-3.e-01	3.e-03	83/14	90	2.e-10	-4.e-01	4.e-04	
$\text{sSFR} (\text{yr}^{-1})$	76/14	6	1.e-02	5.e-02	7.e-01	77/14	78	2.e-04	9.e-02	4.e-01	37/12	1112	2.e-02	-1.e-01	4.e-01	36/12	101	1.e-07	-3.e-01	9.e-02	
$[\text{X}/\text{H}]$	134/9	1	3.e-04	-4.e-01	4.e-07	134/9	113	5.e-06	-4.e-01	2.e-06	81/7	51	4.e-06	-6.e-02	6.e-01	74/7	30	1.e-06	-5.e-02	7.e-01	
$R_{50} (\text{kpc})$	126/23	173	1.e-05	-4.e-02	7.e-01	128/23	137	5.e-10	-8.e-02	4.e-01	62/20	20	4.e-05	6.e-02	7.e-01	59/20	87	4.e-12	4.e-02	8.e-01	
$R_{\text{off}} (\text{kpc})$	134/27	166	3.e-06	6.e-02	5.e-01	136/27	111	1.e-11	3.e-02	7.e-01	73/24	71	1.e-06	-2.e-02	8.e-01	69/24	86	3.e-14	1.e-01	3.e-01	
$r_{\text{off}} (= R_{\text{off}}/R_{50})$	115/23	154	9.e-04	9.e-02	3.e-01	117/23	108	2.e-09	8.e-02	4.e-01	61/20	68	5.e-05	-5.e-02	7.e-01	58/20	84	5.e-12	1.e-01	4.e-01	
F_{light}	98/19	7	4.e-05	-2.e-01	1.e-01	99/19	41	7.e-10	-2.e-01	6.e-02	53/16	100	2.e-04	2.e-01	2.e-01	50/16	87	4.e-10	9.e-03	1.e+00	

Table 4 Statistical results of 2D.

CHAPTER 3

A COMPARATIVE STUDY OF LONG AND SHORT GRBS. II. A MULTIWAVELENGTH METHOD TO DISTINGUISH TYPE I AND TYPE II GRBS

This chapter is part of a paper in preparation:

Ye Li, Bing Zhang, 2017, in preparation

Introduction

Gamma Ray Bursts (GRBs) are intense seconds-duration γ -ray emitting events in the universe. They are physically classified into Type II GRBs, which originate from core collapse of massive stars, especially for mass higher than $40 M_{\odot}$ (Woosley, 1993; Paczyński, 1998; MacFadyen & Woosley, 1999), and Type I GRBs, which are from compact star mergers, i.e., neutron star - neutron star (NS-NS) or neutron star - black hole (NS-BH) mergers (Paczynski (1986); Eichler et al. (1989); Narayan et al. (1992), see Berger (2014) for a review).

This physical classification of GRBs is largely related to the phenomenological classification of GRBs based on the prompt γ -ray durations. The Type II GRBs are supposed to be those with γ -ray durations (T_{90}) longer than 2 s, which are known as long-duration GRBs (LGRBs). The LGRB hosts are usually dwarf galaxies with high star formation rate and low metallicity (Sahu et al., 1997; Bloom et al., 1998, 2002; Chary et al., 2002; Christensen et al., 2004; Savaglio et al., 2009; Krühler et al., 2015). Typically LGRBs are located in bright regions of their hosts, with small offsets from the galaxy center (Bloom et al., 2002; Fruchter et al., 2006; Blanchard et al., 2016). A smoking gun of the connection between an LGRB and a core collapse event is the discovery of accompanied Type Ic supernova (SN) (Galama et al., 1998; Hjorth et al., 2003a; Stanek et al., 2003; Woosley & Bloom, 2006; Hjorth & Bloom, 2012; Xu et al., 2013b). The Type I GRBs, on the other hand, mostly correspond to those with T_{90} shorter than 2 s, and are called short-duration GRBs (SGRBs). This is supported by the diversity of their hosts, from dwarf to elliptical galaxies (Gehrels et al., 2005; Berger

et al., 2005b). Within the hosts, SGRBs can be located in faint regions with large offsets from the center (Fong et al., 2010; Kann et al., 2011; Fong & Berger, 2013). No association of SN was found for SGRBs, and stringent limits of SNe were set (Fox et al., 2005; Hjorth et al., 2005a,b; Kann et al., 2011; Berger et al., 2013). The “kilonovae/macronovae” events found for a few SGRBs turn out to support the scenario of compact star mergers of SGRBs (Li & Paczyński, 1998; Metzger et al., 2010; Tanvir et al., 2013b; Berger et al., 2013; Yang et al., 2015; Gao et al., 2015; Jin et al., 2016a).

While the duration T_{90} is widely used to relate GRBs with their physical origins, it is not always reliable. GRB 090426 has a T_{90} of 1.24 s. Phenomenologically it was classified as a SGRB, which is presumed to be of compact star merger origin. However, it is located in the central region of a blue interacting host galaxy, and is suggested to be of core collapse origin based on multi-wavelength studies (Antonelli et al., 2009; Levesque et al., 2010b). Another example is GRB 060614, which shows a 4.5 s spike with extended emission in the prompt γ -ray emission (Gehrels et al., 2006; Norris et al., 2010b). It would be phenomenologically classified as an LGRB. However, it is located in a faint region of a passive host galaxy (Gal-Yam et al., 2006; Fynbo et al., 2006; Blanchard et al., 2016). Furthermore, a very tight limit was set against its association with any SN, (Gal-Yam et al., 2006; Della Valle et al., 2006; Fynbo et al., 2006). A putative kilonova was reported, suggesting that it is most likely a Type I GRB with a long duration (Zhang et al., 2007; Yang et al., 2015).

These anomalies suggest that a more robust method to classify GRBs by their physical nature, with multiple observables other than the sole duration is necessary. Zhang et al. (2009) suggested a multi-wavelength scheme to connect a GRB with its physical origin, taking into account the prompt emission, host galaxy, sub-galaxy phenomena, and SN association. Based on this method, we develop a quantitative classifier for GRB classification in this work. In an accompany paper, we gathered multi-wavelength properties of 407 GRBs, including their prompt emission characters such as the duration (T_{90}), the spectral peak energy (E_p), the low energy photon index (α), the isotropic γ -ray energy ($E_{\gamma,\text{iso}}$), the isotropic peak

luminosity ($L_{\text{p,iso}}$), the amplitude parameters (f and f_{eff}), and the host galaxy properties, such as the stellar mass (M_*), the star formation rate (SFR), the metallicity ([X/H]), the half light radius (R_{50}), the angular and physical offset of the afterglow from the center of the host galaxy (R_{off}), the normalized offset ($r_{\text{off}} = R_{\text{off}}/R_{50}$), and the brightness fraction F_{light} . We found that all these properties showed overlapping between the LGRB and SGRB samples. It indicates that a combined method of these multi-wavelength data is required to improve the physical classification of GRBs, which is the goal of this paper. We describe our method in Section 2. The results are shown in Section 3. Section 4 presents our conclusion with some discussion.

Distributions of GRB parameters

Our method is essentially a multi-parameter scheme based on multi-wavelength data of GRBs. We first look at the distributions of observational quantities for different types of GRBs. We use a control sample based on the catalog given in Li et al. (2016), in which the prompt emission and host galaxy parameters of 407 GRBs were compiled. In total there were 16 parameters presented, including the redshift, 7 prompt emission parameters, and 8 host galaxy parameters. The prompt emission parameters include the duration T_{90} , two spectral parameters (the peak energy E_{p} and the low energy index α) of the best-fitting Band function (Band et al., 1993), the isotropic γ -ray energy E_{iso} , the isotropic γ -ray peak luminosity L_{iso} , the amplitude f parameter (the ratio between the peak flux and the background), and the effective f parameter f_{eff} (the f parameter when the background is shifted to make the duration T_{90} be 2 seconds). The host galaxy parameters are the stellar mass of the host M_* , the star formation rate (SFR), the specific star formation rate (sSFR; the ratio between SFR and M_*), the metallicity of the host [X/H], the half-light radius of the host R_{50} , the offset of the GRB from the center of the host galaxy in a unit of kpc and R_{50} , and the fraction of the host area fainter than the magnitude of the GRB position F_{light} .

Their “consensus” LGRBs and SGRBs are defined based on the online catalog¹, which takes the multi-wavelength observational data into account. We consider their LGRBs as preliminary Type II GRBs, and SGRBs as preliminary Type I GRBs. As a control sample, we exclude a few highly debated objects, including GRB 060614, GRB 060505, GRB 090426 and GRB 060121.

For each parameter we use a Gaussian function

$$P(x|\text{Type}) = Ae^{-\frac{(x-\mu)^2}{2\sigma^2}} \quad (3.1)$$

to fit the distribution of each of these two classes of GRBs. For some parameters we adopt proper selections of the sample used for the fitting. For redshifts, we only consider the sample with precise spectral redshifts. The original definition of f_{eff} is around 1. In this work, we use $f_{\text{eff}} - 1$ instead. The stellar mass of the host galaxies M_* is estimated by either the spectral energy density (SED) fitting or the infrared (IR) luminosity. The IR luminosity method assumes a 70 Myr old stellar population, which gives a very large uncertainty of M_* . Therefore, we just take the SED estimated stellar mass into account. The star formation rate (SFR) is estimated by emission lines such as H α , H β , [OIII], [OII], Ly α , as well as continuum such as UV, IR, and SED fitting. Emission lines indicate the SFR with age 0-10 Myr, around the life of stars with mass $> 30 M_\odot$. The continuum, on the other hand, indicates the SFR with age 0-100 Myr (Kennicutt & Evans, 2012). Here only the values obtained by emission lines are used in the fitting. We further exclude the upper and lower limits of the SFR. The metallicity [X/H] estimated with $R_{23} = ([\text{OII}]\lambda 3727 + [\text{OIII}]\lambda 4959, 5007)/\text{H}\beta$, are double-valued (Kewley & Ellison, 2008; Savaglio et al., 2009). Following the suggestions by Kobulnicky & Kewley (2004) and Berger (2009), we use the larger one of those two values as the metallicity of each GRB.

We use a χ^2 fitting method to fit the preliminary Type II sample. For the Type I sample, the Cash likelihood (Cash, 1979) is adopted due to its small sample size. The histogram of

¹<http://www.mpe.mpg.de/~jcg/grbgen.html>

each parameter and the best fit results are shown in the left panels of Fig. 12, with red lines for type II GRBs and blue lines for type I. The fitting results are given in Table. 5. Column 2 of Table. 5 shows the observational range of each parameter. The mean and standard deviation for type II and type I GRBs are listed in columns 4 and 5, 8 and 9 of Table. 5. Column 6 presents the χ^2 value over the degree of freedom (DOF) of the fitting.

We normalize the integral of each distribution within the observational range to unit, and derive the normalization factors, which are shown in columns 3 and 7 in Table. 5. The normalized probability distributions P of each parameter are shown in the right panels of Fig. 12. The ratios between $P(x|\text{TypeII})$ and $P(x|\text{TypeI})$ are presented by green lines.

parameter	range	type II				type I		
		norm A	mean μ	$\sigma(\gamma)$	χ^2/dof	norm A	mean μ	$\sigma(\gamma)$
$\log T_{90}$	(-1.70, 4.40)	0.68	1.68	0.59	5.7/8	0.73	-0.35	0.55
z	(0.01, 8.23)	0.34	1.47	1.38	31.9/29	1.41	0.53	0.29
$\log E_{\text{iso}}$ (erg)	(47.73, 54.60)	0.47	52.70	0.85	18.2/11	0.42	51.11	0.95
$\log L_{\text{iso}}$ (erg s $^{-1}$)	(46.67, 54.63)	0.45	52.15	0.88	20.4/16	0.35	51.72	1.15
α	(-1.88, -0.06)	1.38	-1.04	0.29	19.8/16	1.61	-0.55	0.25
$\log E_{\text{P}}$ (keV)	(0.41, 3.63)	0.86	2.17	0.46	2.0/3	0.99	2.62	0.41
$\log f$	(0.02, 1.05)	3.1e+09	-7.09	1.12	19.6/8	1.9e+00	0.43	0.21
$\log (f_{\text{eff}} - 1)$	(-2.00, 0.83)	1.09	-0.93	0.37	15.3/14	1.14	0.13	0.36
$\log \text{SFR} (\text{M}_\odot \text{ yr}^{-1})$	(-1.30, 2.29)	0.49	0.73	0.84	4.1/5	0.54	0.30	0.76
$\log \text{sSFR} (\text{Gyr}^{-1})$	(-2.30, 1.76)	0.60	0.06	0.67	4.2/6	0.43	-0.19	0.96
$\log M_*$ (M_\odot)	(7.74, 11.51)	0.50	9.49	0.82	4.5/7	0.50	9.92	0.81
[X/H]	(-2.14, 0.67)	0.65	-0.59	0.64	24.8/11	2.57	-0.03	0.15
$\log R_{50}$ (kpc)	(-0.47, 1.31)	1.26	0.27	0.32	7.0/6	1.40	0.56	0.29
$\log \text{offset}$ (kpc)	(-1.10, 1.94)	0.73	0.24	0.55	8.0/11	0.77	0.94	0.53
$\log \text{offset}$ (R_{50})	(-1.34, 1.19)	0.96	-0.09	0.42	12.4/8	0.95	0.35	0.43
F_{light}	(0.00, 1.00)	5.8e+05	20.61	3.89	10.4/7	1.1e+37	-29.76	2.30

Table 5 Gaussian fitting results of each parameter for the preliminary type II and I samples of Li et al. (2016).

Classification

Bayesian method to classify Type I and Type II GRBs

According to the Bayesian theorem, the posterior probability of one GRB with parameters $\{x\} = \{x_1, x_2, \dots, x_i\}$ to be a hypothesized Type is

$$P(\text{Type}|\{x\}) = \frac{P(\{x\}|\text{Type})P(\text{Type})}{P(\{x\})}, \quad (3.2)$$

where $P(\text{Type})$ is the prior probability of a GRB to be one specific type, $P(\{x\})$ is probability of the parameter set $\{x\}$, and $P(\{x\}|\text{Type})$ is the likelihood of one specific type of GRB to have a parameter set x . For a GRB with more than one available parameters, $P(\{x\}|\text{Type}) = \prod_i P(x_i|\text{Type})$. The likelihood for each parameter $P(x_i|\text{Type})$ is estimated with the observed sample as presented in the previous section. We assume a uniform prior for both types of GRBs. Different priors will only change the absolute value of the posterior probability, without affecting the relative values of the probability ratios (see below) of these two types.

The ratio of the posterior probabilities

$$O(\text{II} : \text{I}|\{x\}) = \frac{P(\text{TypeII}|\{x\})}{P(\text{TypeI}|\{x\})} \quad (3.3)$$

$$= \frac{P(\text{TypeII})}{P(\text{TypeI})} \frac{P(\{x\}|\text{TypeII})}{P(\{x\}|\text{TypeI})} \quad (3.4)$$

gives the degree that the observed parameter set $\{x\}$ supports Type II against Type I hypothesis. Neglecting the correlation between parameters x_i , we have

$$O(\text{II} : \text{I}|\{x\}) = \frac{P(\text{TypeII}) \prod_i P(x_i|\text{TypeII})}{P(\text{TypeI}) \prod_i P(x_i|\text{TypeI})}. \quad (3.5)$$

For each GRB, i runs over all known parameters. The absence of parameters indicates no preference, and $P(x_i|\text{TypeII}) = P(x_i|\text{TypeI})$ are set. However, there are some obvious correlated parameters, e.g., subsets $\{\text{SFR, sSFR and } M_*\}$, $\{L_{\text{iso}}, E_{\text{iso}} \text{ and } T_{90}\}$, $\{R_{50}, R_{\text{off}} \text{ and } r_{\text{off}}\}$, and redshift z . In order to avoid significant correlation, we exclude the parameter with the least separation capability, i.e., the largest P_{KS} in Table 7 of Li et al. (2016), in each subset. For example, the isotropic peak luminosity L_{iso} is excluded, since it could be roughly reproduced by T_{90} and E_{iso} , and its P_{KS} value for Type II and Type I GRBs is larger than those of T_{90} and E_{iso} . Similarly, we exclude f , SFR, and R_{off} . Finally, as presented in Li et al. (2016), the redshift z is controlled by selection effect and correlated with many parameters, such as E_{iso} , SFR and [X/H]. We do not include z either. In summary, we take

the parameters T_{90} , E_{iso} , α , E_p , f_{eff} , sSFR, M_* , [X/H], R_{50} , $r_{off} = R_{off}/R_{50}$, and F_{light} to calculate the probability ratio.

The priors $P(\text{TypeI})$ and $P(\text{TypeII})$ are unknown. We try three values of them. The first one is considering even priors of them, i.e., $P(\text{TypeII})/P(\text{TypeI}) = 0.5/0.5 = 1$, as statisticians do. The second one is to use the observed number ratio of them, i.e., $P(\text{TypeII})/P(\text{TypeI}) = 370/33 = 11$. The third one is to use the event rate ratio of them (Sun et al., 2015), thus $P(\text{TypeII})/P(\text{TypeI}) = 0.8/1.3 = 0.6$. Different priors would give different absolute values of the probability ratios. However, we only care about the relative values of GRBs and the absolute values do not matter. Thus, the chose of the priors does not influence the conclusion of this work.

The supernova association and/or limits provide important information about the progenitor of GRBs (Galama et al., 1998; Stanek et al., 2003; Hjorth et al., 2005a; Fox et al., 2005; Della Valle et al., 2006; Woosley & Bloom, 2006; Hjorth & Bloom, 2012). The peak magnitude, relative to SN 1998bw, of LGRB-associated SNe has a median and standard deviation of 0.18 ± 0.45 magnitudes (Berger, 2014). The limits of the peak magnitudes of SNe for SGRBs range from 0.6 to 7.4 magnitudes (again relative to SN 1998bw). Assuming the distribution of the peak magnitudes of LGRB-associated SNe to be a Gaussian distribution with a mean of 0.18 and width of 0.45, these limits give a $P(\text{TypeII}|\text{SNlimits})$. No SN is detected to be associated with SGRBs. Thus we set $P(\text{TypeI}|\text{SNlimits}) = 1$. The SN association can be multiplied to the above probability ratio $O(\text{II} : \text{I}|x)$.

Prompt versus host properties

We study the prompt emission properties and host galaxy properties separately. The posterior probability ratios are

$$\log O(\text{II} : \text{I})_{\text{prompt}} = \log O(\text{II} : \text{I}|x)_{\text{prompt}} = \log O(\text{II} : \text{I}|T_{90}, E_{iso}, \alpha, E_{peak}, f_{eff}) \quad (3.6)$$

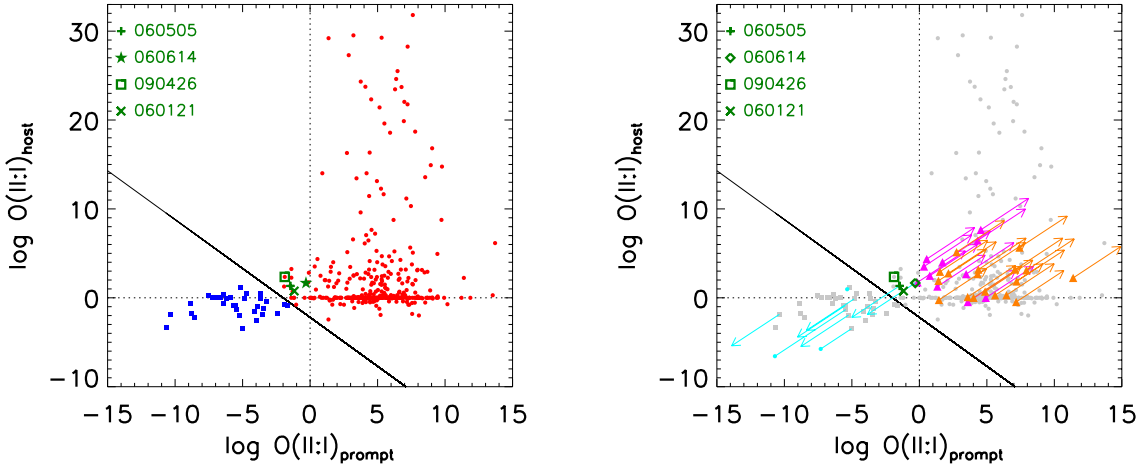


Figure 10 Left: The posterior probability ratios of the prompt emission properties $\log O(\text{II : I})_{\text{prompt}}$ and host galaxy properties $\log O(\text{II : I})_{\text{host}}$. Red dots indicate the preliminary Type II GRBs, and blue squares indicate the preliminary Type I GRBs. Green symbols are the highly debated GRBs. Right: The same with the left panel, with supernovae information added. Triangles represent GRBs with SN associations, with spectral (magenta) or photometric (orange) detections. Cyan lines and points show the correction with SN limits included. The GRBs without SN information (red dots and blue squares in the left panel) are plotted as gray for clearness.

and

$$\log O(\text{II : I})_{\text{host}} \log O(\text{II : I}|\{x\})_{\text{host}} = \log O(\text{II : I}|\{\text{sSFR}, M_*, [X/H], R_{50}, r_{\text{off}}, F_{\text{light}}\}). \quad (3.7)$$

The results of the posterior probability ratios are presented in Fig. 10. The preliminary Type II GRBs are shown with red points, and the preliminary Type I GRBs are shown with blue points. In principle, a positive $\log O(\text{II : I}|\{x\})_{\text{prompt}}$ or $\log O(\text{II : I}|\{x\})_{\text{host}}$ indicates the preference of a Type II GRB over a Type I GRB. It can be seen that most Type II GRB candidates (red dots) indeed locate in the first quadrant, with $\log O(\text{II : I}|\{x\})_{\text{prompt}} > 0$ and $\log O(\text{II : I}|\{x\})_{\text{host}} > 0$, and most Type I candidates (blue dots) locate in the third quadrant. However, the correlations among parameters may not be fully accounted for, and the prior probability of detecting a LGRB/SGRB is ignored. Therefore the absolute value of $\log O$ may be biased. For the purpose of this study, the relative value of $\log O$ is enough

to be a classifier of different types of GRBs. From Fig. 10 we find that a straight line

$$\log O(\text{II} : \text{I} | \{x\})_{\text{host}} = -2.2 - 1.1 \log O(\text{II} : \text{I} | \{x\})_{\text{prompt}}, \quad (3.8)$$

is able to separate these two types of GRBs, as shown by the solid line.

The SN association provides very important information about the physical origin of GRBs. In Fig. 10, GRBs with confirmed SN associations are shown with triangles (Hjorth & Bloom, 2012). They are definitely Type II GRBs from core-collapse of massive stars. For some GRBs, stringent limits of SNe were set, which also give a strong indication of their origins. The inclusion of SN information leads to a correction of the probability ratios, as shown by the cyan lines and dots. For a few cases, the SN limits are so stringent that the correction of $\log O$ values is very large (> 10). In such cases, we use an arrow to illustrate the effect of the SN correction.

The four highly debated objects, which were excluded from our control sample, have been over-plotted in Fig. 10 in dark green. With the SN limit correction, the two Type II candidates, GRB 060614 and 060505, are now shifted to the Type I region. These two GRBs are also widely discussed to be long-duration Type I candidates (Della Valle et al., 2006; Fynbo et al., 2006). Their prompt emission properties are not that typical compared with other Type II GRBs, and their host galaxy properties are similar to Type II GRBs. However, their SN limits dominate over other properties, which strongly favor merger origins of them. GRB 060121A is quite close to the Type I region, although it locates in the Type II region. It has a T_{90} of 2.61 s, longer than the conventional durations of SGRBs. The low energy index α is -0.5 , around typical values of Type I GRBs. The size of its host is $R_{50} = 10^{0.6}$ kpc, which is also a typical value of Type I GRBs. But its offset and fraction of light F_{light} suggest it to be Type II. This object is somewhat between Type II and Type I GRBs. Note that there is no convincing redshift measurement of GRB 060121A, and a redshift of $z = 0.5$ is assumed (Li et al., 2016).

Combined prompt emission and host galaxy probabilities

Multiplying both the prompt and host probabilities together, we get a combined probability ratio, $O(\text{II} : \text{I}|x)$. The distributions of $\log O(\text{II} : \text{I}|x)$ of our control sample are shown in the left panel of Fig. 11, for the preliminary Type II (red) and Type I GRBs (blue). The four exceptions, GRB 060121, GRB 060505, GRB 060614 and GRB 090426 are not included in the histograms, but are presented in green lines. We find that no overlap between these two preliminary classes of GRBs, which means a good separation of them with our joint probability based on both the prompt emission and host galaxy properties. The largest value of $\log O(\text{II} : \text{I}|x)$ is -2.6 for Type I candidates, and the smallest value is -1.7 for Type II candidates. At the current stage, we may set roughly a critical value of -2.2 to distinguish Type I from Type II GRBs. Note again that the relative value instead of the absolute one of $\log O(\text{II} : \text{I}|x)$ is used to distinguish different types.

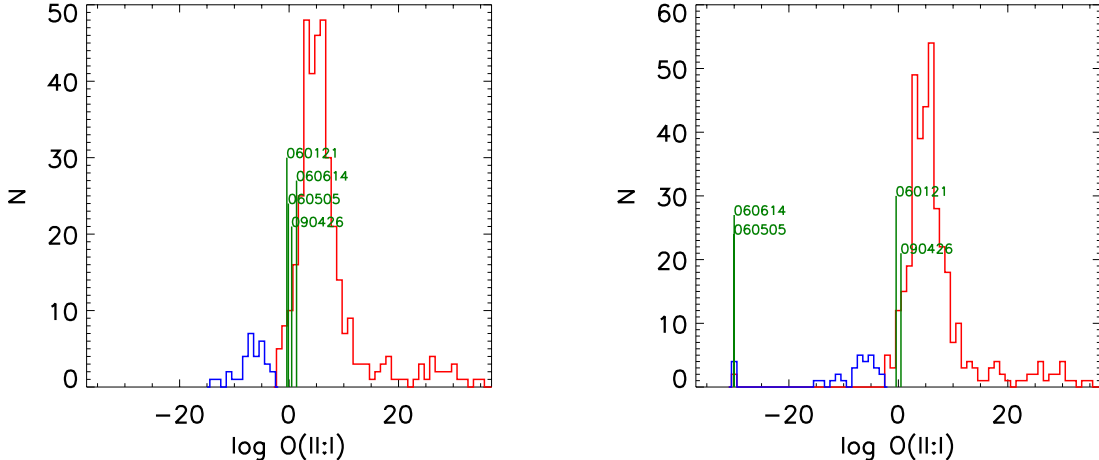


Figure 11 The distribution of $\log O(\text{II} : \text{I}|x)$, without (left) and with (right) the SN limits. GRB 060121, GRB 060505, GRB 060614 and GRB 090426 are labelled with green lines.

We can also add the SN limits to the calculation of $\log O(\text{II} : \text{I}|x)$. The results are shown in the right panel of Fig. 11. The $\log O(\text{II} : \text{I}|x)$ values for a few GRBs with very stringent SN limits (the objects labelled by arrows in Fig. 10) are set to be -30 in order to be shown in this plot with a proper scale. The SN limits shift GRB 060505 and GRB 060614

from the Type II region to the Type I GRB region, as discussed above.

Conclusion and Discussion

In this paper, we utilize the distributions of the prompt emission and host galaxy properties of GRBs (Li et al., 2016) to classify different physical types of them. We estimate the probability of each GRB to be a Type II or Type I GRB, via the distributions of the prompt emission and host galaxy parameters. We define a logarithmic probability ratio, $\log O(\text{II} : \text{I}|\{x\})$, which is the logarithm of the ratio of the probabilities of Type II and Type I, to describe the preference of Type II against Type I. This method is found to be able to efficiently classify GRBs. For the control GRB sample selected from Li et al. (2016), they are well separated into two groups without overlap. Our method provides a quantitative, overall assessment of the physical origin of any GRB with multi-wavelength observational data.

The SN associations or limits provide additional information about the physical origin of GRBs. Through adding the SN limits in the classifier, we find that GRB 060505 and GRB 060614, two objects with many debates, shift from the Type II region to the Type I region. The other two ambiguous objects, GRB 090426 and GRB 060121, remain in the Type II region.

The selection of the control sample might affect our results. We, therefore, test the case with the four highly debated GRBs in the analysis. The results show that there is a slight overlap between the two candidate populations. The overlap fraction is 1.3% for Type II candidates and 7% for Type I candidates. Even in this case, the overlap fraction is much smaller compared with previous methods. For the duration classification method, there are 7% Type II and 20% Type I candidates in the overlapping region. For the f_{eff} parameter method, the corresponding fraction is 7% (48%) for Type II (Type I) candidates. We also test the case with randomly chosen 300 GRBs in the control sample to calculate the distributions of parameters. Similar results with that of the control sample are obtained.

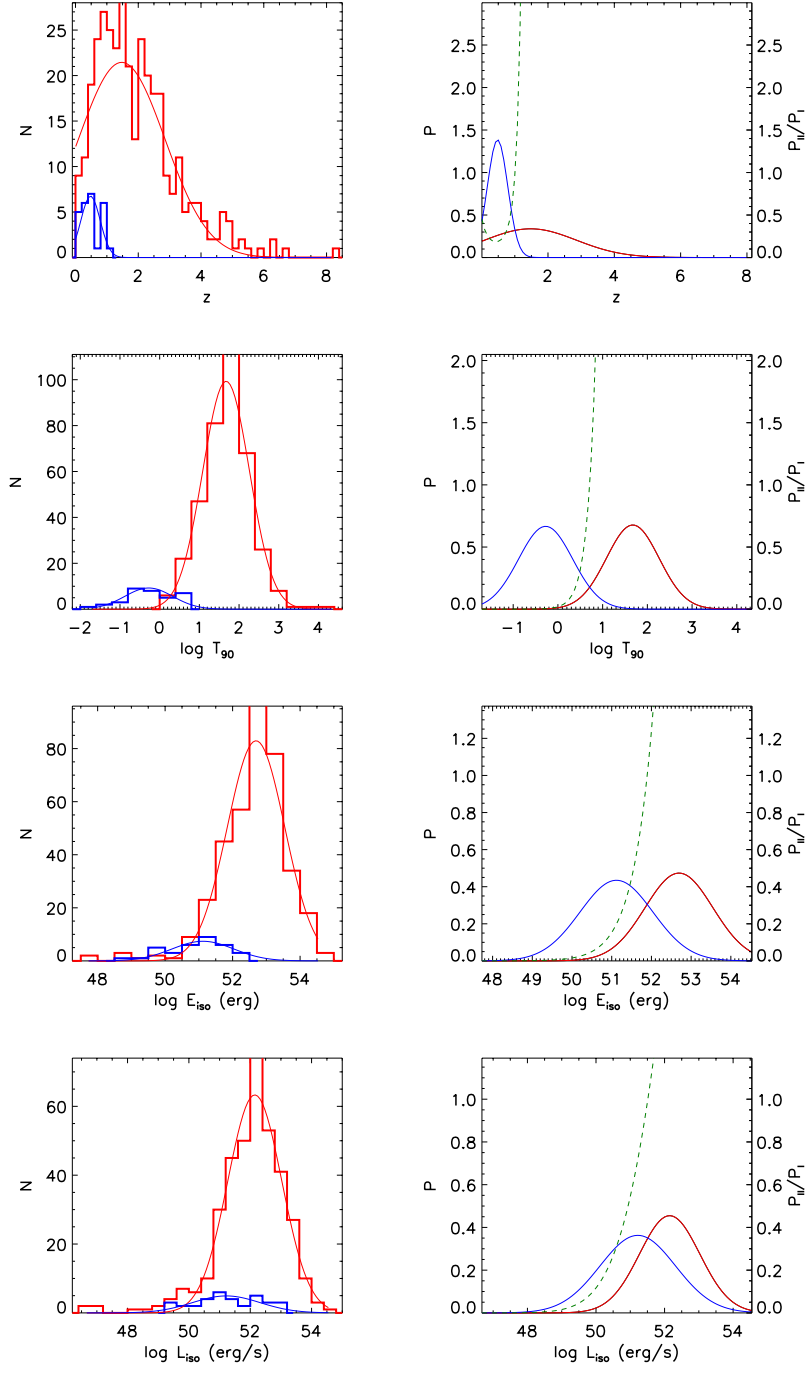


Figure 12 Left panels: Distribution of prompt and host galaxy parameters of LGRBs (red lines) and SGRBs (blue lines), with fitted Gaussian distributions (red and blue solid lines) overplotted. The dashed red line in [X/H] panel shows the two-Gaussian fitting result of LGRB distribution. Right panels: The Gaussian distributions are normalized to have the integrated probability in observational ranges to be unit. The green lines show the ratio between red lines and blue lines.

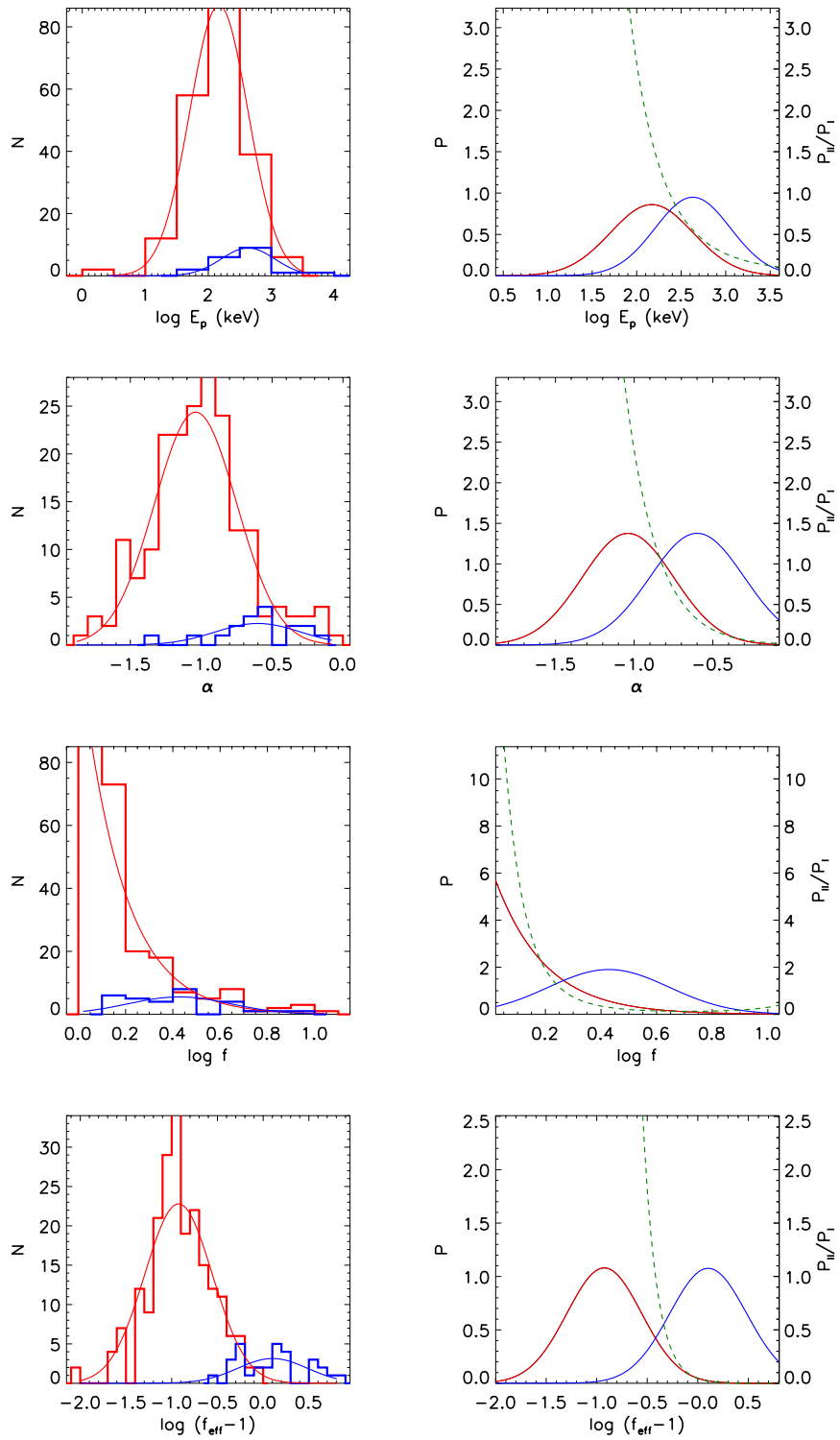


Fig. 12—Continued

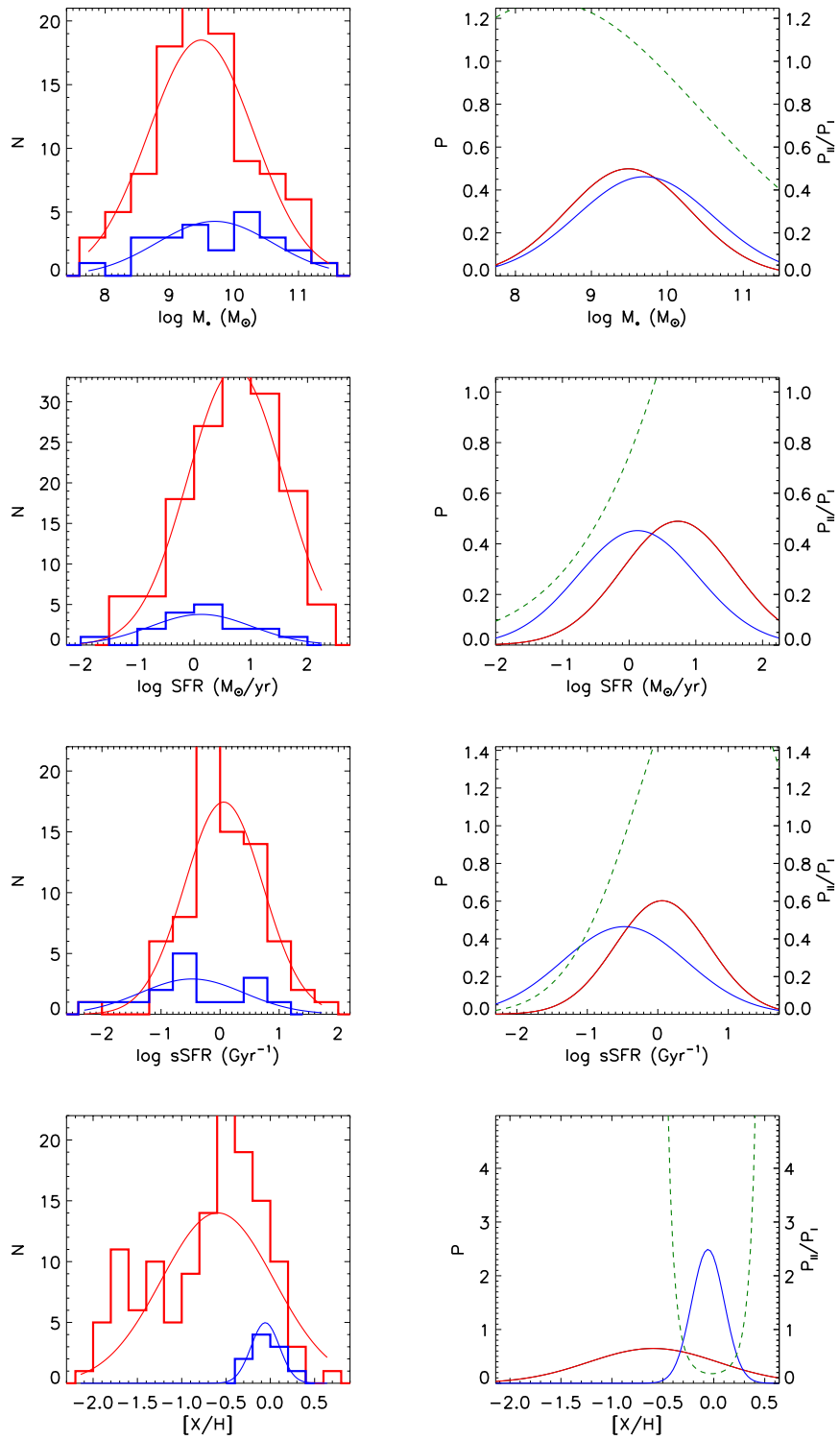


Fig. 12—Continued

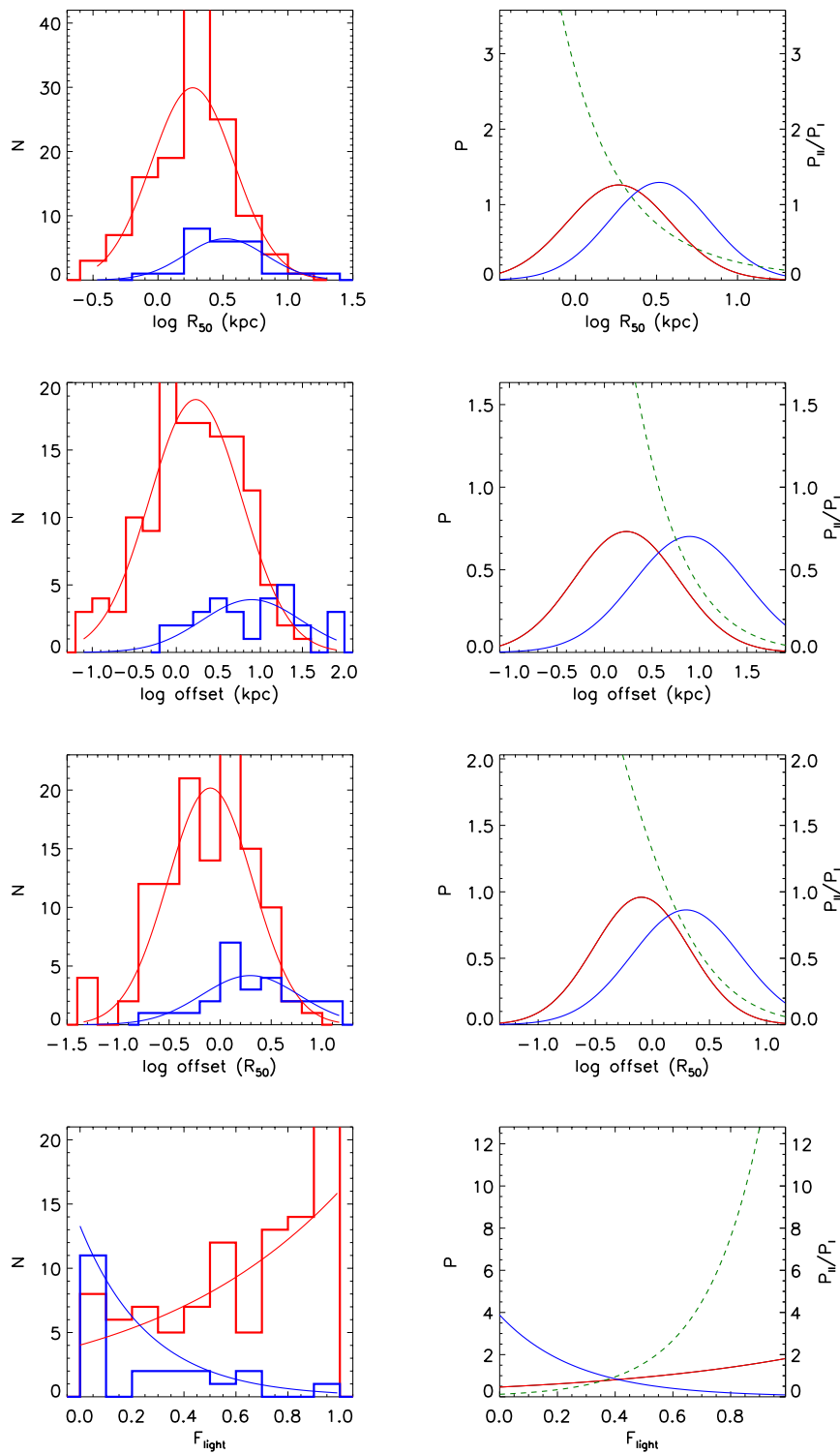


Fig. 12—Continued

CHAPTER 4

SEARCHING FOR NEUTRON STAR-NEUTRON STAR MERGERS AS SGRB-LESS EXTENDED EMISSIONS

This chapter is part of a paper in preparation:

Ye Li, Amy Lien, Bing Zhang, Kazumi Kashiyama, 2017, in preparation

Introduction

The first direct detection of the Gravitational Wave (GW) signal from a Black-Hole (BH) binary, GW150914, by the Advanced Laser Interferometer Gravitational-Wave Observatory (aLIGO) opened a new window to observe the universe (Abbott et al., 2016c). While the GW events themselves provide crucial information about the origin of BH binaries and related fundamental problems of physics and cosmology, the identification of electro-magnetic (EM) counterparts of GW events can precisely locate their hosts, comprehensively describe the physical properties of such events, probe the equation of state of neutron stars (NSs), and even study the evolution of the Universe. Although the existence of EM counterparts of BH-BH mergers is still in debate (Zhang, 2016; Loeb, 2016; Perna et al., 2016), a wealth of follow-up observations were conducted to search for EM counterparts of the GW events, GW150914 (Abbott et al., 2016b; Connaughton et al., 2016), LVT151012, GW151226 (Abbott et al., 2016a; Cowperthwaite et al., 2016; Racusin et al., 2017; Adriani et al., 2016; Yoshida et al., 2017), and GW170104 (Stalder et al., 2017; Bhalerao et al., 2017; Verrecchia et al., 2017). No conclusive counterpart has been detected yet. A tentative counterpart was reported to be potentially associated with GW150914 by Fermi/LAT (Connaughton et al., 2016), and a possible one with GW170104 by AGILE. However, there are continuous debates on such results (Greiner et al., 2016; Xiong, 2016).

While the currently detected GW events are BH-BH mergers, they are Neutron Stars (NS) binary mergers and NS-BH mergers those are highly expected to be possible GW

events associated with EM counterparts (Metzger & Berger, 2012; Chu et al., 2016). There are four types of EM counterparts proposed for NS-NS/BH mergers. The first and the most convincing one is short-duration gamma-ray burst (SGRB). They are intense gamma-ray emission with typical duration < 2 seconds, which arise from the accretion induced relativistic jets (Paczynski (1986); Eichler et al. (1989); Narayan et al. (1992), see Berger (2014) for a review). The jet opening angles are $\theta_j \sim 5^\circ$ to $> 20^\circ$. The benefit of SGRBs is the brightness. However, the narrow opening angle reduces the probability of them to be detected. The second type is the ‘kilonova’ (or ‘macronova’, or ‘Li-Paczyński nova’) proposed by Li & Paczyński (1998). They are optical or near infrared (NIR) transients powered by the decay of heavy r-process elements. They are thus isotropic, and much fainter than SGRBs. The peaks of them are usually days to weeks after the mergers. There are a few candidates reported, such as GRB 130603B, GRB 080503, GRB 060614, and GRB 050709 (Tanvir et al., 2013b; Berger et al., 2013; Yang et al., 2015; Gao et al., 2015; Jin et al., 2016b; Gao et al., 2017). The third is produced by the interaction of the ‘kilonova’ ejecta with the interstellar medium (ISM) (Nakar & Piran, 2011; Gao et al., 2013; Piran et al., 2013). They may be detected in radio in the future, usually years after the mergers. The limited energy budget of ‘kilonova’ has this kind of transient peak in radio band, and they may be detected years after the mergers. But there is still no detection reported.

The above three types of EM counterparts are common in NS-NS and NS-BH mergers. There is another one proposed for NS-NS only. It is the X-ray transients powered by hypermassive, milliseconds, and highly magnetized neutron stars, the magnetars. The hypermassive magnetars produced by NS-NS mergers are believed to power the ~ 100 seconds ‘internal’ plateau in the X-ray afterglow. And the spinning-down of it leads to a temporal decay with an index steeper than 3 (Rowlinson et al., 2010b, 2013; Lü et al., 2015). Lü et al. (2015) found that all extended emissions (EEs) are followed by steep decays, indicating that EEs are in fact part of the magnetar powered X-ray transients. EEs follow 2% - 25% of the short hard spikes, there followed by ~ 10 - 100 seconds soft extended emission (EE) (Lazzati

et al., 2001; Connaughton, 2002; Barthelmy et al., 2005; Villasenor et al., 2005; Norris & Bonnell, 2006; Norris et al., 2010b). Since the magnetar wind which powers EEs are expected to be isotropic, EEs are expected to be found without the short hard spikes (Sun et al., 2017), the SGRB-less extended emissions (SLEE). It will appear to be a long-duration GRB (LGRB) with duration 10-100 seconds, but with other properties quite similar to that of SGRBs.

LGRBs and SGRBs are traditionally classified with their γ -ray durations T_{90} , the time interval with 5% to 95% energy detected (Mazets et al., 1981; Kouveliotou et al., 1993). SGRBs, with $T_{90} < 2$ seconds, are generally expected to originate from NS-NS/BH mergers (Paczynski, 1986; Eichler et al., 1989; Narayan et al., 1992), and LGRBs, with $T_{90} > 2$ seconds, are expected to be from core-collapse of massive stars (Woosley, 1993; Paczyński, 1998; MacFadyen & Woosley, 1999). Compared to SGRBs, the prompt emission of LGRBs has a softer γ -ray spectrum, a higher isotropic energy E_{iso} , and a smaller effective amplitude parameter f_{eff} . The host galaxies of LGRBs are typically dwarf star forming galaxies, with relatively small stellar mass M_* , intense star formation rate (SFR), low metallicity [X/H], and small size R_{50} (Sahu et al., 1997; Bloom et al., 1998, 2002; Chary et al., 2002; Christensen et al., 2004; Savaglio et al., 2009; Krühler et al., 2015). The offsets of LGRBs from the center of their host galaxies are usually small, and they are located in bright regions of the hosts (Bloom et al., 2002; Fruchter et al., 2006; Blanchard et al., 2016). Sometimes they are found to be associated with type Ic supernovae (SNe) (Galama et al., 1998; Hjorth et al., 2003a; Stanek et al., 2003; Woosley & Bloom, 2006; Hjorth & Bloom, 2012; Xu et al., 2013b). On the other hand, the host galaxies of SGRBs have diverse types, from early to late (Gehrels et al., 2005; Berger et al., 2005b). They can have large stellar mass, little SFR, rich metallicity, and large size. SGRBs could also locate in faint regions of the hosts, and sometimes with quite large offsets (Fong et al., 2010; Kann et al., 2011; Fong & Berger, 2013). There is no SN associated with SGRB detected, and stringent SN limits were set (Fox et al., 2005; Hjorth et al., 2005a,b; Kann et al., 2011; Berger et al., 2013). For a few SGRBs, the association

with “kilonovae” were suggested (Li & Paczyński, 1998; Metzger et al., 2010; Tanvir et al., 2013b; Berger et al., 2013; Yang et al., 2015; Gao et al., 2015; Jin et al., 2016a).

While T_{90} is the traditional criterion to classify GRBs into LGRBs and SGRBs, it does not reveal the physical origin of GRBs. Zhang (2006) suggested a physical classification of GRBs into Type II, the core-collapse origin, and Type I, the merger origin. Zhang et al. (2009) proposed a flowchart to identify the physical origin of a GRB from its multi-wavelength properties. Li et al. (2016) systematically compared the prompt emission and host galaxy properties of candidate Type I and Type II GRBs, and found that all of their observational properties overlap. Li, Zhang & Yuan (2017, in preparation; hereafter Li17) proposed a joint likelihood method to quantify the preference of any type based on all available properties of them. Such a method is very effective to classify the GRBs into two distinct types. In this work, we employ this multiple parameter method to search for GRBs with SLEE.

This paper is organized as follows. Section II presents the sample selection method to search for SLEE objects. Section III presents the X-ray and Gamma-Ray properties of the candidates. We conclude in Section IV.

Sample selection

For the purpose of this work, we search for objects with gamma-ray prompt emission properties similar to that of SGRBs with EEs, and with host galaxy properties similar to that of SGRBs. Due to their 10-100 s gamma-ray prompt emission, they would have been considered as LGRBs. We thus search for SLEEs from LGRBs in the catalog of Li17.

Extended emission properties

We first investigate the EE properties from a sample of SGRBs with EEs. Kaneko et al. (2015) systematically searched for SGRB with EE with Swift/BAT and Fermi/GBM data. The spectral and temporal properties of the initial short spike and the EEs were analyzed.

Here we use their results to extract the temporal and spectral information of the EE¹. For the three GRBs with both Swift/BAT and Fermi/GBM detections, we use their properties obtained by Swift/BAT since most information of our sample comes from Swift/BAT.

The durations of the EEs, T_{EE} , range from $10 - 100$ seconds, which give the most basic information about the EE. For a SLEE object, its T_{90} could be in such a range. The spectrum of the EE, if available, if fitted by a cutoff power law (CPL) with energy flux index α and cutoff energy E_p or a power law (PL) function with photon index Γ . We estimate the isotropic energy $E_{\text{iso,EE}}$ and peak luminosity $L_{\text{iso,EE}}$ based on the spectrum, flux and fluence given in Kaneko et al. (2015). When calculating the peak luminosity, a Band function with $\alpha = -1.0$ and $\beta = -2.3$ is assumed for the EE in the $1 - 10^4$ keV band (see Li et al. (2016) for a detailed description). The rough correlation

$$\log E_p = (4.34 \pm 0.48) - (1.32 \pm 0.13)\Gamma \quad (4.1)$$

is used to estimate E_p (Zhang et al., 2007; Sakamoto et al., 2009; Virgili et al., 2012). For those without redshift, $z = 0.5$ is assumed because the median redshift of SGRB and SGRB with EE are both around 0.5. The distribution of these temporal and spectral parameters, duration T_{EE} , redshift z , lower energy index α , spectral peak energy E_p , photon index Γ , isotropic energy E_{iso} and peak luminosity L_p , are presented in Fig. 16 in green lines, with the distribution of LGRB (red lines) and SGRB (blue lines) overplotted. The distribution of EE are fitted with one gaussian using Cash statistics (Cash, 1979)

$$P(x|\text{EE}) = A_0 e^{-\frac{(x-\mu)^2}{2\sigma^2}}. \quad (4.2)$$

The numbers of α , E_p and z of EE are less than 10. For these small samples, the best fit

¹We exclude GRB 070506, because its redshift ($z = 2.31$) is much higher than any SGRB with redshift detection. Note that the classifications of GRB 090927 and GRB 060614 are not clear yet. We classify them to be Type I GRBs, consistent with Kaneko et al. (2015). However, in the website by Greiner they are classified as LGRBs.

result would be influenced by binning when χ^2 statistics is used. We thus use the unbinned Cash-statistics to fit the EE data (Cash, 1979). On the other hand, to be consistent with Li17, we still use χ^2 to fit LGRB and SGRB samples. The best fit results are given in Table 6, and the best fit is overplotted as the dark green solid line in the left panels of Fig. 16. The Gaussian is normalized to be a unit in the detected parameter range, with the normalization factor as A . The normalized Gaussian distributions are presented as the right panels of Fig. 16. The red and blue lines present the distribution of LGRBs and SGRBs for comparison.

parameter	norm A	mean μ	$\sigma(\gamma)$
$\log T_{90}$	0.95	1.59	0.42
z	1.04	0.63	0.41
$\log E_{\text{iso}}$ (erg)	1.57	50.94	0.25
$\log L_{\text{iso}}$ (erg s $^{-1}$)	0.50	50.46	0.80
α	0.92	-1.21	0.47
$\log E_p$ (keV)	0.94	2.09	0.43
Γ	1.00	2.00	0.40

Table 6 The Gaussian fitting results of each parameter of the EE with data from Kaneko et al. (2015).

A Bayesian method to select SLEE candidates

In order to search for SLEEs from LGRBs, we use a Bayesian method to compare the probability of one object as a SLEE and as a LGRB. According to the Bayesian theorem, we use the posterior probability of an event given observables $\{x\}$

$$P(\text{SLEE}|\{x\})_p = \left(\frac{P(\{x\}|\text{SLEE})P(\text{SLEE})}{P(\{x\})} \right)_p = \frac{P(\{x\}|\text{EE})_p P(\text{SLEE})}{P(\{x\})}, \quad (4.3)$$

to describe how likely the prompt emission of one object is an SLEE event. In the above equation, the subscript “p” represents the prompt emission, and $\{x\}$ are relevant observational parameters, including the duration T_{EE} , the redshift z , the isotropic energy E_{iso} , the peak luminosity L_{iso} , the spectral parameters α , E_p or photon index Γ . The $P(\{x\}|\text{SLEE})_p = P(\{x\}|\text{EE})_p$ is the conditional probability (the likelihood). $P(\text{EE})$ is the prior and $P(\{x\})$ is the normalization. If there are no strong correlations among these parameter, we should

have

$$P(\{x\}|\text{EE})_{\text{p}} = \prod_i P(x_i|\text{EE})_{\text{p}}. \quad (4.4)$$

However, as noted in Li17, some parameters are obviously correlated, such as $\{T_{\text{EE}}, E_{\text{iso}}, L_{\text{iso}}\}$, z with other parameters. Following Li17, we exclude L_{iso} and z in the parameter set $\{x\}$. The spectral parameters α and E_{p} are used when available. Otherwise, Γ is used. In summary, for the prompt emission $\{x\}$ includes $T_{\text{EE}}, E_{\text{iso}}, \alpha, E_{\text{p}}$.

The probability of an event for given host galaxy properties as a SLEE is defined as the probability as an SGRB host, i.e.,

$$P(\text{SLEE}|\{x\})_{\text{h}} = \frac{P(\{x\}|\text{SGRB})_{\text{h}} P(\text{SLEE})}{P(\{x\})}, \quad (4.5)$$

with

$$P(\{x\}|\text{SGRB})_{\text{h}} = \prod_i P(x_i|\text{SGRB})_{\text{h}}. \quad (4.6)$$

To avoid obvious correlations among the parameters, we exclude the SFR and the physical offset R_{off} when calculating the probability. In summary $\{x\}$ represents $\{M_*, [\text{X}/\text{H}], \text{sSFR}, R_{50}, r_{\text{off}}, F_{\text{light}}\}$.

Since SLEE events have durations about $10 - 100$ s, they would be classified as LGRBs. We thus need to search for SLEE events from LGRBs. In order to distinguish SLEE events from the traditional LGRBs, we use a logarithmic probability ratio

$$\log O(\text{LGRB} : \text{SLEE}) = \log \frac{P(\text{LGRB}|\{x\})}{P(\text{SLEE}|\{x\})} = \log \frac{P(\text{LGRB}|\{x\})P(\text{LGRB})}{P(\text{SLEE}|\{x\})P(\text{SLEE})} \quad (4.7)$$

to characterize the preference of one LGRB against an SLEE. A large value of $\log O(\text{LGRB} : \text{SLEE})$ means a less probability of an LGRB is an SLEE event. The ratio of the prior $P(\text{LGRB})/P(\text{SLEE})$ is unknown. They are assumed to be $P(\text{LGRB}) = 0.5$ and $P(\text{SLEE}) = 0.5$. And thus $P(\text{LGRB})/P(\text{SLEE}) = 1$. Different priors would influence the absolute value of the $\log O(\text{LGRB} : \text{SLEE})$. However, later, we use the values of observed EEs as the

reference. Thus, the absolute values do not matter. Only the relative values matter.

We discuss the probability ratios of the prompt emission properties $\log O(\text{LGRB} : \text{SLEE})_p$ and the host galaxy properties $\log O(\text{LGRB} : \text{SLEE})_h$ separately. Fig. 13 shows the $\log O(\text{LGRB} : \text{SLEE})_p$ versus $\log O(\text{LGRB} : \text{SLEE})_h$ distributions for the GRB sample of Li et al. (2016). LGRBs are shown in red, and EE events are in green. Although SGRBs are not supposed to be SLEE events, we show them in magenta for comparison. Negative values of $\log O(\text{LGRB} : \text{SLEE})_p$ and $\log O(\text{LGRB} : \text{SLEE})_h$ tend to favor an SLEE event against an LGRB. It can be seen that all EE events have negative $\log O(\text{LGRB} : \text{SLEE})_p$. There are three EE events with positive $\log O(\text{LGRB} : \text{SLEE})_h$. They are GRB 060614, GRB 051016B and GRB 061006, with, $\log O(\text{LGRB} : \text{SLEE})_h$ values 1.67, 0.92 and 0.24, respectively. The T_{90} of GRB 051016B is 4.0 s, and it was classified as an LGRB in Greiner’s catalog and Li16. The origin of GRB 060614 is still in debate. It looks like an LGRB, with a T_{90} of 5.9 s short spike with a 102 seconds EE. Its host galaxy is a dwarf galaxy with a redshift of 0.125. The offset is also small. Although the SFR is quite small, the sSFR is consistent with typical LGRBs due to a small stellar mass M_* . However, strict SN limits strongly suggest it as an SGRB (Gal-Yam et al., 2006; Della Valle et al., 2006; Fynbo et al., 2006), which was further supported by a putative “kilonova” (Yang et al., 2015; Jin et al., 2015).

We thus consider objects with $\log O(\text{LGRB} : \text{SLEE})_p < 0$ and $\log O(\text{LGRB} : \text{SLEE})_p < 1$ as SLEE candidates. In total, we find 24 LGRBs satisfying such criteria, which are presented in Table. 7. Among them, 12 objects do not have host galaxy information. We, therefore, do not consider them as SLEE candidates in this work.

Candidates properties

The lightcurves of prompt emission of the candidate SLEEs are shown in Fig. 14. To be clear, the lightcurves are rebinned with a Bayesian Blocks method. We show the lightcurves in three groups, with peak luminosities on the order of 10^{49} erg/s, 10^{50} erg/s, and 10^{51}

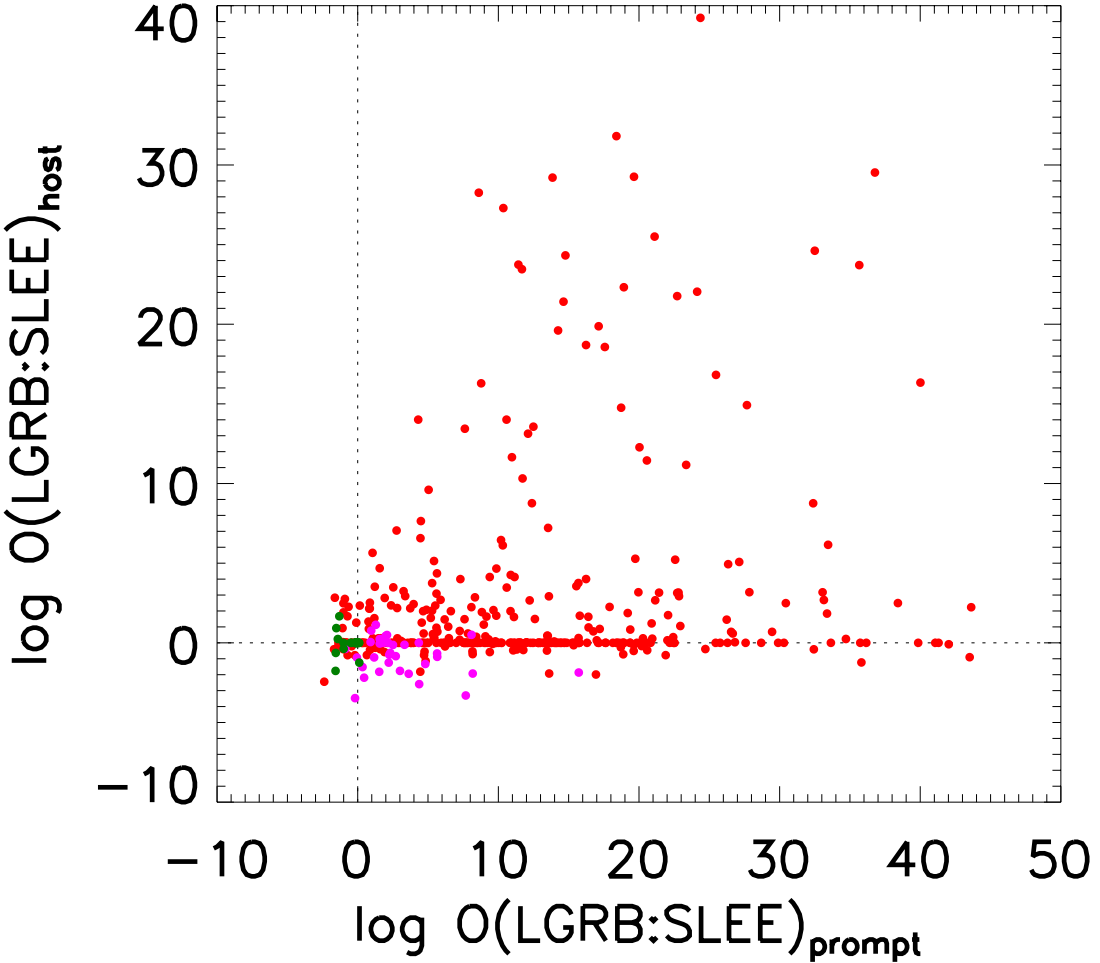


Figure 13 The probability ratios of prompt emission properties $\log O(\text{LGRB} : \text{SLEE})_p$ and host galaxy properties $\log O(\text{LGRB} : \text{SLEE})_h$ of LGRBs (red dots), SGRBs (magenta dots), and EEs (green dots).

erg/s. Example lightcurves of SGRBs with EEs (black or dark blue) are also shown for comparison. As can be seen from this plot, most of the SLEE candidates have somewhat similar lightcurves with the SGRBs with EEs. However, the objects shown in the bottom panel of Fig. 14 may show a little bit strange behaviors. The reference object, GRB 090927, is also not clear whether is an SGRB with EE or an LGRB.

The X-ray afterglows of the candidates observed by Swift/XRT are presented in Fig. 15. XRT afterglows of LGRBs with redshifts less than 1.5 are overplotted as grey lines, and

those of SGRBs with EEs are plotted as blue. The X-ray afterglows of SGRBs with EEs are generally simple. However, for GRB 080520, X-ray flares were detected in the afterglow, which may indicate that it is not a true SLEE event.

Conclusions

We search for NS mergers as SGRB-less extended emissions(SLEE) from the LGRBs in the catalog of Li et al. (2016), with a multi-wavelength Bayesian method. We require the SLEE candidates to have similar prompt emission properties with EEs and similar host galaxy properties with SGRBs. 12(24) candidate SLEE events are found. If they are true SLEE events, the number of SLEE events would be one third of SGRBs with redshifts. Compared with the number of SGRBs with “internal” plateau presented in Lü et al. (2015), 22, the solid angle ratio between free zone and jet zone $\Omega_k = \Omega_{\text{free}}/\Omega_{\text{jet}}$, is expected to be from 12/22=0.5 to 24/22=1.1.

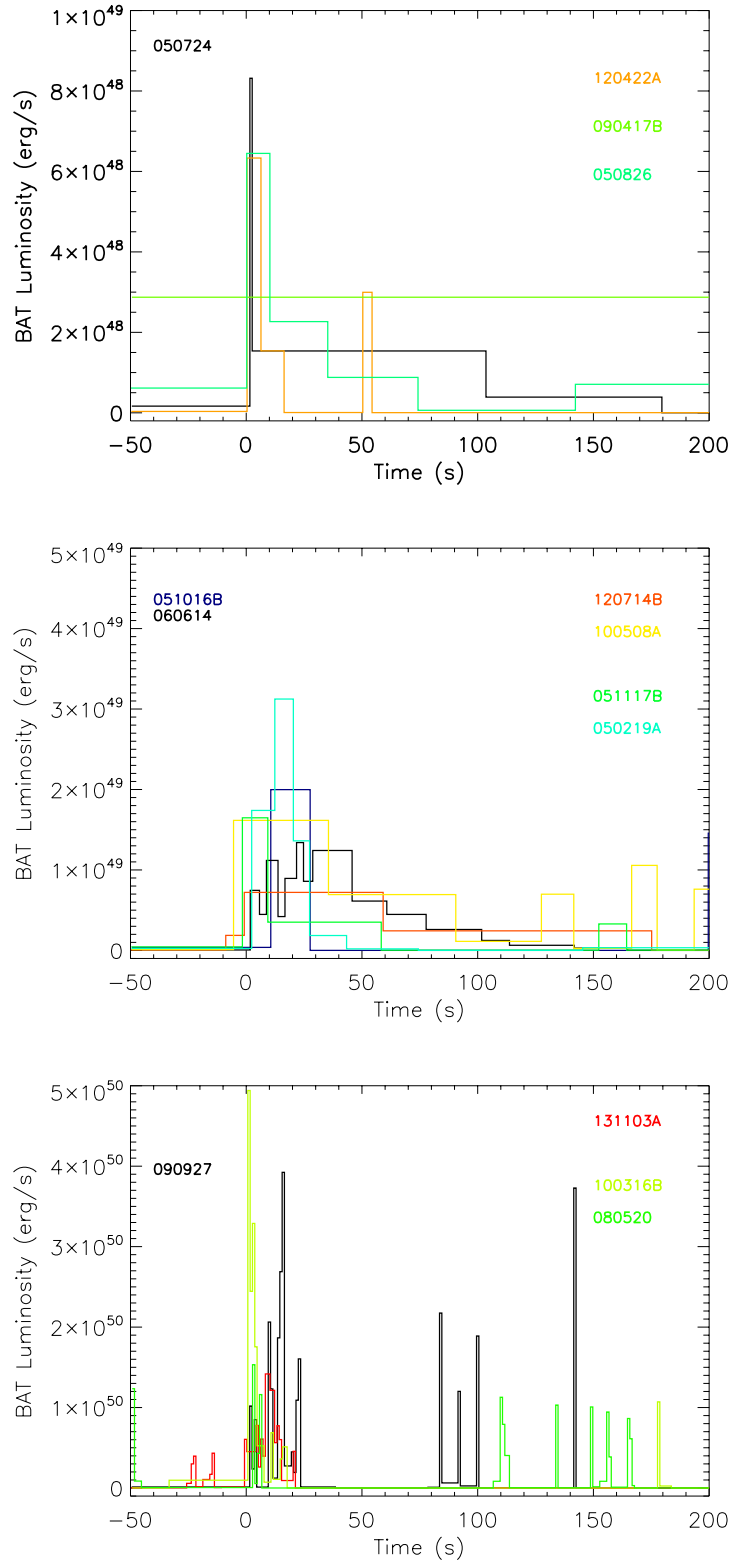


Figure 14 Gamma-ray lightcurves of SLEE candidates, compared with SGRBs with EEs (dark blue). Panels from top to down are those with peak luminosities on the order of 10^{49} erg/s, 10^{50} erg/s, and 10^{51} erg/s.

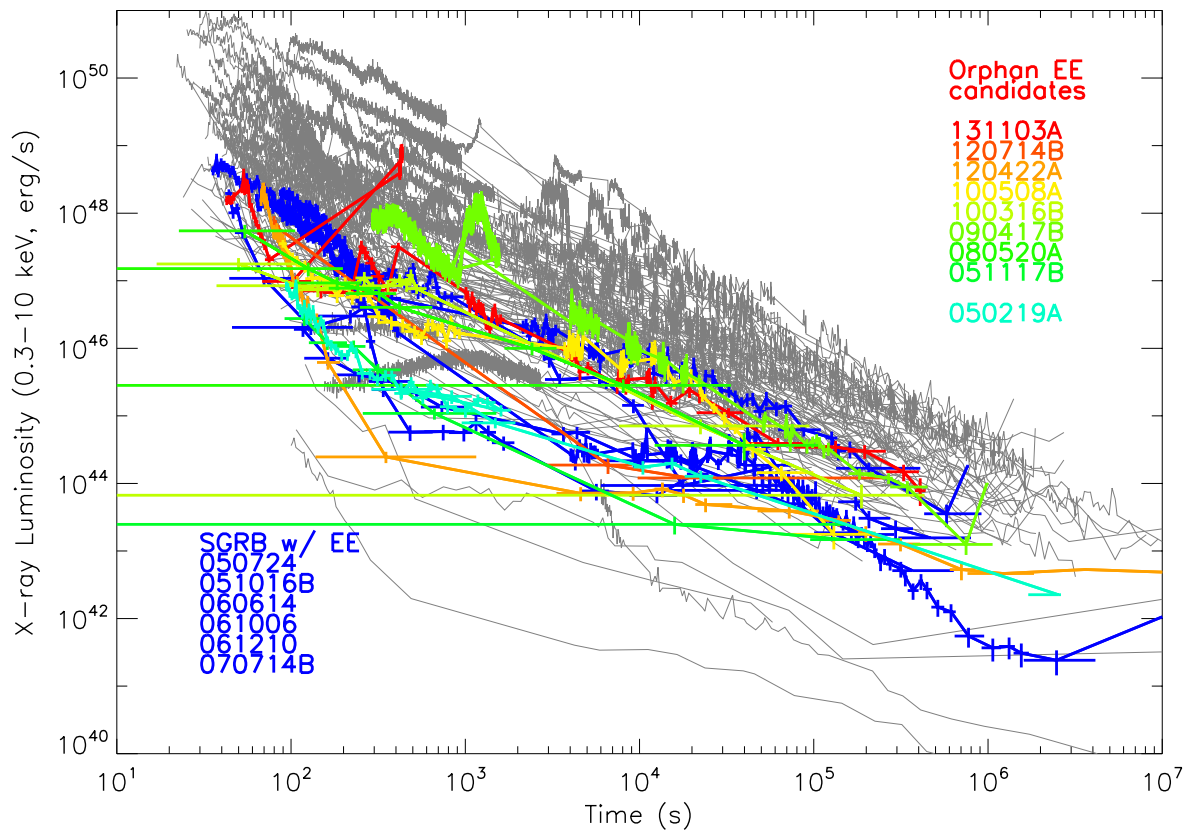


Figure 15 X-ray lightcurves of SLEE candidates (red to green), compared with those of LGRBs (grey) and SGRBs with EEs (blue).

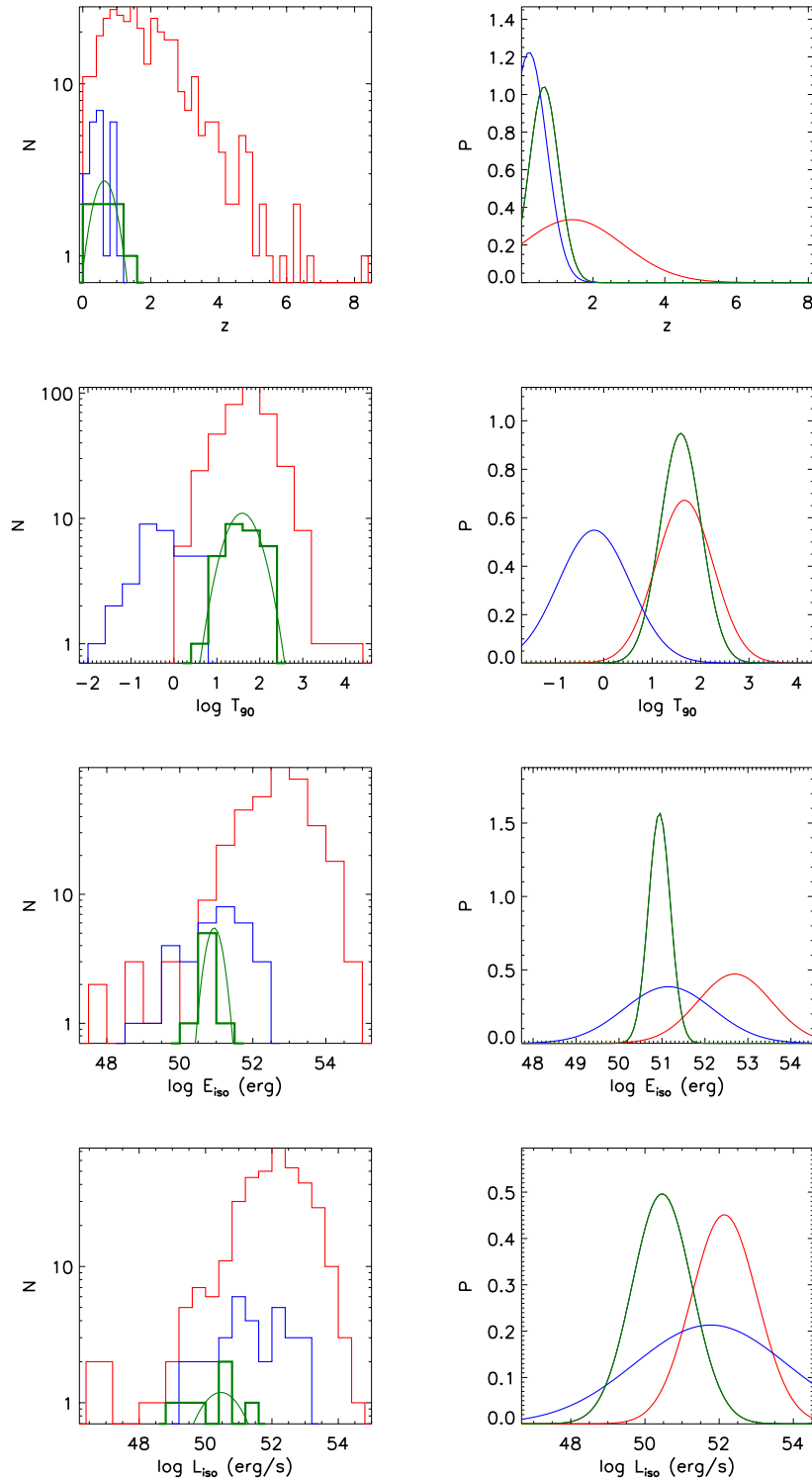


Figure 16 Left panels: Distribution of prompt properties of the extended emissions of SGRBs (green histogram), with the best fit gaussian overplotted (green solid line). The distribution of SGRBs (blue) and LGRBs (red) are also plotted for comparison. Right panels: The Gaussian distributions are normalized to have the integrated probability in observational ranges to be unit.

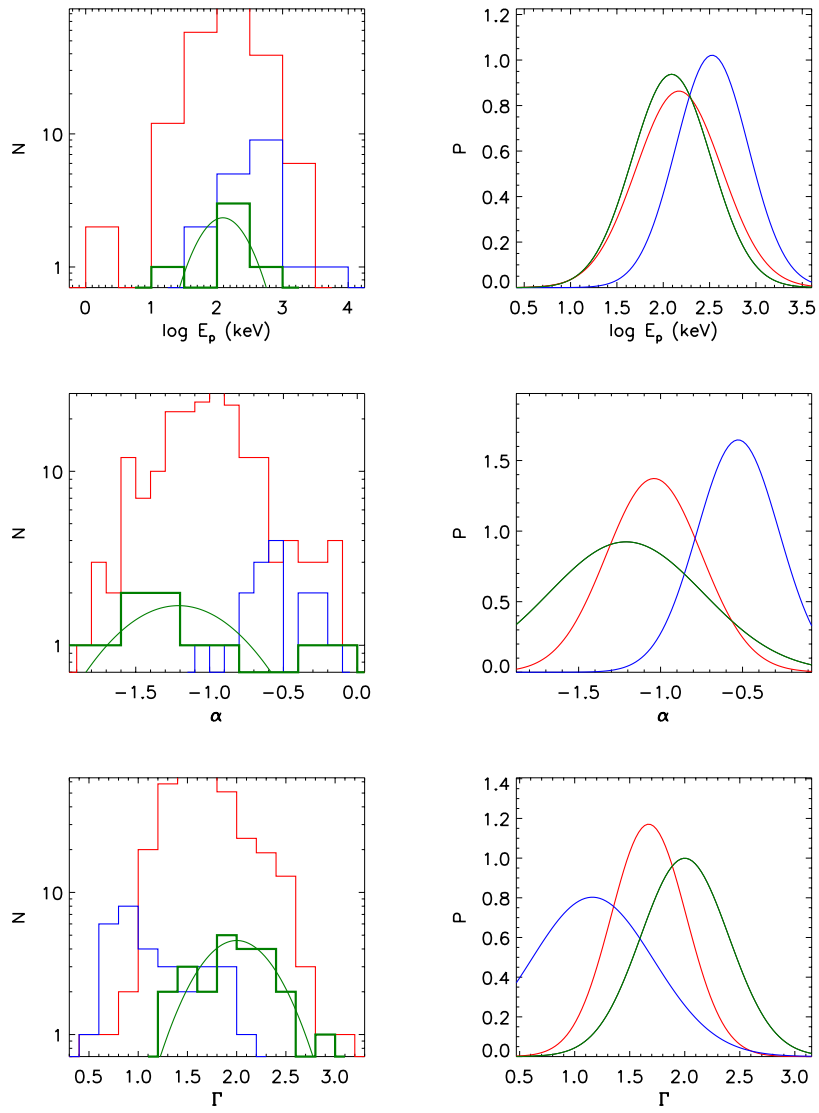


Fig. 16—Continued

Table 7. Candidate of SGRB-less Extended Emissions

	$\log T_{90}$	z	$\log E_{\text{iso}}$	$\log L_{\text{iso}}$	α	$\log E_p$	$\log f$	$f_{\text{eff}} - 1$	$\log M_*$	[X/H]	$\log R_{50}$	$\log \text{offset}$	R_{50}	F_{light}	Γ
$\log O(LGRB : SLEE)_{\text{prompt}} = -1.03$															
131103A	value	1.2	0.6	54.2	50.5	0.6	-0.2	2.0
P(L)	0.51	0.28	0.11	0.08	0.49	0.54	0.77	
P(E)	0.67	1.04	0.86	0.50	0.48	1.35	1.00	
120714B	value	2.2	0.4	54.2	49.8	-0.6	-0.3	1.5
P(L)	0.46	0.25	0.10	0.01	0.15	0.58	1.06	
P(E)	0.33	0.88	0.90	0.35	0.28	0.59	0.49	
120422A	value	0.7	0.3	50.5	50.0	0.1	0.2	8.9	-0.3	0.6	0.9	0.3	...
P(L)	0.18	0.23	0.02	0.02	0.39	0.59	0.40	0.58	0.65	0.35	0.65	0.46	
P(E)	0.12	0.72	0.29	0.41	0.52	0.36	0.19	0.59	1.34	0.75	0.95	0.13	
100508A	value	1.7	0.5	51.5	50.3	0.4	-0.0	1.2
P(L)	0.68	0.27	0.16	0.06	0.46	0.43	0.54	
P(E)	0.91	1.00	0.20	0.49	0.53	2.54	0.16	
100418A	value	0.8	0.6	50.9	50.3	0.6	0.1	9.5	-0.2	2.2
P(L)	0.25	0.28	0.05	0.05	0.49	0.60	0.50	0.52	0.41	
P(E)	0.20	1.04	1.53	0.49	0.49	0.38	0.40	1.75	0.92	
100316B	value	0.6	1.2	51.2	51.1	0.4	-0.3	2.2

Table 7 (cont'd)

	$\log T_{90}$	z	$\log E_{\text{iso}}$ erg	$\log L_{\text{iso}}$ erg s^{-1}	α	$\log E_{\text{p}}$ keV	$\log f$	$f_{\text{eff}} - 1$	$\log \text{SFR}$ $M_{\odot} \text{ yr}^{-1}$	$\log \text{sSFR}$ Gyr^{-1}	$\log M_{*}$ M_{\odot}	[X/H]	$\log R_{50}$ kpc	$\log \text{offset}$ kpc	E_{light} R_{50}	Γ
P(L) P(E)	0.12 0.05	0.33 0.42	0.11 0.87	0.23 0.35	0.46 0.53	0.58 0.66	0.30 0.85
090417B			$\log O(\text{LGRB:SLEE})_{\text{prompt}} = -0.59$													
value P(L) P(E)	2.5 0.28 0.12	0.3 0.24 0.81	51.2 49.2 0.15	0.10 1.8e-03 0.95	9.5 0.7	0.6	-0.0	1.8 1.03 0.90
080520A			$\log O(\text{LGRB:SLEE})_{\text{prompt}} = -0.72$													
value P(L) P(E)	0.5 0.10 0.04	1.5 0.34 0.09	51.1 0.09 0.26	51.2 0.31 0.31	0.50 0.40	0.61 1.32	0.56 0.63	0.95 0.67
060319A			$\log O(\text{LGRB:SLEE})_{\text{prompt}} = -0.43$													
value P(L) P(E)	0.9 0.31 0.30	1.2 0.33 0.44	51.4 0.14 0.40	51.1 0.21 0.38	0.3	0.6	0.3	0.1	2.9 0.56 0.96	2.0e-03 2.99 0.08
051117B			$\log O(\text{LGRB:SLEE})_{\text{prompt}} = -1.33$													
value P(L) P(E)	1.0 0.32 0.30	0.5 0.26 0.97	50.5 0.02 0.41	50.0 0.03 0.43	0.7 0.49 0.47	10.3 0.29 0.48	...	1.0 1.25 0.86
050826A			$\log O(\text{LGRB:SLEE})_{\text{prompt}} = -1.68$													
value P(L) P(E)	1.6 0.67 0.94	0.3 0.24 0.74	50.8 49.8 1.34	0.04 0.01 0.37	1.0 0.48 0.37	0.2 0.59 0.36	0.9.8 0.47 0.47	0.1 0.33 0.37	0.2 0.73 1.37	0.2 0.73 0.32	1.2 0.41 0.11

Table 7 (cont'd)

$\log T_{90}$	z	$\log E_{\text{iso}}$ erg	$\log L_{\text{iso}}$ erg s^{-1}	α	$\log E_p$ keV	$\log f$	$f_{\text{eff}} - 1$	$\log \text{sSFR}$ $\text{M}_\odot \text{ yr}^{-1}$	$\log M_*$ M_\odot	$[\text{X}/\text{H}]$	$\log R_{50}$ kpc	$\log \text{offset}$ R_{50}	F_{light}	Γ		
050219A	value	1.4	$\log O(\text{LGRB:SLEE})_{\text{prompt}} = -2.38$		51.0	50.0	-0.1	2.0	-1.2	$\log O(\text{LGRB : SLEE})_{\text{host}} = -2.44$	10.0	0.7	1.2	0.5	...	1.3
P(L)	0.60	0.22	0.07	0.02	9.4e-03	0.78		0.03	1.9e-03	0.42	...	0.61	0.16	0.29	...	0.69
P(E)	0.83	0.61	1.49	0.42	0.06	0.89		0.07	0.07	0.50	...	1.32	0.69	0.86	...	0.22

Note. —

^{*} parameters those are not included to calculate $\log \Lambda$.[†] $z=0.5$ is assumed for GRB 060121A to calculate E_{iso} , L_{iso} , et al in Li et al. (2016).

CHAPTER 5

CAN LIFE SURVIVE GAMMA RAY BURSTS IN THE HIGH-REDSHIFT UNIVERSE?

This chapter is part of the following published paper :

Ye Li, Bing Zhang, The Astrophysical Journal, Volume 810, Issue 1, article id. 41, 7 pp.
(2015)

Introduction

Nearby high-energy transient sources have been considered as a possible cause of mass extinction events on Earth as well as a potential threat to life in the future (Ruderman, 1974; Thorsett, 1995; Dar et al., 1998; Gehrels et al., 2003; Melott & Thomas, 2011; Svensmark, 2012). Among them, gamma-ray bursts (GRBs), the most violent explosions in the universe, have been regarded as one of the most lethal high-energy transients to life (Scalo & Wheeler, 2002; Thomas et al., 2005a,b). With a 2-D simulation on how Earth's atmosphere responds to an intense γ -ray flux, Thomas et al. (2005a) investigated the effect of a nearby (2 kpc away) GRB to life on Earth. A typical GRB at this distance has a γ -ray fluence of 10^8 erg cm^{-2} ($= 100 \text{ kJ m}^{-2}$), which would cause severe damage to life on Earth. According to Thomas et al. (2005a), such a GRB would lead to a rapid increase of nitrogen compounds (e.g. NO and NO₂) in the atmosphere causing an on-average 35% ozone depletion in the stratosphere, increasing the solar UVB radiation flux at Earth for years. The resulting DNA damage, up to 16 times the normal level, is lethal to many organisms, such as plankton, the base of the food chain. It may lead to the extinction of creatures in higher trophic levels of the food chain due to starvation. Furthermore, the opacity of NO₂ in Earth's atmosphere would result in a decreased surface temperature, which is speculated to be a cause of a long-lasting ice age (Thomas et al. 2005a; but see Thomas et al. 2015). The mass extinction in the late Ordovician (~ 447 Myr ago) could be due to the impact of a nearby GRB (Melott et al., 2004; Bambach, 2006; Melott & Thomas, 2008).

Long-duration GRBs are more dangerous than the short-duration ones (Piran & Jimenez, 2014). Since long GRBs (LGRBs) are related to deaths of massive stars and therefore track the star formation history (SFH) of the universe (Woosley & Bloom, 2006; Kumar & Zhang, 2015), it is naturally expected that GRBs become more lethal at higher redshifts where the star formation rate (SFR) is higher. Indeed, Piran & Jimenez (2014) speculated that life as we know it cannot survive at $z > 0.5$ due to the frequent bombardment of GRBs at any location in a galaxy.

One caveat in drawing such a conclusion is related to the duty cycle of lethal GRBs preventing development of advanced life. The timescale to re-develop advanced life is not well studied. Even though the Ordovician mass extinction happened ~ 447 Myr ago, more recent mass extinction events (e.g. the Cretaceous-Paleogene extinction ~ 65 Myr ago that killed the dinosaurs) did not prevent re-emergence of advanced life forms (humans). Therefore, it may be possible for life to tolerate a shorter (say, 50 Myr) lethal GRB duty cycle. Regardless of the biological details of how a GRB may kill life and how advanced life forms re-emerge, our existence suggests that advanced civilizations can develop if lethal GRBs have a duty cycle comparable to the one inferred for the solar neighborhood in the Milky Way (MW) Galaxy.

In this paper, we quantify the lethal GRB duty cycle in the solar neighborhood, and apply it as a conservative life survival condition to study the “habitability” of various observed galaxies (e.g. Sloan Digital Sky Survey (SDSS) galaxies and the GRB host galaxies). The aim is to address whether or not life can survive GRBs in the high-redshift universe.

Methodology

Following Thomas et al. (2005a), we adopt $F_c = 10^8$ erg cm $^{-2}$ as a critical fluence defining a lethal GRB. Since GRBs trace star formation and most star formation happens in late-type galaxies, we consider our test galaxies to be disk galaxies with an exponential stellar mass column density $\Sigma_* e^{-r/r_d}$, where r_d is the scale length. To the first-order approximation, one

may ignore variations of specific SFR (sSFR) and metallicity within the galaxy. A GRB at r_0 from the galactic center defines a pair of cones where life is damaged. These cones have a radius $R(L, F_c) = \sqrt{L\Delta t/(4\pi F_c)}$ and a solid angle Ω , where L is the peak isotropic luminosity of the GRB, and Δt is the rest-frame duration of the GRB, which is typically ~ 10 s. For a GRB at r_0 , the fraction of mass in the galaxy where life is damaged can be expressed as

$$\begin{aligned} p(L, r_0) &= p[R(L, F_c), r_0] = \frac{\int \Sigma_* e^{-r/r_d} dA}{M_*} \\ &= \int_{r_0-R}^{r_0+R} dx \int_{-\sqrt{R^2-(x-r_0)^2}}^{\sqrt{R^2-(x-r_0)^2}} \Sigma_* e^{-\frac{\sqrt{x^2+y^2}}{r_d}} dy \\ &\times f_b M_*^{-1}, \end{aligned} \quad (5.1)$$

where $f_b = \frac{\Omega}{4\pi}$ is the beaming correction factor. The fraction $p(L, r_0)$ is also the probability for a random GRB in the galaxy (including both those beaming toward and those beaming away from the planet) to kill life on a planet at r_0 from the galactic center.

The high-luminosity LGRB luminosity function (LF), $\phi(L/L^*)$ is characterized by a broken power law with a break luminosity L^* (Liang et al., 2007a; Wanderman & Piran, 2010; Sun et al., 2015), e.g.

$$\phi\left(\frac{L}{L^*}\right) \propto \left[\left(\frac{L}{L^*}\right)^{\alpha_1} + \left(\frac{L}{L^*}\right)^{\alpha_2}\right]^{-1}. \quad (5.2)$$

The number of lethal GRBs that would attack the planet at r_0 within a time duration T is

$$N = \int_{L_{\min}}^{L_{\max}} f_b^{-1} \dot{\rho}_0 \phi(L) p(L, r_0) dL \cdot TV(M_*) f_{\text{sSFR}} f_{\text{Fe}}, \quad (5.3)$$

where the range of integration is $10^{49} - 10^{55} \text{ erg s}^{-1}$, the observed range of LGRBs, and $\dot{\rho}_0$ is the GRB event rate density above a specific luminosity in the local universe. Here, the factor f_b^{-1} makes the correction from the observed GRBs (defined by the observed LF) to the total GRBs (including those not beaming toward us). Note that it cancels out with the f_b factor

in Eq.(5.1), so that the result does not depend on the poorly constrained parameter f_b .

Various studies reach a generally consistent conclusion, but with somewhat different parameters. Here, we adopt the latest analysis by Sun et al. (2015) using the largest long GRB sample. Since there is an evolution of the GRB LF, we use the LF and event rate density derived from the nearby ($z < 1$) sample with the following parameters ((Sun et al., 2015)): $\alpha_1 = 1.57$, $\alpha_2 = 1.8$, $L^* = 4 \times 10^{51}$ erg s $^{-1}$, and $\dot{\rho}(> 10^{50}$ erg s $^{-1}$) = 1.6 Gpc $^{-3}$ yr $^{-1}$. The occupied cosmological volume of a galaxy with mass M_* is estimated as $V(M_*) = M_*/\rho_*(z)$, where $\rho_*(z)$ is the average stellar density obtained by integrating the stellar mass function (Mortlock et al., 2015) from $10^7 - 10^{13} M_\odot$ for different redshifts, which is fit as $\rho_*(z) = 10^{17.46 - 0.39z} M_\odot$ Gpc $^{-3}$ (see also Muzzin et al. (2013) and references therein). A typical time scale $T = 500$ Myr is used to match approximately the epoch of the Ordovician Mass Extinction of $\sim(447 - 443)$ Myr ago (Sutcliffe et al., 2000; Brenchley et al., 2003).

The parameter $\dot{\rho}_0$ denotes the average GRB event rate density in the local universe ($z \sim 0$). We know that the LGRB rate depends on star formation rate and metallicity. It is then relevant to introduce two correction factors for the specific galaxy values with respect to the local average values. The specific SFR correction factor is introduced as

$$f_{\text{sSFR}} = \frac{\text{sSFR}}{\text{sSFR}_0}, \quad (5.4)$$

where the local sSFR is $\text{sSFR}_0 = 0.1$ Gyr $^{-1}$ (Weinmann et al., 2011). The metallicity correction factor is defined as

$$f_{\text{Fe}} = \frac{P([\text{Fe}/\text{H}])}{P_0([\text{Fe}/\text{H}]_0)}. \quad (5.5)$$

Here, $P([\text{Fe}/\text{H}])$ is the fraction of stars with metallicity poorer than $[\text{Fe}/\text{H}] = -0.43$ (equivalent to $0.4 Z_\odot$) (Bertelli et al., 1994; Virgili et al., 2011), assuming that the metallicity of the galaxy is a Gaussian distribution with the detected metallicity as the medium value and the standard deviation $\sigma_{\text{Fe}} = 0.22$, similar to the MW (Casagrande et al., 2011). The function $P([\text{Fe}/\text{H}]_0)$ is a similar fraction, but with median value being the mean metallicity of the

local universe $[\text{Fe}/\text{H}]_0 = -0.006$ (Gallazzi et al., 2008; Madau & Dickinson, 2014).

The short GRB (SGRB) impact rate can be estimated with a similar method. The typical duration of a SGRB Δt is ~ 0.5 s. The LF depends on the model of the merger delay time distribution, but can be generally fitted as a single power law (Sun et al., 2015). We use the best-fit LF parameters for a Gaussian delay time distribution, i.e. $\phi(L) \propto L^{-1.7}$ with $\dot{\rho}_0(> 10^{50} \text{ erg s}^{-1}) = 1.3 \text{ Gpc}^{-3} \text{ yr}^{-1}$. The range of integration is $10^{49} - 2 \times 10^{54} \text{ erg s}^{-1}$ as observed. Since the SGRBs are likely due to mergers of two neutron stars or a neutron star–black hole system, the probability of a short GRB is no longer directly related to the fraction of the mass. Rather, we derive the probability by introducing an offset distribution of the afterglow with respect to the host galaxies. Using the observational data (Fong et al., 2010; Fong & Berger, 2013), we find that the normalized (in units of the host galaxy scale length) offset distribution can be approximated as a Gaussian function in logarithmic space, i.e., $(G\log_{10}(r/r_d), \mu=0.32, \sigma=0.57)$, so the probability of a SGRB located in an area dA is

$$\begin{aligned} p(L, r_0) &= \frac{\int G(\log_{10}(r/r_d))dA}{(\ln 10)2\pi r^2} \\ &\times \frac{1}{\int G(\log_{10}(r/r_d))d(\log_{10}(r/r_d))}, \end{aligned} \quad (5.6)$$

where the integration in the numerator is over the damaging region around r_0 and the integration in the denominator is over the entire galaxy. Also, there is no direct connection between the SGRB rate and sSFR or metallicity, so that $f_{\text{sSFR,SGRB}} = 1$ and $f_{\text{Fe,SGRB}} = 1$ are adopted.

Lethal GRB RATE IN MILKY WAY

We first apply our methodology to the Milky Way (MW). The stellar mass of the MW is $M_* = 6.08 \pm 1.14 \times 10^{10} \text{ M}_\odot$ (McMillan, 2011), so that the occupied cosmological volume is $V = 2.1 \times 10^{-7} \text{ Gpc}^{-3}$. With $\text{sSFR} = 2.71 \pm 0.59 \times 10^{-2} \text{ Gyr}^{-1}$ (Licquia & Newman, 2014), which is relatively small in the local universe, we get the sSFR correction factor

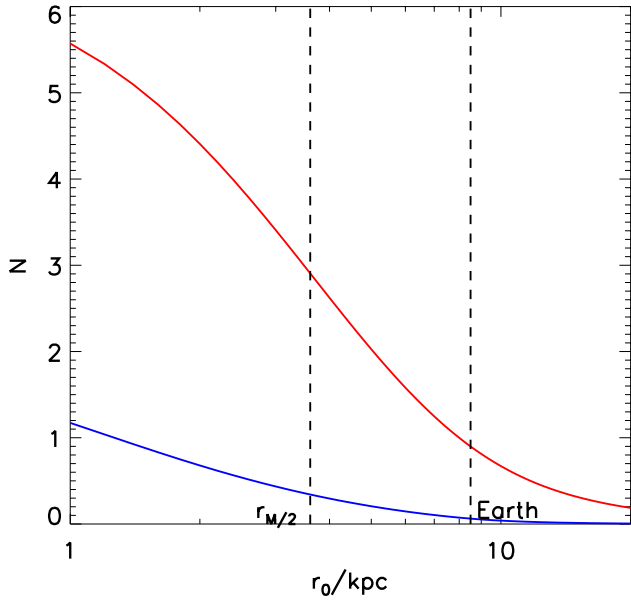


Figure 17 The number of lethal LGRBs (red solid line) and SGRBs (blue solid line) within 500 Myr as a function of distance r_0 from the Galactic Center. Two vertical black dashed lines indicate the half-mass radius ($r_{M/2}$) and the Earth position, respectively.

$f_{\text{ssFR}} = 0.27$. The metallicity distribution function of the MW is a Gaussian with the mean value $[\text{Fe}/\text{H}] = -0.06$ and $\sigma_{\text{Fe}} = 0.22$ (Casagrande et al., 2011). It is relatively metal poor compared to the average value in the local universe, and the metallicity correction factor is $f_{\text{Fe}} = 1.7$. The half mass radius of the MW is $r_d = 2.15 \pm 0.14$ kpc (Bovy & Rix, 2013), and our Earth is located at $r_0 = 8.33 \pm 0.35$ kpc away from the Galactic center (Reid, 1993; Eisenhauer et al., 2003; Gillessen et al., 2009).

The red line in Fig.17 denotes the number of lethal LGRBs for planets at different radii r_0 in the Milky Way within 500 Myr. At Earth’s location, the number of lethal LGRBs is 0.93 within 500 Myr. This is consistent with the hypothesis connecting the Ordovician mass extinction with GRB activity. The number is larger than 1 for $r_0 < 8$ kpc. At the half mass radius, the number of lethal GRBs is $N_{M/2} = 2.91$. The number increases to even larger values at smaller radii, suggesting that the regions close to the Galactic center are less habitable. Our existence suggests that $N \sim 1$ per 500 Myr can be regarded as a *conservative*

criterion for the survival of advanced life forms.

The blue line in Fig.17 shows the number of lethal SGRBs as a function of r_0 per 500 Myr. They are much rarer than LGRBs, suggesting that the LGRBs are the dominant species limiting life in the universe (see also Piran & Jimenez, 2014). In the rest of the paper, we ignore the contributions of SGRBs.

Lethal GRB rate in other galaxies

Galaxies at high redshifts have higher sSFR (Weinmann et al., 2011; Ilbert et al., 2014) and lower metallicity (Maiolino et al., 2008; Mannucci et al., 2010) on average. These result in higher f_{Fe} and f_{sSFR} correction factors, so that the number of lethal GRBs is expected to increase with redshift. In this section, we investigate the lethal GRB rate for other galaxies making use of the observational data directly. We employ the SDSS DR8 and DR12 galaxy samples (Aihara et al., 2011; Smee et al., 2013; Alam et al., 2015) as the starting point, and extrapolate the sample to even higher redshifts with a Monte Carlo simulation, aiming at quantifying the redshift-dependence of the fraction of benign galaxies where life as we know it can survive GRBs. GRB host galaxies are also studied for comparison. For all the galaxies, instead of studying the r_0 -dependent lethal GRB rate, we only investigate the rate at the half-stellar-mass radius $N_{M/2}$ as a representation of the “habitability” of the galaxy.

SDSS DR8 and SDSS/BOSS DR12 Samples

The SDSS DR8 sample includes all spectroscopically classified galaxies in SDSS-I/II. It covers 9274 deg² of the sky and includes 860,836 unique galaxies, with a median redshift 0.12. The SDSS/BOSS DR12 sample is the SDSS-III’s Baryon Oscillation Spectroscopic Survey (BOSS) galaxy catalog, which includes a LOWZ sample and a CMASS sample. There are 1,376,823 galaxies in total, with a median redshift 0.5.

These samples are subject to observational selection effects. Since our primary aim is to check whether life can survive GRBs at high redshifts, for the first step we work on the

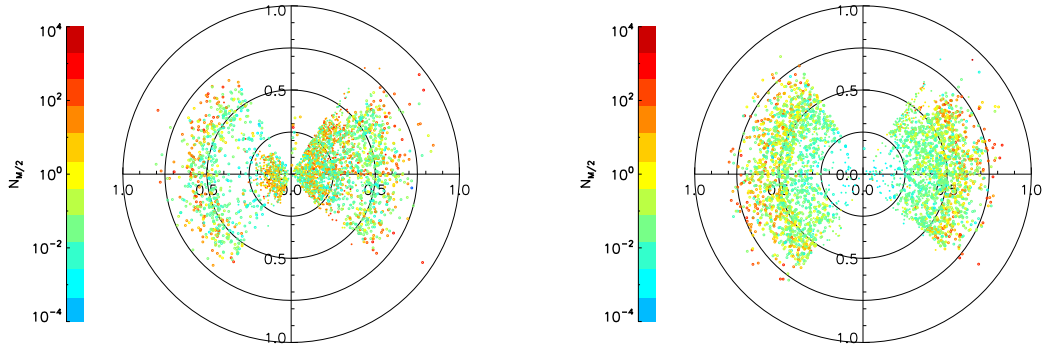


Figure 18 3-D maps of SDSS DR8 (filled circles) and DR12 (open circles) galaxies with Dec in the range $[0^\circ, 0.5^\circ]$. Colors are encoded with the number of lethal GRBs within 500 Myr at the half mass radius $N_{M/2}$ for each galaxy. The larger the $N_{M/2}$, the more dangerous the galaxy. Left Panel: $10^{10} M_\odot < M_* < 10^{11} M_\odot$; Right Panel: $10^{11} M_\odot < M_* < 10^{12} M_\odot$.

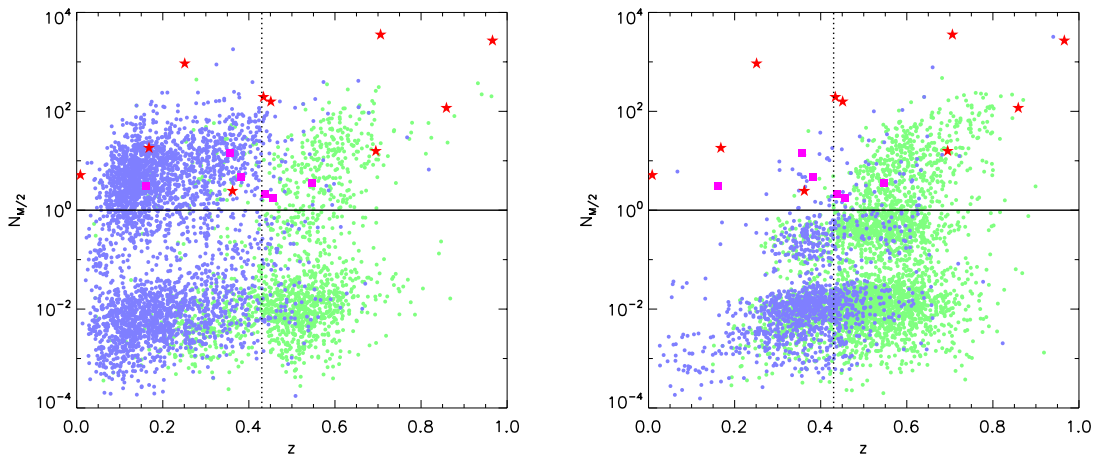


Figure 19 The number of lethal GRBs within 500 Myr at the half mass radius $N_{M/2}$ in the galaxies at different redshifts. Blue points indicate the SDSS DR8 galaxies, and green dots indicate the SDSS/BOSS DR12 galaxies. Red stars are LGRB host galaxies and magenta squares are SGRB host galaxies. Left panel: $10^{10} M_\odot < M_* < 10^{11} M_\odot$; Right panel: $10^{11} M_\odot < M_* < 10^{12} M_\odot$. GRB hosts are plotted in both panels regardless of their masses.

observed sample only to make the case.

We use the SDSS DR8 and SDSS/BOSS DR12 galaxy properties obtained from the Portsmouth Group¹. In this sample, stellar mass, star formation rate, and metallicity are estimated by fitting the *ugriz* photometric data with the publicly available code Hyper-Z

¹http://www.sdss.org/dr12/spectro/galaxy_portsmouth/

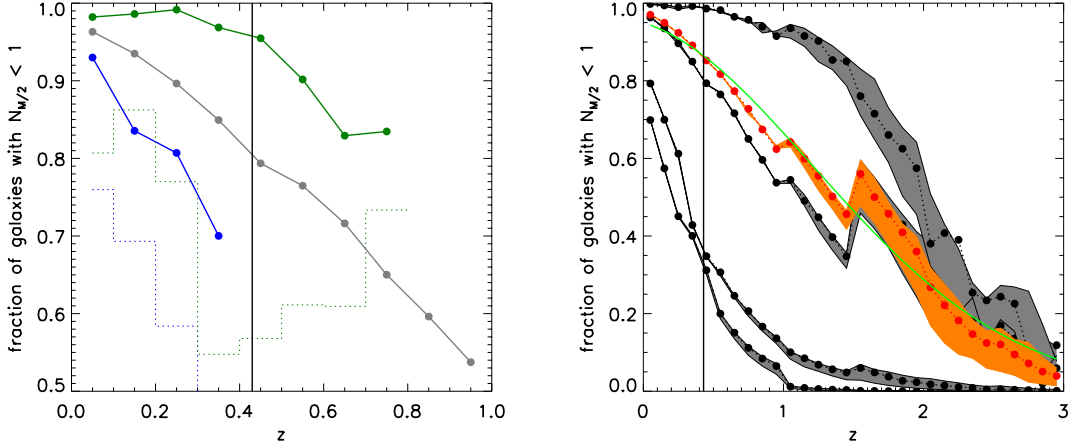


Figure 20 Left panel: The fraction of benign galaxies with $N_{M/2} < 1$ as a function of redshift for the galaxies. SDSS DR8 galaxies (blue line) and SDSS/BOSS DR12 galaxies with $10^{10} < M < 10^{11} M_\odot$ (green line) are shown. Monte Carlo simulated galaxies in the same mass bin (grey) are also shown for comparison. Right panel: The fraction of benign galaxies as a function of redshift according to Monte Carlo simulations. Different black lines denote different mass bins: from bottom up: $10^8 < M_* < 10^9 M_\odot$, $10^9 < M_* < 10^{10} M_\odot$, $10^{10} < M_* < 10^{11} M_\odot$ and $10^{11} < M_* < 10^{12} M_\odot$, respectively. Red line shows the mass weighted fraction, which is similar to the result of mass bin $10^{10} < M_* < 10^{11} M_\odot$. The shaded regions denote the uncertainty range of the sSFR factor between red and blue galaxies for each redshift bin (grey) or for mass-weighted case (orange). The green line shows a Gaussian fit with $G(\text{peak} = 0.96, \mu = -0.24, \sigma = 1.44)$.

(Bolzonella et al., 2000). The stellar population models of Maraston (2005) and Maraston et al. (2009) are employed. Star formation rate is estimated with an exponentially declining star formation history (SFH), truncated SFH, or constant SFH model, whichever gives the best fit. The Initial Mass Function is Kroupa (Kroupa, 2001).

Figure 18 displays two 3-D maps of the galaxies in the samples. For clear illustration, only galaxies with declinations in the range of $[0^\circ, 0.5^\circ]$ are shown here. The left panel shows the galaxies with stellar mass $10^{10} M_\odot < M_* < 10^{11} M_\odot$, and the right panel shows the galaxies with $10^{11} M_\odot < M_* < 10^{12} M_\odot$. DR8 galaxies are shown as filled circles and DR12 galaxies are shown as open circles. Colors are encoded with the estimated number of lethal LGRBs at half mass radius $N_{M/2}$ in 500 Myr. “Blue” and “green” galaxies have $N_{M/2} < 1$, so that they are safe for life. “Red” and “orange” galaxies have $N_{M/2} > 1$, which

are the most dangerous. “Yellow” galaxies are MW-like galaxies. One can see that although “red” and “orange” galaxies gradually increase with redshift, there are still “blue” / “green” galaxies up to redshift 0.7. The naive speculation that no life can survive beyond $z = 0.5$ is not confirmed.

In order to take a closer look at how galaxies become more dangerous at higher redshifts, in Fig.19 we display $N_{M/2}$ of galaxies as a function of redshift. The left and right panels show the galaxies with stellar mass in the range of $10^{10} M_\odot < M_* < 10^{11} M_\odot$, and $10^{11} M_\odot < M_* < 10^{12} M_\odot$, respectively. In each panel, DR8 galaxies are shown as blue points and DR12 galaxies are shown as green points. The vertical dashed line shows the corresponding redshift ($z = 0.43$) when Earth was formed. The horizontal solid line marks $N_{M/2} = 1$, above which most regions in the galaxy are dangerous for life. One can see in general for both mass ranges, galaxies become more dangerous at higher redshifts. There seems to be an offset (especially in the left panel) between the DR8 (blue) and DR12 (green) galaxies, but it is caused by the different selection effects for the two samples.

The fraction of galaxies with $N_{M/2} < 1$ is shown in the left panel of Fig. 20. The blue and green lines are for DR8 and DR12, respectively. In order to avoid the selection effects on luminosity and mass, we only focus on one mass bin $10^{10} M_\odot < M_* < 10^{11} M_\odot$ here. The results have similar trends for other mass bins. Each redshift bin is required to have more than 5,000 galaxies. Some galaxies are marked as $SFR = 0$. Most of them have a truncated SFH. Some others have a large age for an exponential decay of SFH as a function of time. For each redshift bin, the fraction of galaxies with $SFR = 0$ are plotted as the dotted histograms.

Since the DR8 sample tends to have more blue (late type) galaxies for a particular stellar mass bin whereas the DR12 sample originally searched for red (early type) galaxies, the two samples are both subject to a sample selection effect. In any case, the fraction lines (blue and green) derived from these two samples set the lower and upper limits of the fraction of benign galaxies as a function of redshift.

Monte Carlo Simulations

In order to reduce the sample selection effects and investigate redshift-dependence of the fraction of benign galaxies for life, we apply a Monte Carlo simulation aimed at achieving a more complete and unbiased sample.

We simulate blue and red galaxies separately since they follow different correlations among redshift, stellar mass, sSFR and metallicity (Kimm et al., 2009; Mortlock et al., 2015). We simulate 100,000 blue galaxies in each $\Delta z = 0.1$ redshift bin. The number of red galaxies is estimated by the ratio between the number of red and blue galaxies. The ratio is estimated by integrating the stellar mass function of blue and red galaxies from $10^8 - 10^{13} M_\odot$ in each redshift bin (Mortlock et al., 2015; Muzzin et al., 2013), which gives an empirical relation $\log_{10}(r/b) = -0.16 - 0.74z$.

For blue galaxies in each redshift bin, galaxy mass is given by a stellar mass function as a function of redshift (Mortlock et al., 2015). The sSFR distribution is considered as a Gaussian distribution. The median sSFR is a function of redshift and stellar mass (Eq.5 of Ilbert et al. 2014). The dispersion σ_{sSFR} is given as 0.4 Gyr^{-1} , a mean value of their Fig. 6. The metallicity distribution is also assumed to be a Gaussian function. The median value is a function of stellar mass and SFR (Eq.4 of Mannucci et al. 2010). In order to avoid the abnormal increase of very small and very large $\mu_{0.32}$, the fourth-order term of that equation is dropped. A dispersion $\sigma_{\text{Fe}} = 0.07$ is used, which is the median value of the dispersions in those stellar mass-SFR bins.

The mass distribution of red galaxies as a function of redshift in Mortlock et al. (2015) is used to simulate the masses of the red galaxies. They are mostly passive galaxies (Strateva et al., 2001) and their sSFRs are generally 0.01 to 0.001 times of those of blue galaxies (Kimm et al., 2009). One may assume that their sSFRs follow the same relation with stellar mass (Kimm et al., 2009), but have sSFRs a factor 0.001/0.003/0.010 of those of blue galaxies with the same masses. The effect of different sSFRs of red galaxies are shown as the shadows in the right panel of Fig.20.

The fraction of MC simulated galaxies with $N_{M/2} < 1$ is shown in the right panel of Fig.20. Black lines are for different stellar mass bins. From the bottom up, the lines are for $10^8 - 10^9 M_\odot$, $10^9 - 10^{10} M_\odot$, $10^{10} - 10^{11} M_\odot$ and $10^{11} - 10^{12} M_\odot$, respectively. The shaded regions enclose the results for different median sSFRs ratio between red and blue galaxies. The center line is for 0.003, while the lower and upper ones are for 0.010 and 0.001, respectively. It reveals that the fraction of benign galaxies in the small galaxy sample ($M_* < 10^{10} M_\odot$) is low, which becomes smaller than 50% at $z = 0.5$. The fraction of benign galaxies increases with mass bins. For example, for $M_* > 10^{10} M_\odot$, the fraction is still 50% at $z \leq 1.5$. The red line and the orange shaded region show the mass-weighted fraction of benign galaxies with $N_{M/2} < 1$. They are similar to the fraction line and shaded region for MW-like galaxies in the mass bin $10^{10} M_\odot < M_* < 10^{11} M_\odot$. This is because these galaxies are massive and relatively common, and occupy most of the mass in each redshift bin. The fraction of benign galaxies is $\sim 50\%$ at $z \sim 1.5$, and is $\sim 10\%$ even at $z \sim 3$.

GRB host galaxies

LGRBs tend to reside in late type galaxies with high star formation rate and low metallicity (e.g. Savaglio et al., 2009), whereas SGRB host galaxies tend to be more diverse (Fong & Berger, 2013; Berger, 2014). We study the GRB host galaxies, both for LGRBs and SGRBs, for their habitability. Table 8 lists the information of some LGRB and SGRB host galaxies with the desired information, including stellar mass, SFR, metallicity, and scale length. Also listed are the $N_{M/2}$ values of those galaxies. They are also overplotted as red stars (LGRB host galaxies) and magenta squares (SGRB host galaxies) in Fig.19. One can see that LGRB host galaxies are among the extremely dangerous galaxies for life. The number of lethal LGRBs at half mass radius within 500 Myr in all of the LGRB host galaxies is much greater than 1, suggesting that life can hardly survive in these galaxies. Meanwhile, SGRB hosts are relatively safer than LGRB hosts due to their much higher metallicity and lower sSFR. However, in all cases studied in our sample one has $N_{M/2} > 1$, so that they still

Table 8. GRB host galaxy properties

GRB	z	$\log M$ M_{\odot}	sSFR Gyr^{-1}	12+ $\log(\text{O}/\text{H})$	r_d kpc	$N_{M/2}$	Ref
970228	0.695	8.65	1.19	8.47	2.458	15.74	1,2,3
980425	0.009	8.68	0.54	8.16	3.266	5.14	1,2,3
980703	0.966	10.00	1.66	8.14	1.342	2696.83	1,2,3
990712	0.434	9.29	1.23	8.10	1.591	194.86	1,2,3
991208	0.706	8.53	13.34	8.02	0.344	3558.73	1,2,3
010921	0.451	9.69	0.51	8.15	1.903	157.67	2,3
11121	0.362	9.81	0.35	8.60	12.671	2.46	2,3
020903	0.251	8.87	3.57	8.22	0.431	927.26	2,3
030329	0.168	7.74	2.00	7.97	0.804	18.18	2,3
040924	0.859	9.20	1.19	8.23	2.382	117.08	2,3
SGRB							
050709	0.161	8.80	0.24	8.50	2.080	3.08	4,5
051221A	0.546	9.40	0.38	8.80	2.290	3.62	4,5
061006	0.438	9.00	0.24	8.60	3.220	2.14	4,5
070724A	0.457	10.10	0.20	8.90	3.640	1.73	4,5
071227	0.381	10.40	0.02	8.50	4.720	4.75	4,5
130603B	0.356	9.70	0.34	8.70	2.020	14.36	4,5,6

References. — (1)Bloom et al. (2002); (2)Wainwright et al. (2007); (3)Savaglio et al. (2009); (4)Leibler & Berger (2010); (5)Fong & Berger (2013); (6)de Ugarte Postigo et al. (2014b)

belong to dangerous galaxies.

Conclusions and Discussion

In this paper, we examined the duty cycle of lethal GRBs ($F_c = 10^8 \text{ erg cm}^{-2}$) in the Milky Way as well as observed galaxies at different redshifts. The duty cycle of lethal GRBs attacking Earth is about 1 per 500 Myr, consistent with the time scale of the Ordovician mass extinction. Our existence suggests that such a duty cycle is long enough to allow advanced life (such as human beings) to survive, so that such a duty cycle can be regarded as a conservative criterion for a benign environment. Adopting such a criterion, we investigated the fraction of benign galaxies as a function of redshift using the SDSS DR8 and SDSS/BOSS DR12 samples and through MC simulations. We find that this fraction is as high as 99% in the local universe, suggesting that the current era is most suitable to the development of advanced life. As expected, the benign galaxy fraction decreases with increasing redshift due to the increase of SFR and decrease of metallicity at progressively higher redshifts.

However, contrary to the naive expectation that no life can survive beyond $z > 0.5$, we show that benign galaxies do exist at redshifts much higher than 0.5. In particular, the fraction is $\sim 50\%$ around $z \sim 1.5$, and is still $\sim 10\%$ even at $z \sim 3$. In view that the birth of Earth itself corresponds to $z \sim 0.43$, our results raise the exciting possibility that advanced civilizations are in principle not excluded even before the formation of the solar system, even though the fraction of “habitable” galaxies is smaller in the higher redshift universe.

Finally, we discuss some possible uncertainties inherent to this analysis. 1. Many uncertainties are involved in making the argument that a GRB is lethal. These include how the atmosphere reacts to intense γ -ray flux, how DNA/life reacts to exposure to UV light, and how alien life forms may be different from the ones of which we are aware. On the other hand, since our analysis focuses on how life *survives* a GRB, these uncertainties do not affect our argument. The only biological connection used in this paper is our existence, suggesting that the local lethal LGRB event rate (1 per 500 Myr) can be regarded as a safe (conservative) duty cycle for life to survive. If the GRB damage is less severe, as suggested by some recent studies (e.g. Thomas et al., 2015), or if advanced life can tolerate a higher lethal GRB rate (argument presented in the second to last paragraph in introduction), then the fraction of benign galaxies at high- z is even larger. 2. There exist uncertainties in the local GRB event rate density, which affects the estimated lethal GRB duty cycle on Earth. We used the latest results of Sun et al. (2015) with the largest LGRB sample. Adopting the GRB event rate results derived by other authors would give a local lethal GRB rate generally consistent with our value, with a difference at most a factor of 2-3. 3. The two galaxy samples included in our study are subject to substantial selection effects. The derived fractions, even with MC simulations, may not fully represent the true fractions due to some un-modeled biases. In any case, we have argued that the DR8 and DR12 samples would bracket the true population. The fact that at least some galaxies are benign against lethal GRBs at high redshifts is robust, which is the main conclusion of this paper. 4. The dependence of LGRBs on SFR and metallicity is evidenced by the observations, but the

exact correction factors (especially the metallicity one f_{Fe}) are not fully constrained. In any case, the general conclusion of this paper does not depend on the concrete form of f_{sSFR} and f_{Fe} . 5. We did not study the impact of SGRBs in other galaxies. For most star formation galaxies, their contribution to lethal GRB number is negligible. However, for early-type galaxies where SFR is extremely low, SGRBs may dominate the lethal GRB attacking duty cycle. In any case, $N_{M/2}$ is always much less than unity in these early-type galaxies. For the purpose of this paper (to claim the fraction of benign galaxies at high redshifts), ignoring the SGRB contribution does not affect the conclusions and is therefore justified. 6. We did not study the life-damaging effect of other transients such as supernovae, which may have comparable damaging effects as GRBs in the local universe (e.g. Melott & Thomas, 2011; Svensmark, 2012). While a more detailed study is needed to address the supernova effect, the general conclusion of this paper may not be modified when supernovae are considered. This is because supernovae also follow star formation history, so that they may be subject to the same f_{sSFR} correction factor. On the other hand, their metallicity dependence is less apparent than LGRBs, so that their f_{Fe} correction factor, if any, should be smaller than that of LGRBs. Overall, their rate of increase with redshift is slower than LGRBs, so that their role in damaging life at high- z would be less significant than LGRBs.

APPENDIX: PROPERTIES OF GRBs

Table 9. basic

GRB	redshift				Detector	T_{90} [s]	Ref	$E_{\gamma,\text{iso}}$ [erg]	$L_{\text{p},\text{iso}}$ [erg s $^{-1}$]	f	f_{eff}
	(1)	z (2)	method (3)	Ref (4)							
140606B	0.384	E	279	Fermi	23.6	39	4.60×10^{51}	1.88×10^{51}
140518A	4.707	A	272	Swift	60.5	42	7.92×10^{52}	2.89×10^{52}	1.18	1.02 ± 0.01	
140515A	6.32	A	271	Swift	23.4	42	7.08×10^{52}	5.23×10^{52}	1.21	1.04 ± 0.02	
140512A	0.725	A	273	Swift	154.8	42	5.63×10^{52}	6.71×10^{51}	1.78	1.25 ± 0.13	
140508A	1.027	A	270	Fermi	44.3	38	2.26×10^{53}	6.74×10^{52}
140506A	0.8893	E	275	Swift	111.1	42	1.83×10^{52}	1.01×10^{52}	1.50	1.13 ± 0.06	
140430A	1.6019	E	275	Swift	173.6	42	1.51×10^{52}	5.73×10^{51}	1.44	1.06 ± 0.03	
140428A	4.7	A	269	Swift	17.42	42	3.69×10^{52}	3.10×10^{52}
140423A	3.26	A	268	Swift	134	42	5.45×10^{53}	6.19×10^{52}	1.19	1.03 ± 0.01	
140419A	3.956	A	267	Swift	94.7	42	1.43×10^{54}	5.73×10^{53}	1.63	1.06 ± 0.03	
140318A	1.02	E	266	Swift	8.43	42	3.49×10^{51}	1.07×10^{51}	1.14	1.04 ± 0.02	
140311A	4.954	A	265	Swift	71.4	42	2.28×10^{53}	6.10×10^{52}
140304A	5.283	A	264	Swift	15.6	42	1.28×10^{53}	1.04×10^{53}	1.30	1.05 ± 0.03	
140301A	1.4155	E	275	Swift	31.0	42	4.82×10^{51}	1.22×10^{51}	1.10	1.02 ± 0.01	
140226A	1.98	A	276	Konus-Wind	15	37	4.81×10^{52}	2.20×10^{52}
140213A	1.2079	E	275	Swift	60.0	42	1.05×10^{53}	3.70×10^{52}	3.00	1.38 ± 0.19	
140206A	2.739	A	263	Swift	93.6	42	3.00×10^{53}	1.86×10^{53}	4.38	1.75 ± 0.38	
140114A	3 ± 0.1	A	275	Swift	139.7	42	1.28×10^{53}	8.96×10^{51}
131231A	0.6427	E	275	Fermi	31	36	2.21×10^{53}	2.18×10^{52}
131227A	5.3	A	258	Swift	18.0	42	1.42×10^{53}	1.03×10^{53}	1.18	1.03 ± 0.01	
131117A	4.042	A	256	Swift	11.00	42	1.44×10^{52}	1.34×10^{52}	1.16	1.04 ± 0.02	
131108A	2.4	A	255	Fermi	19	33	5.95×10^{53}	2.14×10^{53}
131105A	1.6854	E	275	Swift	112.3	42	2.21×10^{53}	2.72×10^{52}	1.10	1.03 ± 0.01	
131103A	0.5960	E	275	Swift	17.3	42	1.65×10^{51}	3.17×10^{50}	1.25	1.09 ± 0.04	
131030A	1.293	A	254	Swift	41.1	42	2.97×10^{53}	1.03×10^{53}	4.63	1.25 ± 0.13	
131011A	1.874	A	253	Fermi	77	32	1.05×10^{53}	1.59×10^{52}
131004A	0.717	E	252	Swift	1.54	42	8.01×10^{50}	1.48×10^{51}	1.94	1.94 ± 0.16	
130925A	0.3483	E	275	Swift	7000	34	3.21×10^{50}	8.56×10^{49}	1.81	1.09 ± 0.04	
130907A	1.238	A	251	Swift	> 360	42	2.98×10^{54}	1.86×10^{53}	4.75	1.38 ± 0.19	
130831A	0.4791	A	250	Swift	32.5	42	6.63×10^{51}	3.23×10^{51}	3.13	1.25 ± 0.13	
130702A	0.145	E	236	Fermi	59	31	5.05×10^{50}	3.15×10^{49}
130701A	1.1548	E	275	Swift	4.38	42	2.22×10^{52}	3.55×10^{52}	2.13	1.19 ± 0.09	
130612A	2.006	A	249	Swift	4.0	42	9.11×10^{51}	9.28×10^{51}	1.23	1.03 ± 0.01	
130610A	2.092	A	248	Swift	46.4	42	5.20×10^{52}	1.33×10^{52}	1.23	1.04 ± 0.02	
130606A	5.913	A	235	Swift	276.58	42	2.02×10^{53}	2.52×10^{53}	1.44	1.06 ± 0.03	
130604A	1.06	E	247	Swift	37.7	42	1.35×10^{52}	1.34×10^{51}	1.13	1.03 ± 0.01	
130528A	1.25	E	260	Swift	59.4	42	5.31×10^{52}	6.09×10^{51}	1.38	1.06 ± 0.03	
130518A	2.49	A	245	Fermi	48	30	1.78×10^{54}	6.01×10^{53}
130511A	1.3033	A	244	Swift	5.43	42	4.18×10^{51}	5.01×10^{51}	1.35	1.05 ± 0.03	
130505A	2.27	A	243	Swift	88	42	2.76×10^{54}	1.99×10^{54}	3.00	1.50 ± 0.25	
130427B	2.78 ± 0.02	A	242	Swift	27.0	42	6.49×10^{52}	3.95×10^{52}	1.31	1.11 ± 0.06	
130427A	0.3401	E	275	Swift	162.83	42	1.17×10^{54}	1.85×10^{53}	42.50	4.75 ± 1.88	
130420A	1.297	A	241	Swift	123.5	42	6.54×10^{52}	5.43×10^{51}	1.38	1.15 ± 0.08	
130418A	1.217	A	240	Swift	> 300	42	9.34×10^{52}	3.30×10^{51}	1.05	1.01 ± 0.01	
130408A	3.757	A	239	Swift	28	42	2.80×10^{53}	5.77×10^{53}	1.21	1.06 ± 0.03	
130215A	0.597	A	238	Swift	65.7	42	4.17×10^{52}	2.13×10^{51}	1.08	1.03 ± 0.01	
130131B	2.5393	E	275	Swift	4.30	42	2.98×10^{52}	2.81×10^{52}	1.21	1.08 ± 0.04	
121229A	2.707	A	233	Swift	100	27	1.97×10^{52}	8.70×10^{50}
121211A	1.023	A	232	Swift	182	42	2.18×10^{51}	2.06×10^{51}	1.19	1.05 ± 0.03	
121209A	2.1 ± 0.3	A	275	Swift	42.7	42	1.09×10^{53}	3.44×10^{52}	1.36	1.05 ± 0.03	
121201A	3.3830	E	275	Swift	85	42	3.81×10^{52}	1.18×10^{52}	1.18	1.08 ± 0.04	
121128A	2.20	A	231	Swift	23.3	42	1.21×10^{53}	5.33×10^{52}	2.75	1.63 ± 0.31	
121027A	1.7732	E	275	Swift	62.6	42	3.46×10^{52}	4.54×10^{51}	1.19	1.02 ± 0.01	
121024A	2.3012	E	275	Swift	69	42	5.00×10^{52}	1.70×10^{52}	1.24	1.09 ± 0.04	
120922A	3.1	P	230	Swift	173	42	2.06×10^{53}	2.56×10^{52}	1.20	1.03 ± 0.01	
120909A	3.93	A	229	Fermi	112	26	3.78×10^{53}	9.46×10^{52}	1.16	1.04 ± 0.02	

Table 9 (cont'd)

GRB	redshift			Detector	T_{90} [s]	Ref (7)	$E_{\gamma,\text{iso}}$ [erg] (8)	$L_{\text{p},\text{iso}}$ [erg s $^{-1}$] (9)	f (10)	f_{eff} (11)
	(1)	z (2)	method (3)							
120907A	0.970	A	228	Swift	16.9	42	2.55×10^{51}	3.14×10^{51}	1.29	1.06 ± 0.03
120815A	2.3587	E	275	Swift	9.7	42	1.47×10^{52}	1.24×10^{52}	1.28	1.10 ± 0.05
120811C	2.671	A	227	Swift	26.8	42	6.24×10^{52}	3.45×10^{52}	1.54	1.06 ± 0.03
120805A	3.1 ± 0.1	A	275	Swift	48.00	42	8.82×10^{52}	1.47×10^{52}
120802A	3.796	A	226	Swift	50	42	1.15×10^{53}	5.67×10^{52}	1.35	1.10 ± 0.05
120729A	0.80	A	225	Swift	71.5	42	1.89×10^{52}	5.87×10^{51}	1.51	1.11 ± 0.05
120724A	1.48	A	224	Swift	72.8	42	8.10×10^{51}	1.02×10^{51}
120722A	0.9590	E	275	Swift	42.4	42	6.37×10^{51}	7.16×10^{50}	1.09	1.02 ± 0.01
120716A	2.486	A	223	Fermi	234	25	2.91×10^{53}	7.96×10^{52}
120714B	0.3985	E	275	Swift	159	42	1.61×10^{51}	6.33×10^{49}
120712A	4.1745	A	222	Swift	14.7	42	1.76×10^{53}	1.27×10^{53}	1.41	1.06 ± 0.03
120711A	1.405	A	221	Fermi	44.0 ± 0.7	35	1.82×10^{54}	1.71×10^{53}
120624B	2.1974	E	275	Konus-Wind	300	24	3.21×10^{54}	2.32×10^{53}	1.62	1.09 ± 0.05
120422A	0.2826	E	275	Swift	5.35	42	2.97×10^{50}	8.97×10^{49}	1.13	1.05 ± 0.03
120404A	2.876	A	220	Swift	38.7	42	6.16×10^{52}	1.28×10^{52}	1.09	1.01 ± 0.01
120327A	2.813	A	219	Swift	62.9	42	1.88×10^{53}	6.53×10^{52}	1.69	1.13 ± 0.06
120326A	1.798	A	218	Swift	69.6	42	3.19×10^{52}	1.55×10^{52}	1.58	1.06 ± 0.03
120224A	1.1 ± 0.2	HA	275	Swift	8.13	42	1.75×10^{51}	7.79×10^{50}
120211A	2.4 ± 0.1	HA	275	Swift	61.7	42	3.38×10^{52}	6.02×10^{51}	1.15	1.05 ± 0.03
120119A	1.7291	E	275	Swift	253.8	42	3.56×10^{53}	5.64×10^{52}	2.33	1.14 ± 0.07
120118B	2.9428	E	275	Swift	23.26	42	5.65×10^{52}	1.61×10^{52}	1.22	1.04 ± 0.02
111229A	1.3805	A	213	Swift	25.4	42	3.68×10^{51}	1.84×10^{51}	1.17	1.13 ± 0.43
111228A	0.7164	E	275	Swift	101.20	42	3.91×10^{52}	4.27×10^{51}	1.62	1.30 ± 0.19
111225A	2.012	E	278	Swift	106.8	42	3.08×10^{52}	3.91×10^{51}	1.16	1.13 ± 0.16
111215A	$2.06^{+0.10}_{-0.16}$	P	278	Swift	796	42	1.11×10^{53}	2.95×10^{51}
111211A	0.4786	E	275	Konus-Wind	25	23	1.49×10^{52}	9.04×10^{51}
111209A	0.6770	E	275		25000	28	8.03×10^{53}	2.82×10^{50}
111129A	1.0796	E	275	Swift	7.6	42	1.65×10^{51}	9.40×10^{50}	1.10	1.10 ± 0.12
111123A	3.1513	E	275	Swift	290.0	42	3.68×10^{53}	1.49×10^{52}	1.17	1.13 ± 0.16
111107A	2.893	A	212	Swift	26.6	42	2.05×10^{52}	2.95×10^{52}	1.21	1.15 ± 0.23
111008A	4.9898	A	211	Swift	63.46	42	3.93×10^{53}	3.66×10^{53}	1.52	1.27 ± 0.03
111005A	0.0133	E	210	Swift	26	42	5.39×10^{47}	6.12×10^{46}	1.24	1.16 ± 0.07
110918A	0.9843	E	275	Konus-Wind	19.6 ± 0.1	29	1.84×10^{54}	4.23×10^{54}
110818A	3.3609	E	275		Swift	103	42	1.71×10^{53}	6.05×10^{52}	1.26
110808A	1.3490	E	275	Swift	48	42	5.74×10^{52}	9.27×10^{53}	1.05	1.08 ± 0.11
110801A	1.858	A	209	Swift	385	42	9.65×10^{52}	5.09×10^{51}	1.09	1.10 ± 0.24
110731A	2.83	A	208	Swift	38.8	42	4.91×10^{53}	3.16×10^{53}	3.50	1.25 ± 0.29
110726A	1.036	A	207	Swift	5.2	42	1.27×10^{51}	7.59×10^{50}	1.25	1.17 ± 0.07
110715A	0.82	A	206	Swift	13.0	42	4.81×10^{52}	4.18×10^{52}	9.70	1.15 ± 0.01
110709B	2.09	E	280	Swift	55.6	42	2.69×10^{53}	3.52×10^{53}	1.52	1.27 ± 0.21
110503A	1.613	A	205	Swift	10.0	42	1.80×10^{53}	1.99×10^{53}	3.12	1.28 ± 0.12
110422A	1.770	A	204	Swift	25.9	42	7.20×10^{53}	2.80×10^{53}	4.00	1.29 ± 0.16
110213B	1.083	A	203	Konus-Wind	50	22	8.08×10^{52}	2.95×10^{51}
110213A	1.46	A	202		Swift	48.0	42	7.34×10^{52}	2.90×10^{52}	1.35
110205A	2.22	A	201	Swift	257	42	6.10×10^{53}	2.74×10^{52}	1.54	1.27 ± 0.11
110128A	2.339	A	200	Swift	30.7	42	2.31×10^{52}	9.70×10^{51}	1.12	1.11 ± 0.29
110106B	0.618	E	199	Swift	24.8	42	5.34×10^{51}	6.68×10^{50}	1.15	1.12 ± 0.01
101225A	0.847	E	262	Swift	> 1088	42	8.21×10^{51}	1.62×10^{49}
101219B	0.55185	A	197	Swift	34	42	4.47×10^{51}	2.59×10^{50}
100906A	1.727	A	191	Swift	114.4	42	2.61×10^{53}	5.18×10^{52}	2.35	1.47 ± 0.05
100901A	1.408	A	190	Swift	439	42	3.38×10^{52}	2.61×10^{51}	1.10	1.10 ± 0.2
100814A	1.4392	E	275	Swift	174.5	42	9.39×10^{52}	1.00×10^{52}	1.75	1.34 ± 0.07
100728B	2.106	A	192	Swift	12.1	42	4.86×10^{52}	3.65×10^{52}	1.25	1.17 ± 0.09
100728A	1.5670	E	275	Swift	198.5	42	9.47×10^{53}	3.92×10^{52}	2.37	1.48 ± 0.38
100724A	1.2890	E	275	Swift	1.4	42	1.49×10^{51}	2.74×10^{51}	1.38	1.38 ± 0.21
100621A	0.5426	E	275	Swift	63.6	42	4.39×10^{52}	3.20×10^{51}	4.11	1.21 ± 0.11

Table 9 (cont'd)

GRB	redshift				Detector	T_{90} [s]	Ref (7)	$E_{\gamma, \text{iso}}$ [erg] (8)	$L_{\text{p, iso}}$ [erg s $^{-1}$] (9)	f (10)	f_{eff} (11)
	z (1)	method (2)	Ref (3)	Ref (4)							
100615A	1.3978	E	275		Swift	39	42	7.15×10^{52}	1.88×10^{52}	1.87	1.37 ± 0.21
100606A	1.5545	E	275		Swift	480	42	2.94×10^{53}	4.82×10^{52}	1.75	1.34 ± 0.14
100518A	$4^{+0.3}_{-0.5}$	P	189	INTEGRAL	Swift	84	42	5.52×10^{52}	4.95×10^{52}
100513A	4.772	A	188		Swift	52	42	1.40×10^{53}	2.80×10^{52}	1.15	1.12 ± 0.16
100508A	0.5201	E	275		Swift	37.0	42	2.87×10^{51}	2.24×10^{50}
100425A	1.755	A	187		Swift	104	42	9.42×10^{51}	4.23×10^{51}	1.18	1.13 ± 0.34
100424A	2.4656	E	275		Swift	7.0	42	4.54×10^{52}	3.03×10^{51}
100418A	0.6235	E	275		Swift	26.5 ± 2.1	35	7.66×10^{50}	2.15×10^{50}	1.12	1.11 ± 0.12
100414A	1.368	A	186		Fermi	3.8	42	5.63×10^{53}	3.30×10^{52}
100316D	0.0592	E	275		Swift	> 1300	19	5.74×10^{48}	1.13×10^{47}
100316B	1.180	A	185		Swift	17.9	42	1.65×10^{51}	1.33×10^{51}	1.31	1.19 ± 0.12
100302A	4.813	A	184		Swift	18.8	42	5.58×10^{52}	3.02×10^{52}	1.17	1.13 ± 0.1
090219A	4.6667	A	183		Swift	14.80	21	2.80×10^{52}	2.03×10^{52}	1.81	1.52 ± 0.16
091208B	1.0633	A	157		Swift	7.42	21	1.86×10^{52}	6.24×10^{51}	2.25	1.70 ± 0.03
091127A	0.4904	E	275		Swift	48.03	21	1.42×10^{53}	3.51×10^{52}
091109A	3.076	A	182		Swift	39.18	21	9.50×10^{52}	1.72×10^{52}
091029A	2.752	A	156		Fermi	1020	20	5.15×10^{52}	1.01×10^{52}
091024A	1.092	A	155		Swift	38.92	21	6.85×10^{52}	1.81×10^{52}	1.60	1.09 ± 0.06
091020A	1.71	A	154		Swift	4.37	21	7.07×10^{51}	4.18×10^{51}	2.31	1.39 ± 0.12
091003A	0.8969	E	153		Fermi	20.2 ± 0.4	35	7.17×10^{52}	2.93×10^{52}
090927A	1.37	A	176		Swift	2.16	21	1.83×10^{51}	4.59×10^{51}	1.48	...
090926B	1.2427	E	275		Swift	99.28	21	4.48×10^{52}	3.89×10^{51}	1.50	1.10 ± 0.05
090926A	2.1062	E	180		Fermi	13.8 ± 0.3	35	1.98×10^{54}	6.55×10^{53}
090902B	1.822	A	175		Fermi	19.3 ± 0.3	35	3.05×10^{54}	7.80×10^{53}
090814A	0.696	A	174		Swift	78.22	21	3.68×10^{51}	2.11×10^{50}
090812A	2.452	A	173		Swift	75.09	21	4.45×10^{53}	8.14×10^{52}	1.50	1.11 ± 0.1
090809A	2.737	A	172		Swift	7.84	21	2.48×10^{52}	2.16×10^{52}	1.30	...
090726A	2.71	A	171		Swift	56.68	21	3.17×10^{52}	5.41×10^{51}
090715B	3.00	A	170		Swift	265.39	21	2.10×10^{53}	8.12×10^{52}	1.56	1.09 ± 0.07
090709A	1.7 ± 0.6	P	237		Swift	88.73	21	4.09×10^{52}	2.46×10^{51}	2.50	1.27 ± 0.03
090618A	0.54	A	169		Swift	113.34	21	2.80×10^{53}	1.26×10^{52}	7.50	1.23 ± 0.03
090530A	1.266	A	257		Swift	40.46	21	1.27×10^{52}	5.33×10^{51}	1.50	1.31 ± 0.09
090529A	2.625	A	168		Swift	> 70	21	2.19×10^{52}	3.00×10^{51}
090519A	3.85	A	167		Swift	58.26	21	2.66×10^{53}	1.03×10^{53}
090516A	4.109	A	166		Swift	208.00	21	7.31×10^{53}	8.66×10^{52}
090424A	0.544	E	163		Swift	49.47	21	4.14×10^{52}	1.65×10^{52}	11.25	1.18 ± 0.11
090423A	8.23	A	178		Swift	9.77	21	7.89×10^{52}	1.14×10^{53}	1.31	1.22 ± 0.11
090418A	1.608	A	161		Swift	56.31	21	1.62×10^{53}	1.24×10^{52}
090417B	0.345	E	162		Swift	282.49	21	1.57×10^{51}	1.69×10^{49}
090407A	1.4478	E	275		Swift	315.44	21	1.41×10^{52}	1.45×10^{51}	1.14	1.07 ± 0.07
090328A	0.7357	E	196		Fermi	61.7 ± 1.8	35	9.23×10^{52}	1.36×10^{52}
090323A	3.5832	E	275		Fermi	135.2 ± 1.4	35	3.96×10^{54}	3.24×10^{53}
090313A	3.375	A	160		Swift	70.66	21	6.80×10^{52}	1.16×10^{52}
090205A	4.6497	A	159		Swift	8.80	21	1.54×10^{52}	1.35×10^{52}	1.19	...
090201A	2.1000	E	275		Swift	84.78	21	8.00×10^{53}	2.70×10^{53}	2.00	1.20 ± 0.14
090113A	1.7494	E	275		Swift	9.10	21	1.66×10^{52}	1.25×10^{52}	1.50	1.19 ± 0.16
090102A	1.547	A	158		Swift	29.30	21	2.35×10^{53}	4.80×10^{52}
081222A	2.77	A	146		Swift	33.00	21	2.40×10^{53}	1.22×10^{53}	2.31	1.20 ± 0.12
081221A	2.2590	E	275		Swift	33.91	21	3.95×10^{53}	8.30×10^{52}	3.75	1.20 ± 0.16
081210A	2.0631	E	275		Swift	145.91	21	6.71×10^{52}	2.47×10^{52}	1.45	1.22 ± 0.06
081203A	2.05	A	177		Swift	223.00	21	3.38×10^{53}	3.27×10^{52}	1.50	1.16 ± 0.12
081121A	2.512	A	145		Swift	17.67	21	2.84×10^{53}	8.65×10^{52}	1.14	1.11 ± 0.34
081118A	2.58	A	144		Swift	49.28	21	3.80×10^{52}	4.12×10^{51}
081109A	0.9785	E	275		Swift	221.49	21	3.31×10^{52}	3.46×10^{51}	1.31	1.07 ± 0.1
081029A	3.8479	A	143		Swift	275.05	21	2.03×10^{53}	2.03×10^{52}

Table 9 (cont'd)

GRB	redshift			Detector	T_{90} [s]	Ref (7)	$E_{\gamma, \text{iso}}$ [erg]	$L_{\text{p,iso}}$ [erg s $^{-1}$]	f	f_{eff}
	(1)	(2)	method (3)							
081028A	3.038	A	142	Swift	284.42	21	3.51×10^{53}	1.71×10^{52}
081008A	1.967	A	141	Swift	179.52	21	1.30×10^{53}	1.33×10^{52}	1.31	1.16 ± 0.25
081007A	0.5295	E	140	Swift	9.01	21	1.48×10^{51}	4.53×10^{50}	1.35	1.26 ± 0.03
080928A	1.6919	A	152	Swift	233.66	21	1.37×10^{52}	1.02×10^{52}	1.38	1.22 ± 0.07
080916C	4.35	P	194	Fermi	63.0 ± 0.8	35	2.72×10^{54}	7.01×10^{53}
080916A	0.6887	A	152	Swift	61.35	21	1.81×10^{52}	2.55×10^{51}	1.50	1.15 ± 0.03
080913A	6.7	A	152	Swift	7.46	21	6.37×10^{52}	1.25×10^{53}	1.26	1.19 ± 0.09
080905B	2.3739	A	152	Swift	101.62	21	4.69×10^{52}	1.78×10^{52}	1.26	1.12 ± 0.09
080810A	3.3604	A	152	Swift	107.67	21	3.54×10^{53}	1.05×10^{53}
080805A	1.5052	E	275	Swift	106.62	21	4.46×10^{52}	4.13×10^{51}	1.23	1.12 ± 0.14
080804A	2.2059	E	275	Swift	37.19	21	1.55×10^{53}	4.29×10^{52}	1.50	1.10 ± 0.11
080721A	2.5914	A	152	Swift	176.29	21	1.20×10^{54}	1.00×10^{54}	4.81	1.34 ± 0.07
080710A	0.8454	A	152	Swift	112.06	21	9.34×10^{51}	1.05×10^{51}	1.11	1.10 ± 0.01
080707A	1.2322	A	152	Swift	30.17	21	4.79×10^{51}	1.54×10^{51}	1.25	1.11 ± 0.21
080607A	3.0368	A	152	Swift	78.86	21	1.76×10^{54}	2.13×10^{54}	5.60	1.20 ± 0.07
080605A	1.6408	E	275	Swift	18.05	21	2.31×10^{53}	3.24×10^{53}	1.42	1.11 ± 0.43
080604A	1.4171	A	152	Swift	69.16	21	9.49×10^{51}	8.55×10^{50}
080603B	2.6892	A	152	Swift	59.12	21	9.56×10^{52}	1.18×10^{53}	1.65	1.11 ± 0.19
080603A	1.688	A	138	INTEGRAL	150	43	1.88×10^{52}	2.39×10^{51}
080602A	1.8204	E	275		Swift	74.29	21	8.73×10^{52}	5.97×10^{52}	1.25
080520A	1.5457	E	152	Swift	3.32	21	1.35×10^{51}	1.71×10^{51}	1.32	...
080517A	0.089	E	277	Swift	64.61	21	3.37×10^{49}	3.29×10^{48}
080515A	2.47	E	281	Swift	20.91	21	5.43×10^{52}	2.22×10^{52}	1.12	1.07 ± 0.34
080430A	0.767	A	137	Swift	14.15	21	4.57×10^{51}	1.34×10^{51}	1.46	1.12 ± 0.12
080413B	1.1012	E	275	Swift	8.00	21	2.37×10^{52}	2.15×10^{52}	2.38	1.53 ± 0.16
080413A	2.4330	A	152	Swift	46.36	21	1.74×10^{53}	5.98×10^{52}	1.75	1.13 ± 0.06
080411A	1.0301	A	152	Swift	56.33	21	2.35×10^{53}	9.71×10^{52}	6.85	1.13 ± 0.03
080330A	1.5119	A	152	Swift	67.05	21	5.77×10^{51}	2.10×10^{51}	1.19	1.11 ± 0.23
080325A	1.78	E	237	Swift	162.82	21	9.60×10^{52}	6.02×10^{51}
080319C	1.9492	A	152	Swift	29.55	21	1.36×10^{53}	8.98×10^{52}	1.52	1.09 ± 0.34
080319B	0.9382	A	152	Swift	124.86	21	1.33×10^{54}	9.80×10^{52}	8.00	1.11 ± 0.27
080310A	2.4274	A	152	Swift	352.37	21	7.43×10^{52}	7.97×10^{51}	1.19	1.07 ± 0.07
080210A	2.6419	A	152	Swift	39.36	21	6.33×10^{52}	1.54×10^{52}	1.23	1.09 ± 0.03
080207A	2.0856	E	275	Swift	340	42	1.56×10^{53}	5.80×10^{51}
080129A	4.349	A	151	Swift	50.22	21	1.20×10^{53}	1.27×10^{52}
071122A	1.14	A	131	Swift	80.00	21	4.62×10^{51}	5.11×10^{50}
071117A	1.3308	E	152	Swift	6.07	21	4.09×10^{52}	1.09×10^{53}	2.40	1.44 ± 0.16
071112C	0.8227	A	152	Swift	15	42	4.14×10^{52}	1.83×10^{52}
071031A	2.692	A	152	Swift	150.49	21	3.79×10^{52}	4.25×10^{51}	1.12	1.07 ± 0.09
071021A	2.4515	E	275	Swift	228.72	21	4.30×10^{52}	6.24×10^{51}	1.12	1.09 ± 0.14
071020A	2.1462	A	152	Swift	4.30	21	9.38×10^{52}	2.31×10^{53}	2.25	...
071010B	0.947	A	129	Swift	36.13	21	1.72×10^{52}	6.24×10^{51}	2.25	1.35 ± 0.24
071010A	0.98	A	128	Swift	6.32	21	1.17×10^{51}	5.15×10^{50}	1.11	1.08 ± 0.29
071003A	1.60435	A	136	Swift	148.38	21	3.47×10^{53}	2.07×10^{53}	1.57	1.18 ± 0.11
070810A	2.17	A	127	Swift	9.04	21	1.57×10^{52}	9.36×10^{51}	1.40	1.18 ± 0.14
070802A	2.4538	E	275	Swift	15.80	21	8.61×10^{51}	3.15×10^{51}
070721B	3.6298	A	152	Swift	336.86	21	4.48×10^{53}	9.14×10^{52}	1.38	1.10 ± 0.16
070714A	1.58	E	281	Swift	3.00	21	2.95×10^{51}	4.61×10^{51}	1.50	1.50 ± 0.21
070612A	0.617	E	125	Swift	365.28	21	2.95×10^{52}	6.57×10^{50}	1.12	1.10 ± 0.06
070611A	2.0394	A	152	Swift	13.18	21	9.92×10^{51}	5.04×10^{51}	1.14	1.09 ± 0.12
070529A	2.4996	A	124	Swift	108.90	21	1.52×10^{53}	2.61×10^{52}
070521A	2.0865	E	275	Swift	38.63	21	2.47×10^{53}	1.74×10^{53}	2.29	1.22 ± 0.05
070518A	1.161	E	281	Swift	4.35	21	1.23×10^{51}	6.73×10^{50}	1.20	1.12 ± 0.1
070508A	0.82	E	123	Swift	20.90	21	9.60×10^{52}	3.65×10^{52}	4.38	1.17 ± 0.25
070506A	2.3090	A	152	Swift	4.35	21	6.11×10^{51}	7.10×10^{51}	1.33	...
070419B	1.9586	E	275	Swift	238.14	21	1.78×10^{53}	8.21×10^{51}	1.24	1.09 ± 0.16

Table 9 (cont'd)

GRB	redshift			Detector	T_{90} [s]	Ref (7)	$E_{\gamma, \text{iso}}$ [erg]	$L_{p, \text{iso}}$ [erg s $^{-1}$]	f	f_{eff}
	(1)	(2)	method (3)							
070419A	0.9705	A	152	Swift	160.00	21	4.19×10^{51}	8.63×10^{49}
070411A	2.9538	A	152	Swift	102.04	21	1.18×10^{53}	1.22×10^{52}	1.11	1.07 ± 0.09
070328A	2.0627	E	275	Swift	72.12	21	5.29×10^{53}	1.24×10^{53}	1.73	1.23 ± 0.14
070318A	0.8401	E	275	Swift	131.52	21	1.79×10^{52}	2.03×10^{51}	1.32	1.09 ± 0.11
070306A	1.4965	E	275	Swift	209.24	21	7.91×10^{52}	1.19×10^{52}	1.38	1.09 ± 0.24
070224A	1.9922	E	275	Swift	48.00	21	7.66×10^{51}	1.40×10^{51}	1.11	1.09 ± 0.29
070223A	1.6295	E	280	Swift	100.00	21	2.49×10^{52}	1.89×10^{51}
070208A	1.165	E	122	Swift	64.00	21	3.40×10^{51}	9.97×10^{50}	1.16	1.09 ± 0.01
070129A	2.3384	E	275	Swift	459.05	21	7.90×10^{52}	3.12×10^{51}
070125A	1.547	A	152	Konus-Wind	70	14	9.21×10^{53}	3.03×10^{53}
070110A	2.3523	E	275	Swift	79.71	21	5.79×10^{52}	5.93×10^{51}
070103A	2.6208	E	275	Swift	18.40	21	1.09×10^{52}	8.07×10^{51}
061222B	3.355	A	110	Swift	37.25	21	1.08×10^{53}	1.81×10^{52}
061222A	2.088	E	149	Swift	96.00	21	3.11×10^{53}	2.04×10^{53}	2.62	1.55 ± 0.32
061202A	2.2543	E	275	Swift	94.19	21	1.14×10^{53}	2.25×10^{52}	1.43	1.09 ± 0.43
061126A	1.1588	E	135	Swift	50.28	21	9.05×10^{52}	6.17×10^{52}	2.12	1.27 ± 0.19
061121A	1.3145	A	152	Swift	81.22	21	2.64×10^{53}	1.38×10^{53}	4.81	1.35 ± 0.16
061110B	3.4344	A	152	Swift	132.76	21	2.48×10^{53}	3.50×10^{52}
061110A	0.7578	E	275	Swift	44.51	21	4.64×10^{51}	2.09×10^{50}	1.32	1.07 ± 0.29
061021A	0.3453	E	275	Swift	43.80	21	5.45×10^{51}	2.03×10^{51}	2.06	1.28 ± 0.34
061007A	1.2622	A	107	Swift	75.74	21	9.84×10^{53}	1.74×10^{53}	3.62	1.20 ± 0.16
060927A	5.4636	A	119	Swift	22.42	21	1.10×10^{53}	1.21×10^{53}	1.46	1.11 ± 0.12
060926A	3.2090	E	275	Swift	7.79	21	1.39×10^{52}	1.59×10^{52}	1.21	...
060923B	1.5094	E	275	Swift	8.95	21	7.85×10^{51}	2.98×10^{51}
060923A	2.6	P	237	Swift	51.54	21	3.22×10^{52}	1.41×10^{52}	1.25	1.09 ± 0.23
060912A	0.9362	E	275	Swift	5.03	21	7.62×10^{51}	7.21×10^{51}	1.94	1.40 ± 0.34
060908A	1.8836	A	216	Swift	18.78	21	6.33×10^{52}	1.61×10^{52}	1.60	1.12 ± 0.1
060906A	3.6856	A	152	Swift	44.58	21	1.22×10^{53}	3.22×10^{52}
060904B	0.7029	E	152	Swift	171.90	21	6.15×10^{51}	1.33×10^{51}	1.50	1.19 ± 0.07
060814A	1.9223	E	275	Swift	144.95	21	3.51×10^{53}	8.12×10^{52}	2.15	1.11 ± 0.09
060805A	2.3633	E	275	Swift	4.93	21	2.00×10^{51}	2.03×10^{51}
060729A	0.5429	E	275	Swift	113.04	21	4.86×10^{51}	2.55×10^{50}	1.27	1.10 ± 0.16
060719A	1.5318	E	275	Swift	66.86	21	1.92×10^{52}	4.79×10^{51}	1.38	1.11 ± 0.27
060714A	2.7108	A	94	Swift	116.04	21	9.66×10^{52}	1.09×10^{52}
060707A	3.4246	E	275	Swift	66.65	21	7.50×10^{52}	1.50×10^{52}	1.16	1.07 ± 0.14
060614A	0.125	E	112	Swift	5/106	40	2.13×10^{51}	2.63×10^{50}	2.56	2.26 ± 0.23
060607A	3.0749	A	134	Swift	102.98	21	1.72×10^{53}	3.47×10^{52}	1.25	1.07 ± 0.11
060605A	3.773	A	148	Swift	539.12	21	5.43×10^{52}	1.43×10^{52}	1.21	1.11 ± 0.24
060604A	2.1355	E	275	Swift	96.00	21	9.14×10^{51}	1.55×10^{51}
060602A	0.787	E	130	Swift	74.68	21	1.54×10^{52}	6.32×10^{50}
060526A	3.2213	A	103	Swift	275.20	21	5.63×10^{52}	2.02×10^{52}	1.35	1.09 ± 0.29
060522A	5.11	A	102	Swift	69.12	21	1.35×10^{53}	3.31×10^{52}
060512A	0.4428	E	104	Swift	11.36	21	3.25×10^{50}	9.73×10^{49}	1.15	1.07 ± 0.11
060510B	4.9	A	101	Swift	262.95	21	3.59×10^{53}	2.39×10^{52}
060505A	0.0889	E	117	Swift	4	42	9.24×10^{49}	2.51×10^{49}	1.58	1.27 ± 0.25
060502A	1.5026	A	152	Swift	28.54	21	4.93×10^{52}	8.96×10^{51}	1.31	1.10 ± 0.32
060418A	1.4901	A	114	Swift	109.17	21	1.16×10^{53}	1.77×10^{52}	1.94	1.31 ± 0.29
060319A	1.172	E	237	Swift	8.91	21	2.30×10^{51}	1.14×10^{51}	1.24	1.16 ± 0.16
060306A	1.5597	E	275	Swift	60.94	21	2.97×10^{52}	1.57×10^{52}	2.25	1.51 ± 0.12
060223A	4.406	A	120	Swift	11.32	21	5.53×10^{52}	4.46×10^{52}	1.45	1.20 ± 0.05
060218A	0.03351	E	97	Swift	2100	42	9.33×10^{48}	8.65×10^{46}
060210A	3.9122	A	152	Swift	242.18	21	6.49×10^{53}	9.50×10^{52}	1.58	1.16 ± 0.1
060206A	4.0559	A	152	Swift	7.55	21	5.56×10^{52}	6.63×10^{52}	1.56	...
060204B	2.3393	E	275	Swift	139.46	21	8.31×10^{52}	9.76×10^{51}	1.26	1.07 ± 0.07
060202A	0.785	E	237	Swift	172.16	21	8.66×10^{51}	2.88×10^{50}
060124A	2.3	A	152	Swift	658.2	21	2.11×10^{53}	1.29×10^{53}	3.38	1.34 ± 0.2

Table 9 (cont'd)

GRB	redshift				Detector	T_{90} [s]	Ref (7)	$E_{\gamma,\text{iso}}$ [erg]	$L_{\text{p},\text{iso}}$ [erg s $^{-1}$]	f	f_{eff}
	(1)	z (2)	method (3)	Ref (4)							
060123A	0.56	E	281	Swift	900	42	5.43×10^{50}	7.77×10^{48}
060115A	3.5328	A	152	Swift	122.21	21	1.47×10^{53}	2.67×10^{52}	1.15	1.07 ± 0.07	
060111A	2.32	E	281	Swift	13.21	21	3.18×10^{52}	1.17×10^{52}	1.53	1.14 ± 0.16	
051117B	0.4805	E	275	Swift	9.01	21	3.34×10^{50}	1.07×10^{50}	1.15	1.08 ± 0.29	
051111A	1.55	A	98	Swift	64.00	21	1.12×10^{53}	1.65×10^{52}	1.34	1.07 ± 0.01	
051109B	0.080	E	106	Swift	13.38	21	6.78×10^{48}	1.13×10^{48}	1.16	1.08 ± 0.21	
051109A	2.346	A	88	Swift	37.20	21	8.28×10^{52}	4.02×10^{52}	1.44	1.12 ± 0.32	
051022A	0.8061	E	275	HETE-2	178 ± 8	16	6.06×10^{53}	4.19×10^{52}
051016B	0.9358	E	275	Swift	4.02	21	9.49×10^{50}	8.75×10^{50}	1.30	1.15 ± 0.43	
051008A	$2.77^{+0.15}_{-0.2}$	P	274	Swift	64.0	21	6.22×10^{53}	2.31×10^{53}	1.81	1.17 ± 0.16	
051006A	1.059	E	215	Swift	26.04	21	1.29×10^{52}	2.71×10^{51}	1.27	1.08 ± 0.29	
051001A	2.4295	E	275	Swift	190.63	21	4.94×10^{52}	2.97×10^{51}	1.10	1.06 ± 0.34	
050922C	2.1992	A	94	Swift	4.54	21	9.53×10^{52}	1.88×10^{53}	3.29
050915A	2.5275	E	275	Swift	53.42	21	4.84×10^{52}	1.48×10^{52}	1.26	1.07 ± 0.06	
050908A	3.3467	A	152	Swift	18.29	21	2.34×10^{52}	1.03×10^{52}	1.12	1.07 ± 0.23	
050904A	6.295	A	111	Swift	181.70	21	1.23×10^{54}	1.03×10^{53}
050826A	0.296	E	116	Swift	35.73	21	6.27×10^{50}	6.77×10^{49}	1.14	1.07 ± 0.34	
050824A	0.8277	E	275	Swift	24.82	21	1.72×10^{51}	3.23×10^{50}
050822A	1.434	E	215	Swift	104.12	21	3.25×10^{52}	3.96×10^{51}	1.29	1.10 ± 0.1	
050820A	2.61469	A	121	Swift	26	42	2.59×10^{53}	5.98×10^{52}	1.32	1.14 ± 0.2	
050819A	2.5042	E	275	Swift	37.72	21	1.73×10^{52}	3.60×10^{51}
050814A	5.3 ± 0.3	P	91	Swift	144.00	21	1.98×10^{53}	3.25×10^{52}
050802A	1.7102	A	152	Swift	27.46	21	4.41×10^{52}	1.38×10^{52}	1.18	1.08 ± 0.03	
050730A	3.96855	A	85	Swift	145.05	21	2.06×10^{53}	1.98×10^{52}	1.16	1.08 ± 0.03	
050714B	2.4383	E	275	Swift	46.87	21	1.43×10^{52}	3.16×10^{51}
050525A	0.6063	E	275	Swift	8.84	21	2.84×10^{52}	1.93×10^{52}	9.38	1.83 ± 0.11	
050505A	4.2748	A	96	Swift	58.88	21	2.90×10^{53}	9.86×10^{52}
050502A	3.793	A	86	Swift	17.5 ± 0.2	12	9.17×10^{52}	6.32×10^{52}
050416A	0.6542	E	275	Swift	6.62	21	1.22×10^{51}	9.77×10^{50}	1.54
050408A	1.2356	E	84	HETE-2	28.39 ± 0.56	16	2.33×10^{52}
050401A	2.8983	A	100	Swift	33.30	21	4.20×10^{53}	2.08×10^{53}	1.51	1.10 ± 0.14	
050319A	3.2425	A	152	Swift	151.74	21	5.92×10^{52}	1.85×10^{52}	1.19	1.12 ± 0.19	
050318A	1.4436	A	84	Swift	40.0	21	1.23×10^{52}	5.62×10^{51}	1.56	1.17 ± 0.16	
050315A	1.9500	A	84	Swift	95.57	21	6.34×10^{52}	6.76×10^{51}	1.32	1.08 ± 0.29	
050223A	0.584	E	93	Swift	21.68	21	4.36×10^{51}	3.18×10^{50}
050219A	0.211	E	261	Swift	23.84	21	1.05×10^{51}	9.69×10^{49}	1.75	1.18 ± 0.34	
050215B	2.62	E	281	Swift	10.62	21	6.95×10^{51}	6.38×10^{51}
050126A	1.29002	E	82	Swift	48.00	21	1.59×10^{52}	2.73×10^{51}
041219A	0.31 ± 0.26	P	214	Swift	520	42	6.88×10^{52}	3.74×10^{51}
041006A	0.716	E	95	HETE-2	22.08 ± 0.33	16	2.11×10^{52}
040924A	0.858	E	133	HETE-2	3.37 ± 0.08	16	9.21×10^{51}	2.09×10^{52}
040912A	1.563	E	113	HETE-2	9.21 ± 0.27	16	8.47×10^{51}
031203A	0.1055	E	78	HETE-2	10.38 ± 0.29	16	6.84×10^{49}	1.78×10^{49}
030528A	0.782	E	80	HETE-2	62.8 ± 4.49	16	2.22×10^{52}	1.25×10^{51}
030429A	2.658	A	75	HETE-2	12.95 ± 2.69	16	1.70×10^{52}	7.47×10^{51}
030329A	0.1685	E	73	HETE-2	25.91 ± 0.39	16	1.55×10^{52}	1.65×10^{51}
030328A	1.5216	A	92	HETE-2	138.27 ± 3.05	16	3.59×10^{53}	1.40×10^{52}
030323A	3.3736	E	74	HETE-2	26	10	4.14×10^{52}	3.54×10^{52}
030226A	1.986	A	76	HETE-2	76.23 ± 3.96	16	7.46×10^{52}	5.76×10^{51}
030115A	2	P	259	HETE-2	20.33 ± 3.54	16	3.01×10^{52}	1.11×10^{52}
021211A	1.006	E	72	HETE-2	4.23 ± 0.27	16	1.34×10^{52}	8.62×10^{51}
021004A	2.3351	E	56	HETE-2	48.94 ± 2.5	16	4.33×10^{52}	6.68×10^{51}
020903A	0.251	E	77	HETE-2	3.3	9	2.03×10^{49}	6.36×10^{48}
020819B	0.41	E	81	Ulysses	20	8	1.62×10^{52}	2.05×10^{51}
020813A	1.255	E	67	HETE-2	87.34 ± 0.6	16	1.34×10^{54}	7.36×10^{52}
020427A	BeppoSAX	66	7	1.52×10^{52}	2.35×10^{51}

Table 9 (cont'd)

GRB	redshift				Detector	T_{90} [s]	Ref	$E_{\gamma, \text{iso}}$ [erg]	$L_{\text{p}, \text{iso}}$ [erg s $^{-1}$]	f	f_{eff}
	(1)	z (2)	method (3)	Ref (4)							
020410A ^a	BeppoSAX	1500	11	3.10×10^{52}	1.66×10^{50}
020405A	0.6908	E	65	BeppoSAX	40.0 ± 2.2	18	1.07×10^{53}	1.38×10^{52}	
020331A	HETE-2	179.4 ± 5.99	16	9.31×10^{52}	8.32×10^{51}	
020322A	BeppoSAX	11.0 ± 2.8	18	2.30×10^{52}	1.82×10^{52}	
020305A	2.8	P	79	HETE-2	39.06 ± 1.17	16	3.09×10^{53}	1.25×10^{53}	
020127A	1.9	P	115	HETE-2	6.99 ± 0.26	16	3.36×10^{52}	1.43×10^{52}	
020124A	3.198	A	70	HETE-2	51.17 ± 1.55	16	2.09×10^{53}	5.33×10^{52}	
011211A	2.14	A	57	BeppoSAX	51.0 ± 7.6	18	3.23×10^{52}	2.63×10^{51}	
011121A	0.36	E	71	BeppoSAX	47.0 ± 3.2	18	6.42×10^{52}	5.86×10^{51}	
011030A	< 3	P	63	BeppoSAX	1400	6	1.35×10^{53}	3.37×10^{51}	
010921A	0.4509	E	58	BeppoSAX	22.0 ± 3.6	18	1.51×10^{52}	1.70×10^{51}	
010222A	1.47688	A	61	BeppoSAX	74.0 ± 4.1	18	1.36×10^{54}	3.13×10^{53}	
000926A	2.0379	A	68	BeppoSAX	1.30 ± 0.59	18	7.66×10^{51}	1.93×10^{52}	
000911A	1.0585	E	59	Uly/Ko/NE	500	4	6.53×10^{53}	1.17×10^{53}	
000418A	1.1181	E	66	BeppoSAX	2.0 ± 1.3	18	1.09×10^{51}	1.16×10^{51}	
000301C	2.0404	A	53	BeppoSAX	87.0 ± 4.2	18	1.41×10^{53}	5.82×10^{51}	
000210A	0.846	E	60	BeppoSAX	9.0 ± 1.4	18	1.54×10^{53}	9.74×10^{52}	
000131A	4.5	A	51	Uly/Ko/NE	50	3	1.61×10^{54}	4.14×10^{53}	
991216A	1.02	A	49	BeppoSAX	45.0 ± 5.7	18	6.00×10^{53}	3.33×10^{53}	
991208A	0.7063	E	52	Uly/Ko/NE	60	2	2.66×10^{53}	4.73×10^{52}	
990712A	0.4331	E	54	BeppoSAX	38.0 ± 3.2	18	8.21×10^{51}	2.35×10^{51}	
990705A	0.8424	E	62	BeppoSAX	32.0 ± 1.4	18	2.49×10^{53}	2.26×10^{52}	
990510A	1.619	A	54	BeppoSAX	57.0 ± 3.2	18	1.96×10^{53}	6.68×10^{52}	
990506A	1.30658	E	66	BeppoSAX	129.0 ± 1.4	18	8.66×10^{53}	1.00×10^{53}	
990308A	BATSE	106 ± 12	1	6.32×10^{52}	5.14×10^{52}	
990123A	1.6004	A	50	BeppoSAX	61.0 ± 2.8	18	3.90×10^{54}	5.75×10^{53}	
981226A	1.11 ± 0.06	P	83	BeppoSAX	17.0 ± 5.8	18	5.50×10^{51}	7.40×10^{50}	
980703A	0.966	E	45	BeppoSAX	76.0 ± 10.2	18	1.33×10^{53}	1.17×10^{52}	
980613A	1.0969	E	69	BeppoSAX	42.0 ± 22.1	18	5.94×10^{51}	1.99×10^{51}	
980519A	BeppoSAX	33.0 ± 3.2	18	1.64×10^{53}	2.55×10^{53}	
980425A	0.0085	E	46	BeppoSAX	22.0 ± 4.5	18	9.40×10^{47}	4.71×10^{46}	
980329A	3.5	P	64	BeppoSAX	19.0 ± 2.2	18	2.41×10^{54}	5.18×10^{53}	
980326A	BeppoSAX	312.0 ± 8.1	18	1.77×10^{52}	1.73×10^{52}	
971214A	3.42	E	47	BeppoSAX	6.0 ± 3.2	18	2.87×10^{53}	9.80×10^{52}	
970828A	0.9578	E	55	BATSE	146.59	5	3.00×10^{53}	2.45×10^{52}	
970508A	0.835	A	44	BeppoSAX	14.0 ± 3.6	18	8.12×10^{51}	2.82×10^{51}	
970228A	0.695	E	48	BeppoSAX	56.0 ± 3.2	18	2.75×10^{52}	1.57×10^{52}	
SGRB											
130603B	0.356	E	246	Swift	0.18	42	2.02×10^{51}	4.15×10^{52}	
101224A	Swift	0.2	42	2.34×10^{50}	4.62×10^{50}	1.63	1.63 ± 0.43	
101219A	0.718	E	198	Swift	0.6	42	4.49×10^{51}	6.00×10^{52}	2.75	2.75 ± 0.45	
100816A	0.8048	E	275	Swift	2.9	42	7.93×10^{51}	9.02×10^{51}	2.62	1.52 ± 0.03	
100625A	0.452	HA	234	Swift	0.33	42	9.17×10^{50}	1.65×10^{51}	2.63	2.63 ± 0.26	
100206A	0.4068	E	217	Swift	0.12	42	5.81×10^{50}	7.86×10^{50}	2.70	2.70 ± 0.26	
100117A	0.92	E	195	Swift	0.3	42	1.32×10^{51}	2.22×10^{51}	2.28	2.28 ± 0.21	
091109B	Swift	0.27	21	6.87×10^{51}	1.04×10^{52}	4.93	4.93 ± 0.65	
090515A	Swift	0.04	21	2.90×10^{49}	9.94×10^{50}	2.58	2.58 ± 0.32	
090510A	0.903	E	165	Swift	5.66	21	2.83×10^{52}	5.57×10^{52}	5.00	5.00 ± 0.55	
090426A	2.609	HA	164	Swift	1.24	21	5.50×10^{51}	1.88×10^{52}	2.61	1.48 ± 0.15	
090305A	Swift	0.35	21	2.17×10^{51}	3.68×10^{51}	1.48	1.48 ± 0.16	
080905A	0.1218	E	193	Swift	1.02	21	4.30×10^{49}	3.05×10^{49}	1.85	1.85 ± 0.15	
080503A	Swift	0.32 ± 0.07	17	1.97	1.53 ± 0.18	
080123A	0.495	...	181	Swift	0.04	21	7.43×10^{50}	2.09×10^{50}	
071227A	0.383	E	132	Swift	1.8/100	40	1.04×10^{51}	3.16×10^{51}	3.00	2.80 ± 0.23	
070809A	0.2187	E	139	Swift	1.28	21	3.18×10^{49}	4.08×10^{49}	1.42	1.42 ± 0.25	
070724A	0.457	E	126	Swift	0.43	21	3.68×10^{49}	5.88×10^{49}	1.53	1.53 ± 0.12	

Table 9 (cont'd)

GRB	redshift			Detector	T_{90} [s]	Ref	$E_{\gamma,\text{iso}}$ [erg]	$L_{p,\text{iso}}$ [erg s $^{-1}$]	f	f_{eff}
	(1)	z	method							
070714B	0.923	E	147	Swift	3/100	40	8.36×10^{51}	6.15×10^{51}	2.94	2.54 ± 0.34
070707A	INTEGRAL	0.8	15	6.88×10^{50}	1.03×10^{51}
070429B	0.904	E	147	Swift	0.49	21	3.99×10^{50}	8.52×10^{50}	1.51	1.51 ± 0.19
061217A	0.827	E	118	Swift	0.24	21	2.34×10^{51}	1.69×10^{52}	1.74	1.74 ± 0.12
061210A	0.41	E	108	Swift	0.13/77	41	1.66×10^{51}	1.07×10^{51}	8.13	7.83 ± 0.38
061201A	0.111	E	109	Swift	0.78	21	1.96×10^{50}	1.31×10^{51}	4.67	4.67 ± 0.67
061006A	0.4377	E	118	Swift	0.5/120	40	2.32×10^{51}	1.99×10^{52}	6.01	5.41 ± 0.32
060801A	1.131	E	150	Swift	0.50	21	2.35×10^{52}	8.96×10^{52}	2.19	2.19 ± 0.35
060502B	0.287	E	105	Swift	0.14	21	2.18×10^{50}	3.55×10^{50}	2.33	2.33 ± 0.24
060313A	Swift	0.74	21	1.28×10^{52}	9.44×10^{52}	4.94	4.94 ± 0.43
060121A	HETE-2	2.61 ± 0.1	16	3.91×10^{51}	2.04×10^{52}
051221A	0.5465	E	99	Swift	1.40	21	3.12×10^{51}	6.94×10^{52}	7.00	7.00 ± 0.65
051210A	> 1.4	P	179	Swift	1.27	40	6.27×10^{51}	1.45×10^{52}	1.44	1.44 ± 0.18
050724A	0.258	HA	90	Swift	2.76	41	3.58×10^{50}	1.08×10^{50}	2.50	2.02 ± 0.19
050709A	0.16	E	89	HETE-2	0.22 ± 0.05	13	3.58×10^{49}	5.30×10^{50}
050509B	0.226	HA	87	Swift	0.02	21	6.99×10^{48}	2.20×10^{49}	1.84	1.84 ± 0.29

Note. — Col. (1) GRB name. Col. (2) redshift. Col. (3) Method of redshifts: (A)bsorption from afterglow, (E)mission lines from host galaxy and (P)hotometric redshift. Col. (4) Reference of redshift. Col. (5) Detector of T_{90} . Col. (6) Value of T_{90} . For SGRBs with extended emission (EE), the two values before and after the back slash are the durations without and with extended emission. Col. (7) Reference of T_{90} . Col. (8) Isotropic γ -ray energy in rest frame $1 - 10^4$ keV. $z = 2.0$ is assumed for LGRBs without redshifts and $z = 0.5$ is assumed for SGRBs without redshifts. Spectral parameters in Table 10 are used. Col. (9) γ -ray luminosity in rest frame $1 - 10^4$ keV. Col. (10) Amplitude f parameter, $\frac{F_p}{F_b}$. Col. (11) Effective f parameter, the f parameter by assuming a background making T_{90} to be 2 s.

^a $z = 0.5$ is assumed for LGRB 020410A, according to the possible detection of SN in Levan et al. (2005).

References. (1) Schaefer et al. (1999); (2) Hurley & Cline (1999); (3) Hurley et al. (2000a); (4) Hurley et al. (2000b); (5) Jimenez et al. (2001); (6) Heise et al. (2001); (7) in't Zand et al. (2002); (8) Hurley et al. (2002b); (9) Ricker et al. (2002); (10) Graziani et al. (2003); (11) Nicastro et al. (2004); (12) Cummings et al. (2005); (13) Villasenor et al. (2005); (14) Golenetskii et al. (2007a); (15) McGlynn et al. (2008); (16) Pélangeon et al. (2008); (17) Perley et al. (2009b); (18) Frontera et al. (2009); (19) Sakamoto et al. (2010); (20) Gruber et al. (2011); (21) Sakamoto et al. (2011b); (22) Golenetskii et al. (2011b); (23) Golenetskii et al. (2011k); (24) Golenetskii et al. (2012); (25) Gruber & Goldstein (2012); (26) Chaplin (2012); (27) Krimm et al. (2012); (28) Gendre et al. (2013); (29) Frederiks et al. (2013); (30) Xiong (2013); (31) Collazzi & Connaughton (2013); (32) Jenke (2013); (33) Younes (2013); (34) Greiner et al. (2014); (35) von Kienlin et al. (2014); (36) Jenke & Xiong (2014); (37) Golenetskii et al. (2014a); (38) Yu & Goldstein (2014); (39) Burns (2014); (40) Lü et al. (2015); (41) Kaneko et al. (2015); (42) Swift GRB table; (43) http://ibas.iasf-milano.inaf.it/IBAS_Results.html; (44) Galama et al. (1997); (45) Djorgovski et al. (1998); (46) Tinney et al. (1998); (47) Kulkarni et al. (1998); (48) Djorgovski et al. (1999); (49) Vreeswijk et al. (1999); (50) Kulkarni et al. (1999); (51) Andersen et al. (2000); (52) Castro-Tirado et al. (2001); (53) Jensen et al. (2001); (54) Vreeswijk et al. (2001); (55) Djorgovski et al. (2001); (56) Möller et al. (2002); (57) Holland et al. (2002); (58) Price et al. (2002a); (59) Price et al. (2002b); (60) Piro et al. (2002); (61) Mirabal et al. (2002); (62) Le Floch et al. (2002); (63) Fruchter et al. (2002); (64) Jaunsen et al. (2003); (65) Masetti et al. (2003); (66) Bloom et al. (2003a); (67) Barth et al. (2003); (68) Castro et al. (2003); (69) Djorgovski et al. (2003); (70) Hjorth et al. (2003b); (71) Greiner et al. (2003); (72) Vreeswijk et al. (2003); (73) Hjorth et al. (2003a); (74) Vreeswijk et al. (2004); (75) Jakobsson et al. (2004); (76) Klose et al. (2004); (77) Soderberg et al. (2004); (78) Prochaska et al. (2004); (79) Gorosabel et al. (2005); (80) Rau et al. (2005); (81) Jakobsson et al. (2005); (82) Berger et al. (2005c); (83) Christensen et al. (2005); (84) Berger et al. (2005a); (85) Chen et al. (2005); (86) Prochaska et al. (2005b); (87) Prochaska et al. (2005a); (88) Quimby et al. (2005); (89) Fox et al. (2005); (90) Berger et al. (2005b); (91) Jakobsson et al. (2006a); (92) Maiorano et al. (2006); (93) Pellizza et al. (2006); (94) Jakobsson et al. (2006b); (95) Soderberg et al. (2006a); (96) Berger et al. (2006); (97) Mirabal et al. (2006); (98) Penprase et al. (2006); (99) Soderberg et al. (2006c); (100) Watson et al. (2006); (101) Price (2006); (102) Cenko et al. (2006a); (103) Berger & Gladders (2006); (104) Bloom et al. (2006a); (105) Bloom et al. (2006b); (106) Perley et al. (2006); (107) Osip et al. (2006); (108) Cenko et al. (2006b); (109) Berger (2006a); (110) Berger (2006b); (111) Kawai et al. (2006); (112) Gal-Yam et al. (2006); (113) Stratta et al. (2007); (114) Vreeswijk et al. (2007); (115) Berger et al. (2007b); (116) Mirabal et al. (2007); (117) Ofek et al. (2007); (118) Berger et al. (2007d); (119) Ruiz-Velasco et al. (2007); (120) Chary et al. (2007); (121) Prochaska et al. (2007c); (122) Cucchiara et al. (2007c); (123) Jakobsson et al. (2007b); (124) Berger et al. (2007a); (125) Cenko et al. (2007b); (126) Cucchiara et al. (2007b); (127) Thoene et al. (2007); (128) Prochaska et al. (2007b); (129) Cenko et al. (2007a); (130) Jakobsson et al. (2007a); (131) Cucchiara et al. (2007a); (132) Berger et al. (2007c); (133) Wiersema et al. (2008); (134) Fox et al. (2008); (135) Perley et al. (2008d); (136) Perley et al. (2008c); (137) Cucchiara & Fox (2008); (138) Perley et al. (2008b); (139) Perley et al. (2008a); (140) Berger et al. (2008b); (141) Cucchiara et al. (2008a); (142) Berger et al. (2008a); (143) D'Elia et al. (2008a); (144) D'Elia et al. (2008b); (145) Berger & Rauch (2008); (146) Cucchiara et al. (2008b); (147) Cenko et al. (2008b); (148) Ferrero et al. (2009); (149) Perley et al. (2009c); (150) Berger (2009); (151) Greiner et al. (2009); (152) Fynbo et al. et al. (2009); (153) Cucchiara et al. (2009b); (154) Xu et al. (2009); (155) Cucchiara et al. (2009a); (156) Chornock et al. (2009d); (157) Perley et al. (2009a); (158) de Ugarte Postigo et al. (2009c); (159) Fugazza et al. (2009); (160) Chornock et al. (2009e); (161) Chornock et al. (2009a); (162) Berger & Fox (2009); (163) Chornock et al. (2009b); (164) Levesque et al. (2009); (165) Rau et al. (2009); (166) de Ugarte Postigo et al. (2009b); (167) Thoene et al. et al. (2009); (168) Malesani et al. (2009b); (169) Cenko et al. (2009); (170) Wiersema et al. (2009); (171) Fatkhullin et al. et al. (2009); (172) Malesani et al. (2009a); (173) de Ugarte Postigo et al. (2009a); (174) Jakobsson et al. (2009); (175) Cucchiara et al. (2009c); (176) Levan et al. (2009a); (177) Kuin et al. et al. (2009); (178) Tanvir et al. (2009b); (179) Fong et al. (2010); (180) Rau et al. (2010b); (181) Leibler & Berger (2010); (182) Rau et al. (2010a); (183) Groot et al. (2010); (184) Chornock et al. (2010b); (185) Vergani et al. (2010); (186) Cucchiara & Fox (2010); (187) Goldoni et al. et al. (2010); (188) Cenko et al. (2010); (189) Afonso et al. (2010); (190) Chornock et al. (2010a); (191) Tanvir et al. (2010a); (192) Flores et al. (2010); (193) Rowlinson et al. et al. (2010a); (194) Krühler et al. (2011a); (195) Fong et al. (2011); (196) Cenko et al. (2011c); (197) Sparre et al. (2011b); (198) Chornock & Berger (2011); (199) Chornock et al. (2011b); (200) Sparre et al. (2011a); (201) Cenko et al. (2011a); (202) Milne & Cenko (2011); (203) Cenko et al. (2011b); (204) de Ugarte Postigo et al. (2011a); (205) de Ugarte Postigo et al. (2011b); (206) Piranomonte et al. (2011); (207) Cucchiara et al. (2011a); (208) Tanvir et al. (2011); (209) Cabrera Lavers et al. (2011); (210) Levan et al. (2011); (211) Wiersema et al. (2011); (212) Chornock et al. (2011a); (213) Cucchiara et al. (2011b); (214) Götz et al. (2011); (215) Jakobsson et al. (2012); (216) Milvang-Jensen et al. (2012); (217) Perley et al. (2012a); (218) Tello et al. (2012); (219) Kruehler et al. (2012); (220) Cucchiara (2012); (221) Tanvir et al. (2012c); (222) Xu et al. (2012); (223) Greiner et al. (2012); (224) Cucchiara et al. (2012); (225) Tanvir & Ball (2012); (226) Tanvir et al. (2012a); (227) Thoene et al. (2012); (228) Sanchez-Ramirez et al. (2012); (229) Hartoog et al. (2012); (230) Knust et al. (2012); (231) Tanvir et al. (2012b); (232) Perley et al. (2012b); (233) Fynbo et al. (2012); (234) Fong et al. (2013); (235) Chornock et al. (2013a); (236) Kelly et al. (2013); (237) Perley et al. (2013); (238) Cucchiara & Fumagalli (2013); (239) Tanvir et al. (2013a); (240) Kruehler et al. (2013); (241) de Ugarte Postigo et al. (2013a); (242) Flores et al. (2013); (243) Tanvir et al. (2013c); (244) Cucchiara & Tanvir (2013); (245) Sanchez-Ramirez et al. (2013); (246) Cucchiara et al. (2013); (247) Cenko et al. (2013); (248) Smette et al. (2013); (249) Tanvir et al. (2013d); (250) Cucchiara & Perley (2013); (251) de Ugarte Postigo et al. (2013c); (252) Chornock et al. (2013b); (253) Rau et al. (2013); (254) Xu et al. (2013a); (255) de Ugarte Postigo et al. (2013b); (256) Hartoog et al. (2013); (257) Goldoni et al. (2013); (258) Cucchiara & Cenko (2013); (259) Hunt et al. (2014); (260) Jeong et al. (2014b); (261) Rossi et al. (2014); (262) Levan et al. (2014a); (263) Malesani et al. (2014b); (264) Jeong et al. (2014a); (265) Chornock et al. (2014c); (266) Tanvir et al. (2014a); (267) Tanvir et al. (2014b); (268) Tanvir et al. (2014c); (269) Perley (2014); (270) Malesani et al. (2014a); (271) Chornock et al. (2014a); (272) Chornock et al. (2014b); (273) de Ugarte Postigo et al. (2014a); (274) Volnova et al. (2014); (275) Krühler et al. (2015); (276) Cenko et al. (2015); (277) Stanway et al. (2015); (278) van der Horst et al. (2015); (279) Cano et al. (2015); (280) Perley et al. (2016); (281) Keck GRB Host project;

Table 10. prompt

GRB	Detector	fluence/flux	Γ	α	β	E_p [keV]	fluence S_γ [10^{-7} erg cm $^{-2}$]	Band		peak flux $F_p(P_p)$ Band (10)	reference (11)
								(5)	(8)		
140606B	Fermi	...	-1.24 $^{+0.05}_{-0.05}$	-2.20 $^{+0.52}_{-0.52}$	554 $^{+165}_{-165}$	75.9 ± 0.4	10 - 1000	13.2 $\pm 0.3^{\mathrm{P}}$	10 - 1000	103	
140518A	Swift	1.89	-0.98 $^{+0.64}_{-0.61}$...	47.9 $^{+12.7}_{-12.7}$	10 ± 1	15 - 150	1.0 $\pm 0.1^{\mathrm{P}}$	15 - 150	107	
140515A	Swift	1.78 ± 0.13	-0.98 $^{+0.53}_{-0.53}$...	56.4 $^{+31.3}_{-31.3}$	5.9 ± 0.6	15 - 150	0.9 $\pm 0.1^{\mathrm{P}}$	15 - 150	107	
140512A	Fermi	1.45 ± 0.04	-1.22 $^{+0.05}_{-0.05}$	-3.2 $^{+1.6}_{-1.6}$	682 $^{+70}_{-70}$	293 ± 0	10 - 1000	11.0 $\pm 0.3^{\mathrm{P}}$	10 - 1000	103, 107	
140508A	Fermi	...	-1.19 $^{+0.02}_{-0.02}$	-2.36 $^{+0.10}_{-0.10}$	263 $^{+14}_{-14}$	614 ± 1	10 - 1000	66.8 $\pm 1.0^{\mathrm{P}}$	10 - 1000	103	
140506A	Fermi	1.68 ± 0.16	-1.18 $^{+0.11}_{-0.11}$	-2.3 $^{+0.4}_{-0.4}$	197 $^{+32}_{-32}$	65.9 ± 1.2	10 - 1000	15.7 $\pm 0.7^{\mathrm{P}}$	10 - 1000	103, 107	
140430A	Swift	2.00 ± 0.22	11 ± 2	15 - 150	2.5 $\pm 0.2^{\mathrm{P}}$	15 - 150	107	
140428A	Swift	1.54 ± 0.26	3.4 ± 0.6	15 - 150	0.6 $\pm 0.2^{\mathrm{P}}$	15 - 150	107	
140423A	Fermi	1.33 ± 0.06	-0.58 $^{+0.12}_{-0.12}$	-1.83 $^{+0.05}_{-0.05}$	121 $^{+15}_{-15}$	180 ± 1	10 - 1000	2.99 $\pm 0.20^{\mathrm{P}}$	10 - 1000	103, 107	
140419A	KW	1.21 ± 0.04	-0.63 $^{+0.36}_{-0.22}$	-2.3 $^{+0.4}_{-2.5}$	293 ± 84	580 $^{+280}_{-190}$	20 - 10000	347 $^{+18}_{-19}$	20 - 10000	105, 107	
140318A	Swift	1.35 ± 0.28	2.9 ± 0.5	15 - 150	0.5 $\pm 0.2^{\mathrm{P}}$	15 - 150	107	
140311A	Swift	1.67 ± 0.23	23 ± 3	15 - 150	1.3 $\pm 0.5^{\mathrm{P}}$	15 - 150	107	
140304A	Fermi	1.29 ± 0.08	-0.80 $^{+0.22}_{-0.22}$	-2.35 $^{+0.43}_{-0.43}$	123 $^{+27}_{-27}$	24.3 ± 0.3	10 - 1000	2.69 $\pm 0.22^{\mathrm{P}}$	10 - 1000	103, 107	
140301A	Swift	1.96 ± 0.28	4.4 ± 0.8	15 - 150	0.7 $\pm 0.2^{\mathrm{P}}$	15 - 150	107	
140226A	KW	...	-1.1 ± 0.1	56 ± 11	20 - 10000	78.6 ± 1.7	20 - 10000	104	
140213A	Fermi	1.80 ± 0.04	-1.13 $^{+0.03}_{-0.03}$	-2.26 $^{+0.05}_{-0.05}$	86.6 $^{+3.6}_{-3.6}$	212 ± 0	10 - 1000	36.9 $\pm 0.5^{\mathrm{P}}$	10 - 1000	103, 107	
140206A	Fermi	1.51 ± 0.03	-0.06 $^{+0.10}_{-0.10}$	-2.35 $^{+0.07}_{-0.07}$	120 $^{+5}_{-5}$	155 ± 0	10 - 1000	17.4 $\pm 0.5^{\mathrm{P}}$	10 - 1000	103, 107	
140114A	Swift	2.06 ± 0.09	32 ± 1	15 - 150	0.9 $\pm 0.1^{\mathrm{P}}$	15 - 150	107	
131231A	Fermi	...	-1.21 ± 0.01	-2.3 ± 0.03	178 ± 4	1519 ± 1	10 - 1000	378.8 $\pm 0.6^{\mathrm{P}}$	10 - 1000	103	
131227A	Swift	1.36 ± 0.12	8.4 ± 0.6	15 - 150	1.1 $\pm 0.2^{\mathrm{P}}$	15 - 150	107	
131117A	Swift	1.81 ± 0.18	-0.17 $^{+1.61}_{-1.10}$...	44.4 $^{+10.4}_{-6.0}$	2.5 ± 0.4	15 - 150	0.7 $\pm 0.1^{\mathrm{P}}$	15 - 150	107	
131108A	Fermi	...	-0.91 $^{+0.02}_{-0.02}$	-2.46 $^{+0.15}_{-0.15}$	367 $^{+6.0}_{-17}$	356 ± 1	10 - 1000	19.7 $\pm 0.4^{\mathrm{P}}$	10 - 1000	103	
131105A	Fermi	1.45 ± 0.11	-1.26 $^{+0.03}_{-0.03}$	-2.33 ± 0.33	265 $^{+17}_{-17}$	237 ± 1	10 - 1000	8.4 $\pm 0.3^{\mathrm{P}}$	10 - 1000	103, 107	
131103A	Swift	1.97 ± 0.19	8.2 ± 1.0	15 - 150	1.5 $\pm 0.3^{\mathrm{P}}$	15 - 150	107	
131030A	KW	1.30 ± 0.03	-0.71 ± 0.12	-2.95 ± 0.28	177 ± 10	660 ± 40	20 - 10000	3100 ± 10	20 - 10000	101, 107	
131011A	Fermi	...	-0.88 ± 0.08	-2.08 ± 0.17	218 ± 32	88.8 ± 0.6	10 - 1000	4.67 ± 0.26	10 - 1000	103	
131004A	Fermi	1.81 ± 0.11	-1.36 $^{+0.17}_{-0.17}$	-22.1 $^{+0.0}_{-0.0}$	118 $^{+29}_{-29}$	5.1 ± 0.2	10 - 1000	6.8 $\pm 0.3^{\mathrm{P}}$	10 - 1000	103, 107	
130925A	Fermi	2.05 ± 0.04	-1.39 $^{+0.02}_{-0.02}$	-2.40 $^{+0.14}_{-0.14}$	15.4 $^{+3.7}_{-3.7}$	6.3 ± 0.3	10 - 1000	2.47 $\pm 0.27^{\mathrm{P}}$	10 - 1000	103, 107	
130907A	KW	1.17 ± 0.02	-0.91 ± 0.02	-2.42 ± 0.07	394 ± 11	7900 ± 500	20 - 10000	5220 ± 10	20 - 10000	100, 107	
130831A	KW	1.93 ± 0.05	-1.51 ± 0.1	-2.8 ± 0.1	67 ± 4	76 ± 4	20 - 10000	325 ± 3	20 - 10000	99, 107	
130702A	Fermi	...	-2.49 ± 0.03	10.4 ± 1.1	57.2 ± 1.2	10 - 1000	7.03 $\pm 0.86^{\mathrm{P}}$	10 - 1000	103		
130701A	KW	1.58 ± 0.04	-1.1 ± 0.1	...	58 ± 2	20 - 10000	343 ± 4	20 - 10000	98, 107		
130612A	Fermi	2.00 ± 0.25	-1.01 $^{+2.14}_{-2.14}$	-2.23 $^{+0.15}_{-0.15}$	26.4 $^{+6.8}_{-6.8}$	6.8 ± 0.6	10 - 1000	3.6 $\pm 0.2^{\mathrm{P}}$	10 - 1000	103, 107	
130610A	Fermi	1.27 ± 0.08	-1.58 $^{+0.08}_{-0.08}$...	271 $^{+111}_{-111}$	35.4 ± 0.5	10 - 1000	2.86 $\pm 0.25^{\mathrm{P}}$	10 - 1000	103, 107	
130606A	KW	1.52 ± 0.12	-1.14 ± 0.15	...	294 $^{+90}_{-50}$	44 ± 8	20 - 10000	2.6 $\pm 0.2^{\mathrm{P}}$	15 - 150	97, 107	
130604A	Swift	1.51 ± 0.12	14 ± 1	15 - 150	0.8 $\pm 0.2^{\mathrm{P}}$	15 - 150	107	
130528A	Fermi	1.55 ± 0.09	-1.08 $^{+0.05}_{-0.05}$	-2.6 ± 0.3	122 $^{+7}_{-7}$	110 ± 1	10 - 1000	5.7 $\pm 0.3^{\mathrm{P}}$	10 - 1000	103, 107	
130518A	Fermi	...	-0.91 $^{+0.02}_{-0.02}$	-2.25 $^{+0.07}_{-0.07}$	398 $^{+15}_{-15}$	945 ± 1	10 - 1000	45.4 $\pm 0.4^{\mathrm{P}}$	10 - 1000	103	
130511A	Swift	1.35 ± 0.31	2.2 ± 0.4	15 - 150	1.3 $\pm 0.2^{\mathrm{P}}$	15 - 150	107	

Table 10 (cont'd)

GRB	Detector fluence/flux	Γ	α	β	E_p [keV]	fluence S_γ [10^{-7} erg cm $^{-2}$]	peak flux $F_p(P_p)$		reference	
							(7)	Band		
(1)	(2)	(3)	(4)	(5)	(6)	(8)	(9)	(10)	(11)	
130505A	KW/Swift	1.18 ± 0.07	-0.69 ± 0.04	-2.03 ± 0.03	631 ± 31	3130 ± 60	20 - 10000	3690 ± 30	20 - 10000	94, 95, 107
130427B	Swift	1.64 ± 0.15	15 ± 1	15 - 150	3.0 ± 0.4 ^p	15 - 150	107
130427A	Fermi	1.21 ± 0.02	-0.958 ± 0.006	-4.17 ± 0.16	1028 ± 8	24619 ± 12	10 - 1000	1051 ± 2 ^p	10 - 1000	93, 103, 107
130420A	Fermi	2.18 ± 0.05	-1.13 ± 0.12	...	57.3 ± 3.1	115 ± 2	10 - 1000	5.4 ± 0.5 ^p	10 - 1000	103, 107
130418A	KW	2.12 ± 0.09	157 ± 25	20 - 1200	82.5 ± 0.4	20 - 1200	92
130408A	KW	1.28 ± 0.26	-0.4 ± 0.2	-2.3 ± 0.2	211 ± 29	120 ± 20	20 - 10000	352 ± 5	20 - 10000	91, 107
130215A	Fermi	1.59 ± 0.14	-1.19 ± 0.11	-1.59 ± 0.04	257 ± 130	185 ± 3	10 - 1000	3.5 ± 0.3 ^p	10 - 1000	103, 107
130131B	Swift	1.15 ± 0.20	3.4 ± 0.4	15 - 150	1.0 ± 0.2 ^p	15 - 150	107
121229A	Swift	2.43 ± 0.46	4.6 ± 1.3	15 - 150	0.1 ± 0.0 ^p	15 - 150	107
121211A	Fermi	2.36 ± 0.26	-0.27 ± 0.37	...	100 ± 15	6.4 ± 0.4	10 - 1000	2.37 ± 0.24 ^p	10 - 1000	103, 107
121209A	Swift	1.43 ± 0.08	29 ± 1	15 - 150	3.4 ± 0.3 ^p	15 - 150	107
121201A	Swift	1.90 ± 0.21	7.8 ± 1.0	15 - 150	0.8 ± 0.1 ^p	15 - 150	107
121128A	Fermi	1.32 ± 0.18	-1.00 ± 0.06	-3.36 ± 0.48	76.3 ± 3.0	93.0 ± 1.1	10 - 1000	17.9 ± 0.5 ^p	10 - 1000	103, 107
121027A	Swift	1.82 ± 0.09	20 ± 1	15 - 150	1.3 ± 0.2 ^p	15 - 150	107
121024A	Swift	1.41 ± 0.22	11 ± 1	15 - 150	1.3 ± 0.2 ^p	15 - 150	107
120922A	Fermi	2.00 ± 0.08	-0.62 ± 0.73	-2.23 ± 0.09	36.6 ± 6.7	82.1 ± 1.7	10 - 1000	3.4 ± 0.3 ^p	10 - 1000	103, 107
120909A	Fermi	1.39 ± 0.06	-0.83 ± 0.08	-1.92 ± 0.09	195 ± 25	98.5 ± 1.5	10 - 1000	3.0 ± 0.2 ^p	10 - 1000	103, 107
120907A	Fermi	1.73 ± 0.25	-0.81 ± 0.31	...	122 ± 34	8.1 ± 0.4	10 - 1000	4.3 ± 0.4 ^p	10 - 1000	103, 107
120815A	Swift	2.29 ± 0.23	4.9 ± 0.7	15 - 150	2.2 ± 0.3 ^p	15 - 150	107
120811C	Fermi	1.99 ± 0.06	-0.71 ± 0.27	-2.85 ± 0.32	55.6 ± 5.3	34.5 ± 2.1	10 - 1000	7.7 ± 0.5 ^p	10 - 1000	103, 107
120805A	Swift	1.20 ± 0.28	8.2 ± 1.4	15 - 150	0.37 ± 0.2 ^p	15 - 150	107
120802A	Swift	1.84 ± 0.10	-1.22 ± 0.50	...	57.3 ± 29.9	19 ± 3	15 - 150	3.0 ± 0.2 ^p	15 - 150	107
120729A	Fermi	1.62 ± 0.08	...	-1.62 ± 0.04	...	50.8 ± 0.5	10 - 1000	5.2 ± 0.3 ^p	10 - 1000	103, 107
120724A	Swift	2.43	-0.75 ± 1.69	...	26.7 ± 7.5	6.8 ± 1.1	15 - 150	0.6 ± 0.2 ^p	15 - 150	107
120722A	Swift	1.90 ± 0.25	...	-1.84 ± 0.03	85.1 ± 10.1	12 ± 2	15 - 150	1.0 ± 0.3 ^p	15 - 150	107
120716A	Fermi	...	-0.76 ± 0.12	-1.84 ± 0.03	85.1 ± 10.1	144 ± 0	10 - 1000	8.6 ± 0.3 ^p	10 - 1000	103
120714B	Swift	1.52 ± 0.17	12 ± 1	15 - 150	0.4 ± 0.1 ^p	15 - 150	107
120712A	Fermi	1.36 ± 0.08	44.3 ± 0.5	10 - 1000	3.5 ± 0.2 ^p	10 - 1000	103, 107
120711A	Fermi	...	-0.98 ± 0.01	-2.80 ± 0.09	13.18 ± 45	1942 ± 2	10 - 1000	26.7 ± 0.6 ^p	10 - 1000	103
120624B	Fermi	1.17 ± 0.03	-0.92 ± 0.01	-2.22 ± 0.07	637 ± 24	1916 ± 1	10 - 1000	17.7 ± 0.3 ^p	10 - 1000	103, 107
120422A	Swift	1.19 ± 0.24	2.3 ± 0.4	15 - 150	0.6 ± 0.2 ^p	15 - 150	107
120404A	Swift	1.85 ± 0.13	16 ± 1	15 - 150	1.2 ± 0.2 ^p	15 - 150	107
120327A	Swift	1.52 ± 0.06	36 ± 1	15 - 150	3.9 ± 0.2 ^p	15 - 150	107
120326A	Fermi	1.99	-0.67 ± 0.19	-2.33 ± 0.09	43.9 ± 3.9	32.6 ± 0.5	10 - 1000	7.7 ± 0.3 ^p	10 - 1000	103, 107
120224A	Swift	2.25 ± 0.36	2.4 ± 0.5	15 - 150	0.9 ± 0.2 ^p	15 - 150	107
120211A	Swift	1.50 ± 0.22	8.1 ± 1.2	15 - 150	0.5 ± 0.2 ^p	15 - 150	107
120119A	Fermi	1.38 ± 0.04	-0.96 ± 0.03	-2.37 ± 0.09	183 ± 7	386 ± 1	10 - 1000	16.9 ± 0.4 ^p	10 - 1000	103, 107
120118B	Fermi	2.08 ± 0.11	-0.30 ± 0.29	-2.55 ± 0.15	43.1 ± 3.9	26.6 ± 0.5	10 - 1000	2.83 ± 0.23 ^p	10 - 1000	103, 107
111229A	Swift	1.85 ± 0.33	3.4 ± 0.7	15 - 150	1.0 ± 0.2 ^p	15 - 150	107

Table 10 (cont'd)

GRB	Detector	fluence/flux	Γ	α	β	E_p [keV]	fluence S_γ		peak flux $F_p(P_p)$ Band (10)	reference (11)
							(5)	(6)		
(1)	(2)	(3)	(4)	(5)	(6)	(7)	(8)	(9)	(10)	(11)
111228A	Fermi	2.27 ± 0.06	$-1.55^{+0.08}_{-0.08}$	$-2.44^{+0.06}_{-0.06}$	$26.5^{+1.3}_{-1.3}$	181 ± 0	$10 - 1000$	20.8 ± 0.4^P	$10 - 1000$	103, 107
111225A	Swift	1.70 ± 0.15	13 ± 1.2	$15 - 150$	0.7 ± 0.1^P	$15 - 150$	107
111215A	Swift	1.70 ± 0.18	45 ± 5	$15 - 150$	0.5 ± 0.2^P	$15 - 150$	107
111211A	AGILE	2.77 ± 0.17	92.0 ± 8.0	$20 - 1200$	0.5 ± 0.1^P	$20 - 60$	87, 88
111209A	KW	1.48 ± 0.03	-1.31 ± 0.09	4860 ± 610	$20 - 1400$	0.9 ± 0.2^P	$15 - 150$	86, 107
111209A	Swift	2.56 ± 0.38	1.8 ± 0.4	$15 - 150$	0.9 ± 0.1^P	$15 - 150$	107
111209A	Swift	1.68 ± 0.07	73 ± 3	$15 - 150$	0.9 ± 0.1^P	$15 - 150$	107
111209A	Fermi	1.49 ± 0.14	9.1 ± 0.3	$10 - 1000$	2.28 ± 0.35^P	$10 - 1000$	103, 107
111008A	KW	2.02 ± 0.09	$-1.36^{+0.24}_{-0.21}$	149^{+52}_{-28}	90 ± 9	$20 - 10000$	$5^{+14}_{-14} \pm 3$	20 - 10000
111005A	Swift	2.03 ± 0.27	6.2 ± 1.1	$15 - 150$	1.1 ± 0.3^P	$15 - 150$	107
110918A	KW	...	-1.2 ± 0.1	$-2^{+0.03}_{-0.04}$	150^{+20}_{-18}	7500 ± 200	$20 - 10000$	28700 ± 400	$20 - 10000$	84
110818A	Fermi	1.58 ± 0.11	$-1.11^{+0.17}_{-0.17}$	$-1.76^{+0.10}_{-0.10}$	183^{+85}_{-85}	51.5 ± 0.3	$10 - 1000$	2.79 ± 0.27^P	$10 - 1000$	103, 107
110808A	KW	2.32 ± 0.43	-1.13 ± 0.08	2960^{+1217}_{-796}	160 ± 20	21100 ± 200	$20 - 10000$	82, 107
110801A	KW/Swift	1.84 ± 0.10	$-1.7^{+0.22}_{-0.15}$	140^{+1270}_{-50}	73^{+17}_{-9}	$15 - 1200$	1.1 ± 0.2^P	83, 107
110731A	Fermi	1.15 ± 0.05	$-0.87^{+0.16}_{-0.03}$	$-2.44^{+0.16}_{-0.16}$	319^{+19}_{-19}	228 ± 0	$10 - 1000$	20.9 ± 0.5^P	$10 - 1000$	103, 107
110726A	Swift	1.86	$-0.64^{+0.96}_{-0.96}$	$46.5^{+15.6}_{-15.6}$	2.2 ± 0.3	$15 - 150$	1.0 ± 0.2^P	107
110715A	KW	1.63	$-1.23^{+0.08}_{-0.08}$	$-2.7^{+0.2}_{-0.5}$	120^{+12}_{-11}	230 ± 20	$20 - 10000$	3110 ± 10	$20 - 10000$	81, 107
110709B	KW	1.29 ± 0.04	$-1^{+0.14}_{-0.13}$	278^{+43}_{-32}	260 ± 20	$20 - 5000$	110 ± 10	80, 107
110503A	KW	1.26 ± 0.07	$-0.98^{+0.09}_{-0.08}$	$-2.7^{+0.2}_{-0.5}$	219^{+20}_{-19}	260 ± 20	$20 - 5000$	3110 ± 10	$20 - 5000$	79, 107
110422A	KW	1.34 ± 0.00	-0.65 ± 0.06	$-2.96^{+0.14}_{-0.19}$	152 ± 5	856 ± 2	$20 - 2000$	3120 ± 15	$20 - 2000$	78, 107
110213B	KW/MAXI	...	-1.52 ± 0.25	...	123 ± 19	177 ± 16	$20 - 1400$	$0.83^{+0.02}_{-0.53}$	$2 - 20$	77, 106
110213A	Fermi	1.83 ± 0.12	$-1.42^{+0.09}_{-0.09}$	$-2.13^{+0.09}_{-0.09}$	$74.7^{+13.1}_{-13.1}$	93.7 ± 0.5	$10 - 1000$	17.8 ± 0.5^P	$10 - 1000$	103, 107
110205A	KW	1.80 ± 0.04	-1.52 ± 0.14	...	222 ± 74	366 ± 35	$20 - 1200$	85.1 ± 0.7	$20 - 1200$	76, 107
110128A	Fermi	1.31 ± 0.30	$-1.26^{+0.25}_{-0.25}$...	192^{+112}_{-112}	14.2 ± 1.0	$10 - 1000$	1.55 ± 0.15^P	$10 - 1000$	103, 107
110106B	Fermi	1.76 ± 0.11	$-0.94^{+0.16}_{-0.16}$...	129^{+20}_{-20}	41.1 ± 0.6	$10 - 1000$	2.77 ± 0.27^P	$10 - 1000$	103, 107
101225A	Swift	1.82 ± 0.32	$-1.37^{+0.72}_{-0.72}$	$-2.26^{+0.14}_{-0.14}$	$56.4^{+6.6}_{-6.6}$	39.9 ± 0.5	$10 - 1000$	0.028 ± 0.005^P	$15 - 150$	107
101219B	Fermi	1.56 ± 0.16	$-1.37^{+0.72}_{-0.72}$	$-1.37^{+0.14}_{-0.14}$	135^{+10}_{-10}	149 ± 0	$10 - 1000$	6.2 ± 0.3^P	$10 - 1000$	103, 107
100906A	Fermi	1.78 ± 0.03	$-0.90^{+0.13}_{-0.13}$	$-1.86^{+0.03}_{-0.03}$	$69.7^{+10.1}_{-10.1}$	232 ± 0	$10 - 1000$	14.5 ± 0.4^P	$10 - 1000$	103, 107
100901A	Swift	1.52 ± 0.21	$-0.94^{+0.16}_{-0.16}$	21 ± 3	$15 - 150$	0.8 ± 0.2^P	$15 - 150$	107
100814A	Fermi	1.47 ± 0.04	$-0.37^{+0.10}_{-0.10}$	$-2.43^{+0.21}_{-0.21}$	135^{+10}_{-10}	149 ± 0	$10 - 1000$	4.6 ± 0.3^P	$10 - 1000$	103, 107
100729B	Fermi	1.55 ± 0.14	$-0.78^{+0.17}_{-0.17}$	$-1.98^{+0.14}_{-0.14}$	109^{+22}_{-22}	33.4 ± 0.6	$10 - 1000$	6.2 ± 0.3^P	$10 - 1000$	103, 107
100728A	Fermi	1.18 ± 0.02	-0.64 ± 0.02	-2.7 ± 0.14	290 ± 8	1279 ± 6	$10 - 1000$	510.5 ± 0.3^P	$10 - 1000$	103, 107
100724A	Swift	1.92 ± 0.21	1.6 ± 0.2	$15 - 150$	1.9 ± 0.2^P	$15 - 150$	107
100621A	KW	1.90 ± 0.03	-1.7 ± 0.13	360 ± 40	$20 - 2000$	517 ± 1.3	$20 - 2000$	73, 107
100615A	Fermi	1.87 ± 0.04	$-0.90^{+0.18}_{-0.18}$	$-1.80^{+0.03}_{-0.03}$	$53.3^{+9.9}_{-9.9}$	87.2 ± 0.8	$10 - 1000$	8.3 ± 0.2^P	$10 - 1000$	103, 107
100606A	KW	1.35 ± 0.10	-1.05 ± 0.14	...	945^{+551}_{-266}	390 ± 50	$20 - 2000$	525 ± 2.5	$20 - 2000$	72, 107
100518A	INTEGRAL	$1.28^{+0.05}_{-0.05}$	$5.2^{+4.4}_{-3.8}$	$20 - 200$	0.80 ± 0.20^P	$20 - 200$	102
100513A	Swift	1.62 ± 0.14	14 ± 1	$15 - 150$	0.6 ± 0.1^P	$15 - 150$	107
100508A	Swift	1.23 ± 0.25	7.0 ± 1.1	$15 - 150$	0.4 ± 0.2^P	$15 - 150$	107

Table 10 (cont'd)

GRB	Detector	fluence/flux	Γ	α	β	E_p [keV]	fluence S_γ		peak flux $F_p(P_p)$		reference (11)
							(6)	(7)	(8)	Band (9)	Band (10)
100425A	Swift	2.42 ± 0.32	4.7 ± 0.9	$15 - 150$	1.4 ± 0.2^P	$15 - 150$	107
100424A	Swift	1.83 ± 0.13	15 ± 1	$15 - 150$	0.4 ± 0.1^P	$15 - 150$	107
100418A	Swift	2.16 ± 0.25	3.4 ± 0.5	$15 - 150$	1.0 ± 0.2^P	$15 - 150$	107
100414A	Fermi	...	-0.624 ± 0.014	-3.54 ± 0.48	663 ± 16	885 ± 2	$10 - 1000$	21.9 ± 0.24	$10 - 1000$		103
100316D	Swift	2.29 ± 0.41	3.0 ± 0.8	$15 - 150$	0.1 ± 0.0^P	$15 - 150$	107
100316B	Swift	2.23 ± 0.18	2.0 ± 0.2	$15 - 150$	1.3 ± 0.1^P	$15 - 150$	107
100302A	Swift	1.72 ± 0.19	3.1 ± 0.4	$15 - 150$	0.5 ± 0.1^P	$15 - 150$	107
100219A	Swift	1.33 ± 0.25	3.7 ± 0.6	$15 - 150$	0.4 ± 0.1^P	$15 - 150$	107
091208B	Fermi	$-0.15^{+0.39}_{-0.39}$	$-1.90^{+0.04}_{-0.04}$	$38.5^{+5.8}_{-5.8}$	61.9 ± 1.9	$10 - 1000$	20.6 ± 0.3^P	$10 - 1000$	$75, 103$		
091112A	Fermi	2.05 ± 0.07	$-1.26^{+0.07}_{-0.07}$	$-2.22^{+0.02}_{-0.02}$	35.5 ± 1.5	207 ± 0	$10 - 1000$	68.2 ± 0.5^P	$10 - 1000$	$103, 107$	
0911109A	Swift	$1.306^{+0.254}_{-0.245}$	16.4 ± 2.2	$15 - 150$	0.99 ± 0.30	$15 - 150$	75	
091029A	Swift	1.88 ± 0.07	$-1.46^{+0.28}_{-0.27}$	$61.3^{+25.0}_{-9.1}$	24 ± 1	$15 - 150$	1.8 ± 0.1^P	$15 - 150$	107
091024A	Fermi	1.20 ± 0.08	$-1.32^{+0.08}_{-0.08}$	1730 ± 901	85.6 ± 0.6	$10 - 1000$	4.2 ± 0.3^P	$10 - 1000$	103, 107
091020A	Fermi	1.53 ± 0.07	$-1.26^{+0.06}_{-0.06}$	$-4.0^{+11.1}_{-11.1}$	244 ± 36	83.5 ± 1.5	$10 - 1000$	6.8 ± 0.3^P	$10 - 1000$	$103, 107$	
091018A	Konus-RF	2.31 ± 0.06	$-1.53^{+0.59}_{-0.59}$	< 2.44	28^{+10}_{-10}	$14.4^{+1.9}_{-1.6}$	$20 - 1000$	$54.32^{+0.97}_{-0.94}$	$20 - 1000$	$66, 107$	
091003A	Fermi	...	-1.07 ± 0.39	$-2.23^{+0.11}_{-0.11}$	367 ± 26	23.3 ± 0	$10 - 1000$	29.2 ± 0.5^P	$10 - 1000$	103	
090927A	Fermi	1.80 ± 0.20	3.0 ± 0.2	$10 - 1000$	3.3 ± 0.2^P	$10 - 1000$	$103, 107$	
090926B	Fermi	1.50 ± 0.00	$-0.13^{+0.12}_{-0.12}$	$-3.2^{+0.3}_{-0.3}$	$82.5^{+3.0}_{-3.0}$	107 ± 1	$10 - 1000$	4.6 ± 0.2^P	$10 - 1000$	$103, 107$	
090926A	Fermi	...	$-0.86^{+0.12}_{-0.12}$	$-2.40^{+0.04}_{-0.04}$	339^{+5}_{-5}	1465 ± 3	$10 - 1000$	81.4 ± 0.4^P	$10 - 1000$	103	
090902B	Fermi	...	-1.01 ± 0.00	...	1054^{+17}_{-17}	2217 ± 3	$10 - 1000$	76.9 ± 0.4^P	$10 - 1000$	103	
090814A	Swift	$1.836^{+0.184}_{-0.193}$	12.7 ± 1.6	$15 - 150$	0.43 ± 0.18	$15 - 150$	75	
090812A	KW/Swift	1.24 ± 0.05	-1.03 ± 0.07	572 ± 159	261 ± 34	$15 - 1400$	3.6 ± 0.2^P	$15 - 150$	$71, 107$
090809A	Swift	$1.349^{+0.258}_{-0.254}$	3.7 ± 0.6	$15 - 150$	0.86 ± 0.19	$15 - 150$	75	
090726A	Swift	2.25 ± 0.19	8.6 ± 1.0	$15 - 150$	0.7 ± 0.2^P	$15 - 150$	107	
090715B	KW	$1.582^{+0.065}_{-0.065}$	$-1.1^{+0.40}_{-0.34}$	134^{+56}_{-30}	93^{+15}_{-11}	$20 - 2000$	5.9 ± 2.5	$20 - 2000$	70, 75
090709A	KW	$1.209^{+0.025}_{-0.025}$	-0.85 ± 0.08	$-2.7^{+0.2}_{-0.3}$	298 ± 27	910 ± 7	$20 - 3000$	539 ± 6	$20 - 3000$	$69, 75$	
090618A	Fermi	1.58 ± 0.02	$-1.13^{+0.01}_{-0.01}$	$-2.22^{+0.02}_{-0.02}$	146^{+3}_{-3}	2684 ± 4	$10 - 1000$	68.7 ± 1.1^P	$10 - 1000$	$103, 107$	
090530A	Swift	1.61 ± 0.17	11 ± 1	$15 - 150$	2.5 ± 0.3^P	$15 - 150$	107	
090529A	Swift	2.00 ± 0.3	6.8 ± 1.7	$15 - 150$	0.4 ± 0.1^P	$15 - 150$	107	
090519A	Fermi	1.02 ± 0.20	$-0.95^{+0.10}_{-0.10}$	1618^{+883}_{-883}	57.3 ± 0.6	$10 - 1000$	1.49 ± 0.16^P	$10 - 1000$	$103, 107$
090516A	Fermi	1.84 ± 0.11	$-1.52^{+0.05}_{-0.05}$	$-2.30^{+0.27}_{-0.27}$	142^{+26}_{-26}	172 ± 0	$10 - 1000$	4.4 ± 0.2^P	$10 - 1000$	$103, 107$	
090424A	Fermi	1.53 ± 0.03	$-1.04^{+0.02}_{-0.02}$	$-2.76^{+0.12}_{-0.12}$	153^{+3}_{-3}	463 ± 0	$10 - 1000$	109 ± 0^P	$10 - 1000$	$103, 107$	
090423A	KW/Swift	1.81 ± 0.09	$-0.59^{+0.05}_{-0.05}$	$-2.67^{+0.74}_{-0.74}$	$66.0^{+16.2}_{-16.2}$	8.2 ± 0.7	$10 - 1000$	1.62 ± 0.21^P	$10 - 1000$	$103, 107$	
090417B	Swift	$1.821^{+0.134}_{-0.138}$	179 ± 21	$15 - 1200$	1.58 ± 0.27	$15 - 150$	$68, 75$	
090407A	Swift	1.73 ± 0.29	22.5 ± 1.8	$15 - 150$	0.18 ± 0.09	$15 - 150$	75	
090328A	Fermi	...	$-1.09^{+0.02}_{-0.02}$	$-2.37^{+0.18}_{-0.18}$	639 ± 45	11 ± 2	$15 - 150$	0.6 ± 0.1^P	$15 - 150$	107	
090323A	Fermi	...	$-1.29^{+0.01}_{-0.01}$	$-2.44^{+0.17}_{-0.17}$	632^{+40}_{-40}	1180 ± 1	$10 - 1000$	17.2 ± 0.3^P	$10 - 1000$	103	
090313A	Swift	1.91 ± 0.29	14 ± 2	$15 - 150$	0.8 ± 0.3^P	$15 - 150$	107	

Table 10 (cont'd)

GRB	Detector	fluence/flux	Γ	α	β	E_p [keV]	[10^{-7} erg cm $^{-2}$]	fluence S_γ		peak flux $F_p(P_p)$ Band	reference (11)
								(5)	(6)	(7)	
(1)	(2)	(3)	(4)	(5)	(6)	(7)	(8)	(9)	(10)	(11)	
090205A	Swift	2.15 ± 0.23	1.9 ± 0.3	$15 - 150$	0.5 ± 0.1^P	$15 - 150$	107	
090201A	KW	1.41 ± 0.04	$-0.97^{+0.10}_{-0.09}$	$-2.8^{+0.29}_{-0.92}$	158^{+13}_{-12}	672^{+47}_{-54}	$20 - 2000$	3.73^{+12}_{-13}	$20 - 2000$	67, 107	
090113A	Fermi	1.60 ± 0.10	$-1.20^{+0.19}_{-0.19}$	$-2.06^{+0.29}_{-0.29}$	137^{+57}_{-57}	15.7 ± 0.5	$10 - 1000$	3.8 ± 0.2^P	$10 - 1000$	103, 107	
090102A	Fermi	1.36 ± 0.08	$-0.95^{+0.02}_{-0.02}$...	421^{+18}_{-18}	279 ± 0	$10 - 1000$	11.2 ± 0.2^P	$10 - 1000$	103, 107	
081222A	Fermi	1.41 ± 0.04	$-0.86^{+0.05}_{-0.05}$	$-2.31^{+0.12}_{-0.12}$	142^{+9}_{-9}	118 ± 0	$10 - 1000$	12.8 ± 0.2^P	$10 - 1000$	103, 107	
081221A	Fermi	1.75 ± 0.03	$-0.90^{+0.02}_{-0.02}$	$-3.9^{+0.12}_{-0.05}$	$86.9^{+1.4}_{-1.4}$	300 ± 0	$10 - 1000$	25.4 ± 0.3^P	$10 - 1000$	103, 107	
081210A	Swift	1.42 ± 0.14	18 ± 2	$15 - 150$	2.5 ± 0.2^P	$15 - 150$	107	
081203A	KW	$1.426^{+0.060}_{-0.060}$	$-1.33^{+0.27}_{-0.20}$...	578^{+2398}_{-290}	305^{+140}_{-89}	$20 - 3000$	2.47 ± 0.19	$15 - 150$	63, 75	
081121A	Fermi	1.09 ± 0.11	$-0.43^{+0.13}_{-0.13}$	$-2.09^{+0.09}_{-0.09}$	160^{+16}_{-16}	152 ± 2	$10 - 1000$	7.7 ± 0.4^P	$10 - 1000$	103, 107	
081118A	Swift	2.10 ± 0.16	12 ± 1	$15 - 150$	0.6 ± 0.2^P	$15 - 150$	107	
081109A	Fermi	$1.608^{+0.085}_{-0.085}$	$-0.67^{+1.85}_{-1.85}$	$-1.65^{+0.03}_{-0.03}$	$32.4^{+38.3}_{-38.3}$	65.5 ± 0.6	$10 - 1000$	2.64 ± 0.16^P	$10 - 1000$	75, 103	
081029A	Swift	1.43 ± 0.18	21 ± 2	$15 - 150$	0.5 ± 0.2^P	$15 - 150$	107	
081028A	Swift	1.25 ± 0.38	37 ± 2	$15 - 150$	0.5 ± 0.1^P	$15 - 150$	107	
081008A	Fermi	1.69 ± 0.07	$-1.01^{+0.12}_{-0.12}$	$-2.09^{+0.21}_{-0.21}$	166^{+36}_{-36}	103 ± 1	$10 - 1000$	2.66 ± 0.16^P	$10 - 1000$	103, 107	
081007A	Swift	2.51 ± 0.20	7.1 ± 0.8	$15 - 150$	2.6 ± 0.4^P	$15 - 150$	107	
080928A	Fermi	1.77 ± 0.12	...	$-1.80^{+0.06}_{-0.06}$	$17.9^{+28.3}_{-28.3}$	11.6 ± 0.4	$10 - 1000$	3.2 ± 0.2^P	$10 - 1000$	103, 107	
080916C	Fermi	...	$-1.08^{+0.01}_{-0.01}$	$-2.15^{+0.07}_{-0.07}$	661^{+45}_{-45}	602 ± 0	$10 - 1000$	13.7 ± 0.3^P	$10 - 1000$	103	
080916A	Fermi	$1.546^{+0.046}_{-0.046}$	$-0.82^{+0.13}_{-0.13}$	$-1.78^{+0.05}_{-0.05}$	106^{+19}_{-19}	78.1 ± 0.8	$10 - 1000$	4.5 ± 0.3^P	$10 - 1000$	75, 103	
080913A	KW/Swift	1.20 ± 0.15	$-0.82^{+0.15}_{-0.15}$...	121^{+232}_{-39}	$8.5^{+6.0}_{-2.2}$	$15 - 1000$	1.4 ± 0.2^P	$15 - 150$	62, 107	
080905B	Fermi	$1.657^{+0.142}_{-0.142}$	$-0.86^{+0.22}_{-0.22}$	$-2.29^{+0.65}_{-0.65}$	181^{+60}_{-60}	29.1 ± 0.4	$10 - 1000$	2.32 ± 0.23^P	$10 - 1000$	75, 103	
080810A	Fermi	1.34 ± 0.06	$-1.19^{+0.04}_{-0.04}$...	909^{+184}_{-184}	108 ± 0	$10 - 1000$	3.6 ± 0.2^P	$10 - 1000$	103, 107	
080805A	Swift	1.53 ± 0.07	25 ± 1	$15 - 150$	1.1 ± 0.1^P	$15 - 150$	107	
080804A	Fermi	1.19 ± 0.09	$-0.52^{+0.09}_{-0.09}$	$-1.90^{+0.08}_{-0.08}$	217^{+24}_{-24}	91.3 ± 1.1	$10 - 1000$	3.8 ± 0.2^P	$10 - 1000$	103, 107	
080721A	KW	1.11 ± 0.08	$-0.933^{+0.06}_{-0.084}$	$-2.43^{+0.24}_{-0.42}$	485^{+67}_{-59}	838^{+62}_{-60}	$20 - 5000$	3.196 ± 31	$20 - 5000$	61, 107	
080710A	Swift	1.47 ± 0.23	14 ± 2	$15 - 150$	1.0 ± 0.2^P	$15 - 150$	107	
080707A	Swift	1.77 ± 0.19	5.2 ± 0.6	$15 - 150$	1.0 ± 0.1^P	$15 - 150$	107	
080607A	KW	1.31 ± 0.04	$-1.06^{+0.09}_{-0.08}$	$-2.57^{+0.18}_{-0.26}$	394^{+58}_{-54}	893^{+52}_{-52}	$20 - 4000$	2269 ± 54	$20 - 4000$	60, 107	
080605A	KW	1.32 ± 0.03	-1.02 ± 0.08	$-2.58^{+0.31}_{-0.84}$	246^{+23}_{-18}	302^{+13}_{-12}	$20 - 2000$	2160 ± 33	$20 - 2000$	59, 107	
080604A	Swift	1.78 ± 0.18	8.0 ± 0.9	$15 - 150$	0.4 ± 0.1^P	$15 - 150$	107	
080603B	KW	$1.731^{+0.061}_{-0.061}$	$-0.94^{+1.21}_{-0.75}$...	85^{+91}_{-30}	$45.0^{+15.3}_{-9.0}$	$20 - 1000$	$5.15^{+1.4}_{-3.8}$	$20 - 1000$	58, 75	
080603A	INTEGRAL	1.6 ± 0.2	11 ± 2	$20 - 200$	0.5^P	$20 - 200$	89	
080602A	KW	1.43 ± 0.13	$79.2^{+14.7}_{-14.5}$	$20 - 1000$	$5.19.2 \pm 5.8$	$20 - 1000$	57, 107	
080520A	Swift	2.90 ± 0.51	0.55 ± 0.17	$15 - 150$	0.5 ± 0.1^P	$15 - 150$	107	
080517A	Swift	1.54 ± 0.33	5.6 ± 1.2	$15 - 150$	0.6 ± 0.2^P	$15 - 150$	107	
080515A	Swift	2.19 ± 0.16	$-0.39^{+1.19}_{-0.95}$...	$33.5^{+4.6}_{-6.2}$	20 ± 3	$15 - 150$	3.9 ± 0.7^P	$15 - 150$	107	
080430A	Swift	1.73 ± 0.09	12 ± 1	$15 - 150$	2.6 ± 0.2^P	$15 - 150$	107	
080413B	Swift	$1.742^{+0.058}_{-0.058}$	$-1.230^{+0.256}_{-0.241}$...	$77.67^{+24.35}_{-10.84}$	32.5 ± 1.2	$15 - 150$	14.0 ± 0.6	$15 - 150$	75	
080413A	Suzaku/Swift	$1.529^{+0.052}_{-0.052}$	-1.2 ± 0.1	...	170^{+80}_{-80}	48^{+4}_{-4}	$15 - 150$	4.8 ± 0.2	$15 - 150$	56, 75	
080411A	KW	1.75 ± 0.03	$-1.51^{+0.04}_{-0.05}$...	259^{+35}_{-27}	629^{+31}_{-29}	$20 - 2000$	3.128 ± 16	$20 - 2000$	55, 107	

Table 10 (cont'd)

GRB	Detector	Γ	α	β	E_p [keV]	(6)	fluence S_γ		peak flux $F_p(F_p)$ Band	reference
							(4)	(5)	(7)	
(1)	(2)	(3)	(4)	(5)	(6)	(8)	(9)	(10)	(11)	
080330A	Swift	2.53 ± 0.45	3.4 ± 0.8	15 – 150	0.9 ± 0.2P	15 – 150	107
080325A	Swift	1.68 ± 0.17	49 ± 4	15 – 150	1.4 ± 0.6P	15 – 150	107
080319C	KW	1.285 ± 0.068	-1.01 ± 0.13	-1.87 ± 0.15	307 ± 141	150 ± 34	20 – 4000	533 ± 7.9	20 – 4000	54, 75
080319B	KW	1.051 ± 0.019	-0.822 ± 0.014	-3.87 ± 0.44	651 ± 14	5720 ± 140	20 – 7000	3217 ± 21	20 – 7000	53, 75
080310A	Swift	2.32 ± 0.16	23 ± 2	15 – 150	1.3 ± 0.2P	15 – 150	107
080210A	Swift	1.77 ± 0.12	18 ± 1	15 – 150	1.6 ± 0.2P	15 – 150	107
080207A	Swift	1.56 ± 0.06	-1.25 ± 0.24	...	124 ± 180	61 ± 2	15 – 150	1.0 ± 0.3P	15 – 150	107
080129A	Swift	1.34 ± 0.26	8.9 ± 1.4	15 – 150	0.2 ± 0.1P	15 – 150	107
071122A	Swift	1.77 ± 0.31	278 ± 236	58.4 ± 3.0	20 – 1000	366.6 ± 11.3	20 – 1000	49, 107
071117A	KW	1.57 ± 0.06	-1.53 ± 0.15	30 ± 4	15 – 150	8 ± 1P	15 – 150	107
071112C	Swift	1.09 ± 0.07	9.0 ± 1.3	15 – 150	0.5 ± 0.1P	15 – 150	107
071031A	Swift	2.42 ± 0.29	13 ± 2	15 – 150	0.7 ± 0.1P	15 – 150	107
071021A	Swift	1.70 ± 0.21	322 ± 80	77.1 ± 3.9	20 – 2000	360.4 ± 11.2	20 – 2000	48, 107
071020A	KW	1.11 ± 0.05	-0.65 ± 0.27	...	52 ± 10	47.8 ± 9.5	20 – 1000	38.9 ± 2.3	20 – 1000	47, 75
071010B	KW	1.966 ± 0.043	-1.25 ± 0.32	-2.65 ± 0.29	52 ± 14	20 – 31.2	2.02 ± 0.44	0.45 ± 0.17	15 – 150	75
071010A	Swift	2.238 ± 0.320	799 ± 124	532 ± 30	20 – 4000	3122 ± 19	20 – 4000	46, 107
071003A	KW	1.36 ± 0.07	-0.97 ± 0.07	...	799 ± 100	6.7 ± 0.5	15 – 150	1.26 ± 0.16	15 – 150	75
070810A	Swift	2.055 ± 0.124	2.8 ± 0.5	15 – 150	0.4 ± 0.1P	15 – 150	107
070802A	Swift	1.79 ± 0.128	35.6 ± 2.3	15 – 150	1.57 ± 0.25	15 – 150	75
070721B	Swift	1.238 ± 0.107	1.55 ± 0.16	15 – 150	0.94 ± 0.09	15 – 150	75
070714A	Swift	2.563 ± 0.195	108 ± 6	15 – 150	1.49 ± 0.33	15 – 150	75
070612A	Swift	1.640 ± 0.092	3.91 ± 0.57	15 – 150	0.82 ± 0.21P	15 – 150	107
070611A	Swift	1.66 ± 0.22	25.70 ± 2.45	15 – 150	1.43 ± 0.36P	15 – 150	107
070529A	Swift	1.34 ± 0.16	222 ± 27	181 ± 6	20 – 1000	341.2 ± 7.8	20 – 1000	44, 107
070521A	KW	1.33 ± 0.04	-0.93 ± 0.12	1.62 ± 0.24	15 – 150	0.68 ± 0.13P	15 – 150	107
070518A	Swift	2.11 ± 0.25	188 ± 8	397 ± 7	20 – 1000	383.0 ± 10.3	20 – 1000	43, 107
070508A	KW	1.34 ± 0.02	-0.81 ± 0.07	6.7 ± 1.0	15 – 150	< 0.07	15 – 150	75
070506A	Swift	1.73 ± 0.17	2.10 ± 0.23	15 – 150	0.91 ± 0.13P	15 – 150	107
070419B	Swift	1.651 ± 0.050	74.6 ± 1.9	15 – 150	1.16 ± 0.15	15 – 150	75
070419A	Swift	2.372 ± 0.234	27.00 ± 1.55	15 – 150	0.91 ± 0.13P	15 – 150	107
070411A	Swift	1.72 ± 0.10	595 ± 105	20 – 6000	545.7 ± 10.7	20 – 6000	42, 107
070328A	KW	1.24 ± 0.04	-0.99 ± 0.13	-1.99 ± 0.18	496 ± 172	595 ± 117	24.80 ± 1.12	15 – 150	1.76 ± 0.15P	15 – 150
070318A	Swift	1.42 ± 0.08	53.80 ± 2.86	15 – 150	4.07 ± 0.21P	15 – 150	107
070306A	Swift	1.66 ± 0.10	3.05 ± 0.51	15 – 150	0.34 ± 0.11P	15 – 150	107
070224A	Swift	2.42 ± 0.30	17.00 ± 1.20	15 – 150	0.69 ± 0.15P	15 – 150	107
070223A	Swift	1.85 ± 0.12	4.45 ± 1.01	15 – 150	0.90 ± 0.22P	15 – 150	107
070208A	Swift	1.94 ± 0.36	29.80 ± 2.67	15 – 150	0.55 ± 0.12P	15 – 150	107
070129A	Swift	2.01 ± 0.15	-1.10 ± 0.10	-2.08 ± 0.10	367 ± 65	1740 ± 180	20 – 10000	3225 ± 36	20 – 10000	41
070125A	KW	

Table 10 (cont'd)

GRB	Detector	fluence/flux	Γ	α	β	E_p [keV]	fluence S_γ		peak flux $F_p(P_p)$ Band	reference (11)
							(2)	(3)	(4)	
070110A	Swift	1.58 ± 0.12	16.20 ± 1.08	15 – 150	0.60 ± 0.12P	15 – 150	107
070103A	Swift	1.95 ± 0.21	3.38 ± 0.46	15 – 150	1.04 ± 0.15P	15 – 150	107
061222B	Swift	1.956 ± 0.127	22.7 ± 1.8	15 – 150	0.87 ± 0.23	15 – 150	75
061222A	KW	1.324 ± 0.038	-0.94 ± 0.13	-2.41 ± 0.28	283 ± 59	266 ± 23	20 – 2000	356.5 ± 14.2	20 – 2000	40, 75
061202A	Swift	1.58 ± 0.07	34.20 ± 1.33	15 – 150	2.51 ± 0.17P	15 – 150	107
RHESSI		1.32 ± 0.06	-0.95 ± 0.29	...	935 ± 360	200 ± 2.21	30 – 2000	9.76 ± 0.38P	15 – 150	38, 107
061121A	KW	1.41 ± 0.03	-1.32 ± 0.05	-1.32 ± 0.05	606 ± 90	567 ± 30	20 – 5000	3.128 ± 16	20 – 5000	37, 107
061110B	Swift	0.991 ± 0.165	13.5 ± 1.2	15 – 150	0.43 ± 0.11	15 – 150	75
061110A	Swift	1.643 ± 0.116	11.3 ± 0.8	15 – 150	0.29 ± 0.10	15 – 150	75
061021A	KW	1.30 ± 0.06	-1.22 ± 0.12	...	777 ± 549	134 ± 11	20 – 2000	37.2 ± 5.3	20 – 2000	36, 107
061007A	KW	1.03 ± 0.03	-0.70 ± 0.04	-2.61 ± 0.15	399 ± 18	2490 ± 47	20 – 10000	3.195 ± 31	20 – 10000	35, 107
060927A	Swift	1.61 ± 0.08	-0.81 ± 0.38	-0.81 ± 0.35	70.7 ± 19.4	11.30 ± 0.68	15 – 150	2.70 ± 0.17P	15 – 150	107
060926A	Swift	2.54 ± 0.23	2.19 ± 0.25	15 – 150	1.09 ± 0.14P	15 – 150	107
060923B	Swift	2.474 ± 0.228	4.9 ± 0.6	15 – 150	0.74 ± 0.19	15 – 150	75
060923A	Swift	1.695 ± 0.220	8.8 ± 1.3	15 – 150	1.07 ± 0.21	15 – 150	75
060912A	Swift	1.729 ± 0.080	13.50 ± 0.62	15 – 150	58.55 ± 0.44P	15 – 150	75, 107
060908A	Swift	1.32 ± 0.06	-0.93 ± 0.26	-0.93 ± 0.24	147 ± 138	28.00 ± 1.11	15 – 150	3.03 ± 0.25P	15 – 150	107
060906A	Swift	2.03 ± 0.11	22.10 ± 1.36	15 – 150	1.97 ± 0.28P	15 – 150	107
060904B	Swift	1.604 ± 0.135	16.5 ± 1.4	15 – 150	2.10 ± 0.20	15 – 150	75
060814A	KW	1.53 ± 0.03	-1.43 ± 0.15	-1.43 ± 0.16	257 ± 22	269 ± 12	20 – 1000	521.3 ± 2.9	20 – 1000	33, 107
060805A	Swift	2.105 ± 0.356	0.73 ± 0.19	15 – 150	0.22 ± 0.09	15 – 150	75
060729A	Swift	1.75 ± 0.14	26.10 ± 2.11	15 – 150	1.17 ± 0.13P	15 – 150	107
060719A	Swift	1.91 ± 0.11	15.00 ± 0.91	15 – 150	2.16 ± 0.20P	15 – 150	107
060714A	Swift	1.93 ± 0.11	28.30 ± 1.67	15 – 150	1.28 ± 0.13P	15 – 150	107
060707A	Swift	1.67 ± 0.13	-0.42 ± 0.67	61.9 ± 15.0	16.00 ± 1.51	15 – 150	1.01 ± 0.23P	15 – 150	107	
060614A	KW	2.02 ± 0.04	-1.57 ± 0.15	302 ± 24	409 ± 18	20 – 2000	345.0 ± 7.2	20 – 2000	32, 107	
060607A	Swift	1.450 ± 0.073	25.6 ± 1.1	15 – 150	1.27 ± 0.12	15 – 150	75
060605A	Swift	1.55 ± 0.20	6.97 ± 0.90	15 – 150	0.46 ± 0.12P	15 – 150	107
060604A	Swift	2.01 ± 0.42	4.02 ± 1.06	15 – 150	0.34 ± 0.13P	15 – 150	107
060602A	Swift	1.219 ± 0.162	16.1 ± 1.6	15 – 150	0.37 ± 0.18	15 – 150	75
060526A	Swift	2.01 ± 0.24	12.60 ± 1.65	15 – 150	1.67 ± 0.18P	15 – 150	107
060522A	Swift	1.56 ± 0.15	11.40 ± 1.11	15 – 150	0.55 ± 0.15P	15 – 150	107
060512A	Swift	2.48 ± 0.30	2.32 ± 0.40	15 – 150	0.88 ± 0.20P	15 – 150	107
060510B	Swift	1.767 ± 0.074	39.8 ± 1.6	15 – 150	0.45 ± 0.10	15 – 150	75
060505A	Swift	1.29 ± 0.28	9.44 ± 1.71	15 – 150	2.65 ± 0.63P	15 – 150	107
060502A	Swift	1.429 ± 0.073	23.3 ± 1.0	15 – 150	1.69 ± 0.20	15 – 150	75
060418A	Swift	1.70 ± 0.06	83.30 ± 2.53	15 – 150	6.52 ± 0.35P	15 – 150	107
060319A	Swift	2.33 ± 0.25	2.64 ± 0.34	15 – 150	1.09 ± 0.14P	15 – 150	107
060306A	Swift	1.80 ± 0.10	21.30 ± 1.18	15 – 150	5.97 ± 0.35P	15 – 150	107

Table 10 (cont'd)

GRB	Detector	fluence/flux	Γ	α	β	E_p [keV]	fluence S_γ			peak flux $F_p(P_p)$ Band (10)	reference (11)				
							(1)	(2)	(3)	(4)	(5)	(6)	(7)	(8)	(9)
060223A	Swift	1.689 $^{+0.111}_{-0.113}$	6.7	± 0.5	15	-150	1.00	± 0.14	15	-150	75
060218A	Swift	2.26 ± 0.17	15.70	± 1.52	15	-150	0.25	$\pm 0.11^P$	15	-150	107
060210A	Swift	1.53 ± 0.09	76.60	± 4.09	15	-150	2.72	$\pm 0.28^P$	15	-150	107
060206A	Swift	1.66 ± 0.07	-1.12 $^{+0.32}_{-0.30}$	80.7 $^{+38.8}_{-14.0}$	8.31	± 0.42	15	-150	2.79	$\pm 0.17^P$	15	-150	107
060204B	Swift	1.417 $^{+0.082}_{-0.082}$	-0.785 $^{+0.391}_{-0.358}$	98.39 $^{+16.89}_{-19.90}$	29.3	± 1.8	15	-150	1.03	± 0.14	15	-150	75
060202A	Swift	1.71 ± 0.13	21.30	± 1.65	15	-150	0.51	$\pm 0.17^P$	15	-150	107
060124A	KW	1.84 ± 0.19	-1.29 $^{+0.14}_{-0.11}$	-2.26 $^{+0.27}_{-0.88}$	285 $^{+63}_{-56}$	143 $^{+24}_{-24}$	20	-2000	326.6 $^{+7.4}_{-6.9}$	20	-2000	30,	107		
060123A	Swift	1.9 ± 0.6	3	15	-150	0.04P	15	-150	107		
060115A	Swift	1.71 ± 0.11	-0.74 $^{+0.12}_{-0.1}$	-1.8 $^{+0.12}_{-0.21}$	94.6 $^{+21.4}_{-17.6}$	17.10	± 1.50	15	-150	0.87	$\pm 0.12^P$	15	-150	52, 107	
060111A	Swift	1.621 $^{+0.064}_{-0.064}$	-0.882 $^{+0.303}_{-0.282}$...	73.90 $^{+17.92}_{-9.13}$	12.0	± 0.6	15	-150	1.33	± 0.14	15	-150	75	
051117B	Swift	1.539 $^{+0.297}_{-0.307}$	1.75	± 0.37	15	-150	0.38	± 0.12	15	-150	75
051111A	Swift	1.32 ± 0.06	40.80	± 1.34	15	-150	2.66	$\pm 0.21^P$	15	-150	107
051109B	Swift	1.964 $^{+0.224}_{-0.224}$	-0.230 $^{+1.569}_{-1.473}$...	39.69 $^{+11.37}_{-7.47}$	2.26	± 0.42	15	-150	0.35	± 0.11	15	-150	75	
051109A	KW/Swift	1.505 $^{+0.201}_{-0.201}$	-1.25 $^{+0.44}_{-0.59}$...	161 $^{+224}_{-58}$	40.0 $^{+3.0}_{-34.0}$	20	-500	5.8 $^{+0.3}_{-4.9}$	20	-500	25, 75			
051022A	HETE-2/KW	...	-1.01 $^{+0.25}_{-0.03}$	-1.95 $^{+0.25}_{-0.14}$	213 $^{+18}_{-18}$	2610 $^{+60}_{-110}$	20	-2000	3100.0 ± 13.0	20	-2000	24,	52		
051016B	Swift	2.320 $^{+0.210}_{-0.226}$	1.70	± 0.22	15	-150	0.81	± 0.12	15	-150	75	
051008A	Swift	1.13 ± 0.05	-0.975 $^{+0.078}_{-0.086}$...	39.69 $^{+11.37}_{-7.47}$	50.90	± 1.45	15	-150	5.44	$\pm 0.35^P$	15	-150	23, 107	
051006A	Swift	1.51 ± 0.17	13.40	± 1.41	15	-150	1.62	$\pm 0.30^P$	15	-150	107	
051001A	Swift	2.05 ± 0.15	17.40	± 1.47	15	-150	0.49	$\pm 0.11^P$	15	-150	107	
050922C	HETE-2/KW	1.356 ± 0.056	-0.83 $^{+0.23}_{-0.26}$...	130 $^{+51}_{-27}$	73.0	± 5.0	20	-2000	4.45	± 7.0	20	-2000	21, 22, 75	
050915A	Swift	1.363 $^{+0.166}_{-0.165}$	8.4	± 0.9	15	-150	0.73	± 0.13	15	-150	75	
050908A	Swift	1.88 ± 0.17	4.83	± 0.51	15	-150	0.70	$\pm 0.14^P$	15	-150	107	
050904A	Swift	1.25 ± 0.07	48.30	± 1.80	15	-150	0.62	$\pm 0.17^P$	15	-150	107	
050826A	Swift	1.16 ± 0.31	4.13	± 0.72	15	-150	0.38	$\pm 0.13^P$	15	-150	107	
050824A	Swift	2.76 ± 0.38	2.66	± 0.52	15	-150	0.50	$\pm 0.18^P$	15	-150	107	
050822A	Swift	2.37 ± 0.14	24.60	± 1.72	15	-150	2.24	$\pm 0.22^P$	15	-150	107	
050820A	Swift	1.25 ± 0.12	34.40	± 2.42	15	-150	2.45	$\pm 0.23^P$	15	-150	107	
050819A	Swift	2.71 ± 0.29	3.50	± 0.55	15	-150	0.38	$\pm 0.12^P$	15	-150	107	
050814A	Swift	1.80 ± 0.17	20.10	± 2.20	15	-150	0.71	$\pm 0.23^P$	15	-150	107	
050802A	Swift	1.54 ± 0.13	20.00	± 1.57	15	-150	2.75	$\pm 0.44^P$	15	-150	107	
050730A	Swift	1.53 ± 0.11	23.80	± 1.52	15	-150	0.55	$\pm 0.14^P$	15	-150	107	
050714B	Swift	2.406 $^{+0.270}_{-0.302}$	-0.416 $^{+1.927}_{-1.433}$...	28.71 $^{+7.26}_{-28.70}$	5.3	± 1.0	15	-150	0.34	± 0.16	15	-150	75	
050525A	KW	1.78 ± 0.00	-1.1 ± 0.05	...	84.1	± 1.7	206	± 2	20	-1000	87 ± 7	20	-1000	18, 20, 107	
050505A	Swift	1.41 ± 0.12	24.90	± 1.79	15	-150	1.85	$\pm 0.31^P$	15	-150	107		
050502A	INTEGRAL	...	-1.07 $^{+0.13}_{-0.13}$...	190 $^{+122}_{-12.5}$	13.9 $^{+1.1}_{-4.0}$	20	-200	2.00	20	-200	51, 102			
050416A	Swift	3.180 $^{+0.285}_{-0.319}$	-0.972 $^{+2.279}_{-1.012}$...	13.67 $^{+7.93}_{-7.58}$	4.1	± 0.6	15	-150	1.99	± 0.19	15	-150	75	
050408A	HETE-2	1.40 ± 0.07	-1.15 ± 0.16	-2.2 $^{+0.16}_{-0.28}$	25.9 $^{+7.3}_{-7.3}$	19	30	-400	24.5 ± 1.2	20	-2000	17, 52			
050401A	KW	2.02 ± 0.19	13.10	± 1.48	15	-150	1.52	$\pm 0.21^P$	15	-150	107		
050319A	Swift			

Table 10 (cont'd)

GRB	Detector fluence/flux (2)	Γ (3)	α (4)	β (5)	E_p [keV] (6)	fluence S_{γ} [10^{-7} erg cm $^{-2}$]		peak flux $F_p(P_p)$ Band (10)	reference (11)
						(7)	(8)		
050318A	Swift	1.90 \pm 0.10	-1.03 \pm 0.45	...	49.2 $^{+9.4}_{-5.9}$	10.80 \pm 0.77	15 - 150	3.16 \pm 0.20 ^P	15 - 150
050315A	Swift	2.11 \pm 0.09	32.20 \pm 1.46	15 - 150	1.93 \pm 0.22 ^P	15 - 150
050223A	INTEGRAL	1.44 \pm 0.06	< 15.7	20 - 200	0.69 \pm 0.16 ^P	15 - 150
050219A	Swift	1.305 $^{+0.056}_{-0.056}$	-0.122 $^{+0.300}_{-0.282}$...	90.63 $^{+11.32}_{-7.77}$	40.8 \pm 1.6	15 - 150	3.1 \pm 0.3	15 - 150
050215B	HETE-2	2.173 $^{+0.269}_{-0.223}$...	-2.2 $^{+0.4}_{-0.6}$	17.6 $^{+2.5}_{-12.8}$	1.7 $^{+2.5}_{-1.3}$	30 - 400	0.45 \pm 0.10	15 - 150
050126A	Swift	1.34 \pm 0.15	8.38 \pm 0.80	15 - 150	0.71 \pm 0.17 ^P	15 - 150
041219A	INTEGRAL	...	-1.48 \pm 0.14	-2.01 \pm 0.05	156 $^{+88}_{-754}$	867.3 $^{+5.4}_{-128.9}$	20 - 200	36.0	20 - 200
041006A	HETE-2	...	-1.3 \pm 0.05	...	47.7 $^{+7.3}_{-2.7}$	70	30 - 400	...	13, 52
040924A	HETE-2/KW	...	-1.03 \pm 0.09	...	41.1 $^{+2.3}_{-3.3}$	27.3 \pm 1.2	20 - 500	33.3 \pm 3.5	20 - 500
040912A	HETE-2	...	-1.17 $^{+1.54}_{-0.62}$	-2.49 $^{+0.24}_{-0.4}$	14.16 $^{+3.32}_{-3.32}$	4	30 - 400	...	11, 52
031203A	INTEGRAL	1.51 $^{+0.03}_{-0.03}$	-1.18 $^{+0.11}_{-0.1}$...	148.2 $^{+32.45}_{-23.45}$	10.6 $^{+2.7}_{-3.60}$	20 - 200	2.50	20 - 200
030528A	HETE-2	...	-1.33 $^{+0.15}_{-0.15}$	-2.65 $^{+0.29}_{-0.98}$	31.84 $^{+4.67}_{-4.67}$	119.00 $^{+7.60}_{-7.80}$	2 - 400	17.89 \pm 1.57 ^P	2 - 400
030429A	HETE-2	...	-1.12 $^{+0.25}_{-0.25}$...	35.04 $^{+11.75}_{-11.75}$	8.54 $^{+1.48}_{-1.48}$	2 - 400	3.79 \pm 0.79 ^P	2 - 400
030329A	HETE-2	...	-1.26 $^{+0.22}_{-0.21}$...	67.86 $^{+7.90}_{-7.90}$	1.32	2 - 400	450.88 \pm 24.68 ^P	2 - 400
030328A	HETE-2	...	-1.14 $^{+0.15}_{-0.15}$	-2.28 $^{+0.05}_{-0.06}$	1630.00 $^{+13.00}_{-13.00}$	1.00	2 - 400	11.64 \pm 0.85 ^P	2 - 400
030323A	HETE-2	1.62 $^{+0.24}_{-0.25}$	126.30 $^{+13.80}_{-13.10}$	369.50 $^{+14.00}_{-14.20}$	2 - 400	3.86 \pm 2.11 ^P	2 - 400
030226A	HETE-2	...	-0.89 $^{+0.17}_{-0.15}$	12.30 $^{+3.68}_{-3.68}$	2 - 400	3.86 \pm 2.11 ^P	2 - 400
030115A	HETE-2	...	-1.28 $^{+0.14}_{-0.13}$...	97.12 $^{+26.98}_{-15.97}$	56.12 $^{+6.93}_{-6.93}$	2 - 400	2.69 \pm 0.57 ^P	2 - 400
021211A	HETE-2	...	-0.86 $^{+0.13}_{-0.10}$	-2.18 $^{+0.14}_{-0.25}$	82.79 $^{+52.82}_{-22.26}$	23.05 $^{+3.98}_{-3.98}$	2 - 400	8.13 \pm 1.38 ^P	2 - 400
021004A	HETE-2	...	-1.01 $^{+0.19}_{-0.17}$...	45.56 $^{+17.84}_{-17.84}$	35.34 $^{+3.22}_{-3.22}$	2 - 400	29.97 \pm 1.74 ^P	2 - 400
020903A	HETE-2	...	-0.90 $^{+0.15}_{-0.15}$	-2.62 $^{+0.42}_{-0.55}$	79.79 $^{+6.23}_{-22.97}$	25.45 $^{+6.85}_{-6.85}$	2 - 400	2.69 \pm 0.50 ^P	2 - 400
020819B	HETE2/Ulysses	...	-0.9 \pm 0.2	-2 $^{+0.2}_{-0.5}$	2.6 $^{+1.4}_{-1.4}$	0.95 $^{+0.62}_{-0.62}$	2 - 400	2.78 \pm 0.67 ^P	2 - 400
020813A	HETE-2	...	-0.94 $^{+0.03}_{-0.03}$	-1.57 $^{+0.03}_{-0.04}$	50 $^{+18}_{-12}$	78	25 - 100	7	25 - 100
020427A	BeppoSAX	-2.1 \pm 0.26	142.10 $^{+14.05}_{-12.91}$	142.10 $^{+12.70}_{-12.80}$	2 - 400	32.31 \pm 2.07 ^P	2 - 400
020410A	BeppoSAX/Konus	...	-1.8	...	2.8 \pm 2.8	5.8 \pm 0.4	2 - 28	0.3 \pm 0.04	2 - 28
020405A	BeppoSAX	2.00 \pm 0.13	180	280	15 - 1000	71	15 - 1000
020331A	HETE-2	...	-0.79 $^{+0.13}_{-0.12}$...	91.57 $^{+20.99}_{-14.09}$	422 \pm 24	40 - 700	32.1 \pm 1.9	40 - 700
020322A	BeppoSAX	2.34 \pm 0.24	85.5 \pm 0.8	69.40 $^{+8.45}_{-7.45}$	2 - 400	3.65 \pm 0.51 ^P	2 - 400
020305A	HETE2/Ulysses	...	-0.86 $^{+0.13}_{-0.11}$...	143 $^{+49}_{-30}$	104	30 - 400	2.24 \pm 0.24	40 - 700
020127A	HETE-2	...	-1.03 $^{+0.14}_{-0.13}$...	104.00 $^{+24.00}_{-24.00}$	27.22 $^{+4.43}_{-3.63}$	2 - 400	8.12 \pm 1.50 ^P	2 - 400
020124A	HETE-2	...	-0.79 $^{+0.15}_{-0.14}$	-2.6 $^{+0}_{-0.65}$	86.93 $^{+18.11}_{-12.45}$	81.04 $^{+8.86}_{-8.86}$	2 - 400	9.38 \pm 1.77 ^P	2 - 400
011211A	BeppoSAX	1.00 \pm 0.39	13.5 \pm 2.2	40 - 700	0.35 \pm 0.08	40 - 700
011121A	BeppoSAX	1.22 \pm 0.17	983 \pm 77	40 - 700	65.9 \pm 5.3	40 - 700
011030A	BappoSAX	1.84 \pm 0.17	12	2 - 26	0.075	2 - 26
010921A	BeppoSAX	2.30 \pm 0.24	-1.55 $^{+0.08}_{-0.07}$...	88.63 $^{+21.76}_{-13.79}$	134 \pm 17	40 - 700	10.4 \pm 1.6	40 - 700
010222A	BeppoSAX	1.57 \pm 0.16	-1.35 \pm 0.19	-1.64 \pm 0.02	> 358	925 \pm 28	40 - 700	86.0 \pm 2.0	40 - 700
000926A	BeppoSAX	0.78 \pm 0.78	...	-2.43	365	2.60 \pm 0.70	40 - 700	2.16 \pm 0.87	40 - 700
000911A	KW	...	-0.84	...	134 \pm 10	2300	15 - 8000	200	15 - 8000
000418A	BeppoSAX	2.00 \pm 0.70	2.00 \pm 0.70	40 - 700	1.00 \pm 0.36	40 - 700

Table 10 (cont'd)

GRB	Detector	fluence/flux	Γ	α	β	E_p [keV]	fluence S_γ		peak flux $F_p(P_p)$ Band	reference	
							(1)	(2)	(3)	(4)	(5)
000301C	BeppoSAX	1.79 ± 0.15	83.5 ± 5.3	40 – 700	1.13 ± 0.09	40 – 700	65
000210A	BeppoSAX	1.44 ± 0.16	... −0.91 _{−0.15} ^{+0.20}	−2.02 _{−0.32} ^{+0.18}	−2.22 ± 0.02	168 _{−15} ⁺¹⁷ 382 ± 6	480 ± 37 418	40 – 700 20 – 2000	164.5 ± 13.1 26.7 ± 4.1	40 – 700 30 – 10000	65
000131A	BATSE	...	−1.2 ± 0.01	1730 ± 5	20 – 2000	614 ± 12	30 – 10000	10, 90	
991216A	BATSE	490	25 – 100	51	25 – 100	1	
991208A	Ulysses	1.68 ± 0.19	65.0 ± 3.0	40 – 700	13.0 ± 1.0	40 – 700	3, 65	
990712A	BeppoSAX	1.36 ± 0.18	−1.88 ± 0.07	−2.48 ± 0.56	65.0 ± 10.5	750 ± 80	40 – 700	37.0 ± 1.0	40 – 700	3, 65	
990705A	BeppoSAX	1.40 ± 0.14	−1.05 ± 0.21	−2.2 ± 0.1	188 ± 15	161 ± 16	40 – 700	24.7 ± 2.1	40 – 700	3, 65	
990510A	BeppoSAX	1.98 ± 0.13	−1.23 ± 0.05	−2.7 ± 0.4	161 ± 16	1690 ± 10	20 – 2000	93.6 ± 2.0	30 – 10000	10, 65, 90	
990506A	BATSE	1.48 ± 0.13	−1.17 ± 0.01	−2.62 ± 0.07	341 ± 5	58.9 ± 6.2	20 – 2000	11.9 ± 3.8	40 – 700	65, 90	
990308A	BATSE	...	−0.77 ± 0.14	−2.41 ± 0.41	234 ± 31	3000 ± 400	40 – 700	170 ± 50	40 – 700	3, 65	
990123A	BeppoSAX	1.21 ± 0.13	−0.89 ± 0.08	−2.45 ± 0.97	780 ± 61	5.8 ± 0.8	40 – 700	0.37 ± 0.07	40 – 700	65	
981226A	BeppoSAX	2.38 ± 0.35	398 ± 9	20 – 2000	26.4 ± 5.1	30 – 10000	10, 65, 90	
980703A	BATSE	1.64 ± 0.38	−1.2 ± 0.05	−1.93 ± 0.06	281 ± 32	10.0 ± 2.0	40 – 700	1.60 ± 0.40	40 – 700	3, 65	
980613A	BeppoSAX	0.59 ± 0.35	−1.43 ± 0.24	−2.7 ± 0.6	92.6 ± 42.5	132 ± 8	20 – 2000	29.8	50 – 300	2, 90	
980519A	BATSE	...	−1.47 ± 0.06	−2.23 ± 0.26	252 ± 40.9	45.1 ± 4.18	20 – 2000	1.71 ± 0.27	40 – 700	65, 90	
980425A	BATSE	1.90 ± 0.24	−1.41 ± 0.09	−2.82 ± 0.73	136 ± 12.7	650 ± 50	40 – 700	31.0 ± 1.0	40 – 700	3, 65	
980329A	BeppoSAX	1.74 ± 0.14	−0.64 ± 0.14	−2.2 ± 0.8	236 ± 37	7.5 ± 1.5	40 – 700	2.45 ± 0.15	40 – 700	3, 65	
980326A	BeppoSAX	1.85 ± 0.21	−1.23 ± 0.21	−2.48 ± 0.31	35.5 ± 18.0	88.0 ± 9.0	40 – 700	6.8 ± 0.7	40 – 700	3	
971214A	BeppoSAX	...	−0.76 ± 0.17	−2.7 ± 1.1	154 ± 30	960	20 – 2000	59.3 ± 3.4	30 – 10000	2, 10	
970828A	BATSE	...	−0.45 _{−0.16} ^{+0.06}	−2.06 _{−0.16} ^{+0.08}	379 _{−16} ⁺¹⁵	18.0 ± 3.0	40 – 700	3.4 ± 0.1	40 – 700	3, 65	
970508A	BeppoSAX	1.51 ± 0.18	−1.71 ± 0.10	−2.2 ± 0.25	79.0 ± 23.4	110 ± 10	40 – 700	37.0 ± 1.0	40 – 700	3, 65	
970228A	BeppoSAX	1.92 ± 0.14	−1.54 ± 0.08	−2.5 ± 0.4	115 ± 37	110 ± 10	40 – 700	37.0 ± 1.0	40 – 700	3, 65	
SGRB											
130603B	KW	0.82 ± 0.07	−0.73 ± 0.15	...	660 ± 100	66 ± 7	20 – 10000	21000 ± 200	20 – 10000	96, 107	
101224A	Fermi	1.05 ± 0.26	−0.74 _{−0.43} ^{+0.12}	−1.85 _{−0.12} ^{+0.12}	229 _{−157} ⁺¹⁵⁷	1.91 ± 0.27	10 – 1000	1.31 ± 0.21P	10 – 1000	103, 107	
101219A	KW	0.63 ± 0.09	−0.22 _{−0.30} ^{+0.25}	...	490 _{−79} ⁺¹⁰³	36 ± 5	20 – 10000	2280 ± 80	20 – 10000	74, 107	
100816A	Fermi	1.17 ± 0.06	−0.23 _{−0.09} ^{+0.09}	−2.30 _{−0.09} ^{+0.09}	126 _{−7} ⁺⁷	36.5 ± 0.5	10 – 1000	15.6 ± 0.2P	10 – 1000	103, 107	
100625A	Fermi	0.90 ± 0.10	−0.60 _{−0.15} ^{+0.15}	...	486 _{−80} ⁺⁸⁰	11.0 ± 0.6	10 – 1000	4.9 ± 0.3P	10 – 1000	103, 107	
100206A	Fermi	0.63 ± 0.17	−0.33 _{−0.16} ^{+0.16}	−2.33 _{−0.45} ^{+0.45}	460 _{−92} ⁺⁹²	8.7 ± 0.2	10 – 1000	2.62 ± 0.14P	10 – 1000	103, 107	
100117A	Fermi	0.88 ± 0.22	313 _{−71} ⁺⁷¹	4.2 ± 0.7	10 – 1000	1.59 ± 0.13P	10 – 1000	103, 107	
091109B	Swift	0.70 _{−0.128} ^{+0.132}	1.95 ± 0.16	15 – 150	1.96 ± 0.19	15 – 150	75	
090515A	Swift	1.41 ± 0.24	−0.15 _{−0.24} ^{+1.27}	...	79.8 _{−193} ^{+94.0}	0.2 ± 0.03	15 – 150	5.7 ± 0.9P	15 – 150	107	
090510A	Fermi	0.98 ± 0.20	−0.86 _{−0.03} ^{+0.63}	−2.58 _{−0.29} ^{+0.29}	4301 _{−483} ⁺⁴⁸³	33.7 ± 0.4	10 – 1000	9.1 ± 0.2P	10 – 1000	103, 107	
090426A	Swift	1.93 ± 0.22	1.8 ± 0.3	15 – 150	2.4 ± 0.3P	15 – 150	107	
090305A	Swift	0.789 _{−0.336} ^{+0.367}	0.75 ± 0.14	15 – 150	0.85 ± 0.19	15 – 150	75		
080905A	Fermi	0.795 _{−0.233} ^{+0.251}	...	−2.35 _{−0.67} ^{+0.67}	311 _{−87} ⁺⁸⁷	8.5 ± 0.5	10 – 1000	2.34 ± 0.14P	10 – 1000	75, 103	
080503A	Swift	2.00 ± 0.13	20 ± 1	15 – 150	0.9 ± 0.1P	15 – 150	107		
080123A	Swift	2.15 ± 0.54	5.7 ± 1.7	15 – 150	1.8 ± 0.4P	15 – 150	107		
071227A	KW	0.99 ± 0.22	−0.7	...	1000	16.0 ± 2.0	20 – 1300	335.0 ± 11.0	20 – 1300	50, 107	

Table 10 (cont'd)

GRB	Detector fluence/flux	Γ	α	β	E_p [keV]	fluence S_{γ} [10^{-7} erg cm $^{-2}$]	peak flux $F_p(P_p)$		reference
							Band (8)	(9)	
(1)	(2)	(3)	(4)	(5)	(6)	(7)	(8)	(9)	(11)
070809A	Swift	1.69 ± 0.22	1.0 ± 0.1	15 – 150	1.2 ± 0.2 ^P	15 – 150
070724A	Swift	1.861 ^{+0.296} _{-0.324}	0.31 ± 0.07	15 – 150	0.34 ± 0.09	15 – 150
070714B	Swift	1.398 ^{+0.218} _{-0.219}	7.2 ± 1.0	15 – 150	2.7 ± 0.2 ^P	15 – 150
070707A	INTEGRAL	1.19 ± 0.14	-0.57 ^{+0.43} _{-0.59}	...	427 ⁺³⁷⁴ ₋₁₄₄	2.10	20 – 200	2.10	45, 51
070429B	Swift	1.645 ^{+0.220} _{-0.227}	0.65 ± 0.10	15 – 150	0.73 ± 0.12	15 – 150
061217A	Swift	0.86 ± 0.30	0.42 ± 0.07	15 – 150	1.49 ± 0.24 ^P	15 – 150
061210A	Swift	1.56 ± 0.28	11.10 ± 1.76	15 – 150	5.31 ± 0.47 ^P	15 – 150
061201A	KW	0.81 ± 0.15	-0.36 ^{+0.40} _{-0.65}	...	873 ⁺⁴⁵⁸ ₋₂₈₄	53.3 ^{+44.4} _{-34.4}	20 – 3000	2319 ⁺⁷² ₋₂₇₂	39, 107
061006A	KW	1.72 ± 0.17	-0.62 ^{+0.18} _{-0.21}	...	664 ⁺²²⁷ ₋₁₄₄	35.7 ^{+3.1} _{-19.2}	20 – 2000	2213 ⁺⁴¹ ₋₁₂₀	34, 107
060801A	Swift	0.47 ± 0.24	0.80 ± 0.10	15 – 150	1.27 ± 0.16 ^P	15 – 150
060502B	Swift	0.985 ^{+0.205} _{-0.198}	0.49 ± 0.06	15 – 150	0.62 ± 0.12	15 – 150
060313A	KW	0.70 ± 0.07	-0.60 ^{+0.19} _{-0.19}	...	922 ⁺³⁰⁶ ₋₁₇₇	142 ⁺¹⁰ ₋₈₅	20 – 2000	2700 ⁺¹⁰⁰ ₋₁₃₀	31, 107
060121A	HETE-2/KW	...	-0.51 ^{+0.55} _{-0.60}	-2.39 ^{+0.27} _{-1.41}	104 ⁺¹³⁴ ₋₇₇	47.1 ^{+4.4} _{-37.1}	20 – 1000	3164 ⁺¹⁸ ₋₁₃₂	29
051221A	KW	1.394 ^{+0.055} _{-0.055}	-1.08 ^{+0.13} _{-0.13}	...	402 ⁺⁹³ ₋₇₂	32.0 ^{+17.0} _{-17.0}	20 – 2000	1460 ⁺²⁵⁰ ₋₂₅₀	26, 75
051210A	Swift	1.06 ± 0.28	0.85 ± 0.14	15 – 150	0.75 ± 0.12 ^P	15 – 150
050724A	Swift	1.89 ± 0.22	9.98 ± 1.20	15 – 150	3.26 ± 0.30 ^P	15 – 150
050709A	HETE-2	...	-0.7 ± 0.2	...	83 ⁺¹⁸ ₋₁₂	4 ± 0.4	2 – 400	51 ± 5	2 – 400
050509B	Swift	1.275 ^{+0.405} _{-0.399}	0.07 ± 0.02	15 – 150	0.18 ± 0.10	15 – 150

Note. — Col. (1) GRB name. Col. (2) Detector of fluence and/or peak flux. Col. (3) Spectral Index of power law fitting. Col. (4) Spectral parameters of Band function. Col. (7) γ -ray fluence S_{γ} , in unit of 10^{-7} erg cm $^{-2}$. Col. (8) The observational energy band of the fluence in col. (7). Col. (9) γ -ray 1 second peak flux F_p , in unit of 10^{-7} erg s $^{-1}$ cm $^{-2}$, or peak photon flux P_p , in unit of photons s $^{-1}$ cm $^{-2}$ (with superscript p). ($^{+/-}$) Fluxes from Konus-Wind are not 1 second peak flux. 1. 0.004 s; 2. 0.016 s; 3. 0.064 s; 4. 0.128 s; 5. 0.256 s; 6. 0.5 s; 7. 2.944 s; 8. 3 s. Col. (10) The observational energy band of the flux in col. (9). Col. (11) Reference of prompt emission properties.

References. (1) Hurley et al. (2003); (2) Jimenez et al. (2001); (3) Amati et al. (2002); (4) Price et al. (2002b); (5) Hurley et al. (2002a); (6) Hurley et al. (2002b); (7) Barraud et al. (2004); (8) Amati et al. (2004); (9) Nicastro et al. (2004); (10) Yonetoku et al. (2004); (11) Butler et al. (2004); (12) Golenetskii et al. (2004); (13) Galassi et al. (2004); (14) Sakamoto et al. (2005a); (15) Nakagawa et al. (2005); (16) Golenetskii et al. (2005b); (17) Sakamoto et al. (2005b); (18) Golenetskii et al. (2005c); (19) Boer et al. (2005); (20) Golenetskii et al. (2005a); (21) Crew et al. (2005); (22) Golenetskii et al. (2005d); (23) Golenetskii et al. (2005e); (24) Golenetskii et al. (2005f); (25) Golenetskii et al. (2005g); (26) Golenetskii et al. (2005h); (27) Villasenor et al. (2005); (28) Galli & Piro (2006); (29) Golenetskii et al. (2006b); (30) Golenetskii et al. (2006c); (31) Golenetskii et al. (2006d); (32) Golenetskii et al. (2006e); (33) Golenetskii et al. (2006f); (34) Golenetskii et al. (2006j); (35) Golenetskii et al. (2006g); (36) Golenetskii et al. (2006h); (37) Golenetskii et al. (2006a); (38) Bellm et al. (2006); (39) Golenetskii et al. (2006b); (40) Pal'Shin (2006); (41) Golenetskii et al. (2007b); (42) Golenetskii et al. (2007a); (43) Golenetskii et al. (2007b); (44) Golenetskii et al. (2007c); (45) Golenetskii et al. (2007d); (46) Golenetskii et al. (2007e); (47) Golenetskii et al. (2007f); (48) Golenetskii et al. (2007g); (49) Golenetskii et al. (2007j); (50) Golenetskii et al. (2007h); (51) Foley et al. (2008); (52) Pelandeau et al. (2008); (53) Golenetskii et al. (2008a); (54) Golenetskii et al. (2008b); (55) Golenetskii et al. (2008c); (56) Ohno et al. (2008); (57) Golenetskii et al. (2008d); (58) Golenetskii et al. (2008e); (59) Golenetskii et al. (2008f); (60) Golenetskii et al. (2008g); (61) Golenetskii et al. (2008h); (62) Pal'Shin et al. (2008); (63) Golenetskii et al. (2008i); (64) Nava et al. (2008); (65) Frontera et al. (2009); (66) Golenetskii et al. (2009a); (67) Golenetskii et al. (2009b); (68) Pal'Shin et al. (2009a); (69) Golenetskii et al. (2009b); (70) Golenetskii et al. (2009c); (71) Pal'Shin et al. (2009b); (72) Golenetskii et al. (2010a); (73) Golenetskii et al. (2010b); (74) Golenetskii et al. (2010c); (75) Sakamoto et al. (2011b); (76) Golenetskii et al. (2011a); (77) Golenetskii et al. (2011b); (78) Golenetskii et al. (2011c); (79) Golenetskii et al. (2011d); (80) Golenetskii et al. (2011e); (81) Golenetskii et al. (2011f); (82) Golenetskii et al. (2011g); (83) Sakamoto et al. (2011a); (84) Golenetskii et al. (2011b); (85) Golenetskii et al. (2011c); (86) Golenetskii et al. (2011d); (87) Lazzarotto et al. (2011); (88) Golenetskii et al. (2011k); (89) Guidorzi et al. (2011); (90) Goldstein et al. (2013); (91) Golenetskii et al. (2013e); (92) Golenetskii et al. (2013f); (93) Golenetskii et al. (2013g); (94) Golenetskii et al. (2013h); (95) Frederiks (2013); (96) Golenetskii et al. (2013i); (97) Golenetskii et al. (2013j); (98) Golenetskii et al. (2013a); (99) Golenetskii et al. (2013b); (100) Golenetskii et al. (2013c); (101) Golenetskii et al. (2013d); (102) Bosnjak et al. (2014); (103) Gruber et al. (2014); (104) Golenetskii et al. (2014a); (105) Golenetskii et al. (2014b); (106) Serino et al. (2014); (107) GRBtable; 134

Table 11. Host Information from the Spectrum

GRB	z	Instrument (Spectrum)	log M_*		SFR		[X/H]		A_V method (11)	method (12)	reference (13)
			[M_\odot] (4)	method (5)	[$M_\odot \text{ yr}^{-1}$] (6)	method (7)	sSFR [Gyr^{-1}] (8)	method (9)			
140606B	0.384	GTC/OSRIS	0.052 ± 0.005	H α	0.3 ^{+0.89} _{-0.30}	Balmer	87
140518A	4.707	Gemini/GMOS	79
140515A	6.32	GTC/OSRIS	0.11 ± 0.02	AG-SED	75
140512A	0.725	NOT/ALFOSC	0
140508A	1.027	NOT/ALFOSC	0
140506A	0.8893	VLT/X-Shooter	9	SED	0.35 ^{+0.35} _{-0.19}	H α	0.35	68,77
140430A	1.6019	VLT/X-Shooter	8.5 ^{+7.1} _{-3.8}	H α	...	-0.020 ^{+0.18} _{-0.19}	E	...	77
140428A	4.7	Keck I/LRIS	0
140423A	3.26	Gemini/GMOS	> -1.44	A/Fe	...	79
140419A	3.956	Gemini/GMOS	0
140318A	1.02	WHT/ACAM	0
140311A	4.954	Gemini/GMOS	> -1.65	A/Ni	...	79
140304A	5.283	GTC/OSRIS	0
140301A	1.4155	VLT/X-Shooter	106 ⁺³⁶ ₋₂₅	H α	...	0.200 ^{+0.09} _{-0.09}	E	2.49 ^{+0.36} _{-0.33}	Balmer
140226A	1.98	Keck I/LRIS	> -0.54	A/Fe	...	77
140213A	1.2079	VLT/X-Shooter	0.72 ^{+2.65} _{-0.34}	H α	0.20 ^{+2.39} _{-0.20}	Balmer	77
140206A	2.739	NOT/ALFOSC	UV	0
140114A	3	VLT/X-Shooter	24.5 ^{+6.0} _{-5.3}	81
131231A	0.6427	VLT/X-Shooter	1.38 ^{+0.38} _{-0.20}	H α	...	-0.240 ^{+0.11} _{-0.12}	E	0.07 ^{+0.27} _{-0.07}	Balmer
131227A	5.3	Gemini/GMOS	0
131117A	4.042	VLT/X-Shooter	0
131108A	2.4	GTC/OSRIS	0
131105A	1.6854	VLT/X-Shooter	31 ⁺²⁵ ₋₁₃	H α	...	-0.080 ^{+0.17} _{-0.20}	E	1.76 ^{+0.70} _{-0.60}	Balmer
131103A	0.5960	VLT/X-Shooter	4.4 ^{+1.2} _{-0.9}	H α	...	-0.210 ^{+0.10} _{-0.12}	E	0.20 ^{+0.23} _{-0.20}	Balmer
131030A	1.293	NOT/ALFOSC	0
131011A	1.874	VLT/X-Shooter	0
131004A	0.717	Magellan/LDSS	0
130925A	0.3483	VLT/X-Shooter	9.5 ± 0.2	SED	2.9 ^{+0.5} _{-0.4}	H α	0.92	0.040 ^{+0.08} _{-0.08}	E	1.36 ^{+0.20} _{-0.20}	Balmer
130907A	1.238	NOT/ALFOSC	0
130831A	0.4791	Gemini/GMOS	0
130702A	0.145	Keck II/DEIMOS	7.9 ± 0.7	SED	0.05	H α	0.63	< -0.530	E/PP04/N2	0	Balmer
130701A	1.1548	VLT/X-Shooter	0.78 ^{+2.03} _{-0.60}	[OIII]	57
130612A	2.006	VLT/X-Shooter	77
130610A	2.092	VLT/UVEs	0
130606A	5.913	VLT/X-Shooter	-1.3 ± 0.4	A/Si	...	74
130604A	1.06	Gemini	0
130528A	1.25	GTC/OSRIS	6.8	[OIII]	hostSED	67
130518A	2.49	GTC/OSRIS	0
130511A	1.3033	Gemini/GMOS	0

Table 11 (cont'd)

GRB	z	Instrument (Spectrum) (2)	$\log M_*$ method (4)	$\log M_*$ method (5)		SFR method (6)	[Gyr $^{-1}$] method (7)	sSFR [Gyr $^{-1}$] (8)	[X/H] method (9)	A_V method (11)	A_V method (12)	reference (13)	
				[M \odot] (4)	method (5)								
130505A	2.27	Gemini/GMOS	> -1.42	A/Fe	...	79	
130427B	2.78	VLT/X-Shooter	0	
130427A	0.3401	VLT/X-Shooter	9 ± 0.2	SED	0.34 $^{+0.20}_{-0.06}$	H α	0.34	-0.120 $^{+0.12}_{-0.13}$	E	0.20 $^{+0.63}_{-0.20}$	Balmer	58, 77	
130420A	1.297	GTC/OSIRIS	0	
130418A	1.217	VLT/X-Shooter // GROND	0	
130408A	3.757	VLT/X-Shooter // GROND	-1.24 ± 0.12	A/S	...	79, 81	
130215A	0.597	Shane/KAST	0	
130131B	2.5393	VLT/X-Shooter	8.0 $^{+13.4}_{-5.0}$	[OIII]	77	
121229A	2.707	VLT/X-Shooter	0	
121211A	1.023	Keck I/LRIS	0	
121209A	2.1	VLT/X-Shooter	0	
121201A	3.3830	VLT/X-Shooter	30 $^{+68}_{-21}$	[OIII]	77	
121128A	2.20	Gemini/GMOS	0	
121027A	1.7732	VLT/X-Shooter	9.9 $^{+0.2}_{-0.3}$	SED	24 $^{+41}_{-15}$	[OIII]	77	
121024A	2.3012	VLT/X-Shooter	37 $^{+4}_{-4}$	H α	4.66	-0.280 $^{+0.11}_{-0.12}$	E	0.00 $^{+0.40}_{-0.00}$	Balmer	77, 86
120922A	3.1	VLT/X-Shooter	< 7.5	UV	81	
120909A	3.93	GTC/OSIRIS	24.7	UV	...	-0.66 ± 0.11	A/S	...	79, 81	
120907A	0.970	VLT/X-Shooter	< 10	line-width	...	2.3 $^{+2.7}_{-1.0}$	H α	...	-0.93 ± 0.13	A/Zn	0.20 $^{+1.13}_{-0.20}$	Balmer	52, 77, 79
120815A	2.3587	GTC/OSIRIS	0	
120811C	2.671	VLT/X-Shooter	39.0 $^{+9.5}_{-8.3}$	UV	81	
120805A	3.1	Gemini/GMOS	0	
120802A	3.796	Gemini/GMOS	8.3 ± 0.2	SED	6 $^{+25}_{-4.0}$	SED	30.07	66	
120729A	0.80	VLT/X-Shooter	0	
120724A	1.48	Gemini/GMOS	0	
120722A	0.9590	VLT/X-Shooter	22 $^{+4}_{-4}$	H α	...	-0.210 $^{+0.10}_{-0.10}$	E	1.52 $^{+0.17}_{-0.17}$	Balmer	77
120716A	2.486	VLT/X-Shooter	> -1.76	A/Fe	...	79	
120714B	0.3985	VLT/X-Shooter	0.27 $^{+0.07}_{-0.05}$	H α	...	-0.300 $^{+0.11}_{-0.11}$	E	0.33 $^{+0.27}_{-0.27}$	Balmer	77
120712A	4.1745	VLT/X-Shooter	0	
120711A	1.405	Gemini/GMOS	0	
120624B	2.1974	VLT/X-Shooter	10.6 $^{+0.3}_{-0.2}$	SED	30 $^{+73}_{-13}$	H α	0.75	-0.260 $^{+0.20}_{-0.27}$	E	0.70 $^{+1.66}_{-0.70}$	Balmer	53, 77	
120422A	0.2826	VLT/X-Shooter	8.95 ± 0.04	SED	1.38 $^{+0.13}_{-0.12}$	H α	1.55	-0.300 $^{+0.09}_{-0.09}$	E	0.90 $^{+0.10}_{-0.10}$	Balmer	65, 77	
120404A	2.876	Gemini/GMOS	0	
120327A	2.813	VLT/X-Shooter	> 10	...	5	-1.51 ± 0.11	A/S	0.22	...	63, 79	
120326A	1.798	GTC/OSIRIS	0	
120224A	1.1	VLT/X-Shooter	0	
120211A	2.4	VLT/X-Shooter	0	
120119A	1.7291	VLT/X-Shooter	9.3	SED	43 $^{+24}_{-14}$	H α	21.55	-0.090 $^{+0.14}_{-0.14}$	E	1.16 $^{+0.53}_{-0.46}$	Balmer	71, 77	
120118B	2.9428	VLT/X-Shooter	28 $^{+21}_{-11}$	H β	...	-0.800 $^{+0.23}_{-0.17}$	E	0.00 $^{+0.53}_{-0.00}$	Balmer	77	
111229A	1.3805	Gemini/GMOS	0	

Table 11 (cont'd)

GRB	z	Instrument (Spectrum) (3)	$\log M_*$		SFR [M $_{\odot}$ yr $^{-1}$] (6)	method (7)	sSFR [Gyr $^{-1}$] (8)	[X/H] method (9)	A_V [mag] (11)	A_V method (12)	reference (13)	
			[M $_{\odot}$] (4)	method (5)								
111228A	0.7164	VLT/X-Shooter	0.32 $^{+0.56}_{-0.22}$	H β	77	
111225A	2.012	Keck II/NIRSPEC	34 $^{+13}_{-13}$	SED	1.08	0	
111215A	2.06	Keck II	10.5 $^{+0.1}_{-0.2}$	SED	0.12 $^{+0.29}_{-0.03}$	H α	0.465	hostSED	84	
111211A	0.4786	VLT/X-Shooter	0.35 $^{+0.26}_{-0.13}$	H α	...	-0.740 $^{+0.30}_{-0.17}$	E	0.00 $^{+1.89}_{-0.00}$	Balmer	77
111209A	0.6770	VLT/X-Shooter	5.1 $^{+1.0}_{-1.3}$	[OH]	0.53 $^{+0.66}_{-0.53}$	Balmer	77	
111129A	1.0796	VLT/X-Shooter	77 $^{+163}_{-52}$	[OH]	...	-0.680 $^{+0.28}_{-0.28}$	E	77
111123A	3.1513	VLT/X-Shooter	>-0.45	A/S	77
111107A	2.893	VLT/X-Shooter	<9.9	UV	...	-1.63 ± 0.13	A/Fe	0.11 ± 0.04	...	70, 79, 81
111008A	4.9898	VLT/X-Shooter	0.16	UV	0.03	78	
111005A	0.0133	...	9.68	SED	23 $^{+28}_{-11}$	H α	0.48	0.240 $^{+0.11}_{-0.11}$	E	1.16 $^{+1.03}_{-1.03}$	Balmer	61, 77
110918A	0.9843	VLT/X-Shooter	10.68 ± 0.16	SED	44 $^{+62}_{-26}$	H β	...	-0.440 $^{+0.17}_{-0.25}$	E	77
110818A	3.3609	VLT/X-Shooter	8.3 $^{+11.3}_{-3.6}$	H α	...	-0.760 $^{+0.31}_{-0.23}$	E	0.99 $^{+1.13}_{-0.83}$	Balmer	77
110808A	1.3490	VLT/X-Shooter	0
110801A	1.858	GTC/OIRIS	0
110731A	2.83	Gemini/GMOS	0
110726A	1.036	Gemini/GMOS	0
110715A	0.82	VLT/X-Shooter	0
110709B	2.09	VLT/X-Shooter	1.1	UV	54
110503A	1.613	GTC/OIRIS	0
110422A	1.770	GTC/OIRIS	0
110213B	1.083	Gemini	0
110213A	1.46	Bok/BC	0
110205A	2.22	FLWO/FAST	79
110128A	2.339	VLT/X-Shooter	0
110106B	0.618	Gemini/GMOS	0
101225A	0.847	Gemini/GMOS	0
101219B	0.55185	VLT/X-Shooter	0
100906A	1.727	Gemini/GMOS	0
100901A	1.408	Gemini/GMOS	0
100814A	1.4392	VLT/X-Shooter	3.2 $^{+2.9}_{-0.7}$	H α	0.27 $^{+0.86}_{-0.27}$	Balmer	77	
100728B	2.106	VLT/X-Shooter	0	
100728A	1.5670	VLT/X-Shooter	14.5 $^{+60.6}_{-8.0}$	H α	0.76 $^{+2.29}_{-0.76}$	Balmer	77	
100724A	1.2890	VLT/X-Shooter	3.2 $^{+6.1}_{-1.4}$	H α	...	-0.490 ± 0.1	E/KK04	0.80 $^{+1.23}_{-0.76}$	77, 88	
100621A	0.5426	VLT/X-Shooter	8.98 $^{+0.14}_{-0.10}$	SED	8.7 $^{+0.8}_{-0.8}$	H α	9.11	-0.170 $^{+0.10}_{-0.10}$	E	0.17 $^{+0.10}_{-0.10}$	Balmer	35, 77
100615A	1.3978	VLT/X-Shooter	8.6 $^{+3.9}_{-3.9}$	H α	...	-0.290 $^{+0.12}_{-0.13}$	E	1.59 $^{+1.26}_{-0.93}$	Balmer	77
100606A	1.5545	VLT/X-Shooter	4.9 $^{+5.4}_{-2.9}$	H α	...	0.020 $^{+0.19}_{-0.21}$	E	0.17 $^{+1.99}_{-0.17}$	Balmer	77
100518A	4	<0.5	UV	81	
100513A	4.772	Gemini/GMOS	6.0	UV	...	-0.010 $^{+0.10}_{-0.10}$	E	0.96 $^{+0.30}_{-0.30}$	Balmer	81
100508A	0.5201	VLT/X-Shooter	2.6 $^{+0.7}_{-0.5}$	H α	77	

Table 11 (cont'd)

GRB	z	Instrument (Spectrum) (3)	$\log M_*$			SFR			$[X/H]$			A_V method (12)	reference (13)
			[M $_{\odot}$] (4)		method (5)	[M $_{\odot}$ yr $^{-1}$] (6)		method (7)	[Gyr $^{-1}$] (8)		method (9)		
		
100425A	1.755	VLT/X-Shooter	-0.96 ± 0.42	A/Fe	79
100424A	2.4656	VLT/X-Shooter	21 $^{+20}_{-8}$	H β	...	-0.760 $^{+0.25}_{-0.18}$	E	0.43 $^{+0.60}_{-0.43}$	Balmer	77
100418A	0.6235	VLT/X-Shooter	9.54 $^{+0.28}_{-0.03}$	SED	4.2 $^{+1.0}_{-0.8}$	H α	1.21	-0.170 $^{+0.10}_{-0.10}$	E	0.56 $^{+0.20}_{-0.23}$	Balmer	51,77	
100414A	1.368	Gemini/GMOS	1.7	H α	1.91	-0.390 ± 0.1	E/PP04	0	...	0
100316D	0.0592	Magellan/Clay	8.95	SED	2.5 ± 0.2	[OII]	...	-0.290	E/KK04	0 $^{+0.05}_{-0.00}$	Balmer	32,39,78	
100316B	1.180	VLT/X-Shooter	Balmer	88
100302A	4.813	Gemini	5.1	UV	...	-0.900 ± 0.5	A/O	0.13 ± 0.05	hostSED	0
100219A	4.6667	VLT/X-Shooter	60,81
091208B	1.0633	Keck I/HIRES	0
091127A	0.4904	VLT/X-Shooter	8.3	SED	0.37 $^{+0.10}_{-0.07}$	H α	1.85	-0.620 $^{+0.18}_{-0.20}$	E	0.53 $^{+0.30}_{-0.27}$	Balmer	36,77	
091109A	3.076	VLT/FORS2	4.2	UV	81
091029A	2.752	Gemini/GMOS	0.00 $^{+0.04}_{-0.00}$	AGSED	34
091024A	1.092	Gemini/GMOS	0
091020A	1.71	NOT/ALFOSC	0
091018A	0.9710	VLT/X-Shooter	9.52 $^{+0.08}_{-0.10}$	SED	1.29 $^{+3.46}_{-0.32}$	H α	0.39	0.090 $^{+0.18}_{-0.19}$	E	0.20 $^{+1.86}_{-0.20}$	Balmer	76,77	
091003A	0.8969	Gemini/GMOS	0
090927A	1.37	VLT/FORS2	0
090926B	1.2427	VLT/X-Shooter	10.1 $^{+0.4}_{-0.5}$	SED	26 $^{+1.9}_{-11}$	H α	2.07	-0.350 $^{+0.15}_{-0.17}$	E	2.09 $^{+0.66}_{-0.60}$	Balmer	35,77	
090926A	2.1062	VLT/FORS2	-1.89	A/S	< 0.10	AGSED	27,33	
090902B	1.822	Gemini/GMOS	0.05 ± 0.05	AGSED	33	
090814A	0.696	VLT/FORS2	0.05 $^{+0.14}_{-0.05}$	AGSED	34	
090812A	2.452	VLT/FORS2	0.41 $^{+0.04}_{-0.09}$	AGSED	34,79	
090809A	2.737	VLT/X-Shooter	-0.57 ± 0.10	A/Si	79
090726A	2.71	SAO RAS6m/SCORPIO	0
090715B	3.00	WHT/ISIS	0
090709A	1.7	Lick/KAST	9.98 $^{+0.21}_{-0.08}$	SED	8.0 $^{+4.1}_{-4.1}$	SED	0.84	1.40 $^{+0.12}_{-0.38}$	hostSED	59	
090618A	0.54	VLT/X-Shooter	0
090530A	1.266	VLT/FORS2	0
090529A	2.625	VLT/FORS2	< 2.0	UV	0
090519A	3.85	VLT/FORS2	20.4	UV	> -1.36	A/Si	...	34,81
090516A	4.109	VLT/FORS2	9.38 $^{+0.17}_{-0.19}$	SED	0.56 ± 0.24	Hab	0.23	-0.260	E	79,81
090424A	0.544	VLT/JISAAC	56,76
090423A	8.23	Lick3m/KAST	0
090418A	1.608	Gemini/GMOS	9.54 $^{+0.04}_{-0.06}$	SED	0.5 $^{+0.3}_{-0.3}$	SED	0.14	0.87 $^{+0.12}_{-0.08}$	hostSED	59	
090417B	0.345	VLT/X-Shooter	10.18 $^{+0.17}_{-0.14}$	SED	13.8 $^{+0.8}_{-6.7}$	H α	0.91	0.160 $^{+0.13}_{-0.13}$	E	2.29 $^{+1.13}_{-0.86}$	Balmer	59,77	
090407A	1.4478	VLT/FORS1	9.24	SED	4.8	[OII]	2.76	0.01 $^{+0.19}_{-0.01}$	AGSED	22	
090328A	0.7357	VLT/X-Shooter	11.2 ± 0.75	SED	24 $^{+53}_{-17}$	[OII]	0.15	0.67 ± 0.34	A/Si	0.14 $^{+0.04}_{-0.03}$	AGSED	22,49,77,82	
090323A	3.5832	VLT/X-Shooter	< 14.2	UV	...	-1.7 ± 0.3	A/Fe	0.42 $^{+0.06}_{-0.05}$	AGSED	34,81,82	
090313A	3.375	0

Table 11 (cont'd)

GRB	z	Instrument (Spectrum)	$\log M_*$		SFR		sSFR		[X/H]		A_V		reference (13)
			[M $_{\odot}$] (4)	method (5)	[M $_{\odot}$ yr $^{-1}$] (6)	method (7)	[Gyr $^{-1}$] (8)	method (9)	[mag] (11)	method (12)			
080330A	1.5119	NOT/ALFOSC	... Subaru/MOIRCS	... 11.02 $^{+0.05}_{-0.09}$ 12.22	SED IR	47 \pm 1.5 0.13	H α SED	0.45 1.11	E/KK04	0.10 $^{+0.03}_{-0.08}$ 1.17 $^{+0.14}_{-0.17}$	AGSED hostSED
080325A	1.78	Gemini/GMOS	8.07 $^{+0.98}_{-0.53}$	SED	80
080319C	1.9492	VLT/FORS2	0	hostSED	...	89
080319B	0.9382	VLT/UVES	28
080310A	2.4274	VLT/FORS2	-1.3 \pm 0.2 -1.21 \pm 0.16 0.050 $^{+0.15}_{-0.15}$	A/C A/Si E	0.18 $^{+0.03}_{-0.03}$ 2.19 $^{+0.93}_{-0.83}$ 0.00 $^{+0.06}_{-0.00}$	AGSED Balmer AGSED	
080210A	2.6419	VLT/X-Shooter	11.05 \pm 0.02	SED	H α	0.69	40
080207A	2.0856	VLT/FORS1	50,77
080129A	4.349	Gemini/GMOS	34
071122A	1.14	VLT/FORS1	0
071117A	1.3308	VLT/FORS1	8.89 $^{+0.15}_{-0.18}$	SED	0
071112C	0.8227	VLT/FORS1	76
071031A	2.692	VLT/FORS2	11.08 $^{+0.02}_{-0.03}$	SED	...	1.28 \pm 0.15 32 $^{+20}_{-12}$	Lya H α	...	-1.85 \pm 0.12 0.27	A/Fe	0.02 $^{+0.03}_{-0.02}$ 0.63 $^{+0.53}_{-0.56}$	AGSED Balmer	
071021A	2.4515	VLT/X-Shooter	59,77
071020A	2.1462	VLT/FORS2	0
071010B	0.947	Gemini/GMOS	0
071010A	0.98	Keck/LRIS	0
071003A	1.60435	Keck/LRIS	34
070810A	2.17	Keck/LRIS	0
070802A	2.4538	VLT/FORS2	9.7 $^{+0.2}_{-0.3}$	SED	...	24 $^{+11}_{-8}$	H α	4.79	>-0.54	A/Si	1.03 $^{+0.40}_{-0.40}$	Balmer	
070721B	3.6298	VLT/FORS2	1.25 \pm 0.17	Lya	...	>-2.14	A/Si	47,79
070714A	1.58	Keck/LRIS	0
070612A	0.617	Keck/LRIS	-0.400	E/R23	26
070611A	2.0394	VLT/FORS2	280 \pm 120	[OII] IR	85
070529A	2.4996	Gemini/GMOS	31
070521A	2.0865	VLT/X-Shooter	10.49 $^{+0.27}_{-0.06}$	SED	...	26 $^{+34}_{-17}$	H α	0.84	2.21 $^{+0.15}_{-0.11}$	hostSED	
070518A	1.161	Keck/LRIS	0
070508A	0.82	VLT/FORS1	0.52 \pm 0.13	Lya	0
070506A	2.3090	VLT/FORS1	21 $^{+35}_{-11}$	H α	47,79
070419B	1.9586	VLT/X-Shooter	77
070419A	0.9705	Gemini/GMOS	0
070411A	2.9538	VLT/FORS2	< 0.21	AGSED	
070328A	2.0627	VLT/X-Shooter	8.4 $^{+130.7}_{-4.2}$	H β	0.53 $^{+2.62}_{-0.53}$	Balmer	
070318A	0.8401	VLT/X-Shooter	0.79 $^{+0.44}_{-0.24}$	H α	4.11	-0.150 $^{+0.09}_{-0.09}$	E	0.50 $^{+0.46}_{-0.23}$	Balmer	
070306A	1.4965	VLT/X-Shooter	10.39 $^{+0.19}_{-0.15}$	SED	...	101 $^{+1.8}_{-2.3}$	[OIII]	35,77
070224A	1.9922	VLT/X-Shooter	3.2 $^{+6.5}_{-2.3}$	H α	77
070223A	1.6295	Keck/LRIS	20 $^{+28}_{-7}$	H α	0
070208A	1.165	Gemini/GMOS	< 1	[OIII]	77
070129A	2.3384	VLT/X-Shooter	0.56 $^{+1.16}_{-0.56}$	Balmer	
070125A	1.547	VLT/FORS2	14

Table 11 (cont'd)

GRB	z	Instrument (Spectrum)	$\log M_*$			SFR			[X/H]			A_V			reference
			(1)	(2)	(3)	[M \odot] (4)	method (5)	[M \odot yr $^{-1}$] (6)	method (7)	[Gyr $^{-1}$] (8)	method (9)	[mag] (11)	method (12)	(13)	
070110A	2.3523	VLT/FORS2	8.9 $^{+10.9}_{-2.8}$	H α	...	> -1.32	A/Si	0.00 $^{+1.26}_{-0.00}$	Balmer	77,79		
070103A	2.6208	VLT/X-Shooter	43 $^{+162}_{-17}$	H β	0.00 $^{+1.66}_{-0.00}$	Balmer	77		
061222B	3.355	Keck/LRIS	9.11 $^{+0.37}_{-0.20}$	SED	...	2.7 $^{+0.2}_{-0.2}$	SED	2.10	0.00 $^{+0.00}_{-0.00}$	hostSED	59		
061222A	2.088	VLT/X-Shooter	43 $^{+60}_{-22}$	H α	1.92 $^{+1.13}_{-0.90}$	Balmer	77		
061202A	2.2543	Keck/LRIS	10.31 \pm 0.47	SED	2.38	[OII]	0.12	0.13 $^{+0.03}_{-0.03}$	AGSED	19,31		
061126A	1.1588	Keck/LRIS	5.5	UV	...	> -1.84	A/S	38,79,81	
061121A	1.3145	VLT/FORS1	< 9.30	IR	...	0.23 $^{+0.38}_{-0.15}$	H β	0.36 $^{+0.66}_{-0.36}$	Balmer	76,77		
061110B	0.7578	VLT/X-Shooter	0.05 $^{+0.03}_{-0.01}$	H α	0.16	0.45 \pm 0.01	AGSED	31		
061021A	0.3453	VLT/X-Shooter	8.5 $^{+0.5}_{-0.5}$	SED	38,45,79	
061007A	1.2622	Magellan	< 0.9	UV	...	> -1.55	A/S	38,77,79	
060927A	5.4636	VLT/FORS1	< 9.48	IR	...	26 $^{+47}_{-47}$	[OIII]	2.16	> -1.32	A/Zn	38,77,79	
060926A	3.2090	VLT/FORS1	10.08 \pm 0.18	IR	...	3.0 $^{+1.5}_{-2.9}$	H α	38,77,79	
060923B	1.5094	VLT/X-Shooter	88.4 $^{+3.6}_{-30.3}$	SED	0.86	1.89 $^{+0.15}_{-0.14}$	hostSED	59		
060923A	2.6	VLT/X-Shooter	11.01 $^{+0.03}_{-0.06}$	SED	5.1 $^{+2.1}_{-1.6}$	H α	3.00	-0.080 $^{+0.11}_{-0.12}$	E	0.53 $^{+0.33}_{-0.30}$	Balmer	76,77			
060912A	0.9362	VLT/FORS	9.23 $^{+0.06}_{-0.07}$...	1.76 $^{+0.22}_{-0.22}$	Lya	< 0.17	AGSED	31,47			
060908A	1.8836	VLT/FORS1	< 9.40	IR	< 8.2	UV	...	> -1.72	A/S	38,79,81		
060906A	3.6856	VLT/FORS2		
060904B	0.7029	VLT/X-Shooter	9.99 $^{+0.04}_{-0.05}$	SED	54 $^{+89}_{-19}$	H α	5.53	0.06 \pm 0.02	AGSED	31			
060814A	1.9223	VLT/X-Shooter	9.00 $^{+0.04}_{-0.05}$	SED	9.0 $^{+3.9}_{-5.5}$	H α	0.56 $^{+1.29}_{-0.56}$	Balmer	59,77			
060805A	2.3633	VLT/X-Shooter	0.96 $^{+2.51}_{-2.21}$	H α	0.71	0.00 $^{+0.00}_{-0.00}$	Balmer	77		
060729A	0.5429	VLT/X-Shooter	9.13 $^{+0.04}_{-0.08}$	SED	7.1 $^{+18.69}_{-3.9}$	H α	0.56	-0.080 $^{+0.20}_{-0.24}$	E	2.35 $^{+1.43}_{-1.52}$	Balmer	41,77			
060719A	1.5318	VLT/X-Shooter	10.1 $^{+0.03}_{-0.19}$	SED	1.33 $^{+1.52}_{-1.16}$	Balmer	59,77			
060714A	2.7108	VLT/FORS1	0.8	Lya	...	> -0.97	A/Zn	0.46 $^{+0.12}_{-0.17}$	AGSED	7,31,79		
060707A	3.4246	VLT/FORS2	9.95 \pm 0.39	IR	19.9 $^{+48.0}_{-14.3}$	[OII]	2.23	> -1.69	A/Fe	38,77,79		
060614A	0.125	Gemini/GMOS	7.95 \pm 0.13	SED	0.01	H α	0.11	> -1.3	E	0.05 \pm 0.02	AGSED	11,19,33			
060607A	3.0749	VLT/UVES	< 9.23	IR	< 0.1	UV	< 0.15	AGSED	31,38,81			
060605A	3.773	VLT/X-Shooter	< 9.34	IR	2.07 $^{+0.33}_{-0.36}$	Lya	0.25 $^{+0.06}_{-0.06}$	AGSED	31,38,47			
060604A	2.1355	VLT/FORS1	7.2 $^{+9.4}_{-3.6}$	H α	...	-0.590 $^{+0.28}_{-0.35}$	E	1.26 $^{+1.06}_{-0.90}$	Balmer	77			
060602A	0.787	VLT/FORS1	< 0.4	UV	...	-0.57 \pm 0.25	A/S	...	0	...		
060526A	3.2213	VLT/FORS1	< 9.28	IR	< 0.07	AGSED	25,31,38,81			
060522A	5.11	Keck/LRIS	0	...		
060512A	0.4428	Keck/LRIS	0.47 \pm 0.05	AGSED	31			
060510B	4.9	Gemini/GMOS	12.0	UV	...	> -0.84	A/S	79,81			
060505A	0.0889	VLT/FORS	9.41 \pm 0.01	SED	0.43	H α	0.17	-0.250	E	0.53 \pm 0.08	Balmer	19,20			
060502A	1.5026	Gemini/GMOS	0.51 $^{+0.12}_{-0.10}$	AGSED	31			
060418A	1.4901	Magellan/MIKE	8.3 $^{+6.9}_{-4.3}$	SED	0.39	-1.65	A/Si	< 0.06	AGSED	13,31			
060319A	1.172	Keck/LRIS	10.33 $^{+0.15}_{-0.07}$	SED	17.6 $^{+3.6}_{-11.0}$	H α	2.22	0.91 $^{+0.24}_{-0.24}$	hostSED	59			
060306A	1.5597	VLT/X-Shooter	9.90 $^{+0.09}_{-0.05}$	SED	1.46 $^{+2.29}_{-1.33}$	Balmer	59,77			

Table 11 (cont'd)

GRB	z	Instrument (Spectrum) (3)	$\log M_*$		SFR		[X/H]		A_V		reference (13)
			M_{\odot} (4)	method (5)	$[M_{\odot} \text{ yr}^{-1}]$ (6)	method (7)	[Gyr $^{-1}$] (8)	method (9)	[mag] (11)	method (12)	
060223A	4.406	Keck/LRIS	7.78 ± 0.08	SED	1.1	UV	...	> -1.8	A/S	0.00 ± 0.02	Balmer
060218A	0.03351	VLT/FORS1	10.14 ± 0.32	IR	0.05	H α	0.83	-0.560	E
060210A	3.9122	Gemini/GMOS	< 9.32	IR	45.5	UV	3.30	> -0.83	A/Si
060206A	4.0559	Lick/KAST	1.2	UV	...	> -0.74	A/S	< 0.04	AGSED
060204B	2.3393	VLT/X-Shooter	9.04 $^{+0.20}_{-0.04}$	SED	78 $^{+85}_{-34}$	H α	1.13 $^{+0.96}_{-0.76}$	Balmer
060202A	0.785	Keck/LRIS	5.8 $^{+1.1}_{-2.0}$	SED	5.29	1.00 $^{+0.10}_{-0.20}$	hostSED
060124A	2.3	Keck/LRIS	0.08 ± 0.03	AGSED
0601123A	0.56	Keck/LRIS
060115A	3.5328	VLT/FORS1	< 9.41	IR	2.1	UV	...	> -1.53	A/S
060111A	2.32	Keck/LRIS	0
051117B	0.4805	VLT/X-Shooter	4.7 $^{+4.9}_{-2.2}$	H α	...	0.310 $^{+0.16}_{-0.16}$	E	2.39 $^{+0.90}_{-0.80}$	Balmer
051111A	1.55	Keck/HIRES	30	UV
051109B	0.080	Keck/LRIS
051109A	2.346	Hobby-Eberly/MLRS	< 0.14	AGSED
051022A	0.8061	BTA/SCORPIO	10.42 ± 0.18	SED	60 $^{+12}_{-10}$	H α	2.28	-0.200 $^{+0.09}_{-0.09}$	E	1.86 $^{+0.17}_{-0.13}$	Balmer
051016B	0.9358	VLT/X-Shooter	9.69 $^{+1.43}_{-0.08}$	SED	10.2 $^{+2.6}_{-2.0}$	H α	...	-0.420 $^{+0.15}_{-0.20}$	E	0.17 $^{+0.23}_{-0.17}$	Balmer
051008A	2.77	VLT/FORS2	72.1 $^{+25.5}_{-54.4}$	SED	14.72	0.85 $^{+0.07}_{-0.58}$	hostSED
051006A	1.059	VLT/X-Shooter	110 $^{+124}_{-59}$	H α	0
051001A	2.4295	VLT/UVES
050922C	2.1992	VLT/X-Shooter	10.56 $^{+0.19}_{-0.12}$	SED	196 $^{+1563}_{-174}$	H β	5.40	1.92 $^{+0.93}_{-0.93}$	Balmer
050915A	2.5275	VLT/FORS1	< 9.30	IR	0.7	UV	0.07 ± 0.02	AGSED
050908A	3.3467	Subaru/FOCAS	< 10.0	SED	> -1.0	A/S	0.01 ± 0.02	AGSED
050904A	6.295	MDM2.4m/CCDS	9.79 ± 0.11	SED	9.13	[OII]	1.48	0.140	E/R23	0.1 $^{+0.2}_{-0.1}$	linefit
050826A	0.296	VLT/X-Shooter	1.20 $^{+0.30}_{-0.26}$	H α	...	-0.580 $^{+0.18}_{-0.20}$	E	0.00 ± 0.00	Balmer
050824A	0.8277	VLT/FORS1	9.25 $^{+1.2}_{-0.2}$	SED
050822A	1.434	VLT/UVES	-0.76 ± 0.13	A/S	0.18 $^{+0.01}_{-0.01}$	AGSED
050820A	2.61469	VLT/X-Shooter	22 $^{+426}_{-15}$	H β	1.13 $^{+2.78}_{-1.13}$	Balmer
050819A	2.50412	NOT/ALFOSC	9.93 ± 0.46	IR
050814A	5.3	VLT/UVES	< 9.41	IR	< 0.3	UV	0.06 ± 0.02	AGSED
050802A	1.7102	VLT/X-Shooter	8.1 $^{+0.6}_{-0.6}$	SED	12.9 $^{+14.0}_{-5.3}$	H α	0.56	0.16 ± 0.03	AGSED
050730A	3.96855	VLT/X-Shooter	0.07 $^{+0.21}_{-0.21}$	H α	...	-1.96 ± 0.11	A/S	0.70 $^{+0.93}_{-0.70}$	Balmer
050714B	2.4383	Keck/LRIS	< 9.30	IR	< 3.5	Lya	...	> -1.2	A/S	0.33 $^{+2.06}_{-0.33}$...
050525A	0.6063	Keck/LRIS	9.84 ± 0.74	SED	4.5 $^{+1.6}_{-1.2}$	H α	0.65	-0.230 $^{+0.11}_{-0.11}$	E	1.62 $^{+0.36}_{-0.36}$	Balmer
050505A	4.2748	Magellan/Clay	0
050502A	3.793	VLT/FORS2	> -1.07	A/Zn	0.57	AGSED
050416A	0.6542	NOT/ALFOSC	9.78 ± 0.51	IR	19.7	UV	3.27	> -0.77	A/S	0.07 $^{+0.04}_{-0.03}$	AGSED

Table 11 (cont'd)

GRB	z	Instrument (Spectrum)	$\log M_*$		SFR		[X/H]		A_V		reference	
			[M $_{\odot}$] (4)	method (5)	[M $_{\odot}$ yr $^{-1}$] (6)	method (7)	[Gyr $^{-1}$] (8)	method (9)	[mag] (11)	method (12)		
050318A	1.4436	Magellan / Baade	0.58 ± 0.17	0.53 $^{+0.06}_{-0.06}$	AGSED	31	
050315A	1.9500	VLT/FORS	1.65	Lya	47	
050223A	0.584	VLT/FORS1	9.73 ± 0.36	SED	0.06 $^{+0.01}_{-0.02}$	H β	0.31	-1.190/ -0.030	E	> 2	6, 19	
050219A	0.211	VLT/X-Shooter	9.98	SED	0.01	[OII]	69	
050215B	2.62	Keck/LRIS	0	
050126A	1.29002	Keck/NIRC	0	
041219A	0.31	...	9.7	SED	42	
041006A	0.716	Gemini/GMOS	8.66 ± 0.87	SED	0.34	[OII]	0.74	...	0.00 $^{+0.53}_{-0.00}$	hostSED	19, 59	
040924A	0.858	VLT/FORS2	9.20 ± 0.37	SED	0.85	H β	0.54	-0.460 $^{+0.20}_{-0.30}$	E	0.0 $^{+1.2}_{-0.0}$	linefit	19, 43
040912A	1.563	VLT/FORS2	6.3 ± 0.4	[OII]	12	
031203A	0.1055	Magellan/IMACS	8.82 ± 0.43	SED	12.68	H α	19.19	-0.670	E	0.28 ± 0.04	Balmer	19, 20
030528A	0.782	VLT/FORS2	8.82 ± 0.39	SED	9.96	H β	15.08	-0.590	E	0.0 $^{+0.8}_{-0.0}$	linefit	19, 43
030429A	2.658	VLT/FORS1	0.15	Lya	...	> -1.13	A/Si	...	4, 79	
030329A	0.1685	VLT/FORS2	7.74 ± 0.06	SED	0.11	H α	2.00	-0.720	E	0.24 ± 0.05	Balmer	19, 20
030328A	1.5216	VLT/FORS1	8.83 ± 0.52	SED	3.20	UV	4.73	...	1.06 $^{+0.26}_{-0.29}$	hostSED	19, 59	
030323A	3.3736	VLT/FORS2	< 9.23	IR	1.12 ± 0.09	Lya	...	> -1.32	A/Si	...	3, 38, 79	
030226A	1.986	Keck/ESI	A/Fe	79	
030115A	2	...	10.87	SED	1.6	UV	0.02	64	
021211A	1.006	VLT/FORS2	10.32 ± 0.63	SED	1.4	[OII]	0.07	...	1.78 $^{+0.27}_{-0.09}$	hostSED	5, 19, 59	
021004A	2.3351	VLT/ISAAC	10.20 ± 0.18	SED	40 ± 7	H α	2.52	0	0.42 $^{+0.09}_{-0.07}$	hostSED	15, 19, 23, 59	
020903A	0.251	Keck/ESI	8.87 ± 0.07	SED	2.65	H α	3.57	-0.470	E	0.15 ± 0.09	Balmer	19, 20
020819B	0.41	Keck/LRIS	10.50 ± 0.14	SED	12.5 ± 0.17	H α	0.40	0.290 $^{+0.07}_{-0.07}$	E	1.8 $^{+0.5}_{-0.5}$	linefit	19, 43
020813A	1.255	Keck/LRIS	8.66 ± 1.41	SED	6.76	[OII]	14.79	...	0.00 $^{+0.16}_{-0.00}$	hostSED	19, 59	
020427A	0	0	
020410A	...	Keck/ESI	9.75 ± 0.25	SED	4.29	H β	0.76	-0.910/ -0.250	E	1.93 ± 0.36	Balmer	19, 20
020405A	0.69098	0	0	
020331A	0	0	
020322A	64	
020305A	2.8	11.51	SED	2.7	38, 81	
020127A	1.9	< 9.28	IR	< 0.06	38, 81	
020124A	3.198	VLT/FORS1	9.77 ± 0.47	SED	0.8 ± 0.2	Lya	0.14	> -1.22	A/Si	0.19 $^{+0.70}_{-0.00}$	hostSED	2, 19, 59, 79
011211A	2.14	VLT/FORS2	2.24	H α	0.35	-1.190/ -0.050	E	0.9 $^{+0.1}_{-0.1}$	linefit	19, 43
011121A	0.36	Magellan/LDSS-2	9.81 ± 0.17	SED	0	
011030A	3	Hale	9.69 ± 0.13	SED	2.50	H α	0.51	-0.690/ -0.540	E	1.6 $^{+1.0}_{-1.0}$	linefit	19, 43
010921A	0.4509	Keck/ESI	8.82 ± 0.26	SED	0.34	UV	0.51	...	0.05 $^{+0.33}_{-0.05}$	hostSED	19, 59	
010222A	1.47688	Keck/ESI	9.52 ± 0.84	SED	4.46 ± 0.28	Lya	1.35	> -0.30	A/Zn	0.58 $^{+0.39}_{-0.33}$	hostSED	1, 19, 59, 79
000926A	2.0379	Keck/LRIS	9.32 ± 0.26	SED	1.57	[OII]	0.75	-0.590 ± 0.6	E/KK04	0.80 $^{+1.22}_{-0.80}$	hostSED	19, 59, 88
000911A	1.0585	Keck/ESI	9.26 ± 0.14	SED	10.35	[OII]	5.69	-0.290	E/KK04	1.30 $^{+0.06}_{-0.07}$	hostSED	19, 59, 88

Table 11 (cont'd)

GRB	z	Instrument (Spectrum)	$\log M_*$		SFR [$M_{\odot} \text{ yr}^{-1}$] (6)	method (7)	s_{SFR} [Gyr^{-1}] (8)	[X/H] (9)	method (10)	A_V [mag] (11)	method (12)	reference (13)
			[M_{\odot}] (4)	method (5)								
000301C	2.0404	VLT/FORS1	2.28	[OII]	1.12	-0.490 ± 0.1	E/KK04	0.05 ± 0.35 0.05	hostSED	19,59,88 81
000210A	0.846	VLT/FORS1	9.31 ± 0.08	SED	< 17.9	UV	0
000131A	4.5	VLT/FORS1	0
991216A	1.02	VLT/FORS1	H β	57.93	< -1.290/0.040	E	0.49 $^{+0.25}_{-0.17}$	hostSED	19,59
991208A	0.7063	BTA/MPSF	8.53 ± 0.37	SED	19.63	H α	1.23	-0.590	E	0.55 $^{+0.03}_{-0.03}$	Balmer	19,20
990712A	0.4331	VLT/FORS2	9.29 ± 0.02	SED	2.39	[OII]	0.44	0.00 ± 0.00	hostSED	19,59
990705A	0.8424	VLT/FORS2	10.20 ± 0.76	SED	6.96	0
990510A	1.619	VLT/FORS1	0.00 $^{+1.97}_{-0.00}$	hostSED	19,59
990506A	1.30658	Keck/ESI	9.48 ± 0.18	SED	2.50	[OII]	0.83	0
990308A	0
990123A	1.6004	Keck/LRIS	9.42 ± 0.49	SED	5.72	UV	2.17	1.21 $^{+0.17}_{-0.19}$	hostSED	19,59
981226A	1.11	0
980703A	0.966	Keck/LRIS	9.33 ± 0.36	SED	7.03	H β	3.29	-1.090/-0.550	E	0.14 ± 0.53	Balmer	19,20
980613A	1.0969	Keck/LRIS	8.49 ± 0.21	SED	4.70	[OII]	15.21	0.500000	hostSED	19,29
980519A	0
980425A	0.0085	VLT/FORS2	9.21 ± 0.52	SED	0.21	H α	0.13	-0.530	E	1.9 $^{+0.1}_{-0.1}$	linefit	19,43
980329A	3.5	5.1	UV	81
980326A	0
971214A	3.42	Keck/LRIS	9.59 ± 0.40	SED	11.40	UV	2.93	1.35 $^{+0.18}_{-0.10}$	hostSED	19,59
970828A	0.9578	Keck/LRIS	9.19 ± 0.36	SED	0.87	[OII]	0.56	2.13 $^{+0.10}_{-0.09}$	hostSED	19,59
970508A	0.835	Keck/LRIS	8.52 ± 0.10	SED	1.14	[OII]	3.44	0.84 $^{+0.76}_{-0.19}$	hostSED	19,59
970228A	0.695	Keck/LRIS	8.65 ± 0.05	SED	0.53	[OII]	1.19	-0.220 $^{+0.15}_{-0.24}$	E	0.0 $^{+0.7}_{-0.9}$	linefit	19,43
SGRB												
130603B	0.356	GTC/OSIRIS	9.23	SED	4.85	H α	2.86	-0.240 ± 0.17	E	1.2	Balmer	62
101224A	[OII]	0
101219A	0.718	Gemini/GMOS	9.15	SED	16 $^{+0.4}_{-25}$	H α	11.33	1.5	hostSED	55
100816A	0.8048	VLT/X-Shooter	[OII]	...	0.060 $^{+0.16}_{-0.18}$	E	4.38 $^{+0.80}_{-0.73}$	Balmer	77
100625A	0.452	Magellan/Cay	9.66	SED	< 0.3	[OII]	55
100206A	0.4068	Keck I/LRIS	10.7	SED	30	line/SED	0.60	0.120 $^{+0.10}_{-0.12}$	E/PP04	1.8 ± 0.2	line/SED	48
100117A	0.92	Gemini/GMOS	10.3	SED	0.1	[OII]	0.01	29,37
091109B	0
090515A	29
090510A	0.903	VLT/FORS	9.7	SED	0.6	[OII]	0.12	0.7 $^{+0.2}_{-0.4}$	hostSED	22,29
090426A	2.609	Keck I/LRIS	10.81	...	14.4 ± 2	UV	0.22	30,89
090305A	0
080905A	0.1218	VLT/FORS1	0
080503A	0
080123A	0.495	...	10.1	SED	...	[OII]	0.02	-0.190 ± 0.3	E	1.50000	hostSED	29
071227A	0.383	VLT/FORS2	10.4	SED	0.6	16,29

Table 11 (cont'd)

GRB	z	Instrument (Spectrum)	$\log M_*$		SFR method	[M $_{\odot}$ yr $^{-1}$] (6)	[Gyr] (7)	sSFR method	[X/H] (8)	method	[mag] (11)	AV method	reference (13)
			[M $_{\odot}$]	(4)									
070809A	0.2187	Keck/LRIS	11.4	SED	E	29
070724A	0.457	Gemini/GMOS	10.1	SED	2.5	[OII]	0.20	0.210	17,29
070714B	0.923	Keck/LRIS	9.4	SED	0.4	[OII]	0.16	17,29
070707A	0
070429B	0.904	Keck/LRIS	10.4	SED	1.1	[OII]	0.04	17,29
061217A	0.827	Magellan	9.1	SED	2.5	[OII]	1.99	17,29
061210A	0.41	Keck/LRIS	9.6	SED	1.2	[OII]	0.30	0.110	...	E	17,29
061201A	0.111	Magellan	E	0
061006A	0.4377	Gemini/GMOS	10.43 ± 0.23	SED	0.17	UV	0.01	-0.090	...	E	17,19
060801A	1.131	Gemini/GMOS	9.1	SED	6.1	[OII]	4.85	17,29
060502B	0.287	Keck/LRIS	0
060313A	0
060121A	0
051221A	0.5465	Gemini/GMOS	8.61 ± 0.64	SED	2.11	H β	5.18	-1.090 / -0.100	...	E	19
051210A	1.4	29
050724A	0.258	Gemini/GMOS	10.64 ± 0.05	SED	18.76	UV	0.43	E	19
050709A	0.16	VLT/FORS2	8.66 ± 0.07	SED	0.14	H α	0.31	-0.190	17,19
050509B	0.226	Keck/DEIMOS	11.08 ± 0.03	SED	16.87	UV	0.14	19

Note. — Col. (1) GRB name. Col. (2) redshift. Col. (3) The instrument which obtained the optical spectrum. Col. (4-5) Stellar mass M_* and the methods which derive it. Col. (6-7) Star formation rate and the methods which derive it. Col. (8) Specific SFR, SFR/M_* . Col. (9-10) Metallicity and the methods which derive it. (E)mission line and (A)bsorption line. Metallicities with back slashes are estimated with R_{23} method, and the two values are for the lower and upper branches, respectively. Col. (11-12) Extinction and the methods which derive it. Col. (13) Reference.

References. (1) Fynbo et al. (2002); (2) Fynbo et al. (2003); (3) Vreeswijk et al. (2004); (4) Jakobsson et al. (2004); (5) Vreeswijk et al. (2006); (6) Pellizza et al. (2006); (7) Jakobsson et al. (2006b); (8) Berger et al. (2006); (9) Perprase et al. (2006); (10) Watson et al. (2006); (11) Della Valle et al. (2006); (12) Stratta et al. (2007); (13) Prochaska et al. (2007a); (14) Cenko et al. (2008a); (15) Prochaska et al. (2008); (16) D'Avanzo et al. (2009); (17) Berger (2009); (18) Chen et al. (2009); (19) Savaglio et al. (2009); (20) Han et al. (2010); (21) Zafar et al. (2010); (22) McBreen et al. (2010); (23) Castro-Tirado et al. (2010); (24) D'Avanzo et al. (2010); (25) Thöne et al. (2010); (26) Levesque et al. (2010a); (27) Rau et al. (2010b); (28) Tanvir et al. (2010c); (29) Leibler & Berger (2010); (30) Levesque et al. (2010); (31) Schady et al. (2010b); (32) Chornock et al. (2010c); (33) Schulze et al. (2011); (34) Greiner et al. (2011); (35) Krihler et al. (2011b); (36) Vergani et al. (2011); (37) Fong et al. (2011); (38) Laskar et al. (2011); (39) Levesque et al. (2011); (40) De Cia et al. (2011); (41) Cano et al. (2011); (42) Götz et al. (2011); (43) Mannucci et al. (2011); (44) Guidorzi et al. (2011); (45) Basa et al. (2012); (46) De Cia et al. (2012); (47) Milvang-Jensen et al. (2012); (48) Perley et al. (2012a); (49) Savaglio et al. (2012); (50) Savaglio et al. (2012b); (51) Niino et al. (2012); (52) Krihler et al. (2013); (53) de Ugarte Postigo et al. (2013d); (54) Zauderer et al. (2013); (55) Fong et al. (2013); (56) Jin et al. (2013); (57) Kelly et al. (2013); (58) Xu et al. (2013b); (59) Perley et al. (2013); (60) Thöne et al. (2013); (61) Elliott et al. (2013b); (62) de Ugarte Postigo et al. (2014b); (63) D'Elia et al. (2014); (64) Hunt et al. (2014); (65) Schulze et al. (2014); (66) Cano et al. (2014); (67) Jeong et al. (2014); (68) Fynbo et al. (2014); (69) Rossi et al. (2014); (70) Sparre et al. (2014); (71) Morgan et al. (2014); (72) Olivares E. et al. (2015); (73) Schady et al. (2015); (74) Hartoog et al. (2015); (75) Melandri et al. (2015); (76) Vergani et al. (2015); (77) Krühler et al. (2015); (78) Michalowski et al. (2015); (79) Cucchiara et al. (2015); (80) Hashimoto et al. (2015); (81) Greiner et al. (2015); (82) Arasalmanni et al. (2015); (83) Stanway et al. (2015); (84) van der Horst et al. (2015); (85) Kohn et al. (2015); (86) Friis et al. (2015); (87) Cano et al. (2015); (88) Firanomonte et al. (2015); (89) GHOST;

Table 12. Host Information from the Image

GRB	z	Instrument (Image)	P_{cc}	R_{50} ["]	n	R_{off} ["]	R_{off} [kpc]	r_{off} [R_{50}] (10)	F_{light}	reference
(1)	(2)	(3)	(4)	(5)	(6)	(7)	(8)	(9)	(11)	(12)
140606B	0.384	0
140518A	4.707	HST	0.014	0.12 _{-0.04} ^{+0.05}	0.680 _{-0.23} ^{+0.27}	...	0.210 ± 0.070	1.21 ± 0.40	1.776	47
140515A	6.32	0
140512A	0.725	0
140508A	1.027	0
140506A	0.8893	0
140430A	1.6019	0
140428A	4.7	0
140423A	3.26	0
140419A	3.956	0
140318A	1.02	0
140311A	4.954	0
140304A	5.283	0
140301A	1.4155	0
140226A	1.98	0
140213A	1.2079	0
140206A	2.739	0
140114A	3	0
131231A	0.6427	0
131227A	5.3	0
131117A	4.042	0
131108A	2.4	0
131105A	1.6854	0
131103A	0.5960	0
131030A	1.293	0
131011A	1.874	0
131004A	0.717	0
130925A	0.3483	HST	...	0.48	2.400	...	0.120	0.595	0.248	38,43
130907A	1.238	0
130831A	0.4791	0
130702A	0.145	Keck/LRIS	...	0.700*	1.785	...	0.600	1.530	0.857	34,49
130701A	1.1548	0
130612A	2.006	0
130610A	2.092	0
130606A	5.913	HST	0.014	0.190 ± 0.020	1.14 ± 0.10	...	0.060 ± 0.020	0.36 ± 0.12	0.314	47
130604A	1.06	0
130528A	1.25	0
130518A	2.49	0
130511A	1.3033	0

Table 12 (cont'd)

GRB	z	Instrument (Image)	P_{cc}	R_{50} [pc] (5)	R_{50} [pc] (6)	n	R_{off} [pc] (7)	R_{off} [pc] (8)	r_{off} [pc] (10)	F_{light} (11)	reference (12)
130505A	2.27	0
130427B	2.78	0
130427A	0.3401	HST	...	0.400*	1.954	...	0.83 ± 0.03	4.1 ± 0.1	2.075	...	41
130420A	1.297	0
130418A	1.217	0
130408A	3.757	0
130215A	0.597	0
130131B	2.5393	0
121229A	2.707	0
121211A	1.023	0
121209A	2.1	0
121201A	3.3830	0
121128A	2.20	0
121027A	1.7732	0
121024A	2.3012	0
120922A	3.1	0
120909A	3.93	0
120907A	0.970	0
120815A	2.3587	0
120811C	2.671	0
120805A	3.1	0
120802A	3.796	0
120729A	0.80	0
120724A	1.48	0
120722A	0.9590	0
120716A	2.486	0
120714B	0.3985	0
120712A	4.1745	0
120711A	1.405	0
120624B	2.1974	VLT	...	< 0.190	< 1.60	32
120422A	0.2826	Magellan	...	1.000	4.299	...	1.900	8.167	1.900	...	29
120404A	2.876	0
120327A	2.813	0
120326A	1.798	0
120224A	1.1	0
120211A	2.4	0
120119A	1.7291	HST	0.003	0.202	1.752	...	0.012 ± 0.017	0.104 ± 0.147	0.059 ± 0.086	1.000	48
120118B	2.9428	0
111229A	1.3805	0

Table 12 (cont'd)

GRB	z	Instrument (Image)	P_{cc}	R_{50} ["]	R_{50} [kpc] (6)	n	R_{off} ["]	R_{off} [kpc] (8)	r_{off} [R_{50}] (10)	F_{light} (11)	reference (12)
(1)	(2)	(3)	(4)	(5)	(6)	(7)	(8)	(9)	(10)	(11)	
111228A	0.7164	0
111225A	2.012	HST	...	0.250*	2.143	...	0.310*	2.657	1.240	...	0
111215A	2.06	HST	45
111211A	0.4786	HST	...	0.06	0.400	...	0.011 ± 0.038	0.079 ± 0.272	0.198	...	0
111209A	0.6770	HST	40
111129A	1.0796	0
111123A	3.1513	0
111107A	2.893	0
111008A	4.9898	0
111005A	0.0133	6.300*	1.712	...	3.500*	0.951	0.555	44
110918A	0.9843	GROND	0.010	1.30	10.600	1.48	12.000	1.132	31
110818A	3.3609	0
110808A	1.3490	0
110801A	1.858	0
110731A	2.83	HST	0.005	0.121	0.977	...	0.182 ± 0.010	1.47 ± 0.08	1.50 ± 0.09	0.029	48
110726A	1.036	0
110715A	0.82	0
110709B	2.09	HST	0.111	0.073	0.625	...	0.067 ± 0.323	0.57 ± 2.76	0.92 ± 4.43	0.055	48
110503A	1.613	0
110422A	1.770	0
110213B	1.083	0
110213A	1.46	0
110205A	2.22	0
110128A	2.339	0
110106B	0.618	0
101225A	0.847	HST	...	< 0.040	< 0.34	...	0.016 ± 0.020	0.124 ± 0.156	0.365	...	40
101219B	0.55185	0
100906A	1.727	0
100901A	1.408	0
100814A	1.4392	0
100728B	2.106	0
100728A	1.5670	0
100724A	1.2890	0
100621A	0.5426	HST	0.002	0.262	1.688	...	0.045 ± 0.069	0.290 ± 0.444	0.172 ± 0.263	0.914	48
100615A	1.3978	HST	0.034	0.083	0.716	...	0.246 ± 0.320	2.12 ± 2.76	2.96 ± 3.85	0.051	48
100606A	1.5545	0
100518A	4	0
100513A	4.772	0
100508A	0.5201	0

Table 12 (cont'd)

GRB	z	Instrument (Image)	P_{cc}	R_{50} [pc] (5)	R_{50} [pc] (6)	n	R_{off} [pc] (7)	R_{off} [pc] (8)	r_{off} [R_{50}] (9)	F_{light} (11)	reference (12)
(1)	(2)	(3)	(4)	(5)	(6)	(7)	(8)	(9)	(10)	(11)	
100425A	1.755	0
100424A	2.4656	0
100418A	0.6235	0
100414A	1.368	0
100316D	0.0592	HST	0.879	48
100316B	1.180	0
100302A	4.813	GTC/OSIRIS	...	1.400*	9.408	...	0.40 ± 0.30	2.69 ± 2.02	0.286	...	0
100219A	4.6667	GTC/OSIRIS	...	1.400*	9.408	...	0.221 ± 0.049	1.35 ± 0.30	0.54 ± 0.12	0.833	37
091208B	1.0633	0
091127A	0.4904	HST	0.011	0.411	2.509	0
091109A	3.076	0
091029A	2.752	0
091024A	1.092	0
091020A	1.71	0
091018A	0.9710	0
091003A	0.8969	0
090927A	1.37	0
090926B	1.2427	NTT	0.018	< 0.60	< 5.1	27
090926A	2.1062	0
090902B	1.822	0
090814A	0.696	0
090812A	2.452	0
090809A	2.737	0
090726A	2.71	0
090715B	3.00	0
090709A	1.7	HST	0.010	0.256	2.222	...	0.283 ± 0.036	2.46 ± 0.31	1.10 ± 0.14	0.461	48
090618A	0.54	HST	0.020	0.519	3.335	...	0.69 ± 0.05	4.5 ± 0.3	1.33 ± 0.09	0.260	48
090530A	1.266	0
090529A	2.625	0
090519A	3.85	0
090516A	4.109	0
090424A	0.544	HST	0.005	0.407	2.625	...	0.41 ± 0.04	2.62 ± 0.24	1.00 ± 0.09	0.740	48
090423A	8.23	0
090418A	1.608	HST	0.009	0.214	1.858	...	0.096 ± 0.211	0.83 ± 1.83	0.45 ± 0.98	0.367	48
090417B	0.345	HST	0.006	< 0.91	< 4.5	...	0.88 ± 1.00	4.3 ± 4.9	0.966	...	26, 36
090407A	1.4478	HST	0.026	0.336	2.905	...	0.172 ± 0.410	1.49 ± 3.54	0.51 ± 1.22	0.245	48
090328A	0.7357	GROND	0.140	1.035	23
090323A	3.5832	0
090313A	3.375	0

Table 12 (cont'd)

GRB	z	Instrument (Image)	P_{cc}	R_{50} [r°]	R_{50} [kpc]	n	R_{off} [r°]	R_{off} [kpc]	r_{off} [R_{50}]	F_{light}	reference
(1)	(2)	(3)	(4)	(5)	(6)	(7)	(8)	(9)	(10)	(11)	(12)
090205A	4.6497	VLT/FORS1	0.40 ± 0.30	2.69 ± 2.02	24
090201A	2.1000	0
090113A	1.7494	0.090 ± 0.060	0.78 ± 0.52	22
090102A	1.547	HST	0
081222A	2.77	0.39 ± 0.07	3.3 ± 0.6	0.95 ± 0.18	0.761	48	48
081221A	2.2590	HST	0.013	0.409	3.462	0
081210A	2.0631	0
081203A	2.05	0.262 ± 0.122	2.17 ± 1.01	1.32 ± 0.61	0.197	48	48
081121A	2.512	HST	0.010	0.198	1.644	0
081118A	2.58	< 0.200	< 1.62	27
081109A	0.9785	VLT	0.002	0
081029A	3.8479	0
081028A	3.038	0
081008A	1.967	HST	0.066	0.236	2.032	1.66 ± 0.03	14.3 ± 0.2	7.0 ± 0.1	0.000	48	48
081007A	0.5295	HST	0.011	0.277	1.762	0.111 ± 0.029	0.71 ± 0.18	0.40 ± 0.10	0.792	48	48
080928A	1.6919	HST	0.035	0.442	3.836	1.71 ± 0.03	14.8 ± 0.3	3.9 ± 0.1	0.009	48	48
080916C	4.35	0
080916A	0.6887	HST	0.004	0.240	1.728	0.011 ± 0.061	0.079 ± 0.439	0.046 ± 0.254	0.930	48	48
080913A	6.7	0
080905B	2.3739	0
080810A	3.3604	0
080805A	1.5052	HST	0.010	0.275	2.383	0.47 ± 0.05	4.0 ± 0.4	1.69 ± 0.17	0.517	48	48
080804A	2.2059	0
080721A	2.5914	0
080710A	0.8454	0
080707A	1.2322	HST	0.005	0.263	2.236	0.089 ± 0.054	0.76 ± 0.46	0.34 ± 0.20	0.836	48	48
080607A	3.0368	HST	0.036	0.419	3.317	0.68 ± 0.24	5.4 ± 1.9	1.62 ± 0.57	0.177	48	48
080605A	1.6408	HST	0.002	0.198	1.719	0.081 ± 0.031	0.70 ± 0.27	0.41 ± 0.16	0.820	48	48
080604A	1.4171	0
080603B	2.6892	0
080603A	1.688	HST	0.003	0.202	1.753	0.089 ± 0.030	0.77 ± 0.26	0.44 ± 0.15	0.880	48	48
080602A	1.8204	0
080520A	1.5457	HST	0.011	0.223	1.934	0.47 ± 0.18	4.1 ± 1.6	2.10 ± 0.82	0.117	48	48
080517A	0.089	WHT	...	1.70 ± 0.80	2.83 ± 1.33	1.5	3.00 ± 1.20	5.0 ± 2.0	1.764	...	46
080515A	2.47	0
080430A	0.767	HST	0.011	0.282	2.118	0.108 ± 0.049	0.81 ± 0.37	0.38 ± 0.17	0.645	48	48
080413B	1.1012	0
080413A	2.4330	0
080411A	1.0301	0

Table 12 (cont'd)

GRB	z	Instrument (Image)	P_{cc}	R_{50} [r°]	n	R_{off} [r°]	R_{off} [kpc]	r_{off} [R_{50}] (10)	F_{light}	reference
(1)	(2)	(3)	(4)	(5)	(6)	(7)	(8)	(9)	(11)	(12)
080330A	1.5119	0.017	0.443	...	0.70 ± 0.07	6.0 ± 0.7	1.57 ± 0.17	0.134
080325A	1.78	HST	0.023	0.638	5.498	...	0.85 ± 0.05	7.4 ± 0.4	1.34 ± 0.08	0.599
080319C	1.9492	HST	0.015	0.147	1.179	...	0.215 ± 0.118	1.72 ± 0.95	1.46 ± 0.80	0.598
080319B	0.9382	HST	0
080310A	2.4274	0
080210A	2.6419	0
080207A	2.0856	HST	0.047	0.683	5.846	...	0.77 ± 0.44	6.6 ± 3.7	1.13 ± 0.64	0.207
080129A	4.3449	0.009	0.393	3.298	0.075 ± 0.053	0.63 ± 0.45	0.191 ± 0.134	0.951
071122A	1.14	HST	0
071117A	1.3308	0
071112C	0.8227	HST	0.016	0.398	3.065	...	0.202 ± 0.027	1.55 ± 0.21	0.51 ± 0.07	0.774
071031A	2.692	0.48 ± 0.50	4.0 ± 4.2
071021A	2.4515	Keck	0.006	36
071020A	2.1462	0
071010B	0.947	HST	0.004	0.257	2.067	...	0.109 ± 0.025	0.88 ± 0.20	0.42 ± 0.10	0.825
071010A	0.98	0
071003A	1.60435	0
070810A	2.17	0
070802A	2.4538	HST	0.014	0.348	2.903	...	0.132 ± 0.048	1.10 ± 0.40	0.38 ± 0.14	0.692
070721B	3.6298	HST	0.011	0.057	0.425	...	0.045 ± 0.054	0.34 ± 0.40	0.79 ± 0.94	0.211
070714A	1.58	0
070612A	0.617	0
070611A	2.0394	0
070529A	2.4996	0
070521A	2.0865	HST	0.072	0.90 ± 1.40	7.7 ± 12.0	...	36
070518A	1.161	0.027	0.592	4.554	0.42 ± 0.03	3.3 ± 0.3	0.71 ± 0.06	0.517
070508A	0.82	HST	0
070506A	2.3090	0
070419B	1.9586	0
070419A	0.9705	0
070411A	2.9538	0
070328A	2.0627	0
070318A	0.8401	HST	0.005	0.205	1.590	...	0.109 ± 0.060	0.84 ± 0.47	0.53 ± 0.29	0.781
070306A	1.4965	HST	0.002	0.209	1.810	...	0.090 ± 0.045	0.78 ± 0.39	0.43 ± 0.21	0.798
070224A	1.9922	0
070223A	1.6295	0
070208A	1.165	HST	0.005	0.368	3.100	...	0.099 ± 0.040	0.83 ± 0.34	0.269 ± 0.108	0.928
070129A	2.3384	0
070125A	1.547	Keck	HST	3.200	27.753	...

Table 12 (cont'd)

GRB	z	Instrument (Image)	P_{cc}	R_{50} [r] (5)	R_{50} [kpc] (6)	n	R_{off} [r] (8)	R_{off} [kpc] (9)	r_{eff} [R_{50}] (10)	F_{light}	reference
(1)	(2)	(3)	(4)	(5)	(6)	(7)	(8)	(9)	(10)	(11)	(12)
070809A	0.2187	HST	...	0.610	2.168	3.03	5.6 ± 0.5	20.0 ± 1.6	9.2 ± 0.8	0	35
070724A	0.457	HST	...	0.630	3.696	0.92	0.94 ± 0.03	5.5 ± 0.2	1.49 ± 0.04	0.23	35
070714B	0.923	HST	...	0.340	2.714	0.76	1.55 ± 0.11	12.4 ± 0.9	4.6 ± 0.3	0	35
070707A	...	HST	...	0.360	2.221	0.89	0.40 ± 0.03	2.47 ± 0.24	1.11 ± 0.08	0	35
070429B	0.904	HST	...	0.650	5.158	2.15	< 1.46	< 11.6	< 2.25	...	35
061217A	0.827	0
061210A	0.41	0
061201A	0.111	HST	...	1.090	2.209	1.03	16.2 ± 0.0	32.9 ± 0.1	14.9 ± 0.0	0	35
061006A	0.43777	HST	...	0.650	3.719	0.7	0.230 ± 0.043	1.32 ± 0.25	0.35 ± 0.07	0.63	25
060801A	1.131	0
060502B	0.287	0
060313A	...	HST	...	0.230	1.419	1.3	0.284 ± 0.062	1.75 ± 0.50	1.24 ± 0.23	...	0
060121A	...	HST	...	0.670	4.133	1.4	0.119 ± 0.046	0.73 ± 0.37	0.178 ± 0.070	0.41	25
051221A	0.5465	HST	...	0.390	2.521	0.9	0.30 ± 0.03	1.95 ± 0.19	0.77 ± 0.08	0.65	25
051210A	1.14	HST	...	0.630	5.433	1.0	4.2 ± 1.7	36.2 ± 14.7	6.7 ± 2.7	...	25
050724A	0.258	HST	...	0.978	3.936	2.9	0.67 ± 0.02	2.68 ± 0.08	0.68 ± 0.02	0.33	25
050709A	0.116	HST	...	0.640	1.771	0.6	1.36 ± 0.00	3.8 ± 0.0	2.13 ± 0.01	0.09	25
050509B	0.226	HST	...	5.653	20.600	5.6	17.8 ± 3.4	64.8 ± 12.4	3.1 ± 0.6	...	25

Note. — Col. (1) GRB name. Col. (2) redshift. Col. (3) The instrument which obtained the optical image. Col. (4) Probability of Chance Coincidence. Col. (5-6) Half light radius in unit of arcsec and kpc. Col. (7) Sérsic index $\Sigma(r) = \Sigma_e \exp\{-k_n[(r/r_e)^{1/n} - 1]\}$. Col. (8-9) Offset of GRB from the center of host galaxy, in unit of arcsec and kpc. Col. (10) Normalized offset $r_{\text{off}} = R_{\text{off}}/R_{50}$. Col. (11) The fraction of area within host galaxy which is brighter than the GRB region. 1.0 indicates GRB is in the brightest region of the host and 0.0 indicates GRB is in the faintest region of the host. Col. (12) Reference.

a. $z = 0.5$ is assumed for GRB 020410A, according to the possible detection of SN in Levan et al. (2005).

*. Estimated from the images in the references.

References. (1) Burnd et al. (2001); (2) Bloom et al. (2002); (3) Price et al. (2002a); (4) Price et al. (2002b); (5) Piro et al. (2002); (6) Castro et al. (2003); (7) Galama et al. (2003); (8) Bloom et al. (2003b); (9) Greiner et al. (2003); (10) Vreeswijk et al. (2004); (11) Cobb et al. (2004); (12) Gorosabel et al. (2005); (13) Masetti et al. (2005); (14) Jakobsson et al. (2005); (15) Fynbo et al. (2005); (16) Fruchter et al. (2006); (17) Wainwright et al. (2007); (18) Mirabal et al. (2007); (19) Perley et al. (2008d); (20) Cenko et al. (2008a); (21) Chen et al. (2009); (22) Levan et al. (2009b); (23) McBreen et al. (2010); (24) D'Avanzo et al. (2010); (25) Fong et al. (2010); (26) Holland et al. (2010); (27) Krichler et al. (2011b); (28) Tanvir et al. (2012); (29) Levesque et al. (2012); (30) Perley et al. (2012a); (31) Elliott et al. (2013a); (32) de Ugarte Postigo et al. (2013d); (33) Fong et al. (2013); (34) Kelly et al. (2013); (35) Fong & Berger (2013); (36) Perley et al. (2013); (37) Thöne et al. (2013); (38) Greiner et al. (2014); (39) Rossi et al. (2014); (40) Levan et al. (2014a); (41) Levant et al. (2014b); (42) Tunncliffe et al. (2014); (43) Schady et al. (2015); (44) Michalowski et al. (2015); (45) Dominik et al. (2015); (46) Stanway et al. (2015); (47) McGuire et al. (2015); (48) Blanchard et al. (2016); (49) Toy et al. (2016),

REFERENCES

- Abbott, B. P., Abbott, R., Abbott, T. D., et al. 2016a, Physical Review Letters, 116, 241103
- . 2016b, ApJ, 826, L13
- . 2016c, Physical Review Letters, 116, 061102
- Adriani, O., Akaike, Y., Asano, K., et al. 2016, ApJ, 829, L20
- Afonso, P., Schady, P., Kruehler, T., & Greiner, J. 2010, GRB Coordinates Network, 10782, 1
- Aihara, H., Allende Prieto, C., An, D., et al. 2011, ApJ, 193, 29
- Alam, S., Albareti, F. D., Allende Prieto, C., et al. 2015, ArXiv e-prints, arXiv:1501.00963
- Amati, L., Frontera, F., Tavani, M., et al. 2002, A&A, 390, 81
- Amati, L., Frontera, F., in't Zand, J. J. M., et al. 2004, A&A, 426, 415
- Andersen, M. I., Hjorth, J., Pedersen, H., et al. 2000, A&A, 364, L54
- Antonelli, L. A., D'Avanzo, P., Perna, R., et al. 2009, A&A, 507, L45
- Arabsalmani, M., Møller, P., Fynbo, J. P. U., et al. 2015, MNRAS, 446, 990
- Asplund, M., Grevesse, N., Sauval, A. J., & Scott, P. 2009, Annual Review of Astronomy and Astrophysics, 47, 481
- Bambach, R. K. 2006, Annual Review of Earth and Planetary Sciences, 34, 127
- Band, D., Matteson, J., Ford, L., et al. 1993, ApJ, 413, 281
- Barraud, C., Olive, J.-F., Lestrade, J. P., et al. 2003, A&A, 400, 1021
- Barth, A. J., Sari, R., Cohen, M. H., et al. 2003, ApJ, 584, L47
- Barthelmy, S. D., Chincarini, G., Burrows, D. N., et al. 2005, Nature, 438, 994
- Basa, S., Cuby, J. G., Savaglio, S., et al. 2012, A&A, 542, A103
- Bellm, E., Bandstra, M., Boggs, S., et al. 2006, GRB Coordinates Network, 5867, 1
- Berger, E. 2006a, GRB Coordinates Network, 5952, 1
- . 2006b, GRB Coordinates Network, 5962, 1
- . 2009, ApJ, 690, 231
- . 2010, ApJ, 722, 1946
- . 2014, Annual Review of Astronomy and Astrophysics, 52, 43

- Berger, E., Foley, R., Simcoe, R., & Irwin, J. 2008a, GRB Coordinates Network, 8434, 1
- Berger, E., Fong, W., & Chornock, R. 2013, ApJ, 774, L23
- Berger, E., & Fox, D. B. 2009, GRB Coordinates Network, 9156, 1
- Berger, E., Fox, D. B., & Cucchiara, A. 2007a, GRB Coordinates Network, 6470, 1
- Berger, E., Fox, D. B., Cucchiara, A., & Cenko, S. B. 2008b, GRB Coordinates Network, 8335, 1
- Berger, E., Fox, D. B., Kulkarni, S. R., Frail, D. A., & Djorgovski, S. G. 2007b, ApJ, 660, 504
- Berger, E., & Gladders, M. 2006, GRB Coordinates Network, 5170, 1
- Berger, E., Morrell, N., & Roth, M. 2007c, GRB Coordinates Network, 7154, 1
- Berger, E., Penprase, B. E., Cenko, S. B., et al. 2006, ApJ, 642, 979
- Berger, E., & Rauch, M. 2008, GRB Coordinates Network, 8542, 1
- Berger, E., Kulkarni, S. R., Fox, D. B., et al. 2005a, ApJ, 634, 501
- Berger, E., Price, P. A., Cenko, S. B., et al. 2005b, Nature, 438, 988
- Berger, E., Fox, D. B., Kulkarni, S. R., et al. 2005c, ApJ, 629, 328
- Berger, E., Fox, D. B., Price, P. A., et al. 2007d, ApJ, 664, 1000
- Bertelli, G., Bressan, A., Chiosi, C., Fagotto, F., & Nasi, E. 1994, A&AS, 106, 275
- Bhalerao, V., Kasliwal, M. M., Bhattacharya, D., et al. 2017, ArXiv e-prints, arXiv:1706.00024
- Bissaldi, E., von Kienlin, A., Kouveliotou, C., et al. 2011, ApJ, 733, 97
- Blanchard, P. K., Berger, E., & Fong, W.-f. 2016, ApJ, 817, 144
- Bloom, J. S., Berger, E., Kulkarni, S. R., Djorgovski, S. G., & Frail, D. A. 2003a, AJ, 125, 999
- Bloom, J. S., Djorgovski, S. G., Kulkarni, S. R., & Frail, D. A. 1998, ApJ, 507, L25
- Bloom, J. S., Foley, R. J., Kocevski, D., & Perley, D. 2006a, GRB Coordinates Network, 5217, 1
- Bloom, J. S., Fox, D., van Dokkum, P. G., et al. 2003b, ApJ, 599, 957
- Bloom, J. S., Kulkarni, S. R., & Djorgovski, S. G. 2002, AJ, 123, 1111
- Bloom, J. S., Perley, D., Kocevski, D., et al. 2006b, GRB Coordinates Network, 5238, 1

- Boer, M., Ricker, G., Atteia, J.-L., et al. 2005, GRB Coordinates Network, 3653, 1
- Bolzonella, M., Miralles, J.-M., & Pelló, R. 2000, A&A, 363, 476
- Bošnjak, Ž., Götz, D., Bouchet, L., Schanne, S., & Cordier, B. 2014, A&A, 561, A25
- Bovy, J., & Rix, H.-W. 2013, ApJ, 779, 115
- Brenchley, P. J., Carden, G. A., Hints, L., et al. 2003, Geological Society of America Bulletin, 115, 89
- Bromberg, O., Nakar, E., & Piran, T. 2011, ApJ, 739, L55
- Bruzual, G., & Charlot, S. 2003, MNRAS, 344, 1000
- Burgess, J. M. 2014, MNRAS, 445, 2589
- Burns, E. 2014, GRB Coordinates Network, 16363, 1
- Burud, I., Rhoads, J., Fruchter, A., & Hjorth, J. 2001, GRB Coordinates Network, 1213, 1
- Butler, N., Ricker, G., Atteia, J.-L., et al. 2004, GRB Coordinates Network, 2701, 1
- Cabrera Lavers, A., de Ugarte Postigo, A., Castro-Tirado, A. J., et al. 2011, GRB Coordinates Network, 12234, 1
- Campana, S., Mangano, V., Blustin, A. J., et al. 2006, Nature, 442, 1008
- Cano, Z., Bersier, D., Guidorzi, C., et al. 2011, MNRAS, 413, 669
- Cano, Z., de Ugarte Postigo, A., Pozanenko, A., et al. 2014, A&A, 568, A19
- Cano, Z., de Ugarte Postigo, A., Perley, D., et al. 2015, MNRAS, 452, 1535
- Casagrande, L., Schönrich, R., Asplund, M., et al. 2011, A&A, 530, A138
- Cash, W. 1979, ApJ, 228, 939
- Castro, S., Galama, T. J., Harrison, F. A., et al. 2003, ApJ, 586, 128
- Castro-Tirado, A. J., Sokolov, V. V., Gorosabel, J., et al. 2001, A&A, 370, 398
- Castro-Tirado, A. J., Møller, P., García-Segura, G., et al. 2010, A&A, 517, A61
- Cenko, S. B., Berger, E., Djorgovski, S. G., Mahabal, A. A., & Fox, D. B. 2006a, GRB Coordinates Network, 5155
- Cenko, S. B., Cucchiara, A., Fox, D. B., Berger, E., & Price, P. A. 2007a, GRB Coordinates Network, 6888, 1
- Cenko, S. B., Fox, D. B., Cucchiara, A., et al. 2007b, GRB Coordinates Network, 6556, 1
- Cenko, S. B., Hora, J. L., & Bloom, J. S. 2011a, GRB Coordinates Network, 11638, 1

- Cenko, S. B., Kasliwal, M., Cameron, P. B., Kulkarni, S. R., & Fox, D. B. 2006b, GRB Coordinates Network, 5946, 1
- Cenko, S. B., Levan, A. J., & Cucchiara, A. 2013, GRB Coordinates Network, 14762, 1
- Cenko, S. B., Perley, D. A., Junkkarinen, V., et al. 2009, GRB Coordinates Network, 9518, 1
- Cenko, S. B., Perley, D. A., Morgan, A. N., et al. 2010, GRB Coordinates Network, 10752, 1
- Cenko, S. B., Prochaska, J. X., Cucchiara, A., Perley, D. A., & Bloom, J. S. 2011b, GRB Coordinates Network, 11736, 1
- Cenko, S. B., Fox, D. B., Penprase, B. E., et al. 2008a, ApJ, 677, 441
- Cenko, S. B., Berger, E., Nakar, E., et al. 2008b, ArXiv e-prints, arXiv:0802.0874
- Cenko, S. B., Frail, D. A., Harrison, F. A., et al. 2011c, ApJ, 732, 29
- Cenko, S. B., Urban, A. L., Perley, D. A., et al. 2015, ApJ, 803, L24
- Chaplin, V. 2012, GRB Coordinates Network, 13737
- Chary, R., Becklin, E. E., & Armus, L. 2002, ApJ, 566, 229
- Chary, R., Berger, E., & Cowie, L. 2007, ApJ, 671, 272
- Chen, H.-W., Prochaska, J. X., Bloom, J. S., & Thompson, I. B. 2005, ApJ, 634, L25
- Chen, H.-W., Perley, D. A., Pollack, L. K., et al. 2009, ApJ, 691, 152
- Chornock, R., & Berger, E. 2011, GRB Coordinates Network, 11518, 1
- Chornock, R., Berger, E., & Fox, D. 2011a, GRB Coordinates Network, 12537, 1
- Chornock, R., Berger, E., Fox, D., et al. 2010a, GRB Coordinates Network, 11164, 1
- Chornock, R., Berger, E., & Fox, D. B. 2011b, GRB Coordinates Network, 11538, 1
- Chornock, R., Berger, E., Fox, D. B., et al. 2013a, ApJ, 774, 26
- Chornock, R., Cenko, S. B., Griffith, C. V., et al. 2009a, GRB Coordinates Network, 9151, 1
- Chornock, R., Cucchiara, A., Fox, D., & Berger, E. 2010b, GRB Coordinates Network, 10466, 1
- Chornock, R., Fox, D. B., & Berger, E. 2014a, GRB Coordinates Network, 16269, 1
- Chornock, R., Fox, D. B., Cucchiara, A., Perley, D. A., & Levan, A. 2014b, GRB Coordinates Network, 16301, 1

- Chornock, R., Fox, D. B., Tanvir, N. R., & Berger, E. 2014c, GRB Coordinates Network, 15966, 1
- Chornock, R., Lunnan, R., & Berger, E. 2013b, GRB Coordinates Network, 15307, 1
- Chornock, R., Perley, D. A., Cenko, S. B., & Bloom, J. S. 2009b, GRB Coordinates Network, 9243, 1
- Chornock, R., Perley, D. A., Cenko, S. B., et al. 2009c, GRB Coordinates Network, 8994, 1
- Chornock, R., Perley, D. A., & Cobb, B. E. 2009d, GRB Coordinates Network, 10100, 1
- Chornock, R., Berger, E., Levesque, E. M., et al. 2010c, ArXiv e-prints, arXiv:1004.2262
- Christensen, L., Hjorth, J., & Gorosabel, J. 2004, A&A, 425, 913
- . 2005, ApJ, 631, L29
- Chu, Q., Howell, E. J., Rowlinson, A., et al. 2016, MNRAS, 459, 121
- Church, R. P., Levan, A. J., Davies, M. B., & Tanvir, N. 2011, MNRAS, 413, 2004
- Cline, T. L., Desai, U. D., Klebesadel, R. W., & Strong, I. B. 1973, ApJ, 185, L1
- Cobb, B. E., Bailyn, C. D., van Dokkum, P. G., Buxton, M. M., & Bloom, J. S. 2004, ApJ, 608, L93
- Collazzi, A. C., & Connaughton, V. 2013, GRB Coordinates Network, 14972
- Connaughton, V. 2002, ApJ, 567, 1028
- Connaughton, V., Burns, E., Goldstein, A., et al. 2016, ApJ, 826, L6
- Costa, E., Frontera, F., Heise, J., et al. 1997a, Nature, 387, 783
- Costa, E., Feroci, M., Frontera, F., et al. 1997b, IAUC, 6572
- Costa, E., Feroci, M., Piro, L., et al. 1997c, IAUC, 6576
- Cowperthwaite, P. S., Berger, E., Soares-Santos, M., et al. 2016, ApJ, 826, L29
- Crew, G., Ricker, G., Atteia, J.-L., et al. 2005, GRB Coordinates Network, 4021, 1
- Cucchiara, A. 2012, GRB Coordinates Network, 13213, 1
- Cucchiara, A., Bloom, J. S., & Cenko, S. B. 2011a, GRB Coordinates Network, 12202, 1
- Cucchiara, A., & Cenko, S. B. 2013, GRB Coordinates Network, 15624, 1
- Cucchiara, A., Fox, D., & Tanvir, N. 2009a, GRB Coordinates Network, 10065, 1
- Cucchiara, A., & Fox, D. B. 2008, GRB Coordinates Network, 7654, 1

- . 2010, GRB Coordinates Network, 10606, 1
- Cucchiara, A., Fox, D. B., & Cenko, S. B. 2007a, GRB Coordinates Network, 7124, 1
- Cucchiara, A., Fox, D. B., Cenko, S. B., & Berger, E. 2008a, GRB Coordinates Network, 8346, 1
- . 2008b, GRB Coordinates Network, 8713, 1
- Cucchiara, A., Fox, D. B., Cenko, S. B., et al. 2007b, GRB Coordinates Network, 6665
- Cucchiara, A., Fox, D. B., Cenko, S. B., & Price, P. A. 2007c, GRB Coordinates Network, 6083, 1
- Cucchiara, A., Fox, D. B., Cenko, S. B., Tanvir, N., & Berger, E. 2009b, GRB Coordinates Network, 10031, 1
- Cucchiara, A., Fox, D. B., Tanvir, N., & Berger, E. 2009c, GRB Coordinates Network, 9873, 1
- Cucchiara, A., & Fumagalli, M. 2013, GRB Coordinates Network, 14207, 1
- Cucchiara, A., Fumagalli, M., Rafelski, M., et al. 2015, ApJ, 804, 51
- Cucchiara, A., Levan, A. J., & Tanvir, N. 2011b, GRB Coordinates Network, 12777, 1
- Cucchiara, A., & Perley, D. 2013, GRB Coordinates Network, 15144, 1
- Cucchiara, A., Perley, D., & Cenko, S. B. 2013, GRB Coordinates Network, 14748, 1
- Cucchiara, A., & Tanvir, N. R. 2013, GRB Coordinates Network, 14621, 1
- Cucchiara, A., Tanvir, N. R., Perley, D., & Levan, A. J. 2012, GRB Coordinates Network, 13512, 1
- Cucchiara, A., Levan, A. J., Fox, D. B., et al. 2011c, ApJ, 736, 7
- Cummings, J., Barbier, L., Barthelmy, S., et al. 2005, GRB Coordinates Network, 3339, 1
- Dai, Z. G., & Lu, T. 1998, Physical Review Letters, 81, 4301
- Dar, A., Laor, A., & Shaviv, N. J. 1998, Physical Review Letters, 80, 5813
- D'Avanzo, P., Malesani, D., Covino, S., et al. 2009, A&A, 498, 711
- D'Avanzo, P., Perri, M., Fugazza, D., et al. 2010, A&A, 522, A20
- De Cia, A., Jakobsson, P., Björnsson, G., et al. 2011, MNRAS, 412, 2229
- De Cia, A., Ledoux, C., Fox, A. J., et al. 2012, A&A, 545, A64

- de Ugarte Postigo, A., Castro-Tirado, A. J., & Gorosabel, J. 2011a, GRB Coordinates Network, 11978, 1
- de Ugarte Postigo, A., Castro-Tirado, A. J., Tello, J. C., Cabrera Lavers, A., & Reverte, D. 2011b, GRB Coordinates Network, 11993, 1
- de Ugarte Postigo, A., Gorosabel, J., Fynbo, J. P. U., Wiersema, K., & Tanvir, N. 2009a, GRB Coordinates Network, 9771, 1
- de Ugarte Postigo, A., Gorosabel, J., Malesani, D., Fynbo, J. P. U., & Levan, A. J. 2009b, GRB Coordinates Network, 9383, 1
- de Ugarte Postigo, A., Jakobsson, P., Malesani, D., et al. 2009c, GRB Coordinates Network, 8766, 1
- de Ugarte Postigo, A., Tanvir, N., Sanchez-Ramirez, R., et al. 2013a, GRB Coordinates Network, 14437, 1
- de Ugarte Postigo, A., Thoene, C. C., Gorosabel, J., et al. 2013b, GRB Coordinates Network, 15470, 1
- de Ugarte Postigo, A., Xu, D., Malesani, D., et al. 2013c, GRB Coordinates Network, 15187, 1
- de Ugarte Postigo, A., Campana, S., Thöne, C. C., et al. 2013d, A&A, 557, L18
- de Ugarte Postigo, A., Gorosabel, J., Xu, D., et al. 2014a, GRB Coordinates Network, 16310, 1
- de Ugarte Postigo, A., Thöne, C. C., Rowlinson, A., et al. 2014b, A&A, 563, A62
- D'Elia, V., Covino, S., & D'Avanzo, P. 2008a, GRB Coordinates Network, 8438, 1
- D'Elia, V., Thoene, C. C., de Ugarte Postigo, A., et al. 2008b, GRB Coordinates Network, 8531, 1
- D'Elia, V., Fynbo, J. P. U., Goldoni, P., et al. 2014, A&A, 564, A38
- Della Valle, M., Chincarini, G., Panagia, N., et al. 2006, Nature, 444, 1050
- Djorgovski, S. G., Bloom, J. S., & Kulkarni, S. R. 2003, ApJ, 591, L13
- Djorgovski, S. G., Frail, D. A., Kulkarni, S. R., et al. 2001, ApJ, 562, 654
- Djorgovski, S. G., Kulkarni, S. R., Bloom, J. S., & Frail, D. A. 1999, GRB Coordinates Network, 289, 1
- Djorgovski, S. G., Kulkarni, S. R., Bloom, J. S., et al. 1998, ApJ, 508, L17
- Dominik, M., Berti, E., O'Shaughnessy, R., et al. 2015, ApJ, 806, 263

- Draine, B. T. 2011, Physics of the Interstellar and Intergalactic Medium
- Eichler, D., Livio, M., Piran, T., & Schramm, D. N. 1989, Nature, 340, 126
- Eisenhauer, F., Schödel, R., Genzel, R., et al. 2003, ApJ, 597, L121
- Elliott, J., Krühler, T., Greiner, J., et al. 2013a, A&A, 556, A23
- . 2013b, ArXiv e-prints, arXiv:1308.5520
- Fatkullin, T., Gorosabel, J., de Ugarte Postigo, A., et al. 2009, GRB Coordinates Network, 9712, 1
- Ferrero, P., Klose, S., Kann, D. A., et al. 2009, A&A, 497, 729
- Fishman, G. J., Meegan, C. A., Wilson, R. B., et al. 1993, A&AS, 97, 17
- Flores, H., Covino, S., de Ugarte Postigo, A., et al. 2013, GRB Coordinates Network, 14493, 1
- Flores, H., Fynbo, J. P. U., de Ugarte Postigo, A., et al. 2010, GRB Coordinates Network, 11317, 1
- Foley, S., McGlynn, S., Hanlon, L., McBreen, S., & McBreen, B. 2008, A&A, 484, 143
- Fong, W., & Berger, E. 2013, ApJ, 776, 18
- Fong, W., Berger, E., & Fox, D. B. 2010, ApJ, 708, 9
- Fong, W., Berger, E., Chornock, R., et al. 2011, ApJ, 730, 26
- . 2013, ApJ, 769, 56
- Fox, A. J., Ledoux, C., Vreeswijk, P. M., Smette, A., & Jaunsen, A. O. 2008, A&A, 491, 189
- Fox, D. B., Frail, D. A., Price, P. A., et al. 2005, Nature, 437, 845
- Frederiks, D. 2013, GRB Coordinates Network, 14578
- Frederiks, D. D., Hurley, K., Svinkin, D. S., et al. 2013, ApJ, 779, 151
- Friis, M., De Cia, A., Krühler, T., et al. 2015, MNRAS, 451, 167
- Frontera, F., Guidorzi, C., Montanari, E., et al. 2009, ApJ, 180, 192
- Fruchter, A., Pattel, S., Kouveliotou, C., et al. 2002, GRB Coordinates Network, 1268, 1
- Fruchter, A. S., Levan, A. J., Strolger, L., et al. 2006, Nature, 441, 463
- Fugazza, D., Thoene, C. C., D'Elia, V., et al. 2009, GRB Coordinates Network, 8892, 1
- Fynbo, J. P. U., Møller, P., Thomsen, B., et al. 2002, A&A, 388, 425

- Fynbo, J. P. U., Jakobsson, P., Möller, P., et al. 2003, A&A, 406, L63
- Fynbo, J. P. U., Gorosabel, J., Smette, A., et al. 2005, ApJ, 633, 317
- Fynbo, J. P. U., Watson, D., Thöne, C. C., et al. 2006, Nature, 444, 1047
- Fynbo, J. P. U., Jakobsson, P., Prochaska, J. X., et al. 2009, ApJ, 185, 526
- Fynbo, J. P. U., Tanvir, N. R., D'Elia, V., et al. 2012, GRB Coordinates Network, 14120, 1
- Fynbo, J. P. U., Krühler, T., Leighly, K., et al. 2014, A&A, 572, A12
- Gal-Yam, A., Fox, D. B., Price, P. A., et al. 2006, Nature, 444, 1053
- Galama, T. J., Groot, P. J., van Paradijs, J., et al. 1997, IAUC, 6655, 1
- Galama, T. J., Vreeswijk, P. M., van Paradijs, J., et al. 1998, Nature, 395, 670
- Galama, T. J., Reichart, D., Brown, T. M., et al. 2003, ApJ, 587, 135
- Galassi, M., Ricker, G., Atteia, J.-L., et al. 2004, GRB Coordinates Network, 2770, 1
- Gallazzi, A., Brinchmann, J., Charlot, S., & White, S. D. M. 2008, MNRAS, 383, 1439
- Galli, A., & Piro, L. 2006, A&A, 455, 413
- Gao, H., Ding, X., Wu, X.-F., Dai, Z.-G., & Zhang, B. 2015, ApJ, 807, 163
- Gao, H., Ding, X., Wu, X.-F., Zhang, B., & Dai, Z.-G. 2013, ApJ, 771, 86
- Gao, H., Zhang, B., & Lü, H.-J. 2016, Phys. Rev. D, 93, 044065
- Gao, H., Zhang, B., Lü, H.-J., & Li, Y. 2017, ApJ, 837, 50
- Gehrels, N., Laird, C. M., Jackman, C. H., et al. 2003, ApJ, 585, 1169
- Gehrels, N., Ramirez-Ruiz, E., & Fox, D. B. 2009, Annual Review of Astronomy and Astrophysics, 47, 567
- Gehrels, N., Sarazin, C. L., O'Brien, P. T., et al. 2005, Nature, 437, 851
- Gehrels, N., Norris, J. P., Barthelmy, S. D., et al. 2006, Nature, 444, 1044
- Gehrels, N., Barthelmy, S. D., Burrows, D. N., et al. 2008, ApJ, 689, 1161
- Gendre, B., Stratta, G., Atteia, J. L., et al. 2013, ApJ, 766, 30
- Ghirlanda, G., Nava, L., Ghisellini, G., Celotti, A., & Firmani, C. 2009, A&A, 496, 585
- Gillessen, S., Eisenhauer, F., Trippe, S., et al. 2009, ApJ, 692, 1075
- Goldoni, P., de Ugarte Postigo, A., & Fynbo, J. P. U. 2013, GRB Coordinates Network, 15571, 1

- Goldoni, P., Flores, H., Malesani, D., et al. 2010, GRB Coordinates Network, 10684, 1
- Goldstein, A., Preece, R. D., Mallozzi, R. S., et al. 2013, ApJ, 208, 21
- Golenetskii, S., Aptekar, R., Frederiks, D., et al. 2013a, GRB Coordinates Network, 14958, 1
- . 2013b, GRB Coordinates Network, 15145, 1
- . 2013c, GRB Coordinates Network, 15203, 1
- . 2013d, GRB Coordinates Network, 15413, 1
- . 2014a, GRB Coordinates Network, 15889, 1
- Golenetskii, S., Aptekar, R., Mazets, E., et al. 2004, GRB Coordinates Network, 2754, 1
- . 2005a, GRB Coordinates Network, 3660, 1
- . 2005b, GRB Coordinates Network, 3179, 1
- . 2005c, GRB Coordinates Network, 3474, 1
- . 2005d, GRB Coordinates Network, 4030, 1
- . 2005e, GRB Coordinates Network, 4078, 1
- . 2005f, GRB Coordinates Network, 4150, 1
- . 2005g, GRB Coordinates Network, 4238, 1
- . 2005h, GRB Coordinates Network, 4394, 1
- . 2006a, GRB Coordinates Network, 5837, 1
- . 2006b, GRB Coordinates Network, 4564, 1
- . 2006c, GRB Coordinates Network, 4599, 1
- . 2006d, GRB Coordinates Network, 4881, 1
- . 2006e, GRB Coordinates Network, 5264, 1
- . 2006f, GRB Coordinates Network, 5460, 1
- . 2006g, GRB Coordinates Network, 5722, 1
- . 2006h, GRB Coordinates Network, 5748, 1
- . 2006i, GRB Coordinates Network, 5890, 1
- . 2006j, GRB Coordinates Network, 5710, 1

- . 2007a, GRB Coordinates Network, 6049, 1
- . 2007b, GRB Coordinates Network, 6230, 1
- . 2007c, GRB Coordinates Network, 6459, 1
- . 2007d, GRB Coordinates Network, 6615, 1
- . 2007e, GRB Coordinates Network, 6849, 1
- . 2007f, GRB Coordinates Network, 6879, 1
- . 2007g, GRB Coordinates Network, 6960, 1
- . 2007h, GRB Coordinates Network, 7155, 1
- . 2008a, GRB Coordinates Network, 7482, 1
- . 2008b, GRB Coordinates Network, 7487, 1
- . 2008c, GRB Coordinates Network, 7589, 1
- . 2008d, GRB Coordinates Network, 7784, 1
- . 2008e, GRB Coordinates Network, 7812, 1
- . 2008f, GRB Coordinates Network, 7854, 1
- . 2007i, GRB Coordinates Network, 6403, 1
- . 2007j, GRB Coordinates Network, 7114, 1
- . 2009a, GRB Coordinates Network, 10045, 1
- . 2009b, GRB Coordinates Network, 9647, 1
- . 2008g, GRB Coordinates Network, 7862, 1
- . 2008h, GRB Coordinates Network, 7995, 1
- . 2008i, GRB Coordinates Network, 8611, 1

Golenetskii, S., Aptekar, R., Frederiks, D., et al. 2009c, GRB Coordinates Network, 9679, 1

Golenetskii, S., Aptekar, R., Mazets, E., et al. 2009d, GRB Coordinates Network, 8878, 1

Golenetskii, S., Aptekar, R., Frederiks, D., et al. 2010a, GRB Coordinates Network, 10833, 1

- . 2010b, GRB Coordinates Network, 10882, 1
- . 2010c, GRB Coordinates Network, 11470, 1

- Golenetskii, S., Aptekar, R., Mazets, E., et al. 2011a, GRB Coordinates Network, 11659, 1
- . 2011b, GRB Coordinates Network, 11722, 1
- . 2011c, GRB Coordinates Network, 11971, 1
- Golenetskii, S., Aptekar, R., Frederiks, D., et al. 2011d, GRB Coordinates Network, 12008, 1
- . 2011e, GRB Coordinates Network, 12135, 1
- . 2011f, GRB Coordinates Network, 12166, 1
- . 2011g, GRB Coordinates Network, 12270, 1
- . 2011h, GRB Coordinates Network, 12362, 1
- . 2011i, GRB Coordinates Network, 12433, 1
- Golenetskii, S., Aptekar, R., Mazets, E., et al. 2011j, GRB Coordinates Network, 12663, 1
- . 2011k, GRB Coordinates Network, 12676, 1
- Golenetskii, S., Aptekar, R., Frederiks, D., et al. 2012, GRB Coordinates Network, 13382
- . 2013e, GRB Coordinates Network, 14368, 1
- . 2013f, GRB Coordinates Network, 14417, 1
- . 2013g, GRB Coordinates Network, 14487, 1
- . 2013h, GRB Coordinates Network, 14575, 1
- . 2013i, GRB Coordinates Network, 14771, 1
- Golenetskii, S., Aptekar, R., Mazets, E., et al. 2013j, GRB Coordinates Network, 14808, 1
- Golenetskii, S., Aptekar, R., Frederiks, D., et al. 2014b, GRB Coordinates Network, 16134, 1
- Gorosabel, J., Fynbo, J. P. U., Fruchter, A., et al. 2005, A&A, 437, 411
- Götz, D., Covino, S., Hascoët, R., et al. 2011, MNRAS, 413, 2173
- Graziani, C., Shirasaki, Y., Matsuoka, M., et al. 2003, GRB Coordinates Network, 1956, 1
- Greiner, J., Burgess, J. M., Savchenko, V., & Yu, H.-F. 2016, ApJ, 827, L38
- Greiner, J., Rau, A., Schady, P., Saviane, I., & Cenko, B. 2012, GRB Coordinates Network, 13493, 1
- Greiner, J., Klose, S., Salvato, M., et al. 2003, ApJ, 599, 1223

- Greiner, J., Krühler, T., McBreen, S., et al. 2009, ApJ, 693, 1912
- Greiner, J., Krühler, T., Klose, S., et al. 2011, A&A, 526, A30
- Greiner, J., Yu, H.-F., Krühler, T., et al. 2014, A&A, 568, A75
- Greiner, J., Fox, D. B., Schady, P., et al. 2015, ApJ, 809, 76
- Groot, P., Kaper, L., Ellerbroek, L., et al. 2010, GRB Coordinates Network, 10441, 1
- Groot, P. J., Galama, T. J., van Paradijs, J., et al. 1997a, IAUC, 6584
- . 1997b, IAUC, 6588
- Gruber, D., & Goldstein, A. 2012, GRB Coordinates Network, 13498
- Gruber, D., Krühler, T., Foley, S., et al. 2011, A&A, 528, A15
- Gruber, D., Goldstein, A., Weller von Ahlefeld, V., et al. 2014, ApJ, 211, 12
- Guidorzi, C., Kobayashi, S., Perley, D. A., et al. 2011, MNRAS, 417, 2124
- Han, X. H., Hammer, F., Liang, Y. C., et al. 2010, A&A, 514, A24
- Hartoog, O. E., Malesani, D., Wiersema, K., et al. 2012, GRB Coordinates Network, 13730, 1
- Hartoog, O. E., Xu, D., Malesani, D., et al. 2013, GRB Coordinates Network, 15494, 1
- Hartoog, O. E., Malesani, D., Fynbo, J. P. U., et al. 2015, A&A, 580, A139
- Hashimoto, T., Perley, D. A., Ohta, K., et al. 2015, ApJ, 806, 250
- Heise, J., in't Zand, J. J. M., Kulkarni, S. R., & Costa, E. 2001, GRB Coordinates Network, 1138, 1
- Heise, J., in 't Zand, J., Costa, E., et al. 1997, IAUC, 6654
- Higdon, J. C., & Lingenfelter, R. E. 1990, Annual Review of Astronomy and Astrophysics, 28, 401
- Hjorth, J., & Bloom, J. S. 2012, The Gamma-Ray Burst - Supernova Connection, 169–190
- Hjorth, J., Sollerman, J., Møller, P., et al. 2003a, Nature, 423, 847
- Hjorth, J., Møller, P., Gorosabel, J., et al. 2003b, ApJ, 597, 699
- Hjorth, J., Sollerman, J., Gorosabel, J., et al. 2005a, ApJ, 630, L117
- Hjorth, J., Watson, D., Fynbo, J. P. U., et al. 2005b, Nature, 437, 859
- Hogg, D. W., Pahre, M. A., McCarthy, J. K., et al. 1997, MNRAS, 288, 404

- Holland, S. T., Soszyński, I., Gladders, M. D., et al. 2002, AJ, 124, 639
- Holland, S. T., Sbarufatti, B., Shen, R., et al. 2010, ApJ, 717, 223
- Hunt, L. K., Palazzi, E., Michałowski, M. J., et al. 2014, A&A, 565, A112
- Hurley, K., & Cline, T. 1999, GRB Coordinates Network, 450, 1
- Hurley, K., Cline, T., & Mazets, E. 2000a, GRB Coordinates Network, 529, 1
- Hurley, K., Cline, T., Mazets, E., & Golenetskii, S. 2000b, GRB Coordinates Network, 791, 1
- Hurley, K., Cline, T., Mazets, E., et al. 2000c, ApJ, 534, L23
- Hurley, K., Cline, T., Ricker, G., et al. 2002a, GRB Coordinates Network, 1263
- . 2002b, GRB Coordinates Network, 1507, 1
- Ilbert, O., Arnouts, S., Le Floc'h, E., et al. 2014, ArXiv e-prints, arXiv:1410.4875
- . 2015, A&A, 579, A2
- in't Zand, J., Reali, F., Granata, S., Lowes, P., & Piro, L. 2002, GRB Coordinates Network, 1383, 1
- Izotov, Y. I., Stasińska, G., Meynet, G., Guseva, N. G., & Thuan, T. X. 2006, A&A, 448, 955
- Jakobsson, P., de Ugarte Postigo, A., Gorosabel, J., et al. 2009, GRB Coordinates Network, 9797, 1
- Jakobsson, P., Malesani, D., Fynbo, J. P. U., et al. 2007a, GRB Coordinates Network, 6997, 1
- Jakobsson, P., Hjorth, J., Fynbo, J. P. U., et al. 2004, A&A, 427, 785
- Jakobsson, P., Frail, D. A., Fox, D. B., et al. 2005, ApJ, 629, 45
- Jakobsson, P., Levan, A., Fynbo, J. P. U., et al. 2006a, A&A, 447, 897
- Jakobsson, P., Fynbo, J. P. U., Ledoux, C., et al. 2006b, A&A, 460, L13
- Jakobsson, P., Fynbo, J. P. U., Andersen, M. I., et al. 2007b, GRB Coordinates Network, 6398, 1
- Jakobsson, P., Hjorth, J., Malesani, D., et al. 2012, ApJ, 752, 62
- Janiuk, A., Moderski, R., & Proga, D. 2008, ApJ, 687, 433
- Jaunsen, A. O., Andersen, M. I., Hjorth, J., et al. 2003, A&A, 402, 125

- Jenke, P. 2013, GRB Coordinates Network, 15331, 1
- Jenke, P., & Xiong, S. 2014, GRB Coordinates Network, 15644, 1
- Jensen, B. L., Fynbo, J. U., Gorosabel, J., et al. 2001, A&A, 370, 909
- Jeong, S., Sanchez-Ramirez, R., Gorosabel, J., & Castro-Tirado, A. J. 2014a, GRB Coordinates Network, 15936, 1
- Jeong, S., Castro-Tirado, A. J., Bremer, M., et al. 2014b, A&A, 569, A93
- Jimenez, R., Band, D., & Piran, T. 2001, ApJ, 561, 171
- Jin, Z.-P., Li, X., Cano, Z., et al. 2015, ApJ, 811, L22
- Jin, Z.-P., Covino, S., Della Valle, M., et al. 2013, ApJ, 774, 114
- Jin, Z.-P., Hotokezaka, K., Li, X., et al. 2016a, ArXiv e-prints, arXiv:1603.07869
- . 2016b, Nature Communications, 7, 12898
- Kaneko, Y., Bostancı, Z. F., Göğüş, E., & Lin, L. 2015, MNRAS, 452, 824
- Kann, D. A., Klose, S., Zhang, B., et al. 2010, ApJ, 720, 1513
- . 2011, ApJ, 734, 96
- Kawai, N., Kosugi, G., Aoki, K., et al. 2006, Nature, 440, 184
- Kelly, P. L., Filippenko, A. V., Fox, O. D., Zheng, W., & Clubb, K. I. 2013, ApJ, 775, L5
- Kennea, J. A., Burrows, D. N., Nousek, J., et al. 2005, GRB Coordinates Network, 3383
- Kennicutt, R. C., & Evans, N. J. 2012, Annual Review of Astronomy and Astrophysics, 50, 531
- Kennicutt, Jr., R. C. 1998, Annual Review of Astronomy and Astrophysics, 36, 189
- Kewley, L. J., & Dopita, M. A. 2002, ApJ, 142, 35
- Kewley, L. J., & Ellison, S. L. 2008, ApJ, 681, 1183
- Kimm, T., Somerville, R. S., Yi, S. K., et al. 2009, MNRAS, 394, 1131
- Klebesadel, R. W., Strong, I. B., & Olson, R. A. 1973, ApJ, 182, L85
- Klose, S., Greiner, J., Rau, A., et al. 2004, AJ, 128, 1942
- Knust, F., Kruehler, T., Klose, S., & Greiner, J. 2012, GRB Coordinates Network, 13810, 1
- Kobulnicky, H. A., & Kewley, L. J. 2004, ApJ, 617, 240
- Kohn, S. A., Michałowski, M. J., Bourne, N., et al. 2015, MNRAS, 448, 1494

- Kouveliotou, C., Meegan, C. A., Fishman, G. J., et al. 1993, ApJ, 413, L101
- Krimm, H. A., Barthelmy, S. D., Baumgartner, W. H., et al. 2012, GRB Coordinates Network, 14123, 1
- Kroupa, P. 2001, MNRAS, 322, 231
- Kruehler, T., Fynbo, J. P. U., Milvang-Jensen, B., Tanvir, N., & Jakobsson, P. 2012, GRB Coordinates Network, 13134, 1
- Kruehler, T., Xu, D., Sanchez-Ramirez, R., et al. 2013, GRB Coordinates Network, 14390, 1
- Kröhler, T., Schady, P., Greiner, J., et al. 2011a, A&A, 526, A153
- Kröhler, T., Greiner, J., Schady, P., et al. 2011b, A&A, 534, A108
- Kröhler, T., Ledoux, C., Fynbo, J. P. U., et al. 2013, A&A, 557, A18
- Kröhler, T., Malesani, D., Fynbo, J. P. U., et al. 2015, A&A, 581, A125
- Kuin, N. P. M., Landsman, W., Page, M. J., et al. 2009, MNRAS, 395, L21
- Kulkarni, S. R., Djorgovski, S. G., Ramaprakash, A. N., et al. 1998, Nature, 393, 35
- Kulkarni, S. R., Djorgovski, S. G., Odewahn, S. C., et al. 1999, Nature, 398, 389
- Kumar, P., & Zhang, B. 2015, Physics Reports, 561, 1
- Laskar, T., Berger, E., & Chary, R.-R. 2011, ApJ, 739, 1
- Lazzarotto, F., Del Monte, E., Donnarumma, I., et al. 2011, GRB Coordinates Network, 12666
- Lazzati, D., Ramirez-Ruiz, E., & Ghisellini, G. 2001, A&A, 379, L39
- Le Floc'h, E., Duc, P.-A., Mirabel, I. F., et al. 2002, ApJ, 581, L81
- Leibler, C. N., & Berger, E. 2010, ApJ, 725, 1202
- Levan, A., Nugent, P., Fruchter, A., et al. 2005, ApJ, 624, 880
- Levan, A. J., Fynbo, J. P. U., Hjorth, J., et al. 2009a, GRB Coordinates Network, 9958, 1
- Levan, A. J., Tanvir, N. R., Wiersema, K., & O'Brien, P. T. 2011, GRB Coordinates Network, 12414
- Levan, A. J., Malesani, D., Tanvir, N. R., et al. 2009b, GRB Coordinates Network, 8856, 1
- Levan, A. J., Tanvir, N. R., Starling, R. L. C., et al. 2014a, ApJ, 781, 13
- Levan, A. J., Tanvir, N. R., Fruchter, A. S., et al. 2014b, ApJ, 792, 115

- Levesque, E., Chornock, R., Kewley, L., et al. 2009, GRB Coordinates Network, 9264, 1
- Levesque, E. M., Berger, E., Soderberg, A. M., & Chornock, R. 2011, ApJ, 739, 23
- Levesque, E. M., Chornock, R., Soderberg, A. M., Berger, E., & Lunman, R. 2012, ApJ, 758, 92
- Levesque, E. M., Kewley, L. J., Berger, E., & Zahid, H. J. 2010a, AJ, 140, 1557
- Levesque, E. M., Bloom, J. S., Butler, N. R., et al. 2010b, MNRAS, 401, 963
- Li, L., Liang, E.-W., Tang, Q.-W., et al. 2012, ApJ, 758, 27
- Li, L.-X., & Paczyński, B. 1998, ApJ, 507, L59
- Li, Y., Zhang, B., & Lü, H.-J. 2016, ApJ, 227, 7
- Liang, E., Zhang, B., Virgili, F., & Dai, Z. G. 2007a, ApJ, 662, 1111
- Liang, E.-W., Zhang, B.-B., & Zhang, B. 2007b, ApJ, 670, 565
- Licquia, T. C., & Newman, J. A. 2014, ArXiv e-prints, arXiv:1407.1078
- Loeb, A. 2016, ApJ, 819, L21
- Lü, H.-J., & Zhang, B. 2014, ApJ, 785, 74
- Lü, H.-J., Zhang, B., Lei, W.-H., Li, Y., & Lasky, P. D. 2015, ApJ, 805, 89
- Lü, H.-J., Zhang, B., Liang, E.-W., Zhang, B.-B., & Sakamoto, T. 2014, MNRAS, 442, 1922
- MacFadyen, A. I., & Woosley, S. E. 1999, ApJ, 524, 262
- Madau, P., & Dickinson, M. 2014, Annual Review of Astronomy and Astrophysics, 52, 415
- Maiolino, R., Nagao, T., Grazian, A., et al. 2008, A&A, 488, 463
- Maiorano, E., Masetti, N., Palazzi, E., et al. 2006, A&A, 455, 423
- Malesani, D., Fynbo, J. P. U., Christensen, L., et al. 2009a, GRB Coordinates Network, 9761, 1
- Malesani, D., Fynbo, J. P. U., D'Elia, V., et al. 2009b, GRB Coordinates Network, 9457, 1
- Malesani, D., Xu, D., D'Avanzo, P., Palazzi, E., & Perna, D. 2014a, GRB Coordinates Network, 16229, 1
- Malesani, D., Xu, D., Fynbo, J. P. U., et al. 2014b, GRB Coordinates Network, 15800, 1
- Mannucci, F., Cresci, G., Maiolino, R., Marconi, A., & Gnerucci, A. 2010, MNRAS, 408, 2115
- Mannucci, F., Salvaterra, R., & Campisi, M. A. 2011, MNRAS, 414, 1263

- Maraston, C. 2005, MNRAS, 362, 799
- Maraston, C., Strömbäck, G., Thomas, D., Wake, D. A., & Nichol, R. C. 2009, MNRAS, 394, L107
- Masetti, N., Palazzi, E., Pian, E., et al. 2003, A&A, 404, 465
- . 2005, A&A, 438, 841
- Mazets, E. P., Golenetskij, S. V., & Il'inskij, V. N. 1974, Pisma v Zhurnal Eksperimentalnoi i Teoreticheskoi Fiziki, 19, 126
- Mazets, E. P., Golenetskii, S. V., Ilinskii, V. N., et al. 1981, Astrophysics and Space Science, 80, 3
- McBreen, S., Krühler, T., Rau, A., et al. 2010, A&A, 516, A71
- McGlynn, S., Foley, S., McBreen, S., et al. 2008, A&A, 486, 405
- McGuire, J. T. W., Tanvir, N. R., Levan, A. J., et al. 2015, ArXiv e-prints, arXiv:1512.07808
- McMillan, P. J. 2011, MNRAS, 414, 2446
- Meegan, C. A., Fishman, G. J., Wilson, R. B., et al. 1992, Nature, 355, 143
- Meegan, C. A., Pendleton, G. N., Briggs, M. S., et al. 1996, ApJ, 106, 65
- Melandri, A., Bernardini, M. G., D'Avanzo, P., et al. 2015, A&A, 581, A86
- Melott, A. L., & Thomas, B. C. 2008, ArXiv e-prints, arXiv:0809.0899
- . 2011, Astrobiology, 11, 343
- Melott, A. L., Lieberman, B. S., Laird, C. M., et al. 2004, International Journal of Astrobiology, 3, 55
- Mészáros, P., & Rees, M. J. 1997, ApJ, 476, 232
- Metzger, B. D., & Berger, E. 2012, ApJ, 746, 48
- Metzger, B. D., Martínez-Pinedo, G., Darbha, S., et al. 2010, MNRAS, 406, 2650
- Metzger, M. R., Cohen, J. G., Chaffee, F. H., & Blandford, R. D. 1997a, IAUC, 6676
- Metzger, M. R., Djorgovski, S. G., Kulkarni, S. R., et al. 1997b, Nature, 387, 878
- Michałowski, M. J., Gentile, G., Hjorth, J., et al. 2015, A&A, 582, A78
- Milne, P. A., & Cenko, S. B. 2011, GRB Coordinates Network, 11708, 1
- Milvang-Jensen, B., Fynbo, J. P. U., Malesani, D., et al. 2012, ApJ, 756, 25

- Mirabal, N., Halpern, J. P., An, D., Thorstensen, J. R., & Terndrup, D. M. 2006, ApJ, 643, L99
- Mirabal, N., Halpern, J. P., & O'Brien, P. T. 2007, ApJ, 661, L127
- Mirabal, N., Halpern, J. P., Kulkarni, S. R., et al. 2002, ApJ, 578, 818
- Möller, P., Fynbo, J. P. U., Hjorth, J., et al. 2002, A&A, 396, L21
- Morgan, A. N., Perley, D. A., Cenko, S. B., et al. 2014, MNRAS, 440, 1810
- Mortlock, A., Conselice, C. J., Hartley, W. G., et al. 2015, MNRAS, 447, 2
- Moustakas, J., Kennicutt, Jr., R. C., & Tremonti, C. A. 2006, ApJ, 642, 775
- Muzzin, A., Marchesini, D., Stefanon, M., et al. 2013, ApJ, 777, 18
- Nakagawa, Y., Ricker, G., Atteia, J.-L., et al. 2005, GRB Coordinates Network, 3053, 1
- Nakar, E., & Piran, T. 2011, Nature, 478, 82
- Narayan, R., Paczynski, B., & Piran, T. 1992, ApJ, 395, L83
- Nava, L., Ghirlanda, G., Ghisellini, G., & Firmani, C. 2008, MNRAS, 391, 639
- Nemiroff, R. J. 1994, Comments on Astrophysics, 17, 189
- Nicastro, L., in't Zand, J. J. M., Amati, L., et al. 2004, A&A, 427, 445
- Niino, Y., Hashimoto, T., Aoki, K., et al. 2012, Publications of the Astronomical Society of Japan, 64, 115
- Norris, J., Ukwatta, T. N., Barthelmy, S. D., et al. 2010a, GRB Coordinates Network, 11113, 1
- Norris, J. P., & Bonnell, J. T. 2006, ApJ, 643, 266
- Norris, J. P., Gehrels, N., & Scargle, J. D. 2010b, ApJ, 717, 411
- Norris, J. P., Marani, G. F., & Bonnell, J. T. 2000, ApJ, 534, 248
- Nousek, J. A., Kouveliotou, C., Grupe, D., et al. 2006, ApJ, 642, 389
- Ofek, E. O., Cenko, S. B., Gal-Yam, A., et al. 2007, ApJ, 662, 1129
- Ohno, M., Kokubun, M., Suzuki, M., et al. 2008, GRB Coordinates Network, 7630, 1
- Olivares E., F., Greiner, J., Schady, P., et al. 2015, A&A, 577, A44
- Osip, D., Chen, H.-W., & Prochaska, J. X. 2006, GRB Coordinates Network, 5715, 1
- Paciesas, W. S., Meegan, C. A., Pendleton, G. N., et al. 1999, ApJ, 122, 465

- Paciesas, W. S., Meegan, C. A., von Kienlin, A., et al. 2012, ApJ, 199, 18
- Paczynski, B. 1986, ApJ, 308, L43
- Paczyński, B. 1998, ApJ, 494, L45
- Paczynski, B., & Rhoads, J. E. 1993, ApJ, 418, L5
- Pal’Shin, V. 2006, GRB Coordinates Network, 5984, 1
- Pal’Shin, V., Golenetskii, S., Aptekar, R., et al. 2008, GRB Coordinates Network, 8256, 1
- . 2009a, GRB Coordinates Network, 9196, 1
- . 2009b, GRB Coordinates Network, 9821, 1
- Pé langeon, A., Atteia, J.-L., Nakagawa, Y. E., et al. 2008, A&A, 491, 157
- Pellizza, L. J., Duc, P.-A., Le Floc’h, E., et al. 2006, A&A, 459, L5
- Penprase, B. E., Berger, E., Fox, D. B., et al. 2006, ApJ, 646, 358
- Pé rez-Ramírez, D., Norris, J. P., Gorosabel, J., et al. 2013, in EAS Publications Series, Vol. 61, EAS Publications Series, ed. A. J. Castro-Tirado, J. Gorosabel, & I. H. Park, 345–349
- Perley, D. A. 2014, GRB Coordinates Network, 16181, 1
- Perley, D. A., Bloom, J. S., Modjaz, M., et al. 2008a, GRB Coordinates Network, 7889, 1
- Perley, D. A., Bloom, J. S., & Prochaska, J. X. 2008b, GRB Coordinates Network, 7791, 1
- Perley, D. A., Foley, R. J., Bloom, J. S., & Butler, N. R. 2006, GRB Coordinates Network, 5387, 1
- Perley, D. A., Modjaz, M., Morgan, A. N., et al. 2012a, ApJ, 758, 122
- Perley, D. A., Prochaska, J. X., Kalas, P., et al. 2009a, GRB Coordinates Network, 10272, 1
- Perley, D. A., Prochaska, J. X., & Morgan, A. N. 2012b, GRB Coordinates Network, 14059, 1
- Perley, D. A., Li, W., Chornock, R., et al. 2008c, ApJ, 688, 470
- Perley, D. A., Bloom, J. S., Butler, N. R., et al. 2008d, ApJ, 672, 449
- Perley, D. A., Metzger, B. D., Granot, J., et al. 2009b, ApJ, 696, 1871
- Perley, D. A., Cenko, S. B., Bloom, J. S., et al. 2009c, AJ, 138, 1690
- Perley, D. A., Levan, A. J., Tanvir, N. R., et al. 2013, ApJ, 778, 128
- Perley, D. A., Krühler, T., Schulze, S., et al. 2016, ApJ, 817, 7

- Perna, R., Lazzati, D., & Giacomazzo, B. 2016, ApJ, 821, L18
- Pettini, M., & Pagel, B. E. J. 2004, MNRAS, 348, L59
- Piran, T., & Jimenez, R. 2014, Physical Review Letters, 113, 231102
- Piran, T., Nakar, E., & Rosswog, S. 2013, MNRAS, 430, 2121
- Piranomonte, S., Vergani, S. D., Malesani, D., et al. 2011, GRB Coordinates Network, 12164, 1
- Piranomonte, S., Japelj, J., Vergani, S. D., et al. 2015, MNRAS, 452, 3293
- Piro, L., Frail, D. A., Gorosabel, J., et al. 2002, ApJ, 577, 680
- Preece, R. D., Briggs, M. S., Mallozzi, R. S., et al. 2000, ApJ, 126, 19
- Price, P. A. 2006, GRB Coordinates Network, 5104, 1
- Price, P. A., Kulkarni, S. R., Berger, E., et al. 2002a, ApJ, 571, L121
- Price, P. A., Berger, E., Kulkarni, S. R., et al. 2002b, ApJ, 573, 85
- Prochaska, J. X., Chen, H.-W., Dessauges-Zavadsky, M., & Bloom, J. S. 2007a, ApJ, 666, 267
- Prochaska, J. X., Cooper, M., Newman, J., et al. 2005a, GRB Coordinates Network, 3390
- Prochaska, J. X., Dessauges-Zavadsky, M., Ramirez-Ruiz, E., & Chen, H.-W. 2008, ApJ, 685, 344
- Prochaska, J. X., Ellison, S., Foley, R. J., Bloom, J. S., & Chen, H.-W. 2005b, GRB Coordinates Network, 3332, 1
- Prochaska, J. X., Perley, D. A., Modjaz, M., et al. 2007b, GRB Coordinates Network, 6864, 1
- Prochaska, J. X., Bloom, J. S., Chen, H.-W., et al. 2004, ApJ, 611, 200
- . 2006, ApJ, 642, 989
- Prochaska, J. X., Chen, H.-W., Bloom, J. S., et al. 2007c, ApJ, 168, 231
- Qin, Y., Liang, E.-W., Liang, Y.-F., et al. 2013, ApJ, 763, 15
- Quimby, R., Fox, D., Hoeflich, P., Roman, B., & Wheeler, J. C. 2005, GRB Coordinates Network, 4221, 1
- Racusin, J. L., Burns, E., Goldstein, A., et al. 2017, ApJ, 835, 82
- Rau, A., Fynbo, J., & Greiner, J. 2010a, GRB Coordinates Network, 10350, 1

- Rau, A., Kruehler, T., & Greiner, J. 2013, GRB Coordinates Network, 15330, 1
- Rau, A., McBreen, S., & Kruehler, T. 2009, GRB Coordinates Network, 9353, 1
- Rau, A., Salvato, M., & Greiner, J. 2005, A&A, 444, 425
- Rau, A., Savaglio, S., Krühler, T., et al. 2010b, ApJ, 720, 862
- Rees, M. J., & Mészáros, P. 1998, ApJ, 496, L1
- Reid, M. J. 1993, Annual Review of Astronomy and Astrophysics, 31, 345
- Rhoads, J. E. 2010, ApJ, 709, 664
- Richardson, G., Koshut, T., Paciesas, W., & Kouveliotou, C. 1996, in American Institute of Physics Conference Series, Vol. 384, American Institute of Physics Conference Series, ed. C. Kouveliotou, M. F. Briggs, & G. J. Fishman, 87–90
- Ricker, G., Atteia, J.-L., Kawai, N., et al. 2002, GRB Coordinates Network, 1530, 1
- Rossi, A., Piranomonte, S., Savaglio, S., et al. 2014, A&A, 572, A47
- Rowlinson, A., O'Brien, P. T., Metzger, B. D., Tanvir, N. R., & Levan, A. J. 2013, MNRAS, 430, 1061
- Rowlinson, A., Wiersema, K., Levan, A. J., et al. 2010a, MNRAS, 408, 383
- Rowlinson, A., O'Brien, P. T., Tanvir, N. R., et al. 2010b, MNRAS, 409, 531
- Ruderman, M. A. 1974, Science, 184, 1079
- Ruiz-Velasco, A. E., Swan, H., Troja, E., et al. 2007, ApJ, 669, 1
- Sahu, K. C., Livio, M., Petro, L., et al. 1997, Nature, 387, 476
- Sakamoto, T., Barthelmy, S. D., Baumgartner, W. H., et al. 2010, GRB Coordinates Network, 10524, 1
- Sakamoto, T., Lamb, D. Q., Kawai, N., et al. 2005a, ApJ, 629, 311
- Sakamoto, T., Ricker, G., Atteia, J.-L., et al. 2005b, GRB Coordinates Network, 3189, 1
- Sakamoto, T., Sato, G., Barbier, L., et al. 2009, ApJ, 693, 922
- Sakamoto, T., Barthelmy, S. D., Baumgartner, W., et al. 2011a, GRB Coordinates Network, 12276, 1
- Sakamoto, T., Barthelmy, S. D., Baumgartner, W. H., et al. 2011b, ApJ, 195, 2
- Salvaterra, R., Della Valle, M., Campana, S., et al. 2009, Nature, 461, 1258

- Sanchez-Ramirez, R., Gorosabel, J., Castro-Tirado, A. J., Cepa, J., & Gomez-Velarde, G. 2013, GRB Coordinates Network, 14685, 1
- Sanchez-Ramirez, R., Gorosabel, J., de Ugarte Postigo, A., & Gonzalez Perez, J. M. 2012, GRB Coordinates Network, 13723, 1
- Sari, R., & Mészáros, P. 2000, ApJ, 535, L33
- Sari, R., Piran, T., & Narayan, R. 1998, ApJ, 497, L17
- Savaglio, S., Glazebrook, K., & Le Borgne, D. 2009, ApJ, 691, 182
- Savaglio, S., Rau, A., Greiner, J., et al. 2012, MNRAS, 420, 627
- Savchenko, V., Neronov, A., & Courvoisier, T. J.-L. 2012, A&A, 541, A122
- Scalo, J., & Wheeler, J. C. 2002, ApJ, 566, 723
- Schady, P., Page, M. J., Oates, S. R., et al. 2010, MNRAS, 401, 2773
- Schady, P., Krühler, T., Greiner, J., et al. 2015, A&A, 579, A126
- Schaefer, B. E., Snyder, J. A., Hernandez, J., et al. 1999, ApJ, 524, L103
- Schulze, S., Klose, S., Björnsson, G., et al. 2011, A&A, 526, A23
- Schulze, S., Malesani, D., Cucchiara, A., et al. 2014, A&A, 566, A102
- Serino, M., Sakamoto, T., Kawai, N., et al. 2014, Publications of the Astronomical Society of Japan, 66, 87
- Smee, S. A., Gunn, J. E., Uomoto, A., et al. 2013, AJ, 146, 32
- Smette, A., Ledoux, C., Vreeswijk, P., et al. 2013, GRB Coordinates Network, 14848, 1
- Soderberg, A. M., Kulkarni, S. R., Berger, E., et al. 2004, ApJ, 606, 994
- Soderberg, A. M., Kulkarni, S. R., Price, P. A., et al. 2006a, ApJ, 636, 391
- Soderberg, A. M., Kulkarni, S. R., Nakar, E., et al. 2006b, Nature, 442, 1014
- Soderberg, A. M., Berger, E., Kasliwal, M., et al. 2006c, ApJ, 650, 261
- Sparre, M., de Ugarte Postigo, A., Fynbo, J. P. U., et al. 2011a, GRB Coordinates Network, 11607, 1
- Sparre, M., Sollerman, J., Fynbo, J. P. U., et al. 2011b, ApJ, 735, L24
- Sparre, M., Hartoog, O. E., Krühler, T., et al. 2014, ApJ, 785, 150
- Stalder, B., Tonry, J., Smartt, S. J., et al. 2017, ArXiv e-prints, arXiv:1706.00175
- Stanek, K. Z., Matheson, T., Garnavich, P. M., et al. 2003, ApJ, 591, L17

- Stanway, E. R., Levan, A. J., Tanvir, N., et al. 2015, MNRAS, 446, 3911
- Strateva, I., Ivezić, Ž., Knapp, G. R., et al. 2001, AJ, 122, 1861
- Stratta, G., Basa, S., Butler, N., et al. 2007, A&A, 461, 485
- Strong, I. B., Klebesadel, R. W., & Olson, R. A. 1974, ApJ, 188, L1
- Sun, H., Zhang, B., & Gao, H. 2017, ApJ, 835, 7
- Sun, H., Zhang, B., & Li, Z. 2015, ApJ, 812, 33
- Sutcliffe, O. E., Dowdeswell, J. A., Whittington, R. J., Theron, J. N., & Craig, J. 2000, Geology, 28, 967
- Svensmark, H. 2012, MNRAS, 423, 1234
- Svensson, K. M., Levan, A. J., Tanvir, N. R., Fruchter, A. S., & Strolger, L.-G. 2010, MNRAS, 405, 57
- Svensson, K. M., Levan, A. J., Tanvir, N. R., et al. 2012, MNRAS, 421, 25
- Tanvir, N., Levan, A., Wiersema, K., et al. 2009a, GRB Coordinates Network, 9219
- Tanvir, N. R., & Ball, J. 2012, GRB Coordinates Network, 13532, 1
- Tanvir, N. R., Cucchiara, A., & Cenko, S. B. 2013a, GRB Coordinates Network, 14366, 1
- Tanvir, N. R., Fox, D., Fynbo, J., & Trujillo, C. 2012a, GRB Coordinates Network, 13562, 1
- Tanvir, N. R., Kruehler, T., Schulze, S., & Karjalainen, R. 2014a, GRB Coordinates Network, 15988
- Tanvir, N. R., Levan, A. J., Cucchiara, A., Perley, D., & Cenko, S. B. 2014b, GRB Coordinates Network, 16125, 1
- Tanvir, N. R., Levan, A. J., Fruchter, A. S., et al. 2013b, Nature, 500, 547
- Tanvir, N. R., Levan, A. J., & Matulonis, T. 2012b, GRB Coordinates Network, 14009, 1
- Tanvir, N. R., Levan, A. J., Matulonis, T., & Smith, A. B. 2013c, GRB Coordinates Network, 14567, 1
- Tanvir, N. R., Levan, A. J., Wiersema, K., et al. 2014c, GRB Coordinates Network, 16150, 1
- Tanvir, N. R., Wiersema, K., & Levan, A. J. 2010a, GRB Coordinates Network, 11230, 1
- Tanvir, N. R., Wiersema, K., Levan, A. J., Cenko, S. B., & Geballe, T. 2011, GRB Coordinates Network, 12225, 1

- Tanvir, N. R., Wiersema, K., Levan, A. J., et al. 2012c, GRB Coordinates Network, 13441, 1
- Tanvir, N. R., Wiersema, K., Xu, D., & Fynbo, J. P. U. 2013d, GRB Coordinates Network, 14882, 1
- Tanvir, N. R., Fox, D. B., Levan, A. J., et al. 2009b, Nature, 461, 1254
- Tanvir, N. R., Vergani, S., Hjorth, J., et al. 2010b, GRB Coordinates Network, 11123, 1
- Tanvir, N. R., Rol, E., Levan, A. J., et al. 2010c, ApJ, 725, 625
- Tanvir, N. R., Levan, A. J., Fruchter, A. S., et al. 2012d, ApJ, 754, 46
- Tello, J. C., Sanchez-Ramirez, R., Gorosabel, J., et al. 2012, GRB Coordinates Network, 13118, 1
- Thoene, C. C., de Ugarte Postigo, A., Gorosabel, J., et al. 2012, GRB Coordinates Network, 13628, 1
- Thoene, C. C., Perley, D. A., Cooke, J., et al. 2007, GRB Coordinates Network, 6741, 1
- Thoene, C. C., Jakobsson, P., De Cia, A., et al. 2009, GRB Coordinates Network, 9409, 1
- Thomas, B. C., Jackman, C. H., Melott, A. L., et al. 2005a, ApJ, 622, L153
- Thomas, B. C., Neale, P. J., & Snyder, II, B. R. 2015, Astrobiology, 15, 207
- Thomas, B. C., Melott, A. L., Jackman, C. H., et al. 2005b, ApJ, 634, 509
- Thöne, C. C., Kann, D. A., Jóhannesson, G., et al. 2010, A&A, 523, A70
- Thöne, C. C., Fynbo, J. P. U., Goldoni, P., et al. 2013, MNRAS, 428, 3590
- Thorsett, S. E. 1995, ApJ, 444, L53
- Tinney, C., Stathakis, R., Cannon, R., et al. 1998, IAUC, 6896, 3
- Toy, V. L., Cenko, S. B., Silverman, J. M., et al. 2016, ApJ, 818, 79
- Troja, E., Cusumano, G., O'Brien, P. T., et al. 2007, ApJ, 665, 599
- Tunnicliffe, R. L., Levan, A. J., Tanvir, N. R., et al. 2014, MNRAS, 437, 1495
- van der Horst, A. J., Levan, A. J., Pooley, G. G., et al. 2015, MNRAS, 446, 4116
- van der Wel, A., Franx, M., van Dokkum, P. G., et al. 2014, ApJ, 788, 28
- van Paradijs, J., Groot, P. J., Galama, T., et al. 1997, Nature, 386, 686
- Vergani, S. D., D'Avanzo, P., Malesani, D., et al. 2010, GRB Coordinates Network, 10495, 1
- Vergani, S. D., Flores, H., Covino, S., et al. 2011, A&A, 535, A127

- Vergani, S. D., Salvaterra, R., Japelj, J., et al. 2015, A&A, 581, A102
- Verrecchia, F., Tavani, M., Ursi, A., et al. 2017, ArXiv e-prints, arXiv:1706.00029
- Vestrand, W. T., Wozniak, P. R., Wren, J. A., et al. 2005, Nature, 435, 178
- Villasenor, J. S., Lamb, D. Q., Ricker, G. R., et al. 2005, Nature, 437, 855
- Virgili, F. J., Liang, E.-W., & Zhang, B. 2009, MNRAS, 392, 91
- Virgili, F. J., Qin, Y., Zhang, B., & Liang, E. 2012, MNRAS, 424, 2821
- Virgili, F. J., Zhang, B., Nagamine, K., & Choi, J.-H. 2011, MNRAS, 417, 3025
- Volnova, A. A., Pozanenko, A. S., Gorosabel, J., et al. 2014, MNRAS, 442, 2586
- von Kienlin, A., Meegan, C. A., Paciesas, W. S., et al. 2014, ApJ, 211, 13
- Vreeswijk, P., Fruchter, A., Hjorth, J., & Kouveliotou, C. 2003, GRB Coordinates Network, 1785, 1
- Vreeswijk, P. M., Ledoux, C., De Cia, A., & Smette, A. 2012, Memorie della Societa Astronomica Italiana Supplementi, 21, 14
- Vreeswijk, P. M., Rol, E., Hjorth, J., et al. 1999, GRB Coordinates Network, 496, 1
- Vreeswijk, P. M., Fruchter, A., Kaper, L., et al. 2001, ApJ, 546, 672
- Vreeswijk, P. M., Ellison, S. L., Ledoux, C., et al. 2004, A&A, 419, 927
- Vreeswijk, P. M., Smette, A., Fruchter, A. S., et al. 2006, A&A, 447, 145
- Vreeswijk, P. M., Ledoux, C., Smette, A., et al. 2007, A&A, 468, 83
- Wainwright, C., Berger, E., & Penprase, B. E. 2007, ApJ, 657, 367
- Wanderman, D., & Piran, T. 2010, MNRAS, 406, 1944
- Watson, D., Fynbo, J. P. U., Ledoux, C., et al. 2006, ApJ, 652, 1011
- Weinmann, S. M., Neistein, E., & Dekel, A. 2011, MNRAS, 417, 2737
- Wiersema, K., Levan, A., Kamble, A., Tanvir, N., & Malesani, D. 2009, GRB Coordinates Network, 9673, 1
- Wiersema, K., van der Horst, A. J., Kann, D. A., et al. 2008, A&A, 481, 319
- Wiersema, K., Flores, H., D'Elia, V., et al. 2011, GRB Coordinates Network, 12431, 1
- Woosley, S. E. 1993, ApJ, 405, 273
- Woosley, S. E., & Bloom, J. S. 2006, Annual Review of Astronomy and Astrophysics, 44, 507

- Xiong, S. 2013, GRB Coordinates Network, 14674
- . 2016, ArXiv e-prints, arXiv:1605.05447
- Xu, D., Fynbo, J. P. U., D'Elia, V., & Tanvir, N. R. 2012, GRB Coordinates Network, 13460, 1
- Xu, D., Fynbo, J. P. U., Jakobsson, P., et al. 2013a, GRB Coordinates Network, 15407, 1
- Xu, D., Fynbo, J. P. U., Tanvir, N. R., et al. 2009, GRB Coordinates Network, 10053, 1
- Xu, D., de Ugarte Postigo, A., Leloudas, G., et al. 2013b, ApJ, 776, 98
- Yang, B., Jin, Z.-P., Li, X., et al. 2015, Nature Communications, 6, 7323
- Yonetoku, D., Murakami, T., Nakamura, T., et al. 2004, ApJ, 609, 935
- Yoshida, M., Utsumi, Y., Tominaga, N., et al. 2017, Publications of the Astronomical Society of Japan, 69, 9
- Younes, G. 2013, GRB Coordinates Network, 15477, 1
- Yu, H.-F., & Goldstein, A. 2014, GRB Coordinates Network, 16224
- Zafar, T., Watson, D. J., Malesani, D., et al. 2010, A&A, 515, A94
- Zauderer, B. A., Berger, E., Margutti, R., et al. 2013, ApJ, 767, 161
- Zhang, B. 2006, Nature, 444, 1010
- . 2016, ApJ, 827, L31
- Zhang, B., Fan, Y. Z., Dyks, J., et al. 2006, ApJ, 642, 354
- Zhang, B., & Mészáros, P. 2001a, ApJ, 552, L35
- . 2001b, ApJ, 559, 110
- Zhang, B., Zhang, B.-B., Liang, E.-W., et al. 2007, ApJ, 655, L25
- Zhang, B., Zhang, B.-B., Virgili, F. J., et al. 2009, ApJ, 703, 1696
- Zhang, F.-W., Shao, L., Yan, J.-Z., & Wei, D.-M. 2012, ApJ, 750, 88

CURRICULUM VITA

Graduate College
University of Nevada, Las Vegas

Ye Li

Degrees:

Bachelor of Science 2007

East China Normal University

Master of Science 2012

Yunnan Observatories, Chinese Academy of Sciences

Publication list of my Ph.D. study:

[8] **Ye Li**, Amy Lien, Bing Zhang, Kazumi Kashiyama, *Searching for Neutron Star-Neutron Star mergers as SGRB-less Extended Emissions*, in preparation.

[7] **Ye Li**, Bing Zhang, *A Comparative Study of Long and Short GRBs. II. Classification of GRBs with a multi-wavelength method*, in preparation.

[6] **Ye Li**, Bing Zhang, Hou-Jun Lü, *A Comparative Study of Long and Short GRBs. I. Overlapping Properties*, The Astrophysical Journal Supplement Series, Volume 227, Issue 1, article id. 7, 32 pp. (2016)

[5] **Ye Li**, Bing Zhang, *Can Life Survive Gamma-Ray Bursts in the High-redshift Universe?*, The Astrophysical Journal, Volume 810, Issue 1, article id. 41, 7 pp. (2015)

[4] **Ye Li**, Bing Zhang, *Radio transient following FRB 150418: afterglow or coincident AGN flare*, arXiv: 1603.04825, 2016

[3] He Gao, Bing Zhang, Hou-Jun Lü, **Ye Li**, Searching for Magnetar-powered Merger-novae from Short GRBs, The Astrophysical Journal, Volume 837, Issue 1, article id. 50, 9 pp. (2017)

[2] Tong Liu, Bing Zhang, **Ye Li**, Ren-Yi Ma, Li Xue, *Detectable MeV neutrinos from black hole neutrino-dominated accretion flows*, Physical Review D, Volume 93, Issue 12, id.123004 (2016)

[1] Hou-Jun Lü, Bing Zhang, Wei-Hua Lei, **Ye Li**, Paul D. Lasky, *The Millisecond Magnetar Central Engine in Short GRBs*, The Astrophysical Journal, Volume 805, Issue 2, article id. 89, 18 pp. (2015).

Dissertation Title:

Understanding Progenitors of Gamma Ray Bursts with multi-wavelength properties

Dissertation Examination Committee:

Chairperson, Bing Zhang, Ph.D.

Committee Member, Daniel Proga, Ph.D.

Committee Member, George Rhee, Ph.D.

Graduate Faculty Representative, Amei Amei, Ph.D.